NASA Contractor Report 4261

A Study of the Temporal Stability of Multiple Cell Vortices

Mehdi R. Khorrami
Old Dominion University Research Foundation
Norfolk, Virginia

Prepared for
Langley Research Center
under Grant NAG1-530

National Aeronautics and
Space Administration
Office of Management
Scientific and Technical
Information Division

1989

SUMMARY

The present study documents in detail the effect of initial mean velocity field on the stability characteristics of longitudinal vortices. The temporal stability of isolated multiple cell vortices is considered. The types of vortices studied in this work include single cell as well as two and three cell vortices. It is shown that cell multiplicity in the vortex core has drastic effects on the stability characteristics. On the basis of numerical calculations, it is concluded that the growth rates of instabilities in multiple cell vortices are substantially larger (two to three fold increases are observed) than those of a single cell vortex. It is also determined that there is a substantial increase in the effective range of axial and azimuthal wavenumbers where instabilities are present, but of most importance is the appearance of a variety of viscous modes of instability. In the case of vortices, these latter instabilities which highlight the importance of viscous forces have never been reported before. For the case of a two cell vortex, these effects are discussed in detail.

A Chebyshev spectral collocation method with staggered grid was developed for application to stability calculations for general three dimensional swirling flows. The stability problem is formulated in the primitive variable form; hence the use of staggered grid eliminates the need for artificial pressure boundary conditions. It is shown that this method is robust and produces results very accurately and efficiently.

While validating the spectral collocation algorithm, two new viscous modes of instability for Batchelor's vortex were found. These two forms of instabilities include an axisymmetric, $n = 0$, as well as an asymmetric, $n = 1$ mode. Here, n is the azimuthal wavenumber of the disturbance. It is shown that both of these modes are consistent with the pathology of contrail photos of large trailing line vortices as well as with experimental measurements conducted in laboratory wind tunnels. Both of these disturbances are discussed in some detail.

LIST OF SYMBOLS

$\hat{a}$	a constant for coordinate mapping (Eq. (4.4))
C	constant non-dimensional pressure gradient
$\hat{\mathbf{C}}$	center mode instabilities
C_i	perturbation growth rate (ω_i/α)
C_r	perturbation phase speed (ω_r/α)
D	coefficient matrix representing discretized differential operator
$\vec{e}_r, \vec{e}_\theta, \vec{e}_z$	unit vectors in cylindrical (r, θ, z) coordinates
F	radial perturbation eigenfunction
f	a similarity variable for the mean velocity profile
G	azimuthal perturbation eigenfunction
H	axial perturbation eigenfunction
L	eigenvalue coefficient matrix
n	azimuthal wavenumber
P	pressure perturbation eigenfunction
p	perturbation pressure
$\tilde{p}$	combined mean and perturbation pressure
q	a swirl parameter defined as the ratio of maximum azimuthal velocity to the centerline axial velocity
$\tilde{q}$	a swirl parameter related to q as defined on page 44
$\hat{\mathbf{R}}$	ring mode instabilities
Re	Reynolds number based on pipe radius $\frac{W_o R_o}{\nu}$
R_o	pipe radius
r	radial coordinate

r_{max}	the radial position where far field boundary conditions (at infinity) are applied
r_o	a local radius
r_*	dimensional radial coordinate
S_j	scaling factors obtained from coordinate mapping
U	mean radial velocity
u	radial perturbation velocity
$\tilde{u}$	combined mean and perturbation radial velocity
V	mean azimuthal velocity
v	azimuthal perturbation velocity
$\vec{V}$	total velocity vector
$\vec{v}$	perturbation velocity vector
$\tilde{v}$	combined mean and perturbation azimuthal velocity
W	mean axial velocity
w	axial perturbation velocity
$\hat{W}$	wall mode instabilities
$\bar{W}$	a function representing the radially dependent part of the mean axial velocity
$\tilde{w}$	combined mean and perturbation axial velocity
W_o	centerline axial velocity
W_1, W_2	two constants in the axial velocity of a Batchelor vortex (Eq. (4.2))
$\vec{\chi}$	a vector representing the eigenfunctions
z	axial coordinate

Greek Symbols

α	axial wavenumber
β	compressibility factor

ε	Rossby number defined as $\frac{W_o}{2\Omega_o R_o}$
ϕ	angle as defined in Eq. (3.3)
Γ	flow circulation defined as rV
γ_r	a parameter identifying the position of the critical layer as defined in Eq. (1.4)
η	a similarity parameter for the mean velocity profile
λ	eigenvalue of the discretized system
ν	kinematic viscosity
Π	mean pressure
θ	azimuthal coordinate
ρ	density
Ω	angular velocity of the flow
ω	complex angular perturbation frequency
ω_i	imaginary part of ω
ω_r	real part of ω
ξ	independent variable in Chebyshev space
ψ	a parameter representing non-parallel effects in mean velocity profile

Chapter 1

INTRODUCTION

The study of the stability of streamwise vortices is an important and active area of major current research. Control and manipulation of organized longitudinal vortical motions is of interest for several applications such as the wake-vortex hazard problem, three-dimensional flow separation control, and combustor optimization. The breakdown of leading edge vortices on delta wings, which severely reduces lift, and the very stable wing tip vortices shed from large commercial aircraft, which determine the flight frequency at airports, are two classical examples.

Although the best (and natural) way to attack these problems is through theoretical investigations or full numerical simulations, major difficulties exist. The theoretical difficulty with stability analyses was identified in the classic work of Howard and Gupta [1]*. They determined that for steady, inviscid, incompressible three-dimensional vortices subjected to three-dimensional disturbances, no general necessary and sufficient condition for stability (or instability) could be found. Hence, to obtain stability characteristics, each vortex flow must be studied individually. After twenty-five years of active research, the finding [1] still holds today which is a source of major disappointment. Aside from the prohibitive cost of each numerical simulation, computational results lack the needed spatial

---

*The numbers in brackets indicate references.

resolution. They are also restricted to low Reynolds number flows, and the proper imposed outflow boundary conditions are unclear. Therefore, for practical purposes, at the present time, one is forced to rely on the same tools which have been developed as far back as seventy years ago and were applied successfully to studies of the stability of boundary layer flows. One such tool is normal mode analysis. Indeed in the present author's opinion, our current understanding of vortex stability resembles the state of affairs for boundary layer stability in the 1930's. Our total lack of understanding of the importance of such effects as

(a) initial mean velocity profile
(b) non-parallel mean velocity profiles
(c) turbulence
(d) density stratification
(e) compressibility

on the stability characteristics of vortices is widely known and a source of concern. Meaningful experimental data are rare because vortices are very sensitive to probe intrusion and flow visualization is biased by the strong body forces acting on any foreign particles. Also, it is very difficult to isolate the effects of each of the parameters mentioned above on vortices, much less measure them. Even the stability calculations conducted numerically have had their share of problems. The complexity stems from the three-dimensional nature of the phenomena and hence the necessity of finding three-dimensional mean velocity profiles which are solutions of the Navier-Stokes equations. Most of the stability calculations to date have used Batchelor's vortex [2], and in some cases Long's vortex [3, 4] or solid body rotation superimposed on Poiseuille flow in a pipe as the basic unperturbed flow.

The present study is directed toward understanding the influence of the initial mean velocity profile on the stability of an axial vortex. From an engineering standpoint, the research goal is to develop vortex control strategies via alteration of vortex stability characteristics. Vortex stability can be altered through modification of the initial three-dimensional mean-velocity field of the vortex. Bushnell (private communications) has put forth the idea that once the desired stability characteristics are produced by a particular velocity profile, the control problem can be inverted in the sense that the wing tip geometry can be tailored to produce the requisite velocity profile.

First, an overview of some of the important theoretical and computational studies regarding hydrodynamic stability of vortices is given. This review is by no means exhaustive, but the cited papers are those which have been judged relevant to the present research. It must be emphasized here that no attempt has been made to relate the current work to the question of vortex breakdown as described in the open literature. As has been mentioned by Leibovich [5], vortex stability and vortex breakdown are two distinct phenomena (problems) which may, in some circumstances, be interrelated. Many reviews have been written concerning the breakdown of vortices. The reader is referred to the works of Hall [6], Hall [7], Leibovich [5, 8] and Escudier [9] for further information regarding vortex breakdown. In Chap. 2, the stability problem is formulated and the governing equations, along with boundary conditions, are derived. The normal mode analysis is discussed briefly and also the type of mean velocity profiles employed in the present work are explained fully. Chapter 3 contains the numerical algorithm employed in these calculations. It is an extension of the spectral collocation technique developed recently by Khorrami, Malik and Ash [10]; hereafter referred to as KMA. The method is tested for convergence and accuracy against the results of some well known calculations and the results are reported in Chap. 4. Specifically, two cases have been considered; Poiseuille flow in a pipe, and Batchelor's vortex. In the latter case, two new viscous modes of instability have been found which have not been reported previously. Chapter 5 contains the stability results for a variety of mean velocity profiles. The profiles include a single cell vortex as well as multiple cell vortices. Finally, the concluding remarks are presented in Chap. 6. Here the major results obtained in Chaps. 4 and 5 are highlighted and suggestions for future work are given.

The review in this chapter is broken up into four separate sections. Section one contains those stability criteria which are general in nature and do not depend on the form of the assumed mean velocity profile. The stability results for Hagen-Poiseuille flow with superimposed solid body rotation is discussed in section two. Section three is devoted primarily to the stability of Long's vortex but also includes some other miscellaneous profiles. Finally, the stability characteristics of Batchelor's vortex are presented in the fourth section. It must be stressed here that, unless otherwise specified explicitly, the stability results presented in these sections are for inviscid, incompressible fluid. Hence, the viscous results are identified explicitly in this review while the inviscid results are not.

1.1 General Stability Criteria

The hydrodynamic stability of a vortex was first studied by Lord Rayleigh [11]. In his classical paper, he showed (intuitively and using an angular momentum argument) that a necessary and sufficient condition for stability of a vortex without an axial velocity component was that the square of circulation must increase outwards. That is

$$\frac{d(\Gamma^2)}{dr} > 0 \qquad (1.1)$$

everywhere. Here, Γ is the circulation and r is the radial coordinate. Rayleigh's result was proved in a rigorous manner mathematically by Synge [12], who showed that stability of a heterogeneous vortex is assured if and only if

$$\frac{d}{dr}(\rho\Gamma^2) > 0, \qquad (1.2)$$

where ρ is the density. It is clear from Eq. (1.2) that in the case of a constant density fluid, Rayleigh's criterion is obtained. Much later, Howard and Gupta [1] were able to give a sufficient condition for the stability of a vortex with an axial velocity component (subject to axisymmetric disturbances). They found that for stability the local inequality

$$\frac{1}{r^3}\frac{d\Gamma^2}{dr}/\left(\frac{dW}{dr}\right)^2 > 1/4 \qquad (1.3)$$

must be satisfied everywhere. Here, W is the axial velocity. It is obvious from the above criterion that axial shear has a destabilizing effect. It must be emphasized that violation of (1.3) does not necessarily mean instability.

For non-axisymmetric disturbances, Howard and Gupta found a sufficient condition for stability in terms of axial and azimuthal wavenumbers. They stated that this criterion is always violated for sufficiently small axial wavenumbers, and while this does not imply instability, it has led them to suggest that no general necessary and sufficient condition is obtainable. As indicated earlier, their statement still holds and thus far no new general criterion has been obtained.

1.2 Stability of Hagen-Poiseuille Flow with Superimposed Rigid Rotation

The stability of rotating pipe flows has been studied by many investigators. Using the radial disturbance eigenfunction equation derived by

Howard and Gupta, Pedley [13] showed (interestingly in an analytical and tractable manner) that for a very small Rossby number ($\varepsilon \equiv \frac{W_0}{2\Omega_0 R_0}$, where Ω_0 is the angular velocity of the pipe wall, R_0 is the pipe radius and W_0 is the centerline axial velocity) the flow is unstable to non-axisymmetric disturbances of sufficiently large axial wavelength. He found that, although both solid body rotation and Poiseuille flow in a pipe are stable with respect to infinitesimal disturbances, the superimposed combined flow (which resembles a helical vortex) is highly unstable. These disturbances are helical traveling waves which wrap around the mean flow in the opposite direction to the streamlines. The growth rate of the most rapidly growing disturbance is $2\varepsilon\ \Omega_0$. In a follow-up paper, Pedley [14] showed that for viscous disturbances, the critical Reynolds number, Re_c, has a value of 82.9 corresponding to azimuthal wavenumber, $n = -1$. The critical Reynolds number increases as the value of azimuthal wavenumber, n, increases. The disturbances are stationary relative to the rotating frame of reference, and as the Reynolds number increases, the wavenumber of the most rapidly growing disturbance also increases. Pedley's findings were confirmed by Metcalfe and Orszag [15] who employed a spectral tau method; and later on they were reconfirmed by KMA.

Maslowe [16] extended the work of Pedley [13] without making any assumption as to the magnitude of the Rossby number, ε. He showed that the most unstable modes have negative azimuthal wavenumbers, n. They spiral in the same direction as the basic flow rotation (note this is in contradiction to Pedley's finding which is caused by different interpretations of what direction a wave with negative azimuthal wavenumber spirals) but propagate upstream in the axial direction with an axial phase speed $O(\varepsilon^{-1})$. The amplification factor and the axial wavenumber, α, of the fastest growing disturbance peaked at a finite Rossby number ε of O(1) while the growth rate showed little variation with n for $|n| > 2$ at finite values of ε. These instabilities persist at very large values of ε and have larger growth rates than suggested previously. Maslowe was also able to prove that a necessary condition for instability could be predicted using a parameter, γ_r, defined by

$$\gamma_r = \alpha\varepsilon\Omega_0 W + n\,\Omega_0 - \omega_r , \qquad (1.4)$$

where ω_r is the real part of the growth rate, ω. If γ_r was zero anywhere in the interval $(0, R_0)$, the flow was unstable. Condition (1.4) is a formal statement for the existence of a critical layer in inviscid swirling flows.

The neutral stability curves for rotating Poiseuille flow subjected to viscous disturbances is given by MacKrodt [17]. He found that the first mode which becomes unstable is for the case of $n = -1$ with a critical Reynolds number of $Re_c = 82.88$ which is exactly the value obtained by Pedley. However, MacKrodt's major observation was the fact that at high Reynolds numbers, the amount of rotation required for destabilization is much smaller than had been expected.

In a very extensive study by Cotton and Salwen [18], MacKrodt's results were extended to much higher Reynolds numbers, Re, and rotation rates, Ω_0. In their viscous calculations, they found that the instability region is pushed to higher Re and Ω_0 when $\alpha \gtrsim 2$. The disturbances are center mode at least for high α; that is most of their energy is confined near the centerline of the pipe. The bulk of their study was directed toward the $n = -1$ mode where they calculated the neutral stability curves for the primary mode and for several higher modes (the existence of these higher modes were first established by Duck and Foster [19] for the case of a trailing line vortex; we will come back to this point repeatedly as the review proceeds). Cotton and

Salwen found out that although the upper branches of the neutral curves are in excellent agreement with the results of Pedley the lower branches behave in a more complicated manner. That is, there were many kinks, loops, points of degeneracy, branching, and mode crossing or jumping associated with the lower branch which had not been identified previously.

A study of the asymptotic nature of the neutral modes in the case of $|n| >> 1$ was attempted by Maslowe and Stewartson [20] using perturbation theory. Expanding the eigenfunctions in descending powers of n, they showed that the neutral disturbances were of the wall mode type and there are infinite numbers of neutral stability modes for any n and ε, which is consistent with the results of Pedley [13] and Duck and Foster [19]. However, the neutral wall modes obtained by [20] are not the limiting inviscid modes (as $Re \to \infty$) associated with the viscous modes obtained by Cotton and Salwen. This important discrepancy with the viscous results of [18] led [20] to suggest that the role of viscosity in swirling flows is more subtle than previously thought, and that it alters the shape of the perturbation's eigenfunction significantly. For the case of $n = -1$, Maslowe and Stewartson [20] resorted to a numerical method and found the eigenfunction structure differed significantly from the modes with large n. At finite values of ε, the critical layer associated with $n = -1$ was close to the centerline. However, as $\varepsilon \to \infty$, the critical layer moved very slowly toward the pipe wall. Finally, Maslowe and Stewartson postulated from their results that if a swirling pipe flow meets the conditions

$$V(R_0) \neq 0, \qquad (1.5a)$$

and

$$\frac{dW}{dr}(R_0) \neq 0, \qquad (1.5b)$$

then the flow must be unstable.

The results for neutrally stable disturbances were obtained in a closed form by Ito, Suematsu, and Hayase [21]. However, rather than assuming Poiseuille flow, they employed a uniform axial velocity. They found that there are an infinite number of higher modes for each distinct set of flow parameters. Looking for stationary waves, they found the range of the Rossby number for which there exists a stationary axisymmetric mode ($n = 0$) to be

$$0 < \varepsilon < 0.522 \ . \tag{1.6}$$

However, in the case of non-axisymmetric modes, they stated that no such restriction on the value of Rossby number exists. Since they never looked for unstable disturbances, no conclusions can be made with regard to the possibility that a pipe flow might become unstable even though it does not meet the requirement specified in (1.5b).

1.3 Stability of Long's Vortex

The similarity solution for a bathtub vortex due to Long [3, 4], has been employed by several researchers to obtain the stability characteristics of tornado type vortices. Such a vortex was first used by Burggraf and Foster [22]. However, they had great difficulties with their numerical approach (a local shooting method) in obtaining converged solutions. They attributed the failure of the numerical method to the algebraically (as contrasted with exponentially) decaying axial velocity W. An algebraically decaying mean flow requires a large integration radius at which the far field boundary conditions are imposed, which in turn causes great difficulties with the integration step size. The dependency of the eigenvalues on this radius will be explained in greater detail in Chap. 4. Switching to an exponential velocity profile, Burggraf and Foster obtained converged solutions and appear to be the first to report, numerically, the existence of a spectrum of unstable eigenvalues (a result which generally is credited to Duck and Foster [19]). They found that as in the case of a rotating pipe, the most dangerous disturbances have an azimuthal wavenumber, $n = -1$.

The calculations of [22] were extended by Foster and Duck [23]. Employing a global finite difference technique similar to that of [19], they encountered no difficulty in obtaining converged results for Long's vortex. They showed that only the negative azimuthal wavenumbers are unstable and the most unstable mode is approached in the limit as $n \to -\infty$. This result, which apparently holds for all inviscid swirling flows, was first reported by Lessen, Singh, and Paillet [24] for the case of a trailing line vortex. The general belief in the stability community is that viscosity would effect these disturbances so that the most unstable mode would occur at a finite value of n. Foster and Duck mentioned that every effort to obtain instabilities for $n > 0$ failed; and that a vortex with a single cell core is more unstable than a two cell vortex. It is also apparent from their growth rate plots that in the case of the Long vortex, inviscid instabilities are an order of magnitude weaker than for the case of a trailing line vortex.

Staley and Gall [25] employed a vortex which has continuous velocity components, but whose vorticity field has many discontinuities. Their work is mentioned to show that even with such a crude approximation for the mean field of a vortex, they obtained results that in general substantiate the findings of [19, 23, 24]. That is, the solutions indicate an infinite number of higher modes and the most unstable mode is approached as $n \to -\infty$. They also obtained an instability criterion (for large n) in terms of the vorticity field which appears to be another version of the sufficiency condition first reported by Leibovich and Stewartson [26].

1.4 Stability of Batchelor's (Trailing Line) Vortex

The stability of the mean velocity profile of a trailing line vortex (Batchelor [2]) was studied by Lessen et al. [24] with respect to infinitesimal, non-axisymmetric disturbances. It was found that negative azimuthal wavenumbers are destabilized by the addition of swirl. Lessen et al. discovered that the stability characteristics of the vortex are strongly dependent on the value of $\tilde{q}$, a swirl parameter which is related to the ratio of the maximum swirl velocity to the maximum axial velocity (this parameter is defined in Chap. 4). All wavelengths appear to become damped, and the flow is completely stabilized at a value of $\tilde{q}$ slightly greater than 1.5. They found that the most unstable wave is obtained in the limit $n \to -\infty$, while the axial wavenumber associated with maximum growth rate also increases without bound. Following their earlier work, Lessen and Paillet [27] performed a viscous stability calculation for the trailing line vortex. They obtained results similar to those of Pedley [14] which indicated that the critical Reynolds number increases as $|n|$ increases, with the first unstable mode corresponding to $n = -1$. Their calculations of neutral stability curves showed that the values of the critical wavelength and critical Reynolds number are not very sensitive to the exact value of $\tilde{q}$, and at large $\tilde{q}$, stability is insured for any wavelength and Reynolds number. However, their results are limited to a small range of Reynolds numbers ($Re \lesssim 150$) which later will be shown to be inadequate. Duck and Foster [19] extended the work of Lessen et al. [24] and found a continuous spectrum of unstable modes. The spectrum contains infinite numbers of higher modes for each set of particular values of α, n, and $\tilde{q}$. They showed that the number of unstable modes depends directly on the number of grid points, N, so that as N increases the number of these unstable modes increases as well. It is shown by KMA that although they are inviscid in nature, these higher modes exist at much lower Reynolds numbers than expected.

The asymptotic behavior of the most unstable mode for large azimuthal wavenumber ($|n| >> 1$) was obtained by Leibovich and Stewartson [26]. They showed that as $n \to -\infty$, the maximum growth rate, ω_i, approaches a constant value, $\omega_{i\infty}$. These disturbances are ring modes; that is they are confined to the vicinity of a local radius -- say $r = r_0$. There are also multiple critical layers where $\gamma_r = 0$; and it was pointed out by [26] that both the ring modes and the wall modes obtained by Maslowe and Stewartson [20] may coexist. As will be shown later, this indeed is the case for multiple cell vortices where wall modes, ring modes and center modes all coexist. Leibovich and Stewartson were able to confirm the results of [19] and showed that as one gets nearer to the neutral stability curves, the wave speeds of different modes approach each other. This effect causes many mode jumpings as pointed out by Cotton and Salwen [18] (in the case of a rotating pipe) and numerical calculations become extremely difficult. Also the mode jumping becomes more severe as n becomes large. Leibovich and Stewartson's analysis is valid only for the case of the most unstable mode and $1/2\ \tilde{q} < \alpha/n < 1/\tilde{q}$ with α/n sufficiently distant from the end points of the intervals. Finally, for a columnar vortex, they were able to obtain a sufficient condition which states that the flow is unstable if

$$V \frac{d\Omega}{dr} \left[\frac{d\Omega}{dr} \frac{d\Gamma}{dr} + \left(\frac{dW}{dr}\right)^2\right] < 0 , \tag{1.7}$$

where Ω is the local angular velocity and V is the velocity component in the azimuthal direction. Using a Taylor series expansion of the flow variables about a local radius $r = r_0$, Emanuel [28] showed that when viewed from a plane which contains all of the shear stress components, condition (1.7) is nothing but a restatement of Rayleigh's criterion (centrifugal instability or inertial instability). In this particular plane then, the disturbances are helically symmetric. This idea which was first put forward by Pedley [14] has gained widespread attention in recent years.

The results of [26] were extended by Stewartson [29] to include the effect of viscosity. Using asymptotic analysis, Stewartson was able to show that viscosity has a stabilizing influence which lowers the critical value of $\tilde{q}$, below which all disturbances are stable; and the most unstable mode occurs at a finite value of n. He found that when the Reynolds number $Re \gg 1$, the sufficiency condition (1.7) for instability holds and the most unstable mode has $-n = O(Re^{3/5})$. It must be emphasized that the results of [29] are valid only in the limit of high Re.

Employing an asymptotic expansion, Stewartson and Capell [30] attempted to delineate the mode-jumping and separate the higher modes in the case of large n and $\alpha/n \to 1/\tilde{q}$. They indicated (although not very convincingly) that $\omega \to 0$ as $\alpha/n \to 1/\tilde{q}$ for all modes. The analysis of [30] breaks down completely for moderate values of the azimuthal wavenumber. In a follow on paper, Stewartson and Brown [31] showed the existence of near neutral center-modes (modes that are confined to the vicinity of $r \approx 0$) for moderate values of the azimuthal wavenumber, n. They reported that this instability exists only in distinct intervals of the swirl parameter, $\tilde{q}$. As n changes, so do the intervals. Since their analysis is valid for moderate values of n, it can and should be checked with numerical calculations.

The conclusions of Leibovich and Stewartson [26] were confirmed by Duck [32] using a rather different asymptotic expansion. He showed a more complete description of higher unstable modes and his results indicate that the neutral state is not attained but rather approached asymptotically. He obtained results for negative n as large as -15, which are in good agreement with his numerically conducted calculations.

It is hoped that this short literature survey has conveyed how difficult it is to obtain the stability characteristics of swirling flows -- even in the context of linear theory. Furthermore, it is the author's belief that the message conveyed by this survey is the fact that any future stability calculations should include the effects of viscosity. This was an important consideration in the formulation of the problem in this study and it will be shown later how fruitful the inclusion of viscous effects has been.

Chapter 2

FORMULATION OF THE STABILITY PROBLEM

A normal mode analysis is chosen for the stability calculations. In this approach, the basic flow state is perturbed by infinitesimal disturbances and the governing equations are then linearized with respect to these disturbances. The perturbations are decomposed into different Fourier modes and, because the equations are linear, each mode can be studied individually. It is further assumed that the flow is locally quasi-parallel and the mean velocity profile depends on the radial coordinate only. This last assumption is justified based on the fact that there is no external pressure gradient acting on the trailing line vortex. Viscous forces are responsible for any changes along the vortex axis and for high Reynolds number flow these changes are small over a wavelength. These assumptions are explained in more detail in the following sections.

2.1 Mean Velocity Profile

The similarity solutions for rotating porous pipe flows due to Donaldson and Sullivan [33] are selected as the mean velocity profiles. Their computed profiles, which are exact solutions to the three-dimensional Navier-Stokes equations of motion, show many of the flow features which are of interest in the study of unconfined trailing line vortices. For example, the solutions range from those which can be characterized as a single cell vortex to multiple cell vortices. In addition, experimental measurements have documented the existence of flows with many of these characteristics (see

Adams and Gilmore [34], Leuchter and Solignac [35], and Graham and Newman [36]).

Cylindrical-polar coordinates (r, θ, z) are chosen as the coordinate system. Following Donaldson and Sullivan [33], the basic flow is taken to be of the form

$$U = U(r)$$

$$V = V(r) \tag{2.1}$$

$$W = z\,\bar{W}(r)$$

where, U, V and W are the radial, tangential and axial velocities, respectively. Note that the flow undergoes linear acceleration in the streamwise direction which is required from continuity considerations.

The z-dependence of the axial velocity, W, indicated above is treated using a quasi-parallel flow approximation. The approximation can be justified on dimensional grounds using arguments similar to those employed by Donaldson and Sullivan in their similarity analysis. Assuming that the axial coordinate (z) has been made dimensionless by tube radius, R_0, and using a Reynolds number, Re, based on tube radius, the axial velocity can be represented as

$$W(r, z) = 4\,C\,\frac{z}{Re}\,f'(\eta) \tag{2.2}$$

where $\eta = C\,\frac{r_*^2}{R_0^2}$ is a similarity variable for the radial coordinate, C represents a non-dimensional pressure gradient parameter, and r_* is the dimensional radial coordinate.

The maximum value for $f'(\eta)$ in Eq. (2.2) is unity. Consequently, if a reference location, z_0, is chosen as

$$z_0 = Re/4C, \tag{2.3}$$

then

$$W(r,\ z_0) = f'(\eta)\ . \tag{2.4}$$

At z_0, the axial gradient of $W(r, z)$ is given by

$$\frac{\partial W}{\partial z}(r,\ z_0) = \frac{4C}{Re} f'(\eta) = \phi \tag{2.5}$$

which is very small since flows of interest have high Reynolds number and C is on the order of O(1). The quasi-parallel flow assumption in the vicinity of z_0 is therefore justified. For cases where z is small or where pressure gradient rather than viscous forces are responsible for the z-dependence, one can use a multiple-scale analysis to account for nonparallel effects (see for example [37]). However, in this study, only the case of a 'quasi parallel' basic flow is presented.

2.2 Governing Equations

The governing equations of motion in nondimensional form for a steady, three-dimensional, constant density, Newtonian fluid (in cylindrical coordinates) are written as

continuity

$$\frac{1}{r}\frac{\partial}{\partial r}(r\tilde{u}) + \frac{1}{r}\frac{\partial \tilde{v}}{\partial \theta} + \frac{\partial \tilde{w}}{\partial z} = 0 \tag{2.6}$$

r-momentum

$$\frac{\partial \tilde{u}}{\partial t} + \tilde{u}\frac{\partial \tilde{u}}{\partial r} + \frac{\tilde{v}}{r}\frac{\partial \tilde{u}}{\partial \theta} + \tilde{w}\frac{\partial \tilde{u}}{\partial z} - \frac{\tilde{v}^2}{r} = -\frac{\partial \tilde{p}}{\partial r}$$

$$+ \frac{1}{Re}\left[\nabla^2\tilde{u} - \frac{\tilde{u}}{r^2} - \frac{2}{r^2}\frac{\partial \tilde{v}}{\partial \theta}\right] \tag{2.7}$$

θ-momentum

$$\frac{\partial \tilde{v}}{\partial t} + \tilde{u}\,\frac{\partial \tilde{v}}{\partial r} + \frac{\tilde{v}}{r}\,\frac{\partial \tilde{v}}{\partial \theta} + \tilde{w}\,\frac{\partial \tilde{v}}{\partial z} + \frac{\tilde{u}\tilde{v}}{r} = -\,\frac{1}{r}\,\frac{\partial \tilde{p}}{\partial \theta}$$

$$+ \frac{1}{Re}\,[\nabla^2 \tilde{v} - \frac{\tilde{v}}{r^2} + \frac{2}{r^2}\,\frac{\partial \tilde{u}}{\partial \theta}] \qquad (2.8)$$

and z-momentum

$$\frac{\partial \tilde{w}}{\partial t} + \tilde{u}\,\frac{\partial \tilde{w}}{\partial r} + \frac{\tilde{v}}{r}\,\frac{\partial \tilde{w}}{\partial \theta} + \tilde{w}\,\frac{\partial \tilde{w}}{\partial z} = -\,\frac{\partial \tilde{p}}{\partial z} + \frac{1}{Re}\,\nabla^2 \tilde{w} \qquad (2.9)$$

where

$$\nabla^2 \equiv \frac{\partial^2}{\partial r^2} + \frac{1}{r}\,\frac{\partial}{\partial r} + \frac{1}{r^2}\,\frac{\partial^2}{\partial \theta^2} + \frac{\partial^2}{\partial z^2}\;.$$

Here, the nondimensionalization has been done with respect to the pipe radius, R_0, centerline axial velocity, W_0, time scale, R_0/W_0, dynamic pressure magnitude $\rho_0\, W_0^2$, and Re is the Reynolds number based on R_0 and centerline velocity. The flow variables are assumed to consist of a mean part and an infinitesimally small perturbation, i.e.

$$\begin{aligned} \tilde{u} &= U + u \\ \tilde{v} &= V + v \\ \tilde{w} &= W + w \\ \tilde{p} &= \Pi + p\;. \end{aligned} \qquad (2.10)$$

Substituting Eq. (2.10) into the equations of motion (Eqs. (2.6-2.9)) and neglecting the quadratic terms, we obtain the linearized small disturbance equations continuity

$$\frac{\partial u}{\partial r} + \frac{u}{r} + \frac{1}{r}\frac{\partial v}{\partial \theta} + \frac{\partial w}{\partial z} = 0, \tag{2.11}$$

r-momentum

$$\frac{\partial u}{\partial t} + U\frac{\partial u}{\partial r} + u\frac{dU}{dr} + \frac{V}{r}\frac{\partial u}{\partial \theta} + W\frac{\partial u}{\partial z} - \frac{2Vv}{r} = -\frac{\partial p}{\partial r}$$

$$+ \frac{1}{Re}\left[\frac{\partial^2 u}{\partial r^2} + \frac{1}{r}\frac{\partial u}{\partial r} + \frac{1}{r^2}\frac{\partial^2 u}{\partial \theta^2} + \frac{\partial^2 u}{\partial z^2} - \frac{u}{r^2} - \frac{2}{r^2}\frac{\partial v}{\partial \theta}\right], \tag{2.12}$$

θ-momentum

$$\frac{\partial v}{\partial t} + U\frac{\partial v}{\partial r} + u\frac{dV}{dr} + \frac{V}{r}\frac{\partial v}{\partial \theta} + W\frac{\partial v}{\partial z} + \frac{Vu}{r} + \frac{vU}{r} = -\frac{1}{r}\frac{\partial p}{\partial \theta}$$

$$+ \frac{1}{Re}\left[\frac{\partial^2 v}{\partial r^2} + \frac{1}{r}\frac{\partial v}{\partial r} + \frac{1}{r^2}\frac{\partial^2 v}{\partial \theta^2} + \frac{\partial^2 v}{\partial z^2} - \frac{v}{r^2} + \frac{2}{r^2}\frac{\partial u}{\partial \theta}\right], \tag{2.13}$$

z-momentum

$$\frac{\partial w}{\partial t} + u\frac{\partial W}{\partial r} + U\frac{\partial w}{\partial r} + \frac{V}{r}\frac{\partial w}{\partial \theta} + W\frac{\partial w}{\partial z} + w\frac{\partial W}{\partial z} = -\frac{\partial p}{\partial z}$$

$$+ \frac{1}{Re}\left[\frac{\partial^2 w}{\partial r^2} + \frac{1}{r}\frac{\partial w}{\partial r} + \frac{1}{r^2}\frac{\partial^2 w}{\partial \theta^2} + \frac{\partial^2 w}{\partial z^2}\right]. \tag{2.14}$$

Since the coefficients of the perturbations in the above equations are functions of r only, the disturbance quantities are assumed to have a helical wave form:

$$\{u, v, w, p\} = \{i\,F(r), G(r), H(r), P(r)\}\, e^{i(\alpha z + n\theta - \omega t)} \tag{2.15}$$

Here, F, G, H and P are the complex disturbance eigenfunctions, α is the wavenumber in the axial direction, n is the wavenumber in the azimuthal direction, and ω is the temporal frequency. In general, both α and ω are complex variables. For a single valued solution, n must be an integer or zero. When n equals zero the disturbances are axisymmetric. When n is a positive or negative integer, asymmetric perturbations exist which represent different spiralling directions of propagation, depending on the sign of n/ω.

If spatial stability is considered, then ω must be real and $\alpha = \alpha_r + i\alpha_i$. On the other hand, for a temporal solution, α is assumed real and $\omega = \omega_r + i\omega_i$. In either case, the sign of the imaginary part indicates decay or growth of the disturbance.

Substituting Eq. (2.15) into the governing equations (Eqs. (2.11-2.14)), the linearized forms of the equations for perturbation eigenfunctions are obtained. They can be written in the form:

continuity

$$F' + \frac{F}{r} + \frac{nG}{r} + \alpha H = 0 \tag{2.16}$$

r-momentum

$$- \frac{i\,F''}{Re} + i\,[U - \frac{1}{Re\,r}]\,F' + [\omega + i\,\frac{dU}{dr} - \frac{nV}{r} - \alpha W$$

$$+ \frac{i}{Re}\,(\frac{n^2+1}{r^2} + \alpha^2)]\,F + [\frac{i2n}{Re\,r^2} - \frac{2V}{r}]\,G + P' = 0 \tag{2.17}$$

θ-momentum

$$- \frac{G''}{Re} + [U - \frac{1}{Re\,r}]\,G' + [-i\omega + \frac{inV}{r} + i\alpha W + \frac{U}{r}$$

$$+ \frac{1}{Re}\,(\frac{n^2+1}{r^2} + \alpha^2)]\,G + [i\,\frac{dV}{dr} + \frac{2n}{Re\,r^2} + \frac{iV}{r}]\,F + \frac{inP}{r} = 0 \tag{2.18}$$

z-momentum

$$-\frac{H''}{Re} + [U - \frac{1}{Re\ r}]\ H' + [-i\omega + \frac{inV}{r} + i\alpha W + \phi$$

$$+ \frac{1}{Re}\ (\frac{n^2}{r^2} + \alpha^2)]\ H + i\ \frac{\partial W}{\partial r}\ F + i\alpha P = 0 \qquad (2.19)$$

where primes denote differentiation with respect to the radial coordinate.

2.3 Boundary Conditions

The boundary conditions for a variety of flow configurations have been given in detail in KMA. However, for the sake of completeness, they will be explained here. The boundary conditions at the outer wall are very simple since the perturbations must be equal to zero. In terms of the eigenfunctions, these conditions are

$$\begin{aligned} F(1) &= 0 \\ G(1) &= 0 \\ H(1) &= 0\ . \end{aligned} \qquad (2.20)$$

Due to the singular nature of the coordinate system, and because all physical quantities must be continuous and bounded on the centerline, some non-trivial requirements exist as $r \rightarrow 0$. There are essentially two ways of treating this singularity. In one method, the entire pipe is treated as the computational domain with $-1<r<1$. Hence, condition (2.20) is enforced at $r = \pm 1$. However, in order to remove the centerline singularity, some parity conditions must be enforced. The nature of these parity conditions and the method of applying them are discussed by Metcalfe and Orszag [15], Leonard and Wray [38], and Orszag and Patera [39]. The second method treats the radius,

$0<r<1$, as the computational domain and hence the centerline is taken to be a boundary. Then, the need arises for a new set of relations to be enforced on the centerline. These compatiblity relations, given previously by Batchelor and Gill [40], and formalized recently by KMA are

$$\lim_{r\to 0} \frac{\partial \vec{V}}{\partial \theta} = 0 \tag{2.21}$$

where $\vec{V}$ is the total velocity vector. This limit represents boundedness and smoothness conditions on the solutions along the centerline. The second approach has been employed in the present study.

In expanding this condition (Eq. (2.21)), we need to consider only the perturbation part of the velocity since the mean flow is independent of the azimuthal direction. Representing the perturbation velocity field by $\vec{v}$, we have

$$\frac{\partial \vec{v}}{\partial \theta} = \frac{\partial}{\partial \theta} (u\, \vec{e}_r + v\, \vec{e}_\theta + w\, \vec{e}_z) \tag{2.22}$$

or

$$\lim_{r\to 0} \frac{\partial \vec{v}}{\partial \theta} = \frac{\partial u}{\partial \theta} \vec{e}_r + u \frac{d\vec{e}_r}{d\theta} + \frac{\partial v}{\partial \theta} \vec{e}_\theta + v \frac{d\vec{e}_\theta}{d\theta}$$

$$+ \frac{\partial w}{\partial \theta} \vec{e}_z + w \frac{d\vec{e}_z}{d\theta} . \tag{2.23}$$

But

$$\frac{d\vec{e}_z}{d\theta} = 0 \tag{2.24}$$

$$\frac{d\vec{e}_r}{d\theta} = \vec{e}_\theta \tag{2.25}$$

$$\frac{d\vec{e}_\theta}{d\theta} = - \vec{e}_r . \tag{2.26}$$

Substituting from Eq. (2.15), we deduce

$$\lim_{r\to 0} \frac{\partial \vec{v}}{\partial \theta} = (-\, nF - G)\, \vec{e}_r + (iF + inG)\, \vec{e}_\theta + inH\, \vec{e}_z = 0\ . \qquad (2.27)$$

In order for the equality to hold, each component of the resultant vector must be zero. Summarizing, in the limit along the centerline ($r = 0$), we have

$$\begin{aligned} nF + G &= 0 \\ F + nG &= 0 \\ nH &= 0\ . \end{aligned} \qquad (2.28)$$

The above conditions depend on the value of the azimuthal wavenumber, n, such that

$$\text{If } n = 0 \quad F(0) = G(0) = 0 \quad \text{and} \quad H(0) \text{ must be finite} \qquad (2.29)$$

$$\text{If } n = \pm 1 \quad F(0) \pm G(0) = 0 \quad \text{and} \quad H(0) = 0 \qquad (2.30)$$

$$\text{If } |n| > 1 \quad F(0) = G(0) = H(0) = 0\ . \qquad (2.31)$$

In the case when $|n| = 1$, two of the conditions become linearly dependent. In KMA, another relation was deduced by enforcing the continuity equation on the centerline, resulting in

$$2F'(0) + nG'(0) = 0\ . \qquad (2.32)$$

However, after carefully examining the radial and azimuthal momentum equations as $r \to 0$, it can be shown that condition (Eq. (2.32)) is identical to the conditions

$$F'(0) = 0 \tag{2.33}$$

or

$$G'(0) = 0 \ . \tag{2.34}$$

Therefore, in the present study, either Eq. (2.33) or (2.34) is used as the appropriate boundary condition for $|n| = 1$.

Chapter 3

NUMERICAL METHOD

3.1 Introduction

Over the past two decades spectral techniques have emerged as primary methods for solving hydrodynamic stability problems. The efficiency and high degree of accuracy obtainable by using these techniques has been demonstrated by others (see references [41, 15, 42, 43]). Very recently, KMA have applied a spectral collocation (pseudospectral) method to a wide class of viscous, incompressible swirling flows. In their method, the flow variables were expanded in terms of a truncated Chebyshev series. The global eigenvalues of the discretized system were then obtained by a generalized complex QZ [44] routine. They have shown that the resulting algorithm is robust and easy to implement while being efficient. The advantages of their method over similar schemes are twofold. First, it is easily extendable to the case of compressible fields, since the coefficients of the flow variables are always evaluated in the physical space. Second, the use of the collocation formulation greatly simplifies the implementation of any new basic flow or coordinate transformation. The present study employs the same method, but with one major modification pertaining to pressure boundary conditions.

The set of governing equations (2.16-2.19) are sixth order. Therefore, the six boundary conditions derived in Eqs. (2.20-2.34) are sufficient for a well posed boundary value problem. However, a straight forward discretization, as employed in KMA, would result in a system which requires two artificial pressure boundary conditions. In KMA Neumann conditions were prescribed on the pressure at the two boundaries. This pressure gradient condition is well known whenever the Navier-Stokes equations are solved in primitive variables, and has been discussed by Orszag and Israeli [45]. The prescribed values are obtained by taking the inner product of the vector momentum equation with the normal to the boundary. In cylindrical-polar coordinates, this turns out to be the r-momentum equation in its original form evaluated at the boundaries. KMA have shown that this formulation is viable and produces eigenvalues as accurate as any other method. However, in recent years it has become common to stagger the pressure cells or grid and eliminate the need for the two artificial pressure conditions. This is the approach taken here and is explained in detail in the next section.

3.2 Chebyshev Spectral Collocation for Staggered Grid

The unique properties of Chebyshev polynomials have been known for many years [46, 47]. Chebyshev polynomials distribute the error evenly, exhibit rapid convergence rates with increasing numbers of terms, and cluster the collocation points near the boundaries [48-50].

The kth Chebyshev polynomial, $T_k(\xi)$, is defined on the interval (-1, 1) by

$$T_k(\xi) = \cos[k \cos^{-1}\xi] \quad . \tag{3.1}$$

Because the spatial range in the present physical problem is (0, 1), a simple transformation is made from the physical variable, r, to the Chebyshev variable via

$$\xi = 1 - 2r \tag{3.2}$$

where

$$-1 < \xi < 1 \quad .$$

If

$$\xi = \cos \phi \ ,$$

it can be seen that relation (3.1) becomes

$$T_k(\xi) = \cos k\phi \quad . \tag{3.3}$$

Next a staggered grid is constructed such that the velocity components and the three momentum equations are evaluated at the cell faces, while pressure and the continuity equation are enforced at the mid cell points. A graphical representation of this grid is shown in Fig. 3.1. The velocities are evaluated at the collocation points ξ_j which are the extrema of the last retained Chebyshev polynomial $(T_N(\xi))$ in the truncated series and are defined by

$$\xi_j = \cos \frac{\pi j}{N} \ , \ j = 0, 1, \ldots, N \tag{3.4}$$

where the centerline and outer wall boundaries, correspond to j equals 0 and N, respectively.

An interpolant polynomial is constructed in terms of the values of the flow variable at the collocation points by employing a truncated Chebyshev series. As an example, we present expressions for $F(\xi)$ since extension to the other velocity components is straight forward. An Nth order polynomial for $F(\xi)$ is written as

$$F(\xi) = \sum_{j=0}^{N} g_j(\xi) \ F(\xi_j) \tag{3.5}$$

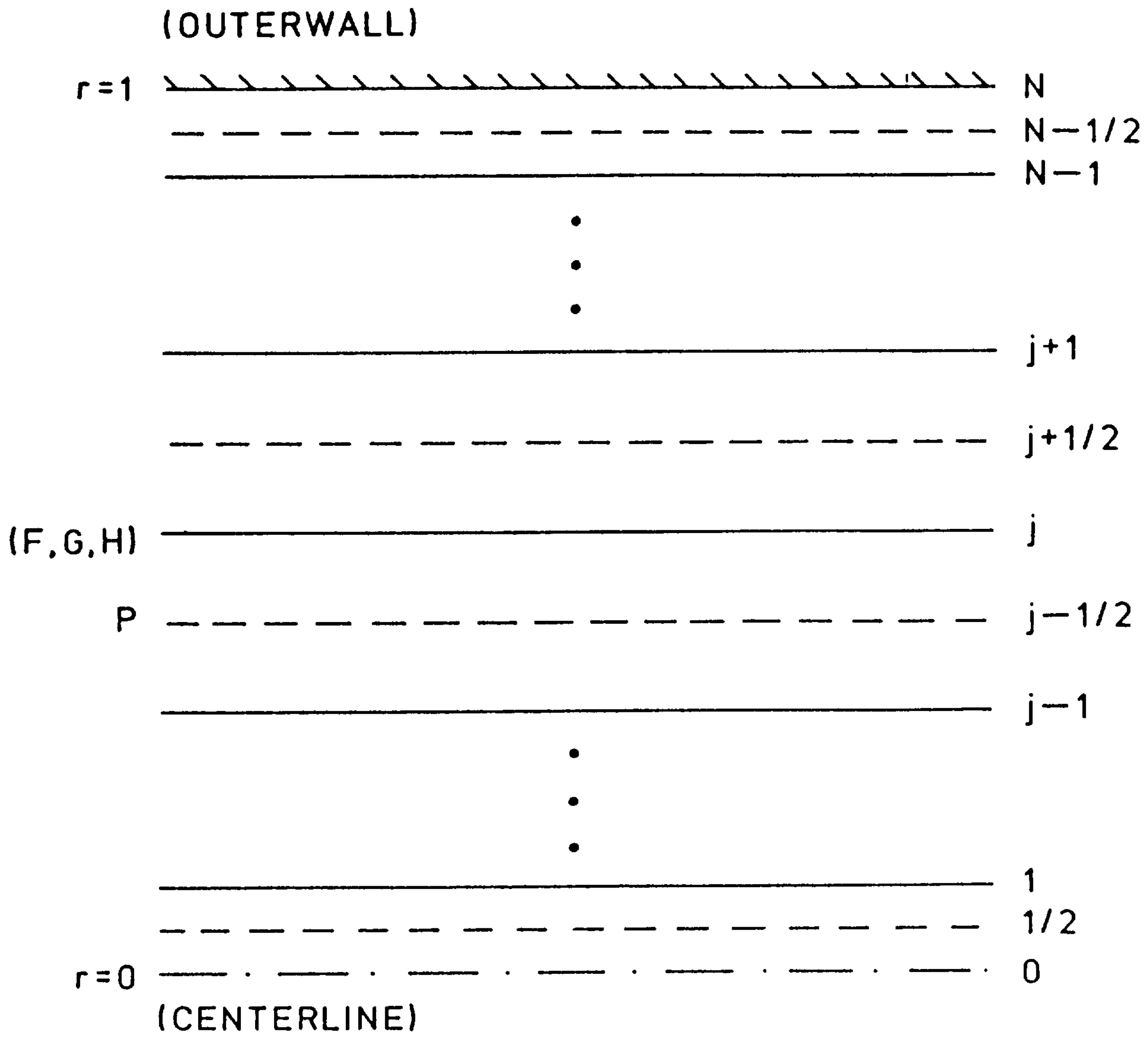

Fig. 3.1 A schematic of the staggered spectral collocation grid showing locations where F, G, H and P are evaluated.

where the interpolant $g_j(\xi)$ is

$$g_j(\xi) = \frac{(-1)^{j+1}}{N^2 C_j} \frac{(1 - \xi_j^2) T_N'(\xi)}{(\xi - \xi_j)} \tag{3.6}$$

with

$$C_0 = C_N = 2, \; C_j = 1, \; (1 < j < N-1) \quad .$$

It can easily be shown that

$$g_j \, (\xi_k) = \delta_{jk} \, , \tag{3.7}$$

where δ_{jk} is the usual Kroneker delta. Next, the first and second derivatives are determined explicitly by differentiating relationship (3.5). The derivatives, evaluated at ξ_j, are written as

$$\left.\frac{dF}{d\xi}\right|_j = \sum_{k=0}^{N} \bar{A}_{jk} \, F_k \tag{3.8}$$

$$\left.\frac{d^2F}{d\xi^2}\right|_j = \sum_{k=0}^{N} \bar{B}_{jk} \, F_k \tag{3.9}$$

$$j = 0, 1, \ldots, N$$

where F_k is simply $F(\xi_k)$, $\bar{A}_{jk}$ and $\bar{B}_{jk}$ are the elements of the derivative matrices and are given [50] by

$$\bar{A}_{jk} = \frac{C_j \, (-1)^{k+j}}{C_k \, (\xi_j - \xi_k)} \qquad (j \neq k) \tag{3.10}$$

$$\bar{A}_{jj} = - \frac{\xi_j}{2(1 - \xi_j^2)}$$

$$\bar{A}_{00} = \frac{2 \, N^2 + 1}{6} = - \, \bar{A}_{NN}$$

and

$$\bar{B}_{jk} = \bar{A}_{jm} \bar{A}_{mk} \quad . \tag{3.11}$$

Now the pressure and the continuity equation are evaluated at the collocation points $\xi_{j+1/2}$ which are the roots of $T_N(\xi)$ and are given by

$$\xi_{j+1/2} = \cos \frac{(2j+1)\ \pi}{2N} , \quad j = 0, 1, \ldots, N-1 . \tag{3.12}$$

Note that this set of points does <u>not</u> include the two boundary points. Next, the pressure is represented with an interpolating polynomial of N-1 (rather than N) degree. Therefore, we write

$$P(\xi) = \sum_{j=0}^{N-1} h_j(\xi)\ P(\xi_{j+1/2}) , \tag{3.13}$$

where the interpolant $h_j(\xi)$ is given as

$$h_j\ (\xi) = \frac{(-1)^j\ (\sin \phi_{j+1/2}\ T_N(\xi))}{N\ (\xi - \xi_{j+1/2})} , \tag{3.14}$$

$$j = 0, 1, \ldots, N-1.$$

Again, it can easily be shown that

$$h_j(\xi_{k+1/2}) = \delta_{jk} \ . \tag{3.15}$$

At this time, two sets of interpolating matrices are needed to interpolate from the staggered points to the grid points and vice versa. That is

$$F_{j+1/2} = \sum_{k=0}^{N} M^{*}_{jk}\ F_k , \tag{3.16}$$

$$j = 0, 1, \ldots, N-1 ,$$

and

$$P_j = \sum_{k=0}^{N-1} M_{jk} \, P_{k+1/2} \, , \qquad (3.17)$$

$$j = 0, 1, \ldots, N \, ,$$

where the elements of the matrix M^* are given as

$$M^*_{jk} = \frac{(-1)^{j+k+1} \, (1 - \xi^2_{j+1/2})^{1/2}}{C_k \, N \, (\xi_{j+1/2} - \xi_k)} \, , \qquad (3.18)$$

$$j = 0, 1, \ldots, N-1 \, ,$$
$$k = 0, 1, \ldots, N \, ,$$

and that of M as

$$M_{jk} = \frac{(-1)^{j+k} \, (1 - \xi^2_{k+1/2})^{1/2}}{N \, (\xi_j - \xi_{k+1/2})} \, , \qquad (3.19)$$

$$j = 0, 1, \ldots, N \, ,$$
$$k = 0, 1, \ldots, N-1 \, .$$

In order for M^* to be a square matrix, an extra row ($j = N$) with zero elements is added. Similarly in the case of M, a column ($k = N$) is added which contains null elements.

In the case of the derivatives there are two different ways to interpolate. In one method the explicit functions g_j and h_j are first differentiated and then evaluated at the required points. Hence, the derivative matrices can be constructed explicitly. An equally valid method is to employ Eq. (3.16). That is, if

$$\left. \frac{dF}{d\xi} \right|_{j+1/2} = \sum_{k=0}^{N} \bar{A}^*_{jk} \, F_k \, , \qquad (3.20)$$

$$j = 0, 1, \ldots, N-1 \, ,$$

then

$$\bar{A}^*_{jk} = M^*_{jm} \bar{A}_{mk} \; . \qquad (3.21)$$

Here we have used a mix of the two methods. That is, if

$$\left.\frac{dP}{d\xi}\right|_j = \sum_{k=0}^{N-1} \frac{dh_k(\xi_j)}{d\xi} P_{k+1/2} \; , \qquad (3.22)$$

$$j = 0, 1, \ldots, N \; ,$$

then we employ

$$\left.\frac{dP}{d\xi}\right|_j = \sum_{k=0}^{N-1} E_{jk} \, P_{k+1/2} \; , \qquad (3.23)$$

where the elements of E are given as

$$E_{jk} = \frac{(-1)^{j+k+1} \, (1 - \xi^2_{k+1/2})^{1/2}}{N \, (\xi_j - \xi_{k+1/2})^2} \; , \qquad (3.24)$$

$$j = 1, 2, \ldots, N-1 \; ,$$
$$k = 0, 1, \ldots, N-1 \; ,$$

$$E_{0k} = \frac{(-1)^k \, (1 - \xi^2_{k+1/2})^{1/2}}{N} \left[\frac{N^2}{(1 - \xi_{k+1/2})} - \frac{1}{(1 - \xi_{k+1/2})^2}\right] \; ,$$

$$k = 0, 1, \ldots, N-1 \; ,$$

$$E_{Nk} = \frac{(-1)^{k+N} \, (1 - \xi^2_{k+1/2})^{1/2}}{N} \left[\frac{N^2}{(1 + \xi_{k+1/2})} - \frac{1}{(1 + \xi_{k+1/2})^2}\right] \; ,$$

$$k = 0, 1, \ldots, N-1 \; ,$$

A null column (k = N) is added to make E a square matrix.

Finally, if the scaling factor for transformation between the physical and computational domain is given as

$$S_j = \frac{d\xi}{dr}\bigg|_j \quad ; \; j = 0, 1, \ldots, N \, ,$$

then the first derivative matrix, $\bar{A}$, in the physical domain may be written as

$$A_{jk} = S_j \, \bar{A}_{jk} \tag{3.25}$$

and

$$A^*_{jk} = M^*_{jm} \; A_{mk} , \tag{3.26}$$

with similar relationships holding in the case of the mid cell points.

Employing all of the relations developed above, the governing equations in discretized form are

continuity:

$$\sum_{k=0}^{N} A^*_{jk} \, F_k + \left(\frac{2}{1-\xi_{j+1/2}}\right) \sum_{k=0}^{N} M^*_{jk} \, F_k$$

$$+ \left(\frac{2n}{1-\xi_{j+1/2}}\right) \sum_{k=0}^{N} M^*_{jk} \, G_k + \alpha \sum_{k=0}^{N} M^*_{jk} \, H_k = 0 \, , \tag{3.27}$$

r-momentum:

$$\sum_{k=0}^{N} B_{jk} \, F_k + \left[\frac{2}{1-\xi_j} - \text{Re} \, U_j\right] \sum_{k=0}^{N} A_{jk} \, F_k$$

$$+ \left[i \, \text{Re} \, \omega - \text{Re} \; S_j \frac{dU}{d\xi}\bigg|_j - \frac{i \; 2 \; \text{Re} \; n \; V_j}{1 - \xi_j} - \left(\frac{4(n^2 + 1)}{(1-\xi_j)^2}\right)\right] F_j$$

$$- \left[\frac{4(2n)}{(1-\xi_j)^2} + \frac{2(i \; 2 \; \text{Re} \; V_j)}{1-\xi_j}\right] G_j + i \, \text{Re} \sum_{k=0}^{N} E_{jk} \, P_{k+1/2}$$

$$- i \, \alpha \, \text{Re} \, W_j \, F_j - \alpha^2 \, F_j = 0 \, , \tag{3.28}$$

θ-momentum:

$$
\begin{aligned}
&- \left[i \operatorname{Re} S_j \left.\frac{dV}{d\xi}\right|_j + \frac{4(2n)}{(1-\xi_j)^2} + \frac{2(i\operatorname{Re} V_j)}{(1-\xi_j)} \right] F_j \\
&+ \sum_{k=0}^{N} B_{jk} G_k + \left[\frac{2}{1-\xi_j} - \operatorname{Re} U_j \right] \sum_{k=0}^{N} A_{jk} G_k \\
&+ \left[i \operatorname{Re} \omega - \frac{2(i \operatorname{Re} n V_j)}{1-\xi_j} - \frac{2(\operatorname{Re} U_j)}{1-\xi_j} - \frac{4(n^2+1)}{(1-\xi_j)^2} \right] G_j \\
&- \frac{2\,(i \operatorname{Re} n)}{1-\xi_j} \sum_{k=0}^{N} M_{jk} P_{k+1/2} - i\,\alpha \operatorname{Re} W_j G_j - \alpha^2 G_j = 0,
\end{aligned}
\tag{3.29}
$$

z-momentum

$$
\begin{aligned}
&- i \operatorname{Re} S_j \left.\frac{\partial W}{\partial \xi}\right|_j F_j + \sum_{k=0}^{N} B_{jk} H_k + \left[\frac{2}{1-\xi_j} - \operatorname{Re} U_j \right] \sum_{k=0}^{N} A_{jk} H_k \\
&+ \left[i \operatorname{Re} \omega - \frac{2(i \operatorname{Re} n V_j)}{1-\xi_j} - \operatorname{Re} \phi_j - \frac{4n^2}{(1-\xi_j)^2} \right] H_j \\
&- i\,\alpha \operatorname{Re} W_j H_j - i\,\alpha \operatorname{Re} \sum_{k=0}^{N} M_{jk} P_{k+1/2} - \alpha^2 H_j = 0\ .
\end{aligned}
\tag{3.30}
$$

The boundary conditions are:

at $\xi = -1$,

$$F(-1) = G(-1) = H(-1) = 0 \quad \text{for all } n \tag{3.31}$$

at $\xi = 1$

$$
\text{If } n = 0 \qquad
\begin{aligned}
&F(1) = G(1) = 0 \\
&H'(1) = 0\ .
\end{aligned}
\tag{3.32a}
$$

$$\text{If } n = \pm 1 \qquad \begin{aligned} &F(1) \pm G(1) = 0 \\ &H(1) = 0 \\ &F'(1) = 0 \text{ or } G'(1) = 0 \ . \end{aligned} \tag{3.32b}$$

$$\text{If } |n| > 1 \qquad F(1) = G(1) = H(1) = 0 \ . \tag{3.32c}$$

3.3 Numerical Scheme

The above equations are rearranged so that they can be represented in the generalized eigenvalue format as

$$D\vec{X} = \lambda\, L\vec{X} \ , \tag{3.33}$$

where D and L are coefficient matrices obtained from the appropriate discretized differential operator, and λ is an eigenvalue. For the temporal stability calculations,

$$\lambda = \omega \ ,$$

and

$$\vec{X} = [F \; G \; H \; P]^T \ . \tag{3.34}$$

Both D and L are square matrices with dimensions of 4N+3. In the case of temporal stability the last six rows of matrix D contain the boundary conditions. Since the boundary conditions do not contain the eigenvalue ω, the submatrix in D containing these conditions was made upper triangular through column operations. If all of the diagonal elements of this submatrix are non-zero, it indicates that the boundary conditions are independent of each other and the ranks of matrices D and L are reduced to 4N-3.

It should be noted that the eigenvalue coefficient matrix, L, is singular. A procedure may be devised, using row and column operations, which reduces the rank of the coefficient matrix and removes the singularity (see, e.g., Metcalfe and Orszag [15]). An alternative approach is to introduce a term $\beta\omega P_{j+1/2}$ in the continuity Eq. (3.27). This additional term makes the coefficient matrix for ω non-singular and may be termed an artificial compressibility factor (see Malik and Poll [51]). Both methods were employed in KMA and it was found that computations using the method of artificial compressibility of Malik and Poll were at least one and one half times faster than the matrix operations of Metcalfe and Orszag [15], and both produced identical eigenvalues. Therefore, only the artificial compressibility approach is used in the present work.

The artificial compressibility parameter, β, is assigned a very small value (on the order of 10^{-18}). This term generates large values for some of the eigenvalues of the matrix $L^{-1}D$; however, experimentation with the value of β demonstrated that for values less than 10^{-9} its effect on the desired (physical) eigenvalues is negligible.

The general complex eigenvalue solver employed in the global calculations is the IMSL QZ routine called EIGZC. If the eigenfunctions are desired the eigenvalues are refined and the eigenfunctions are obtained subsequently using a local method. The local method which was employed here uses an inverse iterative technique (see Wilkinson [52]). The discretization of the governing equations for the local method is spectral but non-staggered. It was found that the eigenvalues obtained by the local procedure always converged to eight or nine significant digits within four iterations. Furthermore, it was found that both methods produced eigenvalues which agreed with up to six digit accuracy.

All of the numerical solutions reported here were obtained on the CDC CYBER 860 and CYBER 205 machines at NASA Langley Research Center.

Chapter 4

TEST CASES

4.1 Introduction

The convergence and accuracy of the non-staggered Chebyshev spectral collocation method has been tested extensively through numerous test cases in KMA. However, it is still desirable to obtain the convergence behavior of the staggered representation to contrast it with the non-staggered or tau formulation. The viability of the present method is examined here through two widely different flow configurations; namely Poiseuille flow in a pipe (confined flow) and for a Batchelor's type vortex (unconfined flow). In each case, numerous results have already been reported by others which greatly simplifies the comparison task. It must be emphasized that the objective here was not to duplicate all of the previous work, but rather to show briefly the efficiency and accuracy of the staggered collocation formulation. However, for one of the flows (Batchelor's vortex) where some quantitative differences with previous results were obtained, it will be necessary to explain the discrepancies.

4.2 Temporal Stability of Poiseuille Flow in a Pipe

The mean velocity for this problem is the well known profile given by

$$
\begin{aligned}
U &= 0 \\
V &= 0 \\
W &= 1 - r^2 \,.
\end{aligned}
\tag{4.1}
$$

The linear stability of Poiseuille flow in circular pipes subjected to azimuthally varying disturbances has been studied by Lessen, Sadler and Liu [53]. Using a shooting method, they found no instability for the $n = 1$ perturbations. Two of their eigenvalues are tabulated in Table 4.1, along with the results of the present calculations. The results from the two methods agree very well. Next, the variation of the least stable mode with Reynolds number was obtained. A comparison of these results with those of Salwen, Cotton and Grosch [54] is given in Table 4.2. The agreement is excellent.

The convergence behavior of the present method as compared to the Chebyshev tau formulation of Metcalfe and Orszag [15] and the non-staggered method of KMA is presented in Table 4.3. It is clear that Chebyshev collocation (in either form) has a much better convergence rate than that of the tau method. However, there is hardly any difference between the convergence rate of the two collocation formulations. This fact suggests that, contrary to prevailing opinion, when the artificial pressure boundary conditions are employed correctly they do not affect the accuracy or the convergence rate of the spectral methods.

Although not reported here, the two collocation methods have been compared for a variety of other flows. In each case, both methods produced identical results up to seven or eight significant digits.

Table 4.1 Comparison of the First Eigenvalue Predicted by Lessen et al. [53] with those Using Chebyshev Collocation

			Lessen et al. [53]		Present Method	
n	α	R_e	C_r	C_i	C_r	C_i
1	1	200	0.645	-0.129	0.64526	-0.129205
1	1	2200	---	-0.067	0.39797	-0.067709
1	1	2200	---	---	0.89663	-0.048114

Table 4.2 A Comparison of the Variations of the Least Stable Modes with Reynolds Number with those of Salwen, Cotton and Grosch [54] (SCG). Here, $\alpha = 1$, $n = 1$. The first entry under each mode is the real part and the second entry is the negative imaginary part.

Re	Mode 1		Mode 2		Mode 3		Mode 4		Mode 5		
100	0.57256	0.14714	0.55198	0.37446	0.78735	0.47946	0.66248	0.74907			Collocation
	0.57256	0.14714	0.55198	0.37446	0.78735	0.47946	0.66247	0.74907			SCG
1000	0.84675	0.07086	0.46914	0.09114	0.74819	0.15122	0.92730	0.15270	0.30948	0.15972	Collocation
	0.84675	0.07086	0.46916	0.09117	---	---	0.92730	0.15270	0.30947	0.15973	SCG
9600	0.95048	0.02317	0.27684	0.04759	0.97668	0.04946	0.91886	0.04994	0.88817	0.07730	Collocation
	0.95048	0.02317	0.27681	0.04760	0.97668	0.04946	---	---	---	---	SCG

Table 4.3 The Convergence Behavior of the Two Least Stable Modes for Poiseuille Flow in a Pipe. N is the number of polynomials used to resolve each flow variable. Here, Re = 10, α = 1, and n = 1.

N	ω_1	ω_2
	Metcalfe and Orszag [15], Chebyshev Tau Formulation	
8	0.501654048-i1.392398524	0.780474345-i2.745100739
12	0.491070208-i1.393534481	0.763978453-i2.807040555
16	0.491063984-i1.393490921	0.762026865-i2.807291233
20	0.491064084-i1.393490894	0.762024215-i2.807286430
	Present Calculations, Staggered Chebyshev Collocation	
8	0.491065536-i1.393490713	0.762034238-i2.807291149
12	0.491064085-i1.393490894	0.762024225-i2.807286425
16	0.491064084-i1.393490894	0.762024223-i2.807286422
20	0.491064084-i1.393490894	0.762024223-i2.807286422
	KMA, Non-Staggered Chebyshev Collocation	
8	0.491067022-i1.393495866	0.762035973-i2.807301022
12	0.491064084-i1.393490896	0.762024226-i2.807286427
16	0.491064084-i1.393490894	0.762024223-i2.807286422
20	0.491064084-i1.393490894	0.762024223-i2.807286421

For Poiseuille flow, 16 Chebyshev polynomials were required for eight figure accuracy. The number of polynomials, N, depends on the particular mean flow, and between 32 and 70 polynomials were used in the present study to insure convergence.

4.3 Temporal Stability of a Trailing Line Vortex

The approximate asymptotic form of the solution for the mean velocity profile of a Batchelor's vortex [24] is

$$U = 0$$

$$V = \frac{\tilde{q}}{r}\,[1 - \exp(-r^2)] \qquad (4.2)$$

$$W = \frac{W_1}{W_2} + \exp(-r^2)\ .$$

where the azimuthal and axial velocities, have been normalized with respect to W_2, which is the difference between the centerline velocity and the far field velocity. The quantity, $\tilde{q}$, in Eq. (4.2) has been called the swirl parameter by Lessen et al. [24] and is related to the ratio of the maximum swirl velocity to the maximum axial velocity excess (or defect)*. Throughout the present study, it is assumed that $\frac{W_1}{W_2} = 1$ and therefore

$$W = 1 + \exp(-r^2)\ . \qquad (4.3)$$

The two components of the mean velocity profile are shown in figure 4.1. It has been pointed out by Lessen et al. [24] that the uniform part of

---

*If q is the ratio of maximum swirl velocity to the maximum axial velocity, then $q = 0.639\,\tilde{q}$ in this case.

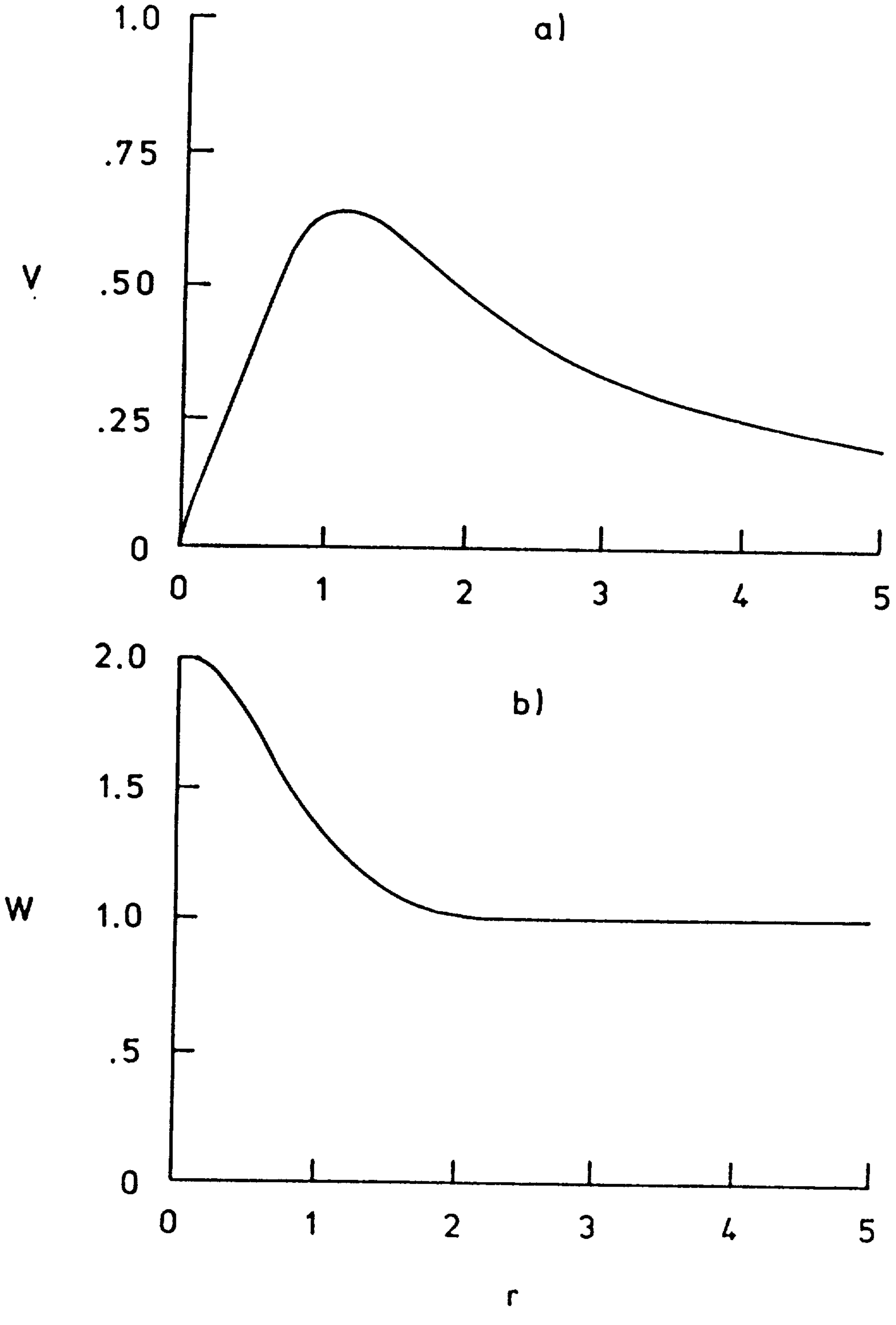

Fig. 4.1 Velocity components for a Batchelor vortex.

the flow in Eq. (4.2) only affects the frequency and not the growth rate of the disturbance.

Since r varies between zero and infinity, it is necessary to map the coordinate system into a Chebyshev (computational) domain. An algebraic transformation given by Malik, Zang and Hussaini [55] is employed in the form

$$r = \hat{a}\,\frac{1 + \xi}{b - \xi} \tag{4.4}$$

where $\hat{a}$ and b are constants. For any arbitrary value of $\hat{a}$, b is uniquely determined by

$$b = 1 + \frac{2\hat{a}}{r_{max}} . \tag{4.5}$$

It should be noted here that parameter, $\hat{a}$, is very significant and that the above transformation concentrates at least half of the collocation points between $r = 0$ and $r = \hat{a}$. Throughout this study, the values of $\hat{a}$ and r_{max} were fixed at 3 and 100, respectively. The convergence behavior of the transformation (Eq. (4.4)) is fully explained in Grosch and Orszag [56] and KMA. Also the tests conducted for the selection of $\hat{a}$ and r_{max} have been discussed in detail in KMA and will not be repeated here.

Figure 4.2 shows the variation of the growth rate of the first three unstable modes with the axial wavenumber, α, for $n = -2$, and $\tilde{q} = 0.8$, at a Reynolds number of 10,000. The curves are identical to the ones resulting from the inviscid calculations of Duck and Foster [19]. Since the present viscous calculations produce identical eigenvalues to those of Duck and Foster, it is logical to assume that the instability is an inviscid one. This would imply that the number of unstable modes depends directly on the number of collocation points as noted by Duck and Foster. However, that conclusion does not appear to be consistent with experiments, and further results in the

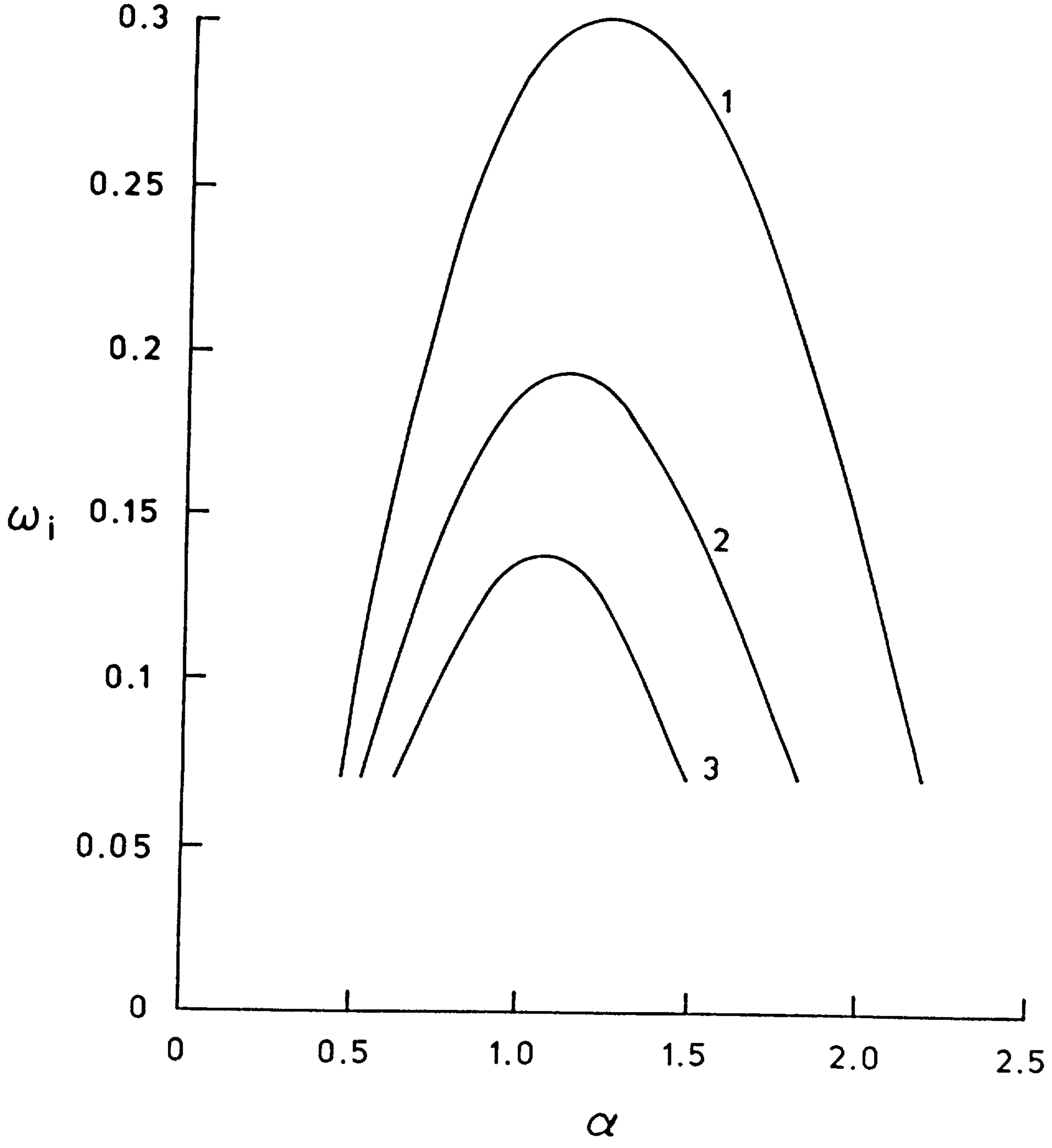

Fig. 4.2 Variation of the growth rate of $n = -2$ disturbances with wavenumber for a trailing line vortex. Here, $\tilde{q} = 0.8$, $Re = 10^4$.

present study will shed some light on this problem. As pointed out by [19], finer resolution is needed to resolve higher modes. Note that the first mode corresponds to that found by Lessen et al. [24]. The variation of the real part of the frequency (ω_r) vs α is shown in figure 4.3. The curve corresponds to mode 1 in the previous figure. Since the other two modes have real parts which are nearly identical with the one shown, they are not plotted for clarity. The variation of growth rate vs axial wavenumber for the case of $n = -1$ is shown in figure 4.4. The calculations were made at Re = 10,000, $\tilde{q} = 0.4$ and only results for the first three modes are plotted. Again, the primary mode corresponds to the inviscid mode obtained by [24]. The ω_r corresponding to this mode is plotted in figure 4.5. Next, the variation of the first two modes with Reynolds number for the case of $n = -2$ at two different values of α are shown in figures 4.6 and 4.7. It is apparent from these plots that they are indeed inviscid modes for Reynolds numbers above 10,000, since they have almost attained their maximum growth rates and are virtually independent of Re. In the case of $n = +2$, no instability has been observed. Although the results shown in figures 4.8-4.10 confirm this fact, figure 4.10 indicates that as Reynolds number increases, the flow approaches a marginally stable condition for this azimuthal wavenumber.

Even though the Batchelor vortex was chosen primarily as a test case to evaluate the staggered collocation method, new insights and some fundamental results have been produced. The fundamental results are related to the identification of new viscous instability modes and were produced during the testing. Before presenting the discussion of the new results, as mentioned in Sec. 4.1, it is important to explain some discrepancies which exist between this study and earlier work.

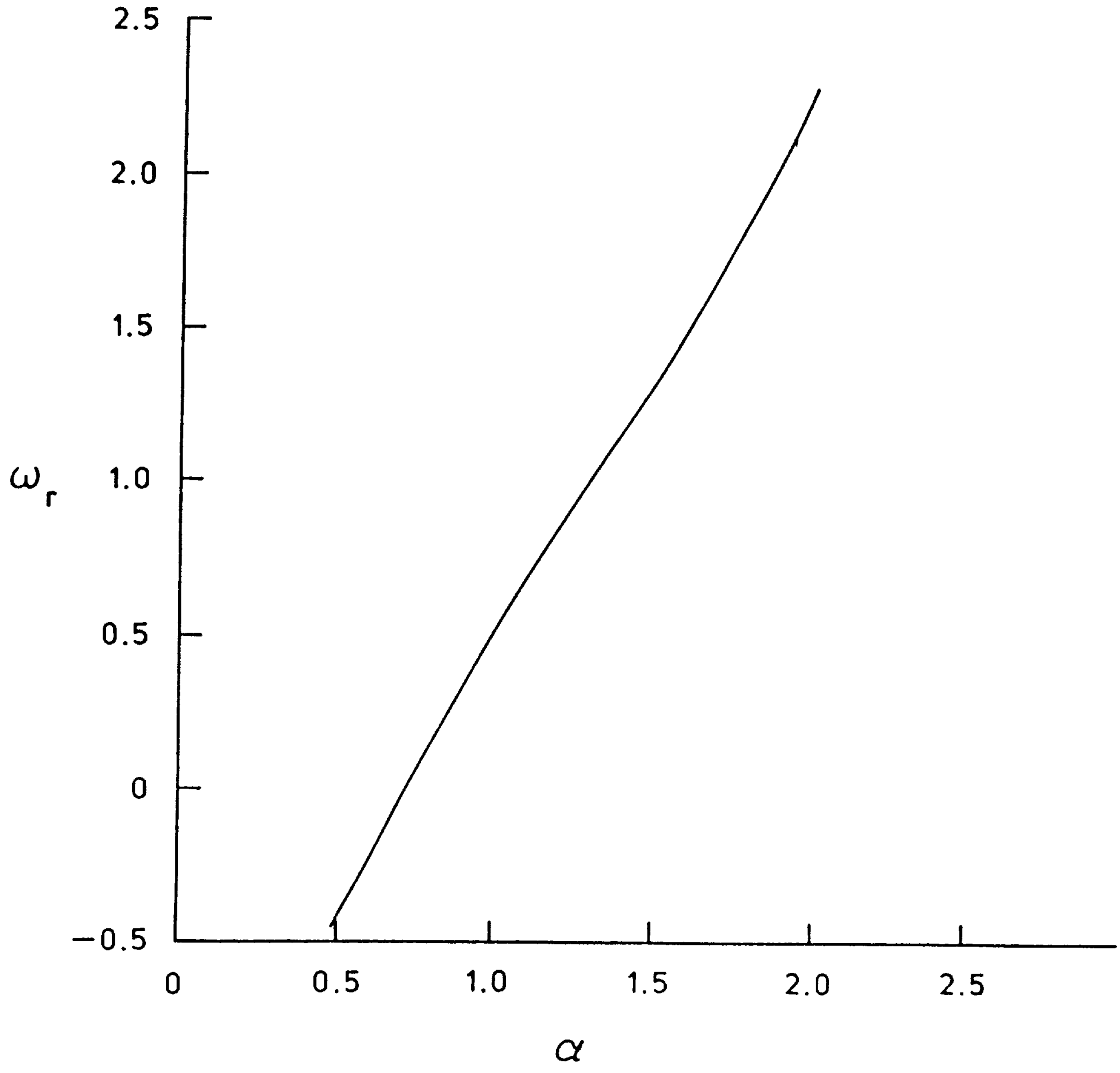

Fig. 4.3 Variation of the real part of frequency of $n = -2$ disturbances with wavenumber for a trailing line vortex. Here, $\tilde{q} = 0.8$, $Re = 10^4$.

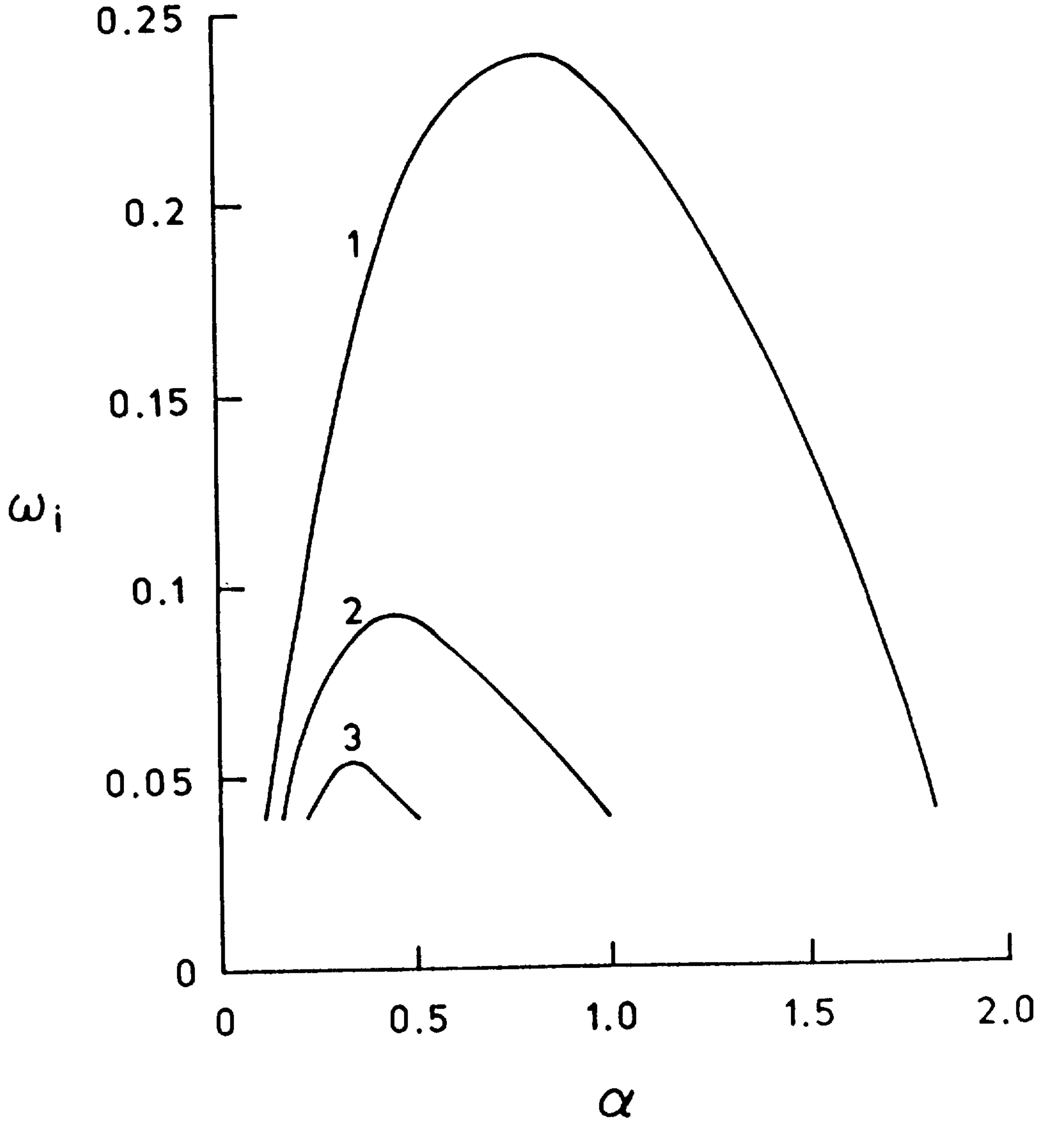

Fig. 4.4 Variation of the growth rate of asymmetric (n =-1) disturbances with wavenumber for a trailing line vortex. Here, $\tilde{q}$ = 0.4, Re = 10^4.

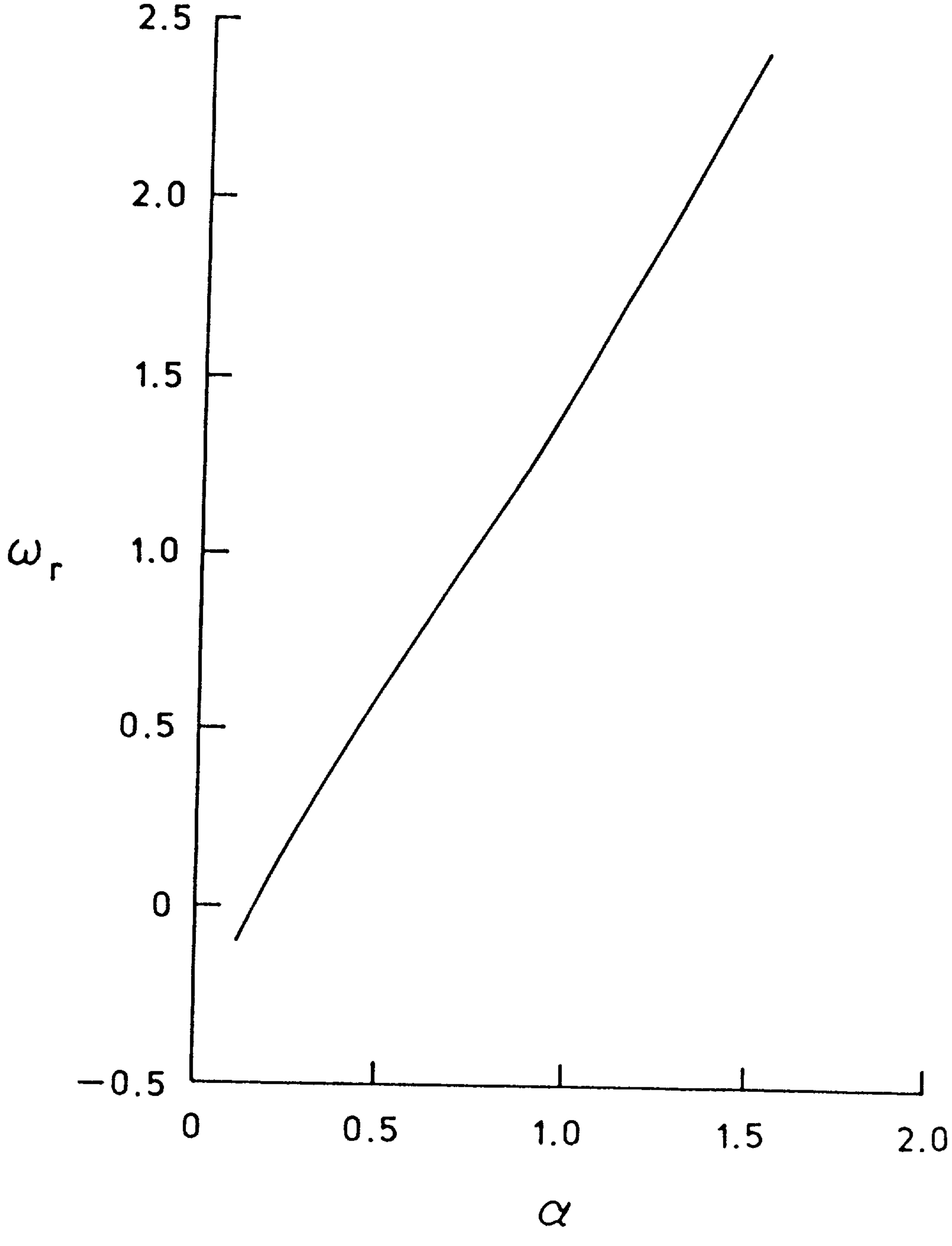

Fig. 4.5 Variation of the real part of frequency of asymmetric (n = -1) disturbances with wavenumber for a trailing line vortex. Here, $\tilde{q} = 0.4$, $Re = 10^4$.

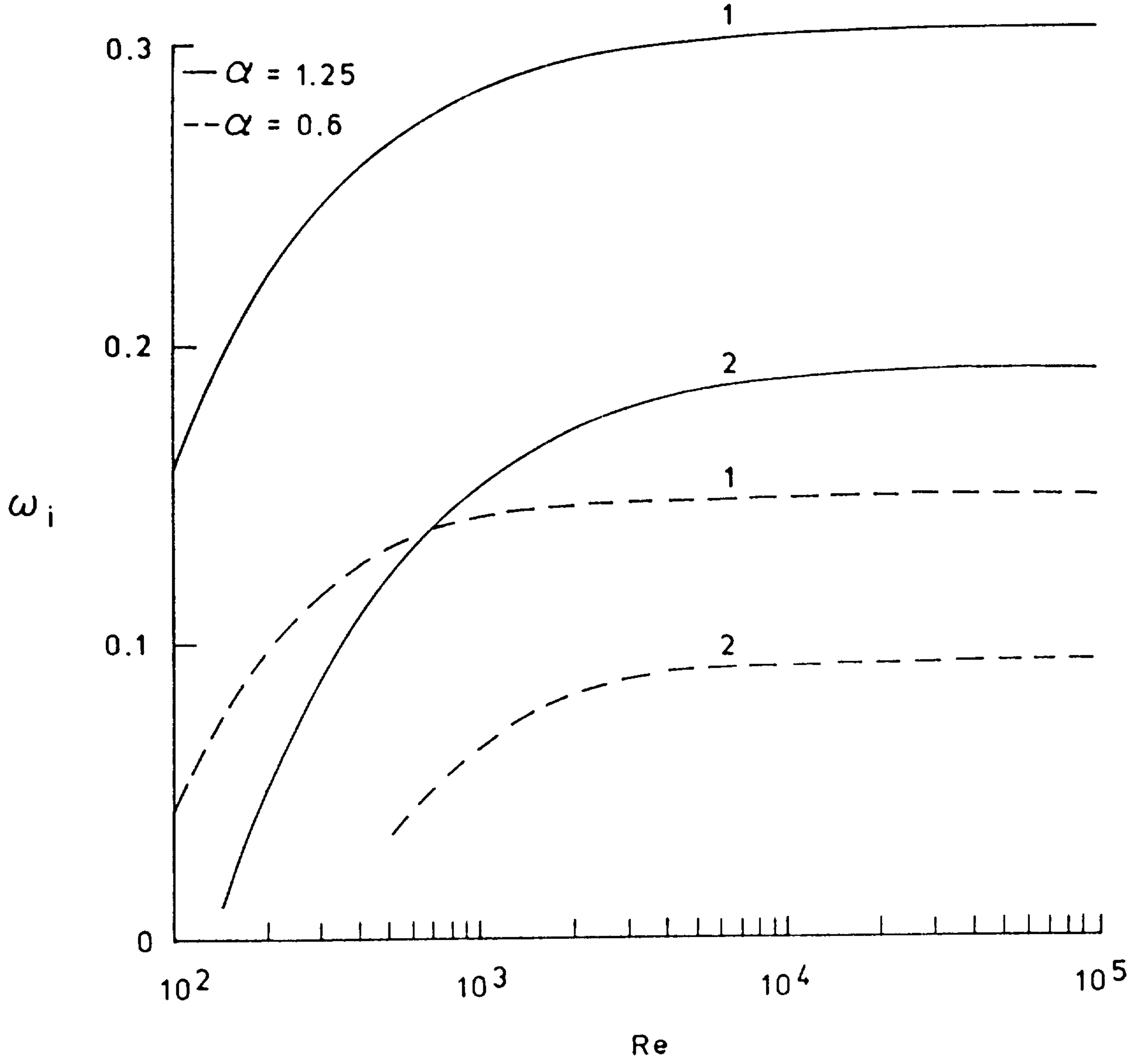

Fig. 4.6 Variation of the growth rate of n = -2 disturbances with Reynolds number for a trailing line vortex. Here, $\tilde{q}$ = 0.8 .

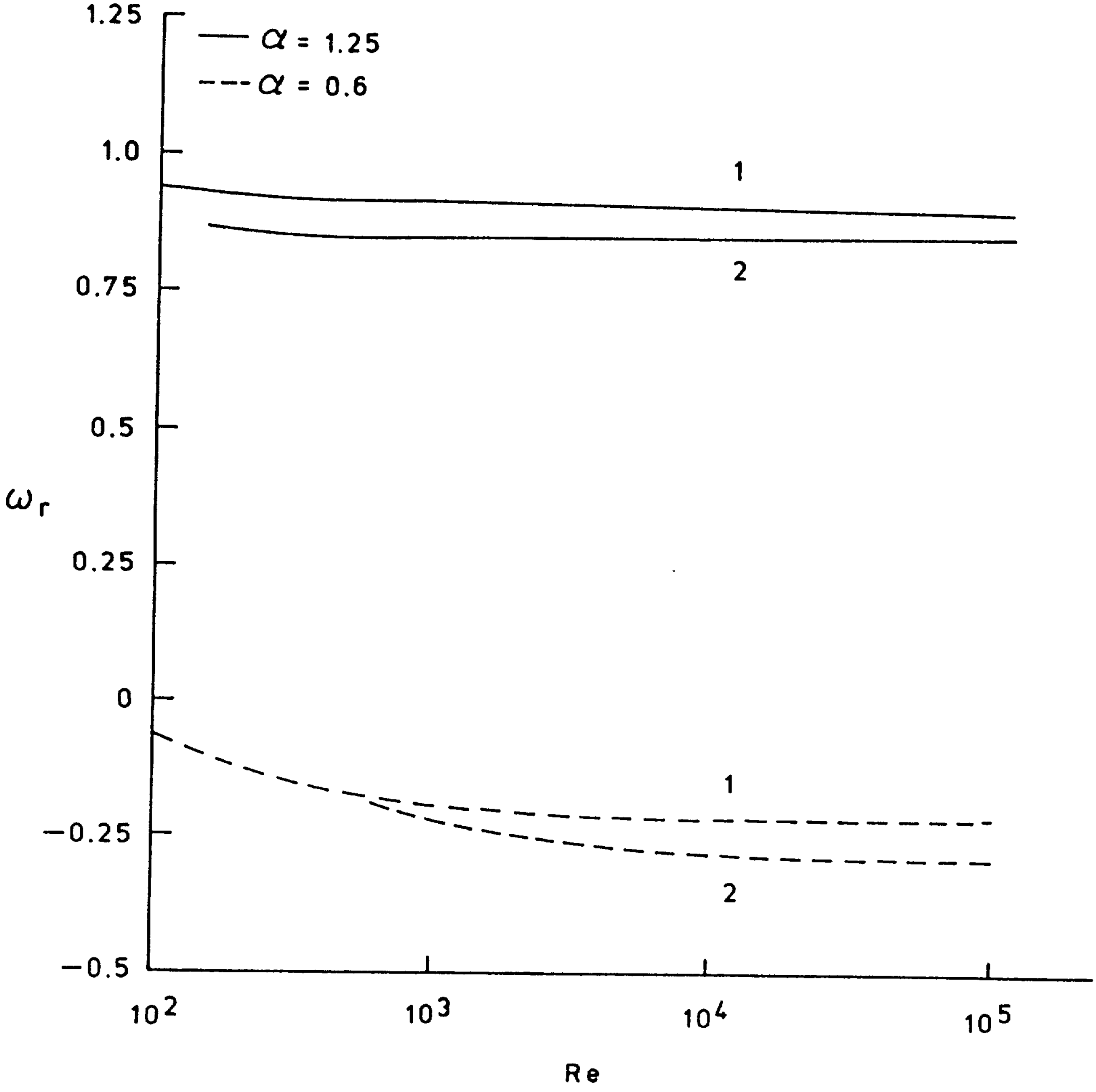

Fig. 4.7 Variation of the real part of frequency of n = -2 disturbances with Reynolds number for a trailing line vortex. Here, $\tilde{q}$ = 0.8.

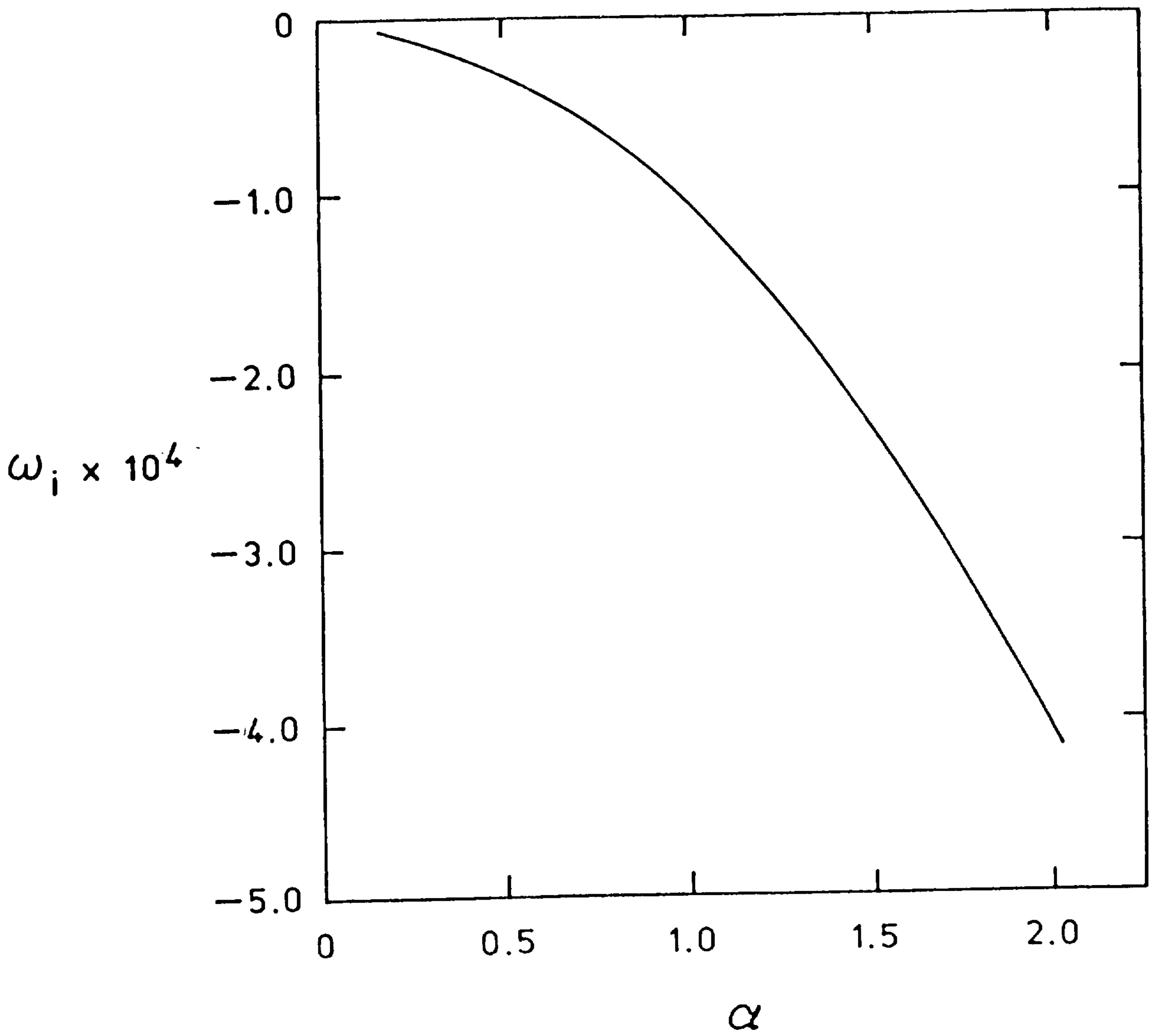

Fig. 4.8 Variation of the growth rate of $n = +2$ disturbances with wavenumber for a trailing line vortex. Here, $\tilde{q} = 0.8$, $Re = 10^4$.

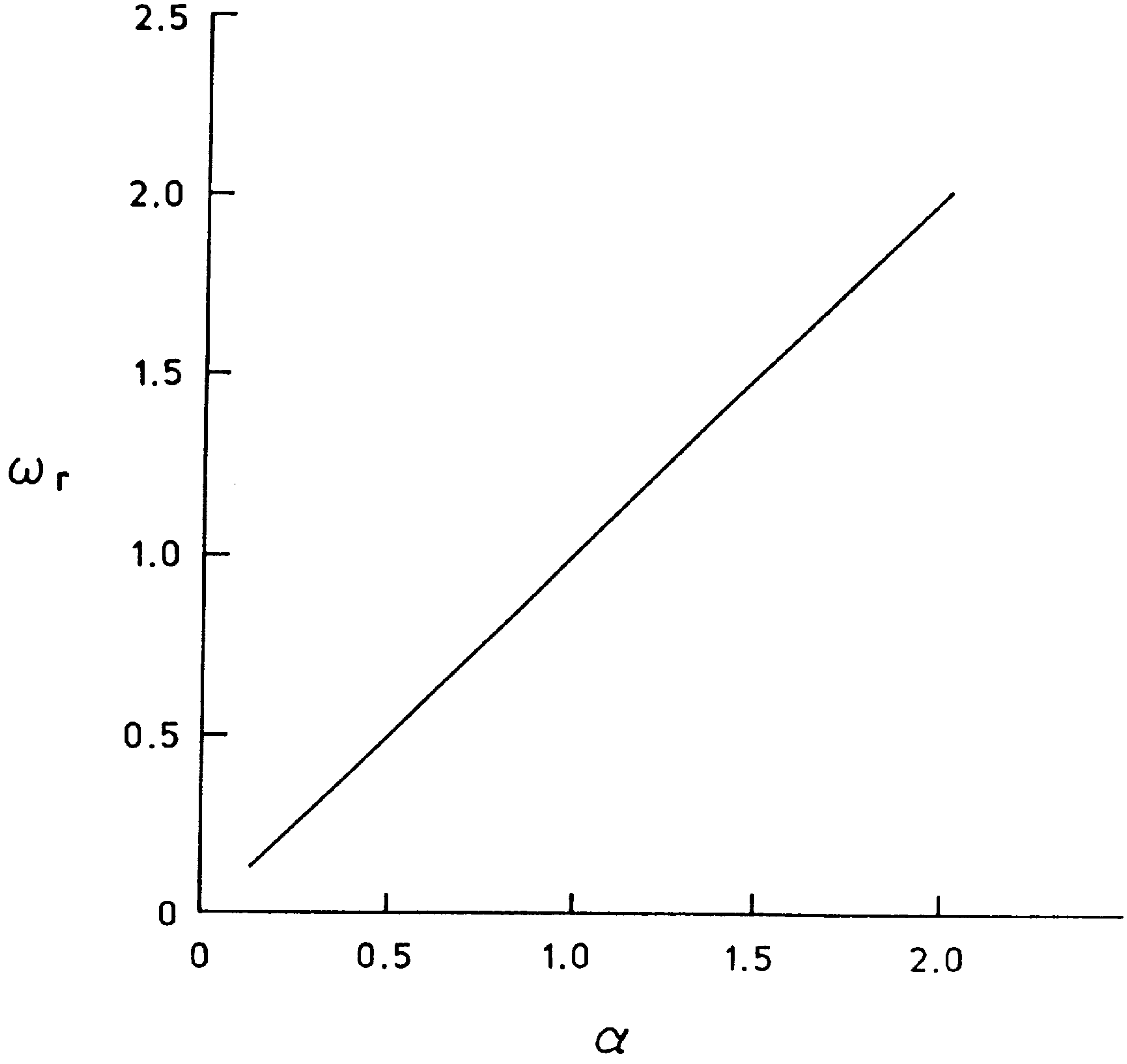

Fig. 4.9 Variation of the real part of frequency of n = +2 disturbances with wavenumber for a trailing line vortex. Here, $\tilde{q} = 0.8$, Re = 10^4.

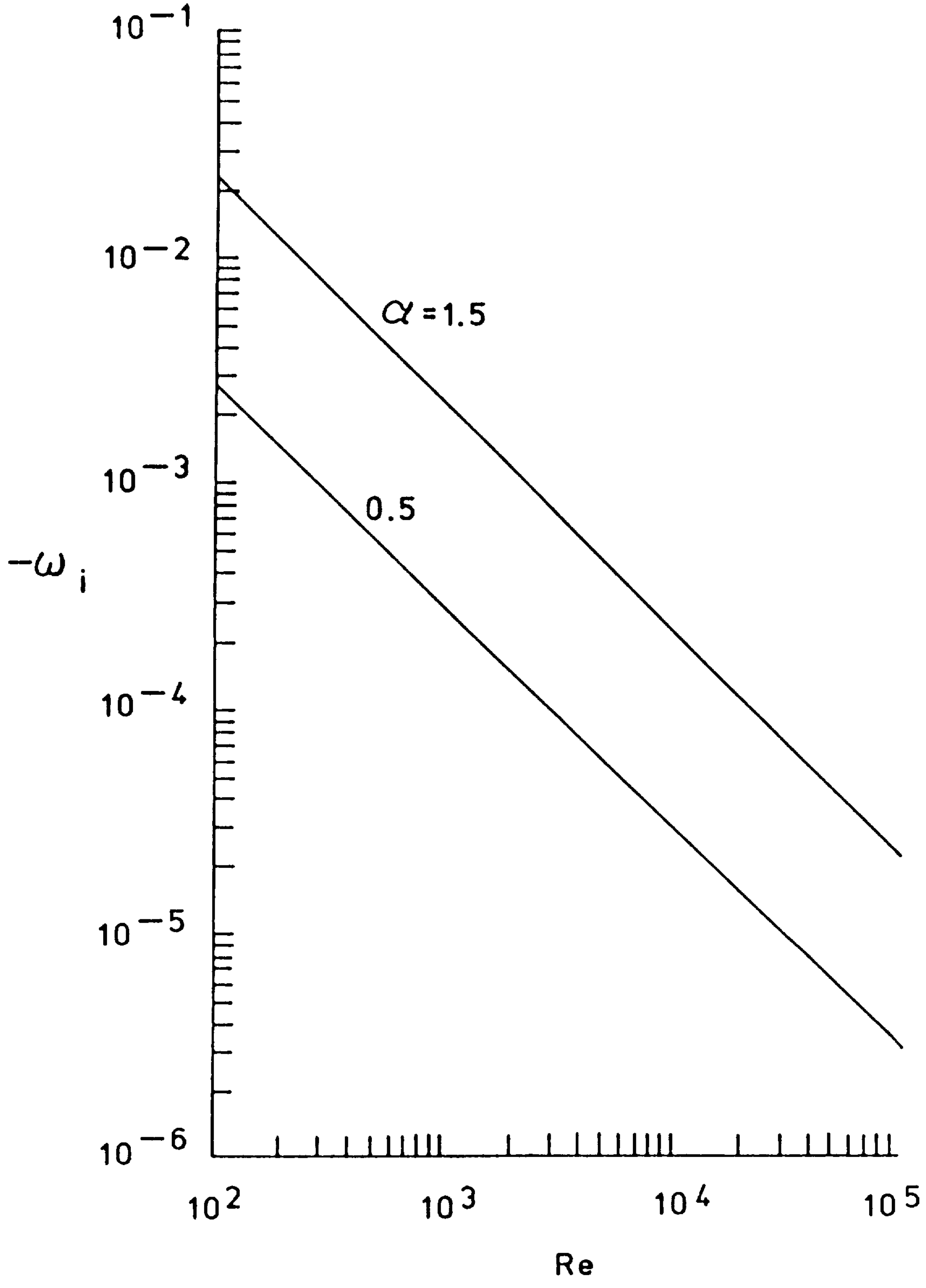

Fig. 4.10 Variation of the growth rate ρf $n = +2$ disturbances with Reynolds number for trailing line vortex. Here, $\tilde{q} = 0.8$.

Recently, results were reported in KMA which indicated that although qualitative agreement exists between the collocation method and the viscous calculations of Lessen and Paillet [27], there are quantitative disagreements. The disagreement is shown in figure 4.11 (taken from KMA) which presents the variation of ω_i, with the swirl parameter $\tilde{q}$. Of interest is the existence of a second mode of instability which was not obtained by [27]. The staggered collocation method employed here has confirmed KMA's earlier findings and their two curves shown in the figure were reproduced identically. The above result indicates that these inviscid higher modes exist at much lower Reynolds numbers than had been expected. A further test was conducted in which the critical values, given by Lessen and Paillet [27], were used as input for the present method and ω_i was calculated. The results are tabulated in Table 4.4. It is clear from the magnitude of ω_i's that the values taken from [27] are not very close to the critical point. In order to show the accuracy obtainable by the collocation method, the critical value for the axisymmetric case is presented in Table 4.5. After careful examination, it was determined that the discrepancies are only with the viscous results of [27]. The inviscid calculations of Lessen et al. [24], which employed similar methods to those used in the later viscous analysis, are consistent with the collocation results. The discrepancy can be explained by a detailed examination of the approach taken by Lessen and Paillet.

Starting the solution at $r = 0$ with a Frobenius series and at $r = r_{max}$ with an asymptotic solution, Lessen and Paillet [27] integrated from both limits using a Taylor series expansion and matching the solutions at some intermediate radius. They mentioned that the results were strongly dependent on the radius of integration, r_{max} as well as the intermediate matching condition. The dependency of the eigenvalue on r_{max} has been demonstrated by

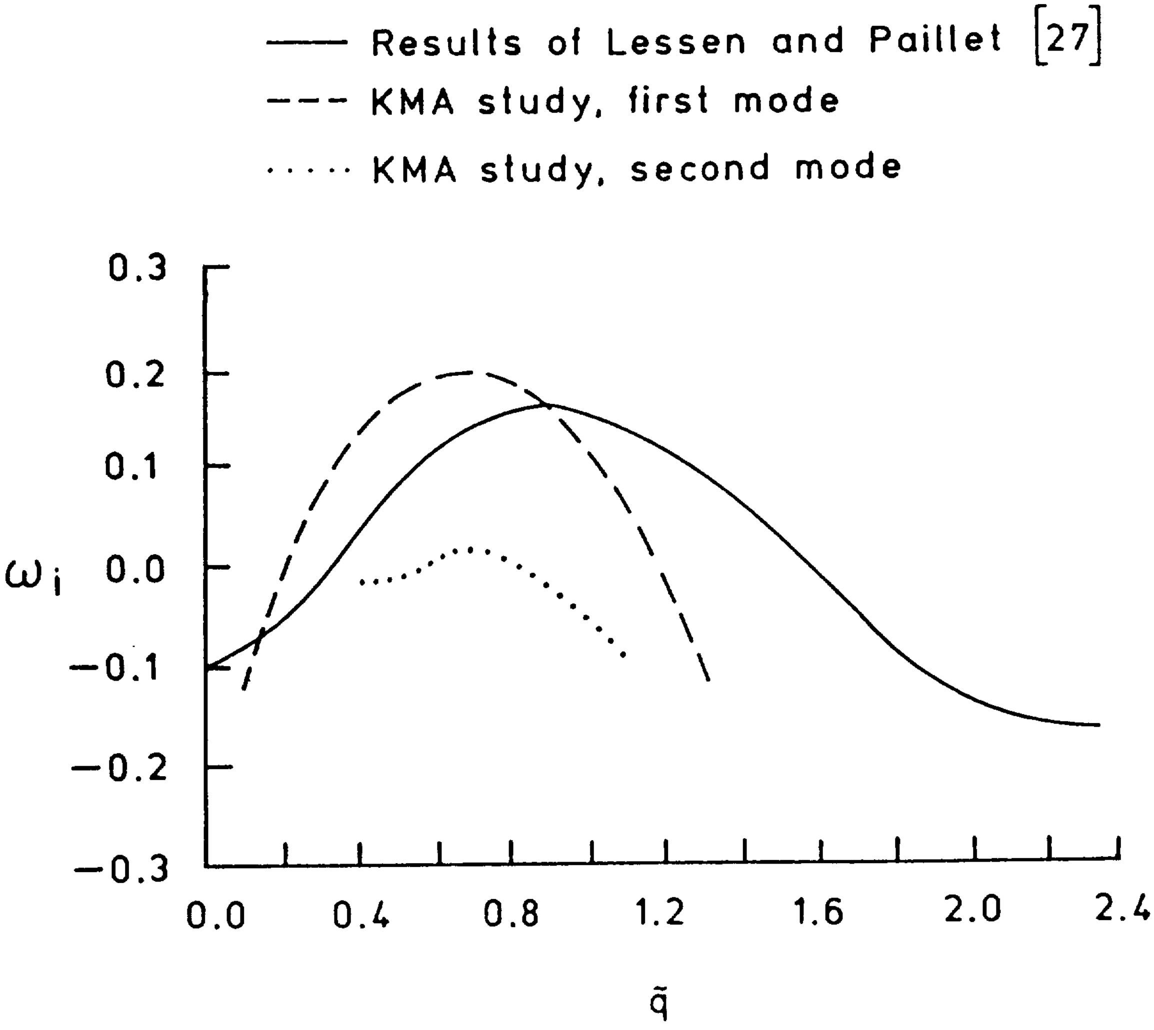

Fig. 4.11 Variation of the growth rate with swirl parameter, $\tilde{q}$, for a trailing line vortex. Here, $n = -2$, $\alpha = 1.34$ and $Re = 141.4$.

Table 4.4 The Critical Values of ω_i Obtained by the Present Method for Different Azimuthal Wavenumbers. The Critical Values for Re_c, α_c, $\tilde{q}_c$ were Taken from Lessen and Paillet [27].

n	α_c	$\tilde{q}_c$	Re_c	ω_i
-1	0.42	0.45	13.9	-0.002547
-2	0.91	0.70	27.9	-0.029787
-3	1.62	0.95	48.2	-0.05455

Table 4.5 Critical Values of Different Parameters for the Axisymmetric Case $n = 0$.

α_c	Re_c	$\tilde{q}_c$	ω
0.468	322.35	1.08	$0.441679 - i4.97\times10^{-7}$

further testing. Table 4.6 shows the variation of the maximum growth rate for different azimuthal wavenumber, n, as compared with the inviscid calculations of [19, 24]. Remember that the values of Re apply only to the present viscous calculations. The results obtained by the present method indicate very good agreement with those of [19, 24]. In the case of n = - 1, as the Reynolds number increases, the convergence of the eigenvalue toward the value obtained by the finite difference global method of Duck and Foster [19] is excellent, while it is acceptable with respect to that of [24]. Duck and Foster [19] have indicated that for n = -1, they had to go to larger values of r_{max} such as 10 or 12 in order to obtain convergent results. The present result was obtained with $r_{max} = 100$, which is much larger than their r_{max}, and substantiates their findings. Finally, the dependency of the eigenvalues on r_{max} is clearly demonstrated in the work of Paillet [57] and was recently confirmed by Lessen (private communication).

It is well known that in the previous stability calculations of the Batchelor vortex, axisymmetric instability was not observed. However, while conducting some routine calculations in the present study, two new modes of instability were discovered. One instability mode was an axisymmetric, n = 0, mode and the other was an asymmetric, n = 1, mode. Both are viscous modes. Figure 4.12 shows the variation of growth rate, ω_i with α for $n = 0$, $\tilde{q} = 1$ and Re = 10,000. The figure indicates that this mode has a growth rate which is orders of magnitude smaller than the inviscid modes. The maximum value of ω_i occurs roughly at $\alpha \simeq 0.3$ which suggests that the disturbance's wavelength is on the order of the core radius of the vortex. The variation of the real part of the frequency with α is plotted in figure 4.13. The nearly straight line indicates that the axial phase speed of the wave, $C_r = \omega_r/\alpha$, is constant and equal to unity over a wide range of α. Variation of ω vs

Table 4.6 Comparison of Maximum Growth Rate for Different Azimuthal Wavenumber.

Re	n	α_{max}	$\tilde{q}_{max}$	Inviscid Lessen et al. [24] ω_i	Inviscid Duck and Foster [19] ω_i	Present Method ω_i
20000	-1	0.3	0.32	0.1470	0.14955	0.14904
100000	-1	0.3	0.32	0.1470	0.14955	0.14935
20000	-2	1.2	0.70	0.3138	0.31392	0.31274
50000	-2	1.2	0.70	0.3138	0.31392	0.31332
100000	-2	1.2	0.70	0.3138	0.31392	0.31352
100000	-3	1.7	0.79	0.3544	0.35462	0.35404
100000	-4	2.15	0.82	0.3777	0.37754	0.37687

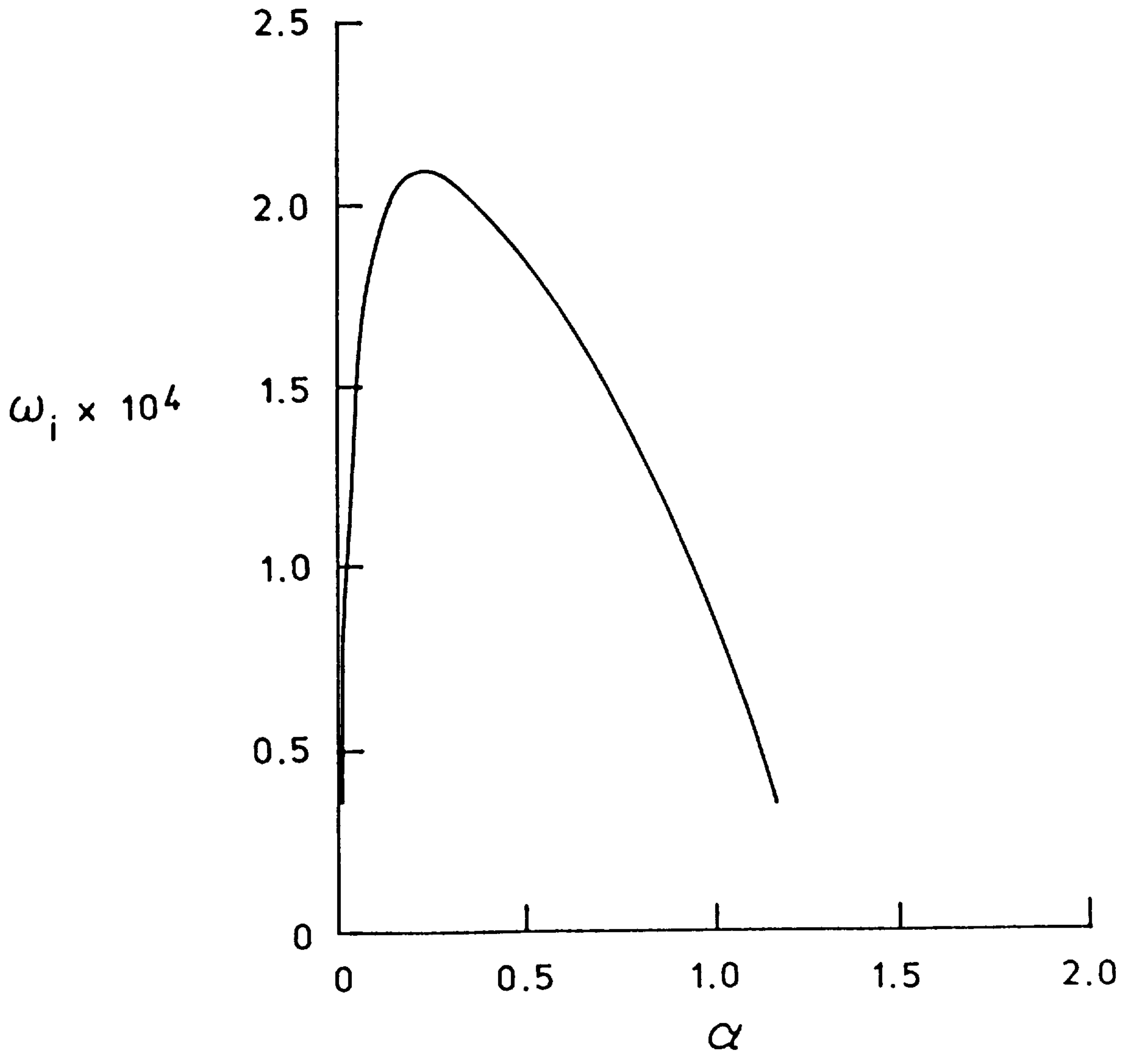

Fig. 4.12 Variation of the growth rate of axisymmetric (n = 0) disturbances with wavenumber for a trailing line vortex. Here, $\tilde{q}$ = 1.0, Re = 10^4.

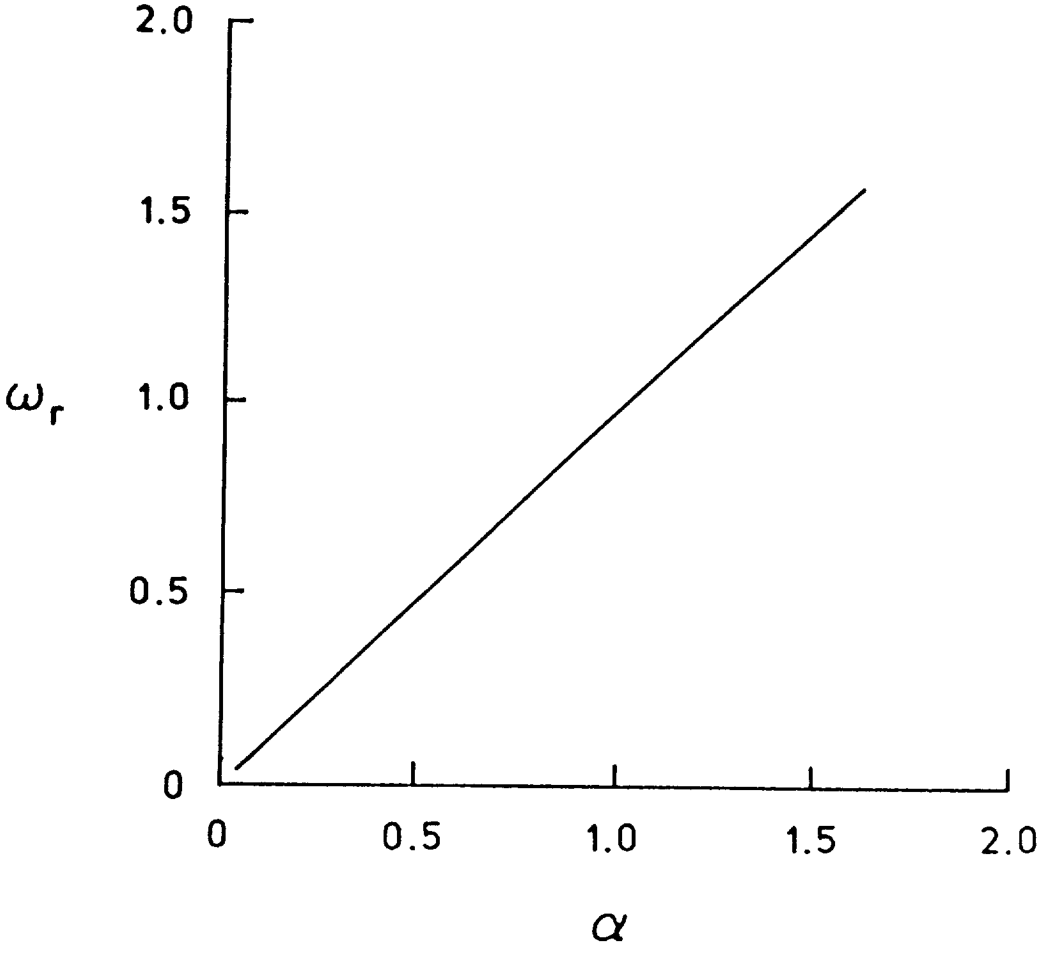

Fig. 4.13 Variation of the real part of frequency of axisymmetric ($n = 0$) disturbances with wavenumber for a trailing line vortex.
Here, $\tilde{q} = 1.0$, $Re = 10^4$.

Reynolds number are presented in figures 4.14 and 4.15, for two distinct wavenumbers. As the Reynolds number increases, the disturbance attains its maximum growth rate very rapidly and then drops gradually. The maximum of ω_i shifts to higher Re as α increases and there is a significant drop in its magnitude. Figure 4.15 shows that the phase speed is constant over a wide range of Reynolds number and has a magnitude which is slightly less than the uniform outer flow. The variation of the wavenumber of the maximum growth rate with Reynolds number is shown in figure 4.16. The curve is consistent with the behavior of a viscous mode and shows the damping effect of viscosity on the wavenumber at moderate Reynolds numbers. Finally, the critical values are compiled for the different control parameters for this axisymmetric mode in Table 4.5.

The axisymmetric mode just described has been observed in many experiments and photographs of many contrails of commercial aircraft. Although the phenomena is termed "core bulging" or "core bursting" in the open literature, the present author believes that is a misnomer since the phenomena is traveling outside the core and the core remains intact. This fact is demonstrated in the photographs shown in figures 4.17-4.19. These photos which are contrails of a large commercial aircraft were reproduced from the work of Bisgood [58]. They were taken from the ground with the vortices at heights between 10,000 and 12,000 meters. The separation distance between the vortices was between 25 and 40 meters. Figure 4.17 shows clearly that, while axisymmetric instability waves are present, the core still remains intact. The next two photos (figures 4.18 and 4.19) show the amplification and growth of these waves. It must be emphasized here that these photographs are not sequential and might not even be the same contrails. However, of importance here is the presence of the Crow [59] instability in every photo. It seems

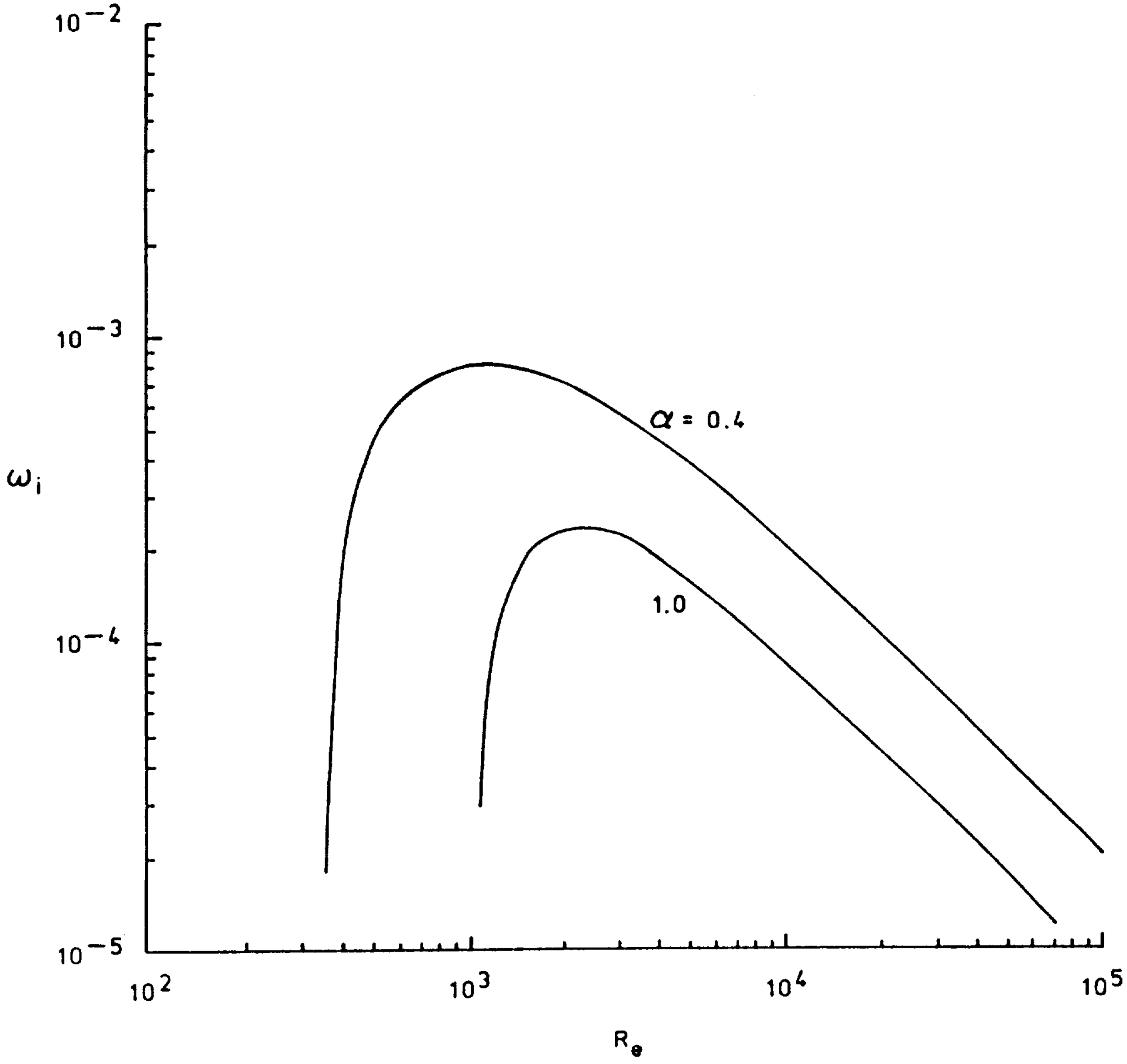

Fig. 4.14 Variation of the growth rate of axisymmetric ($n = 0$) disturbances with Reynolds number for a trailing line vortex. Here, $\tilde{q} = 1.0$.

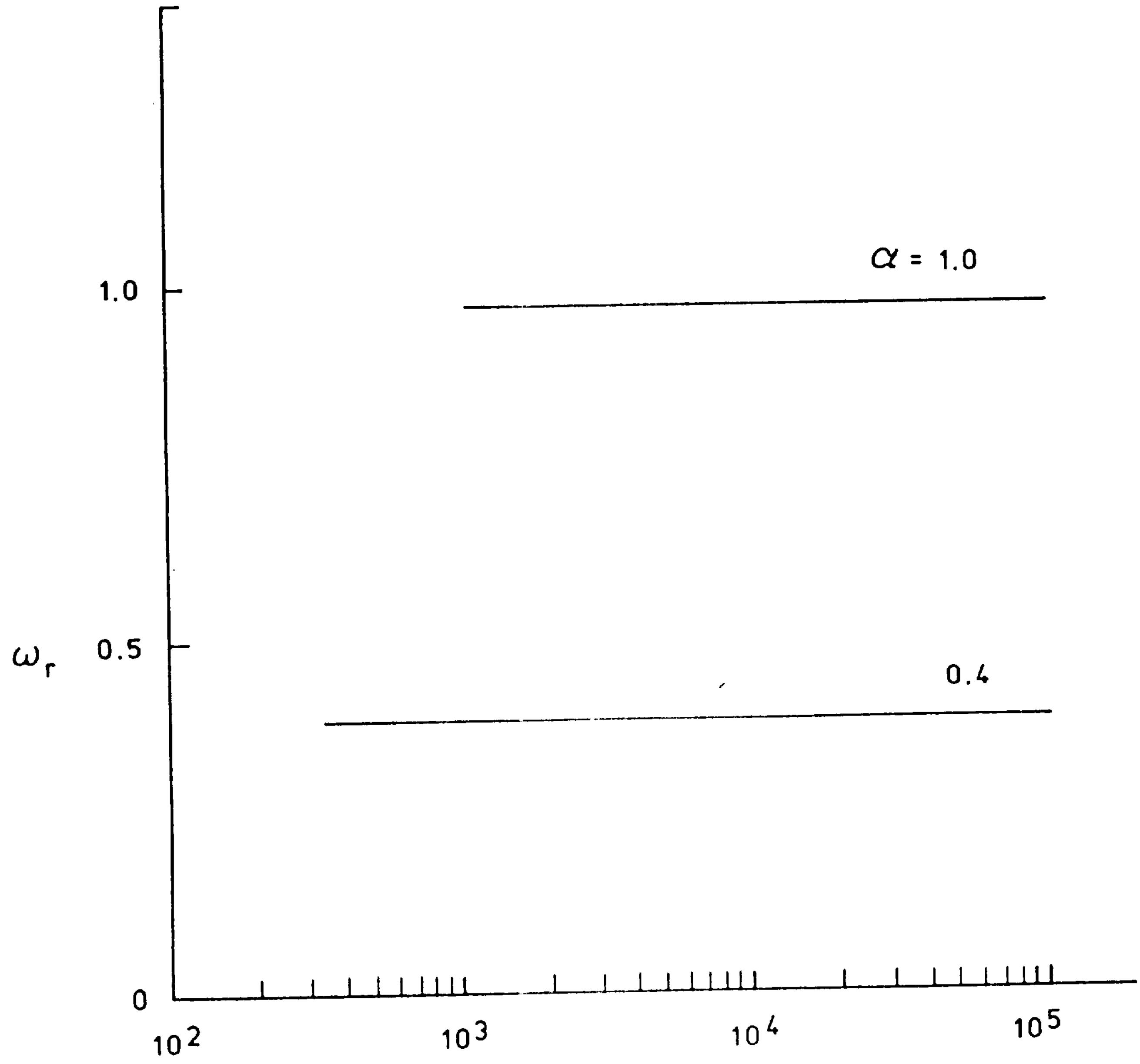

Fig. 4.15 Variation of the real part of frequency of axisymmetric (n = 0) disturbances with Reynolds number for a trailing line vortex. Here, $\tilde{q} = 1.0$.

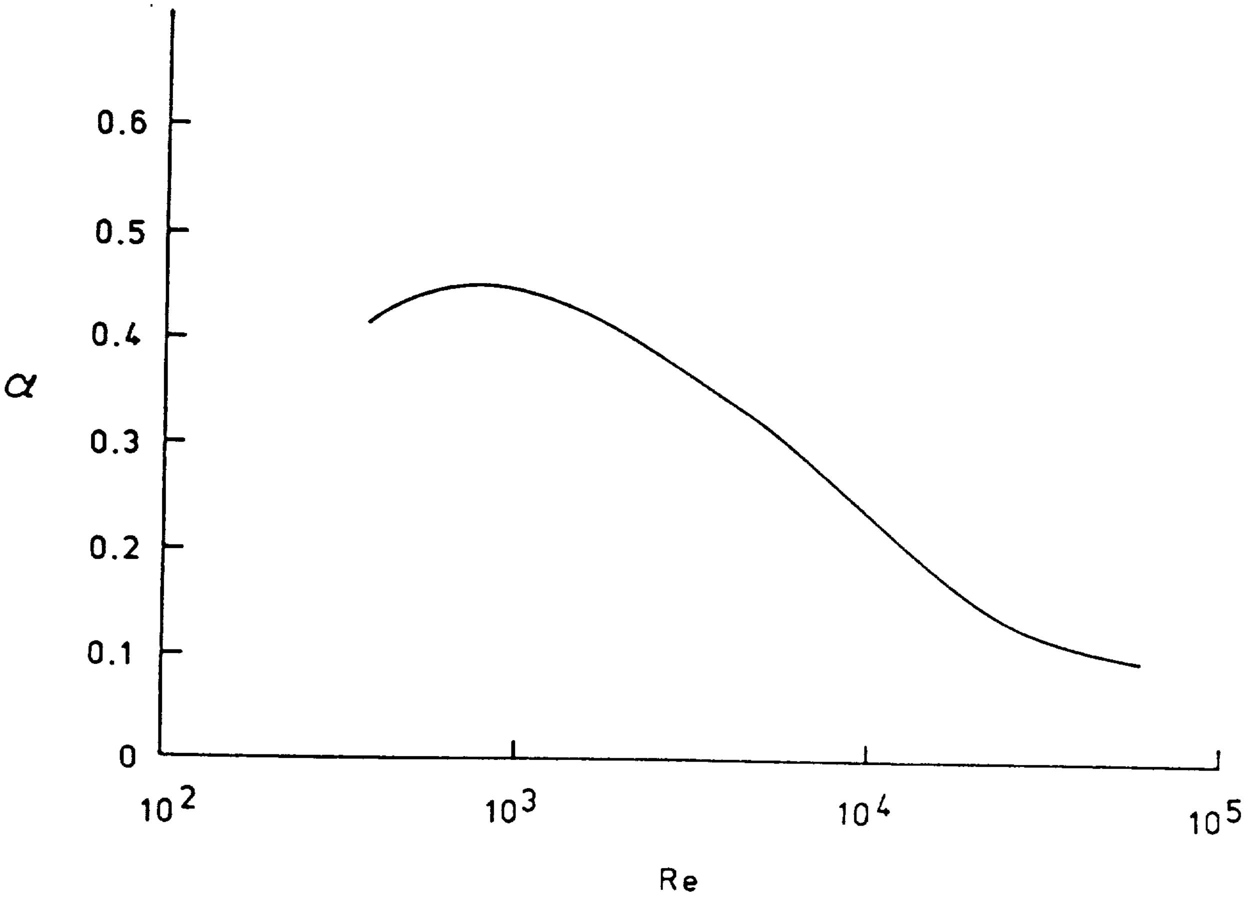

Fig. 4.16 Influence of Reynolds number on the variation of the axial wavenumber associated with maximum growth rate of axisymmetric ($n = 0$) disturbances for a trailing line vortex. Here, $\tilde{q} = 1.0$.

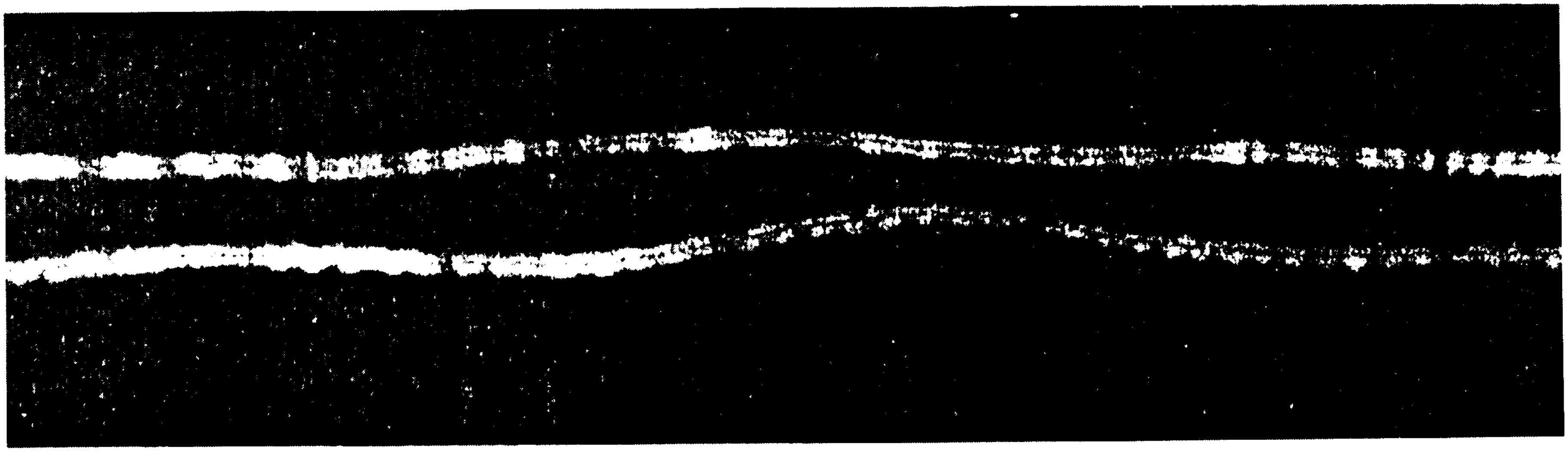

Fig. 4.17 Photographic evidence of growth of axisymmetric (n = 0) disturbances on an aircraft contrail (From Bisgood [58]).

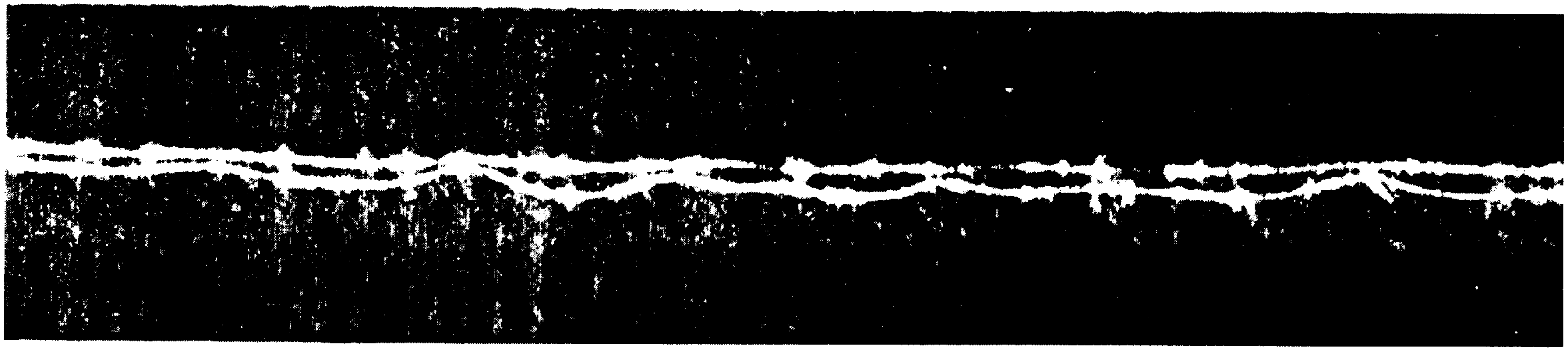

Fig. 4.18 Photographic record of amplification of axisymmetric ($n = 0$) waves on an aircraft contrail (Also from Bisgood [58]).

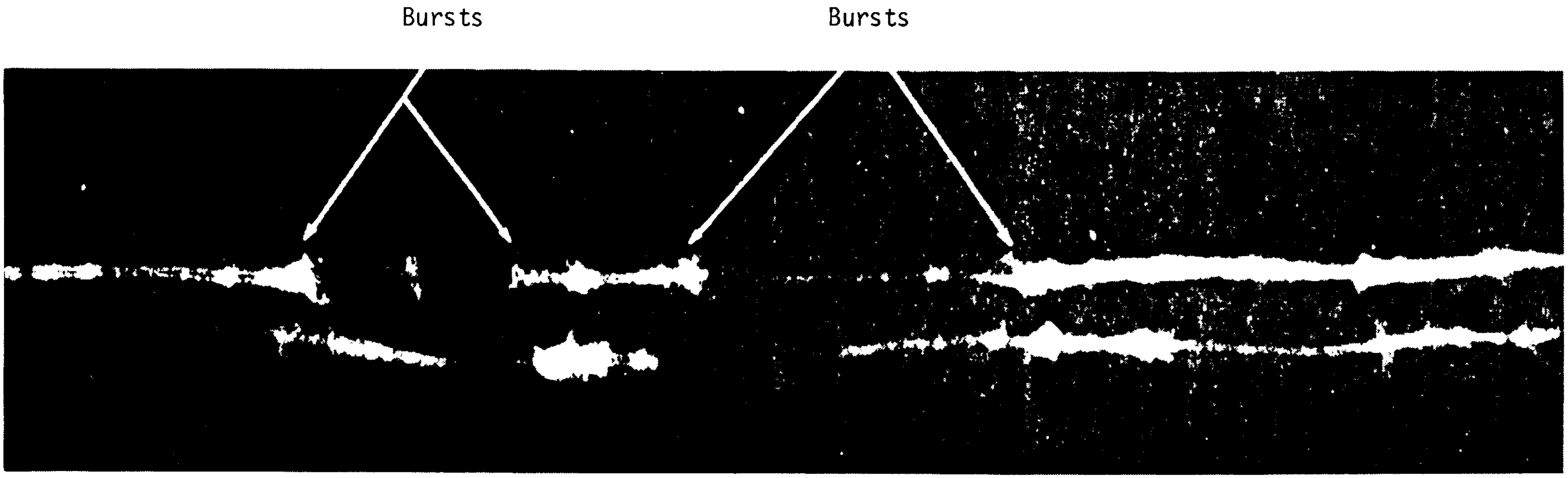

Fig. 4.19 Further growth and bursting of axisymmetric (n = 0) wave form on contrails.

that the two forms of instability (core bulging and Crow) do not interact significantly. This fact was established recently by Sarpkaya and Daly [60] who found that any combination of the instabilities might occur.

Figure 4.20 is another photograph which has been reproduced from the work of Bisgood [58]. Sarpkaya's finding can be supported by this picture which shows Crow's classical "sinuosities" mode without any sign of the axisymmetric wave form. Until further research is carried out, further comments on the nature of the interaction between these two distinct forms of instabilities are speculative and therefore unjustified.

The core radius where the azimuthal mean velocity reaches its maximum is approximately at $r = 1.1$. In order to substantiate the fact that the axisymmetric wave is occurring just outside of the core of the vortex, one has to look at the perturbation eigenfunctions. Figures 4.21a-4.21h represent the eigenfunction amplitudes and phase angles for all of the perturbation components near their critical values. The eigenfunction amplitudes have been normalized by the maximum amplitude of the azimuthal eigenfunction throughout this study. Figures 4.21a and 4.21c are significant and show clearly that most of the perturbation energy in the radial and azimuthal directions is spread over a wide distance and is mostly outside of the core. However, there is hardly anything happening beyond $r = 10$. The phase plot for G in figure 4.21d suggests the existence of a critical layer just outside of the core at $r = 1.5$. A similar critical layer exists in the case of the axial perturbation (figure 4.21f); however, it is positioned inside of the core radius at a distance of about $r = 0.7$. This is understandable since the mean axial velocity has an inflectional point close to $r = 0.75$.

Fig. 4.20 Crow's [59] classical "sinuosities" mode.

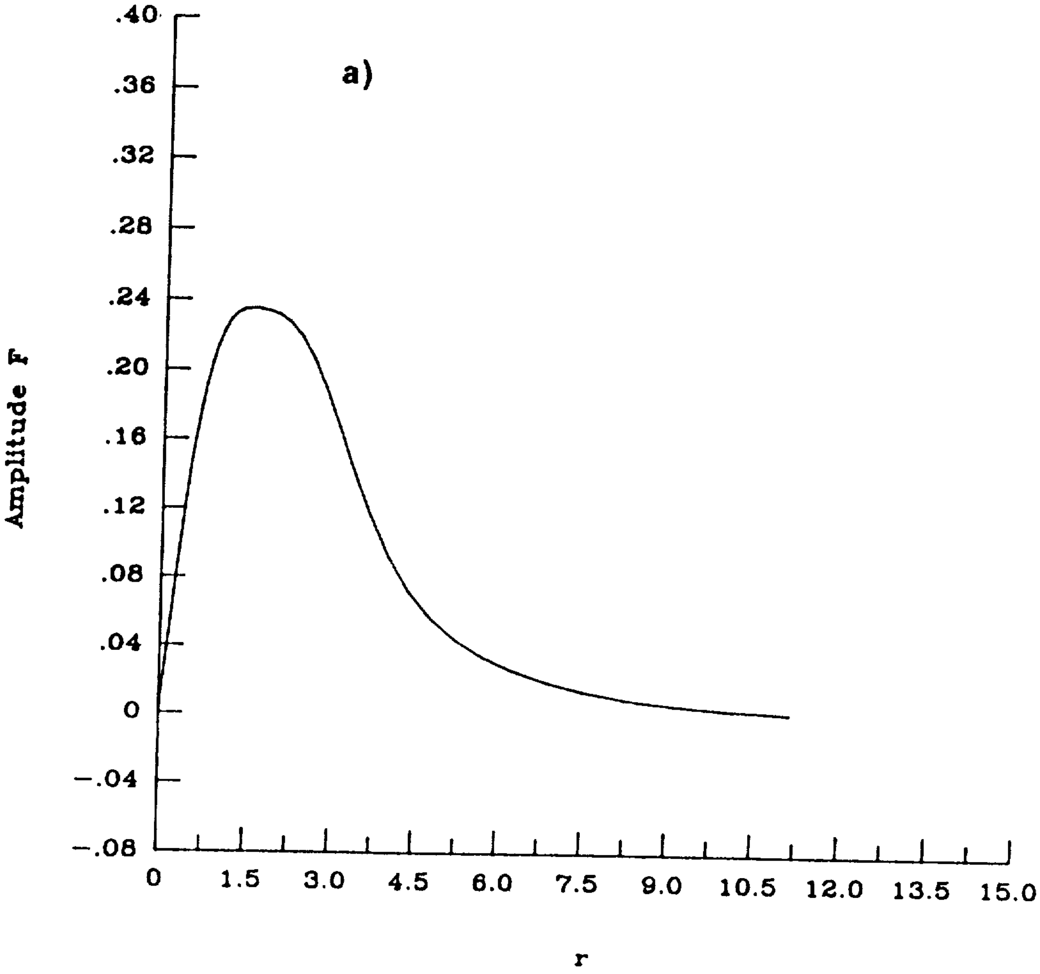

Fig. 4.21 Spatial distribution of amplitude and phase of various eigenfunction components of an axisymmetric (n = 0) perturbation for a trailing line vortex. a) and b) radial velocity, c) and d) azimuthal velocity, e) and f) axial velocity, g) and h) pressure. Here, $\alpha = 0.4$, $\tilde{q} = 1.0$, Re = 400.

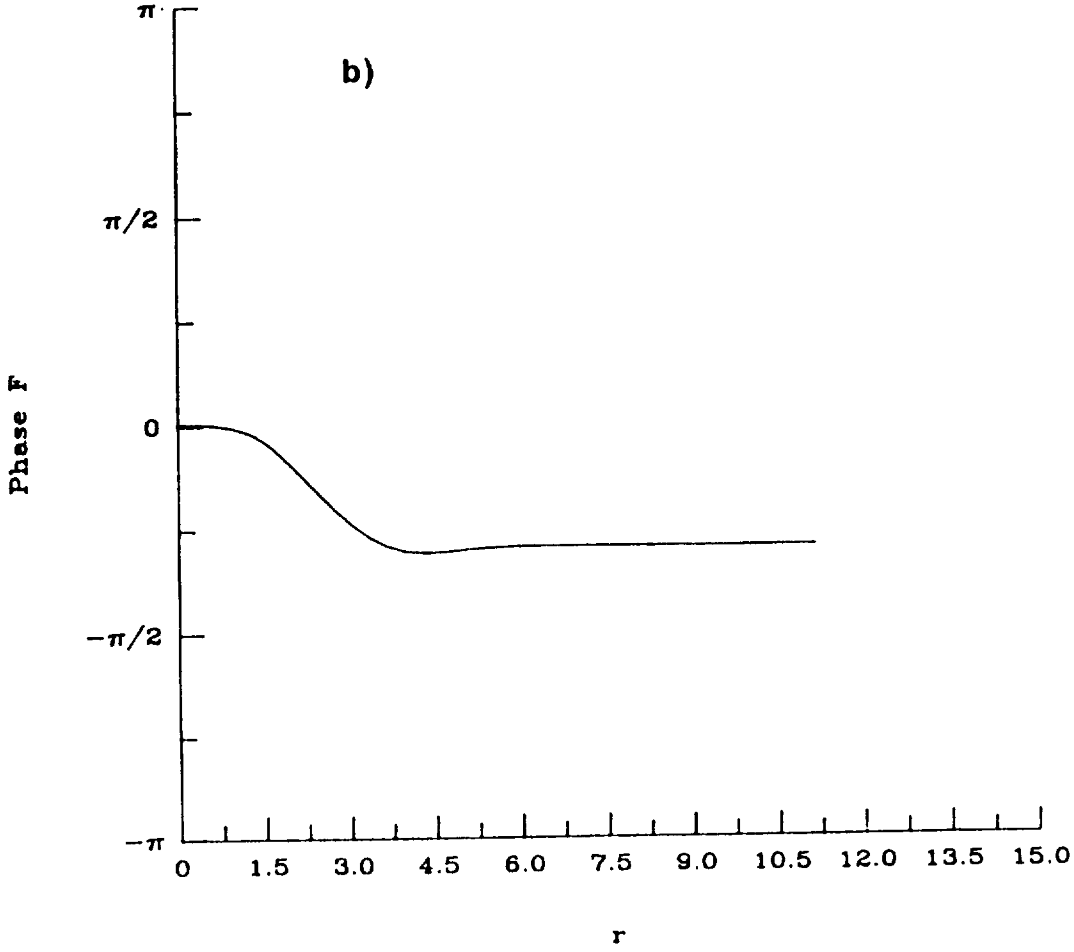

Fig. 4.21b) Continued.

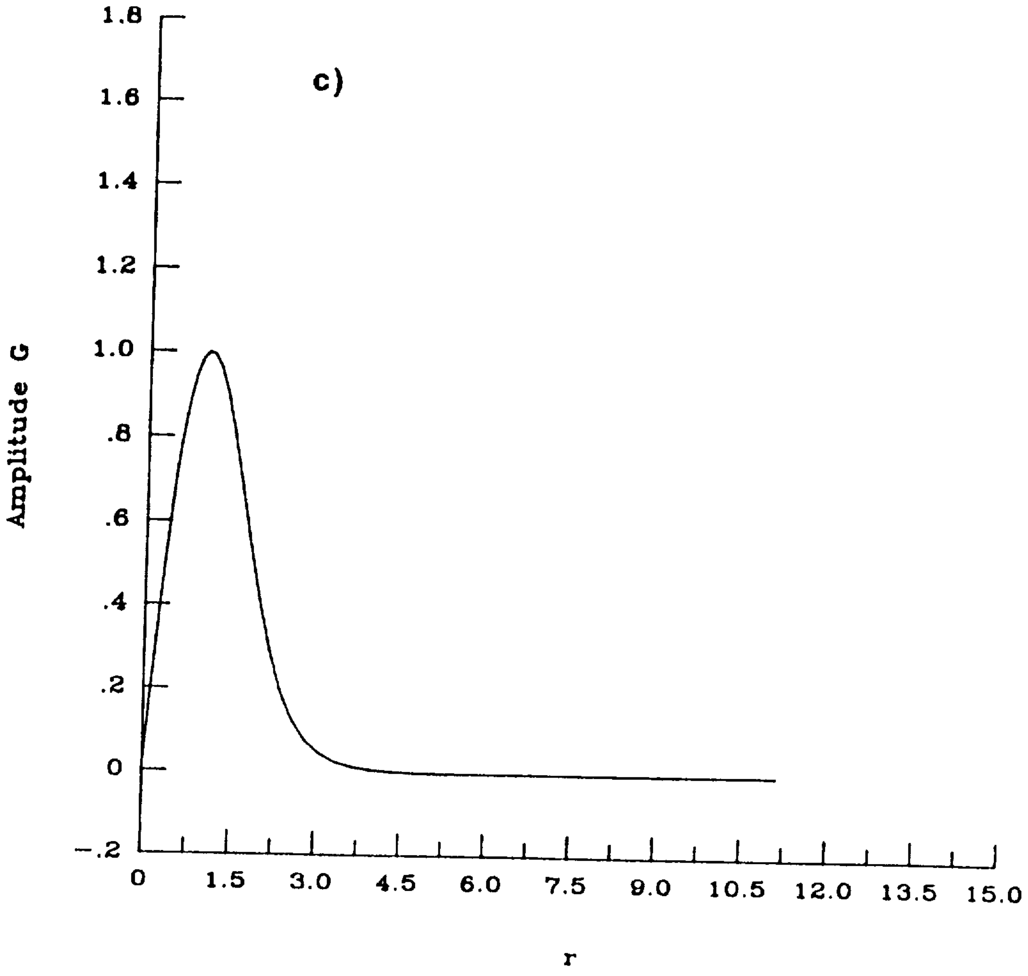

Fig. 4.21c) Continued.

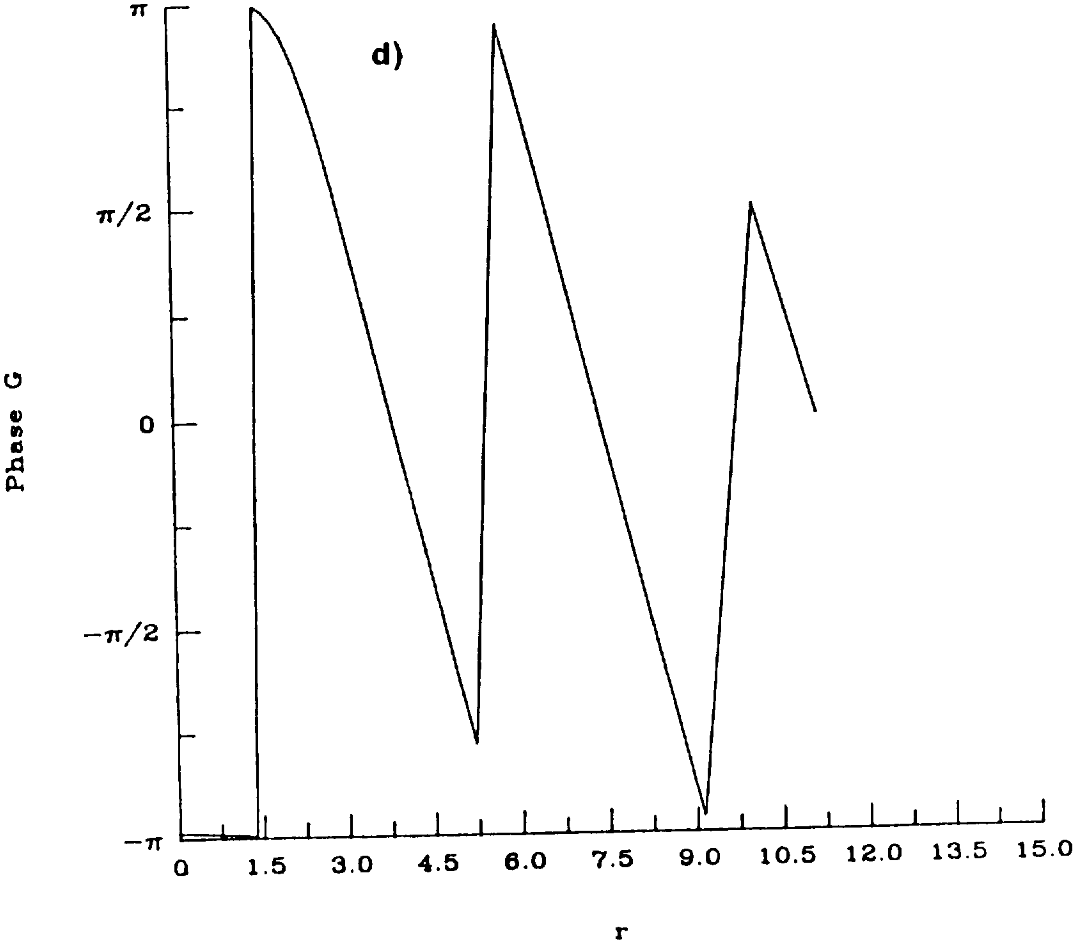

Fig. 4.21d) Continued.

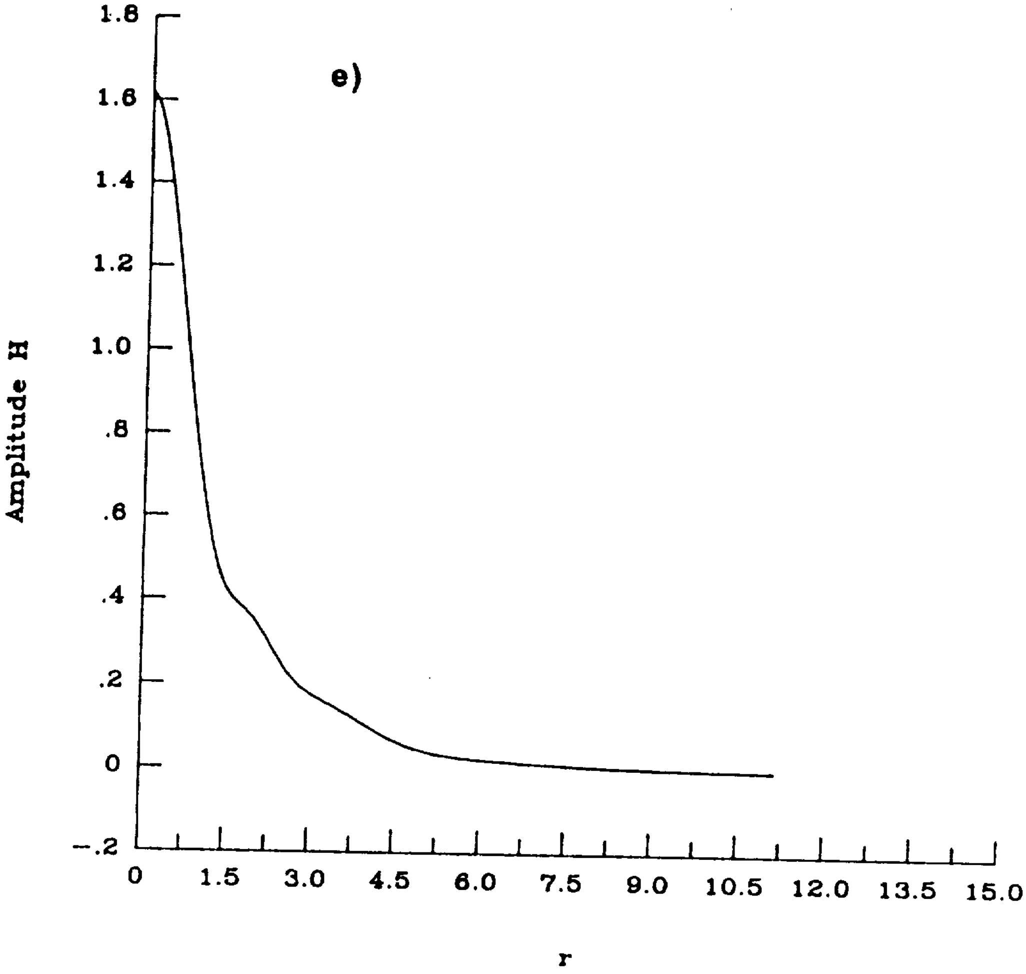

Fig. 4.21e) Continued.

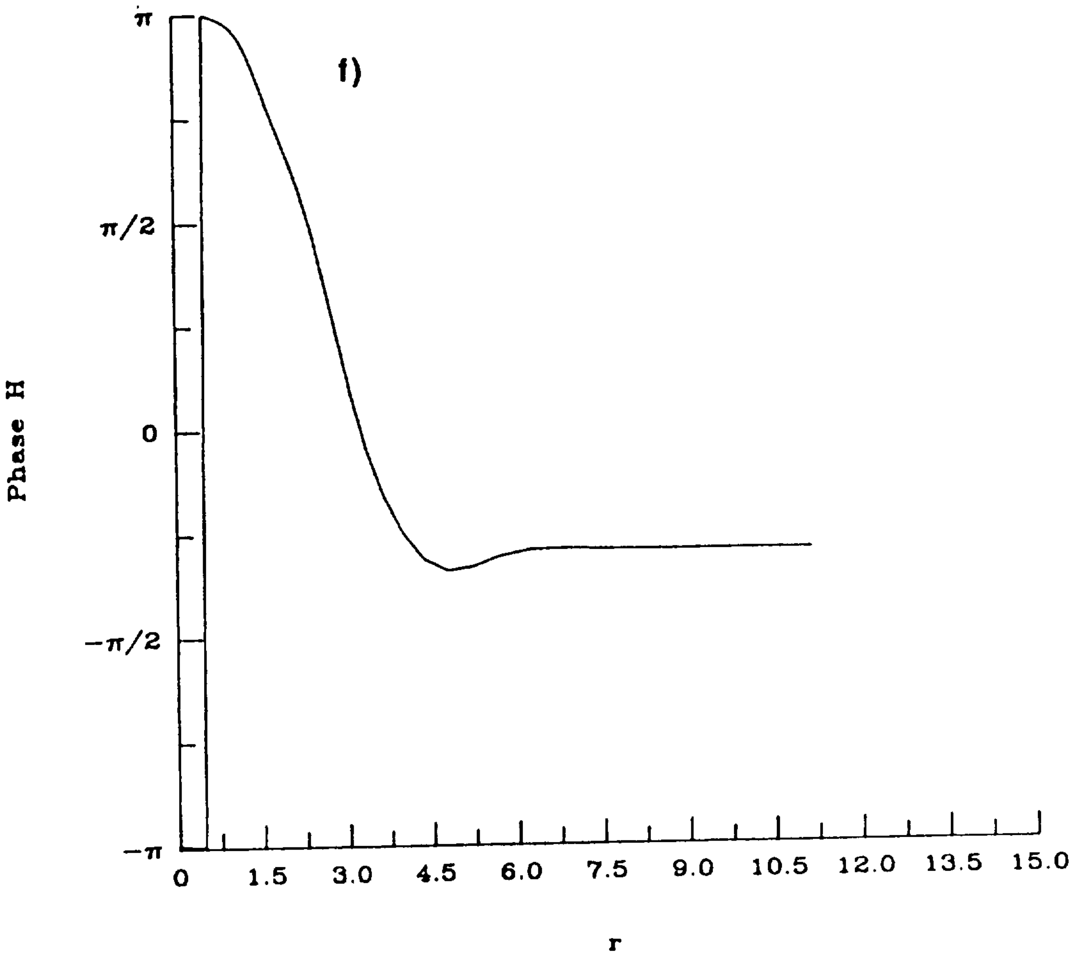

Fig. 4.21f) Continued.

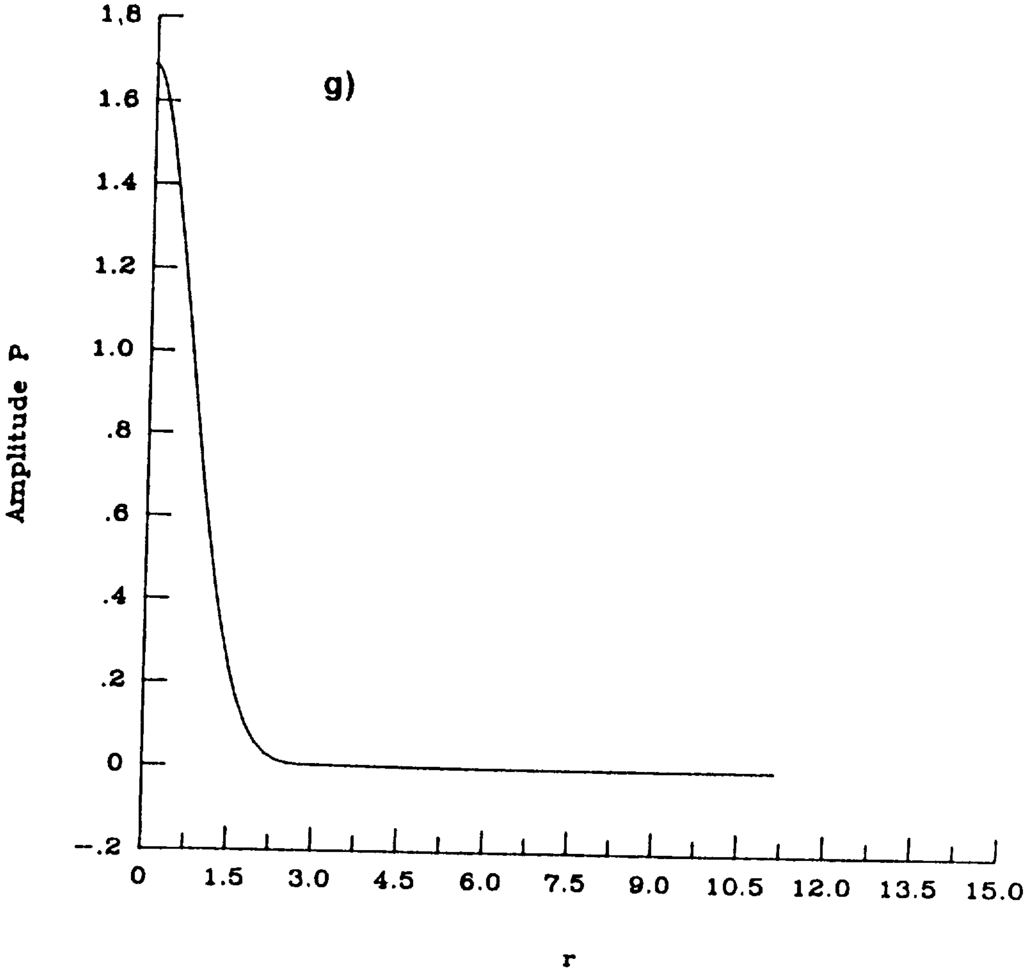

Fig. 4.21g) Continued.

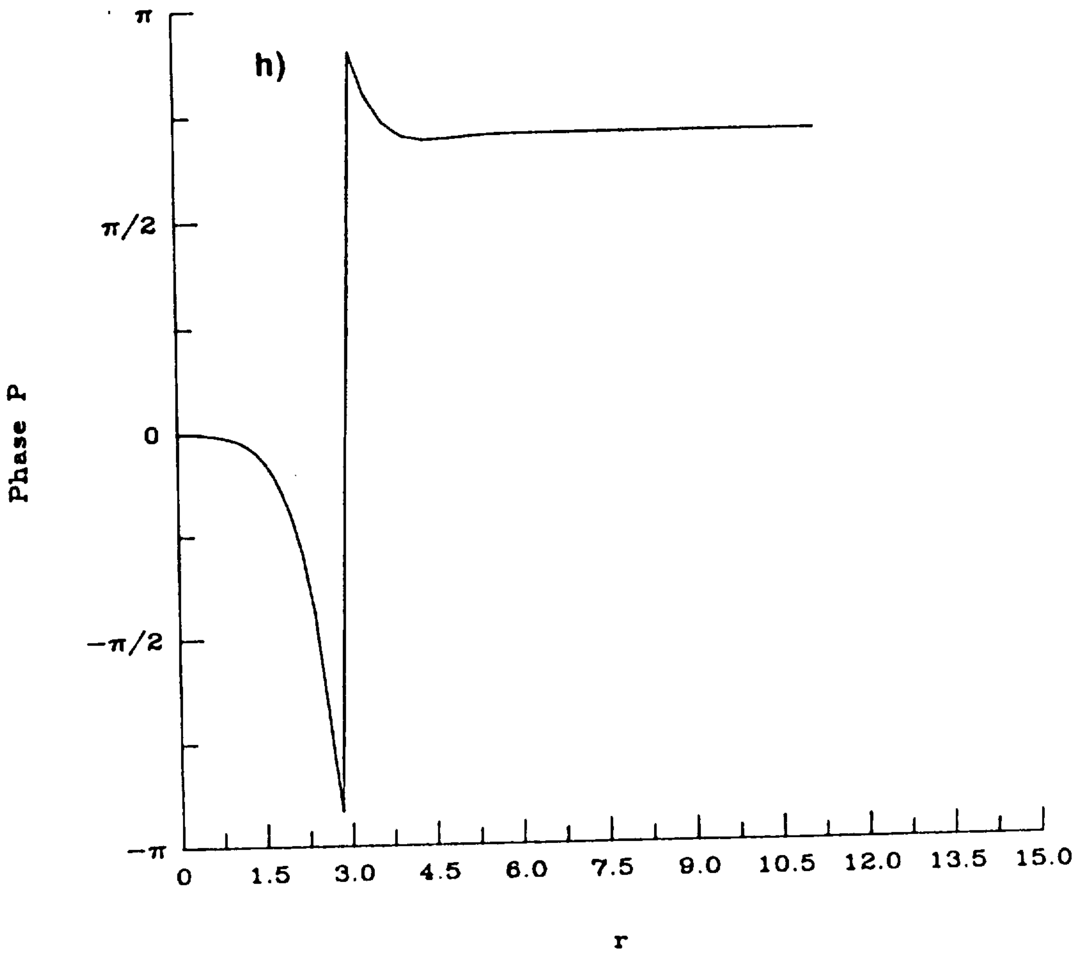

Fig. 4.21h) Concluded.

The variation of the growth rate, ω_i, with the axial wavenumber, α, for the asymmetric mode $n = 1$, is plotted in figure 4.22 with $\tilde{q} = 0.4$ and Re = 10,000. Of the two modes shown, the second mode is stable. The first mode has a growth rate comparable to the axisymmetric wave but is unstable over a smaller range of α. However, like the $n = 0$ case, it is basically a long wave instability. The variation of maximum growth rate of mode 1 with α is shown in figure 4.23. The maximum occurs at $\alpha \simeq 0.34$. The variation of ω_r with α for the first mode is presented in figure 4.24. The nearly linear variation indicates that the axial phase speed of the wave is slightly greater than unity and, like the axisymmetric case, is traveling with the uniform outer mean flow, although it is a bit closer to the core of the vortex. This form of instability has been observed experimentally both in wind tunnel measurements and contrail photos. The measurements of Singh and Uberoi [61] and Strange and Harvey [62] support the existence of an asymmetric disturbance which has an axial wavelength on the order of the core radius. Furthermore, the photograph of condensation trails behind a wide-bodied jet shown in [62] (their Fig. 1) clearly displays the existence of helical disturbances which co-exist along with the Crow instability. The viscous nature of the $n = 1$ mode is shown in figures 4.25 and 4.26. The variation of growth rate ω_i with axial wavenumber, α, shows similar behavior to that of the $n = 0$ disturbance. However, in this case, the instability occurs at much lower Reynolds numbers. Also the maximum growth rate which occurs at Re $\simeq$ 60 is an order of magnitude greater than the ω_{imax} for the $n = 0$ case. But the most interesting phenomenon is the behavior of these two instabilities at high Reynolds numbers. While the asymmetric mode is the stronger of the two instabilities at low Reynolds numbers, as Re increases above 10^4, the axisymmetric disturbance becomes the mode with the higher growth rate. This

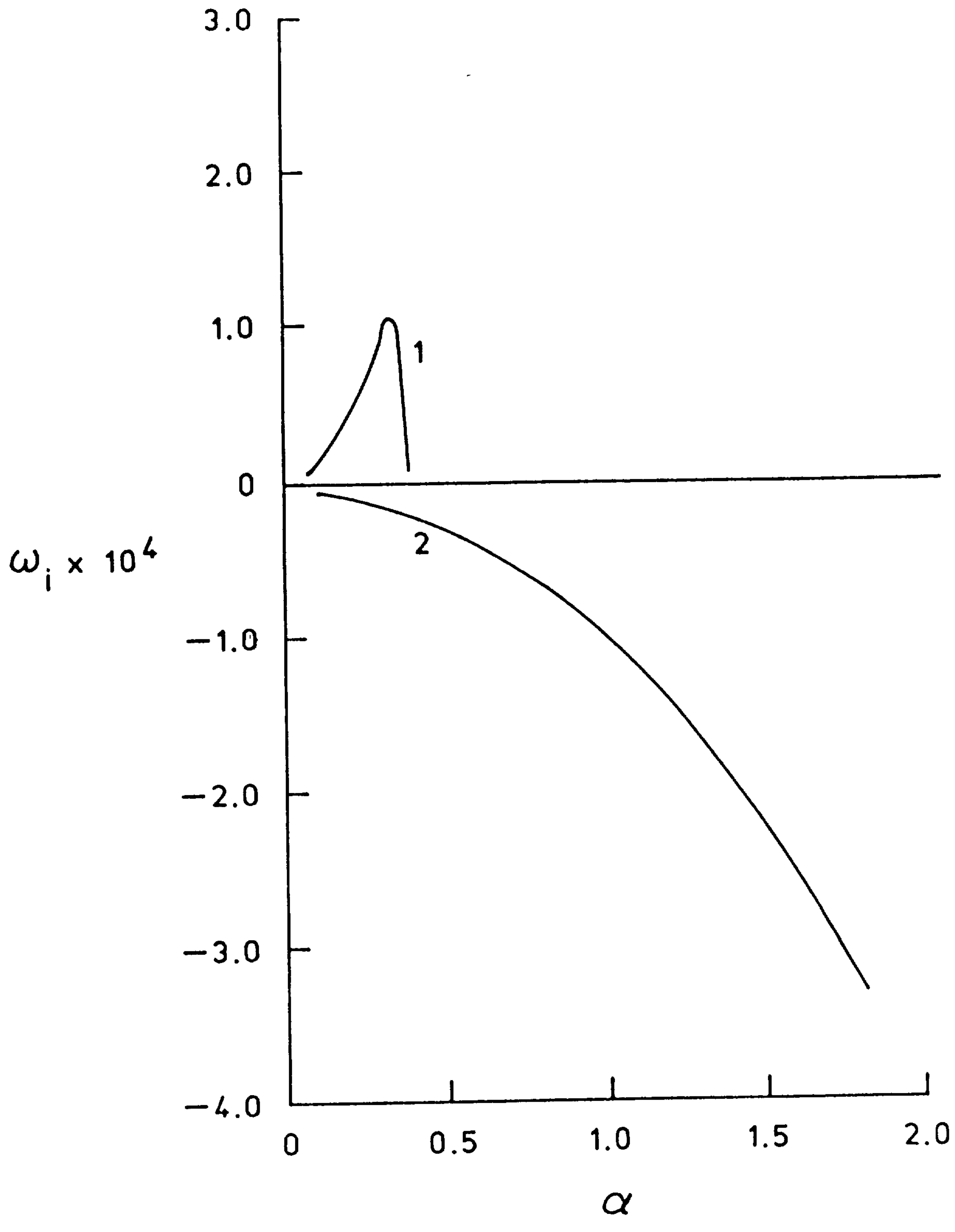

Fig. 4.22 Variation of the growth rate of asymmetric (n = +1) disturbances with wavenumber for a trailing line vortex. Here, $\tilde{q} = 0.4$, Re = 10^4.

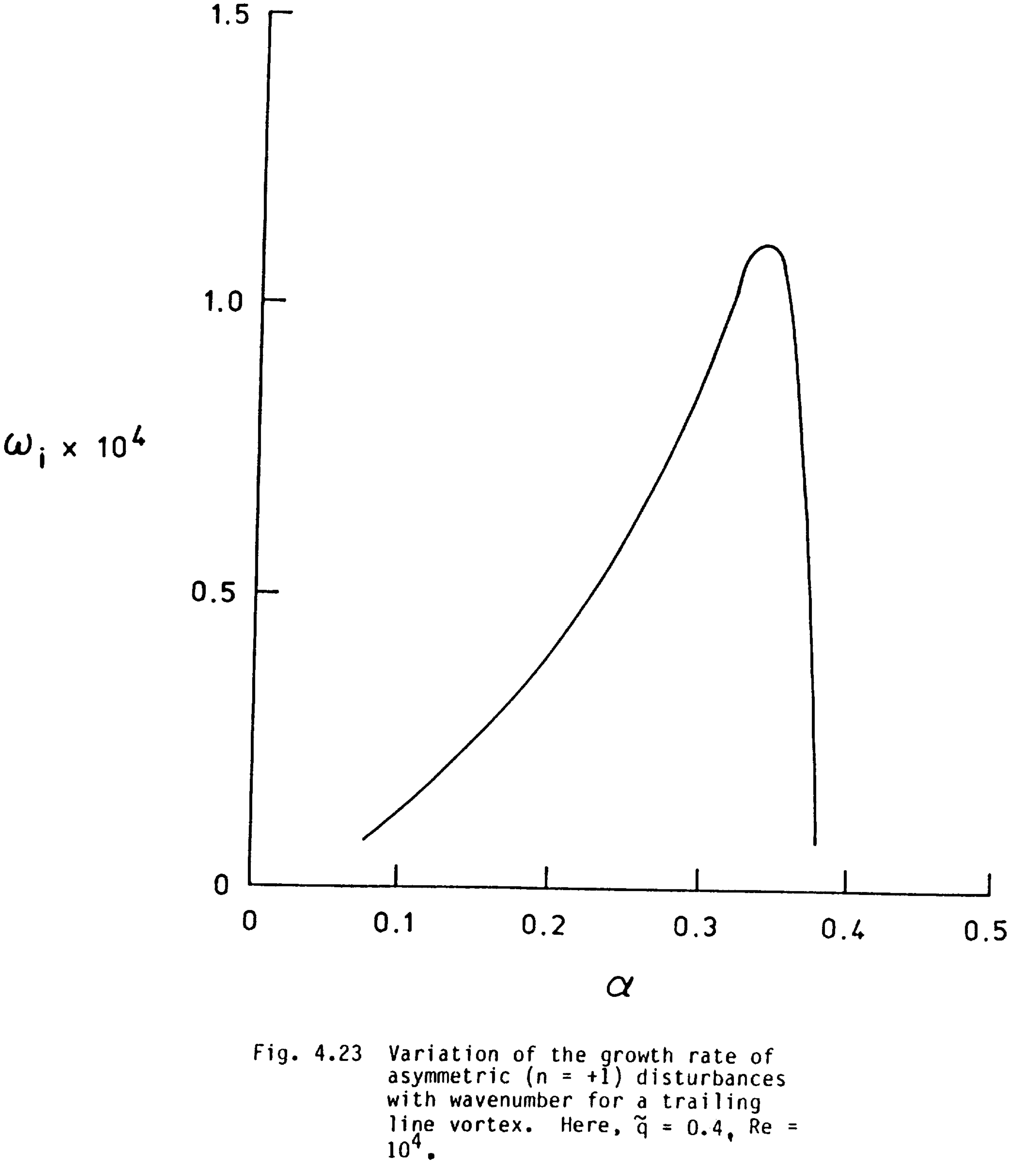

Fig. 4.23 Variation of the growth rate of asymmetric ($n = +1$) disturbances with wavenumber for a trailing line vortex. Here, $\tilde{q} = 0.4$, $Re = 10^4$.

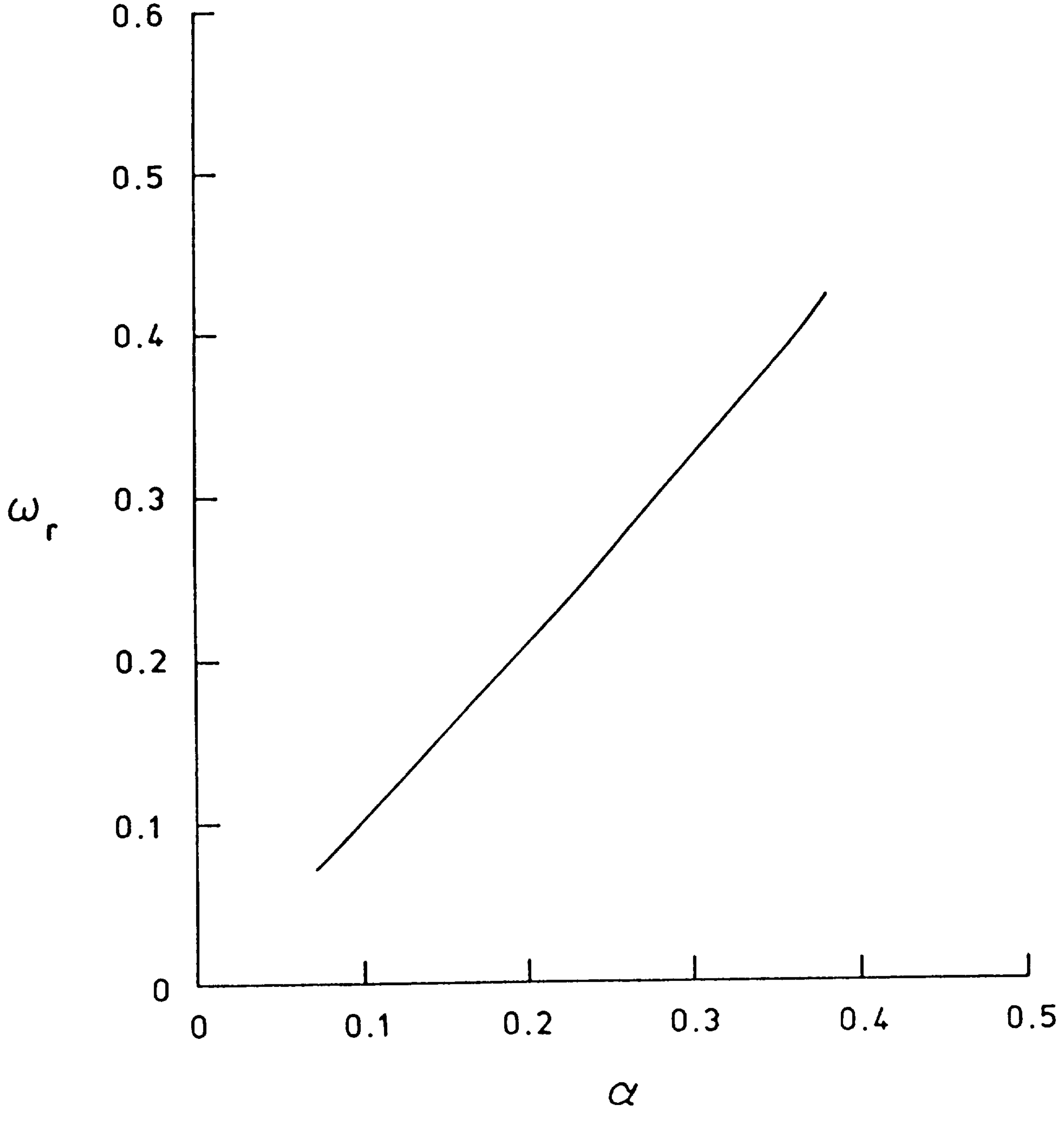

Fig. 4.24 Variation of the real part of frequency of asymmetric (n = +1) disturbances with wavenumber for a trailing line vortex.
Here, $\tilde{q}$ = 0.4, Re = 10^4.

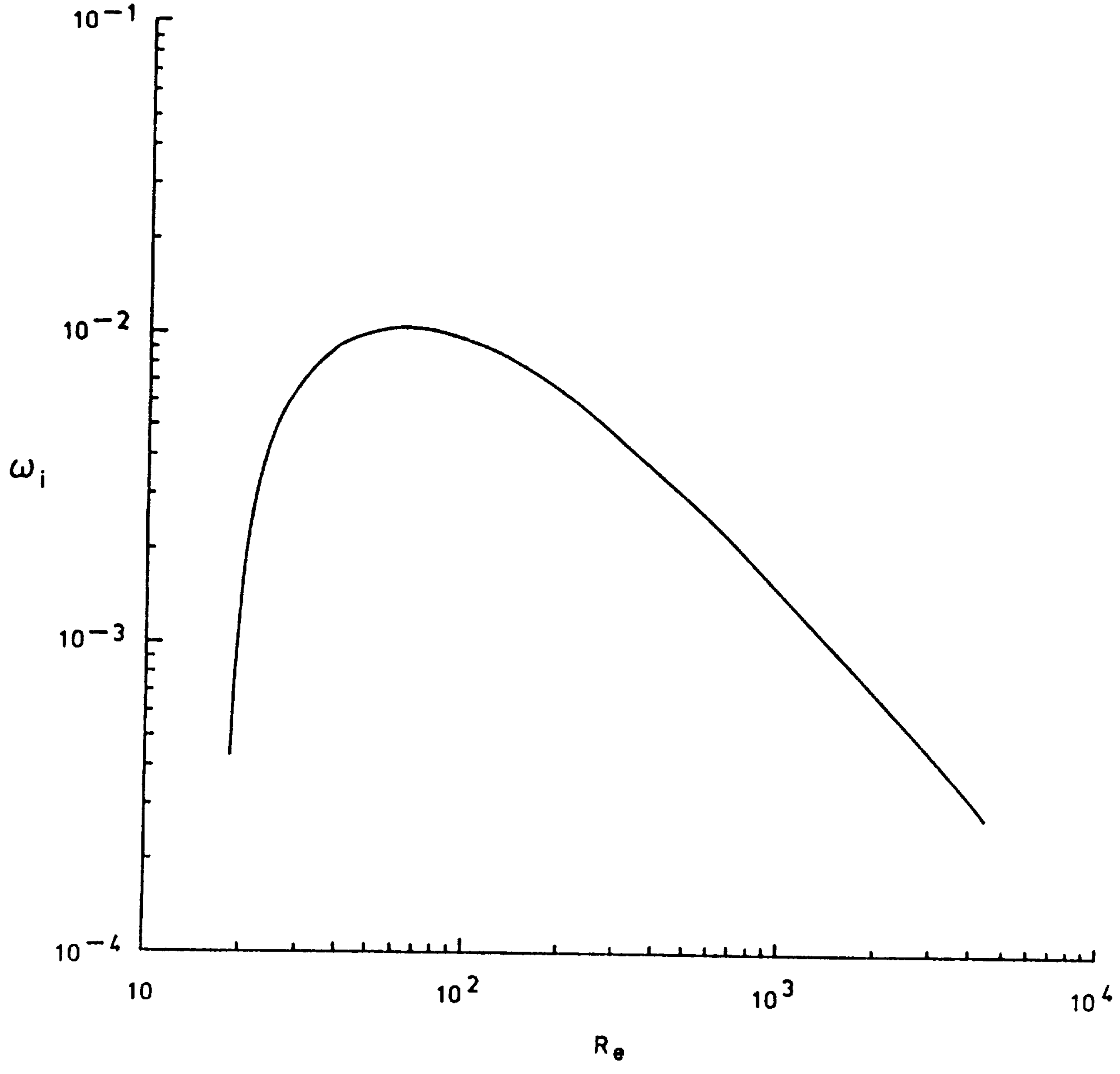

Fig. 4.25 Influence of Reynolds number on the growth rate of asymmetric (n = +1) disturbances for a trailing line vortex. Here, $\alpha = 0.34$, $\tilde{q} = 0.4$.

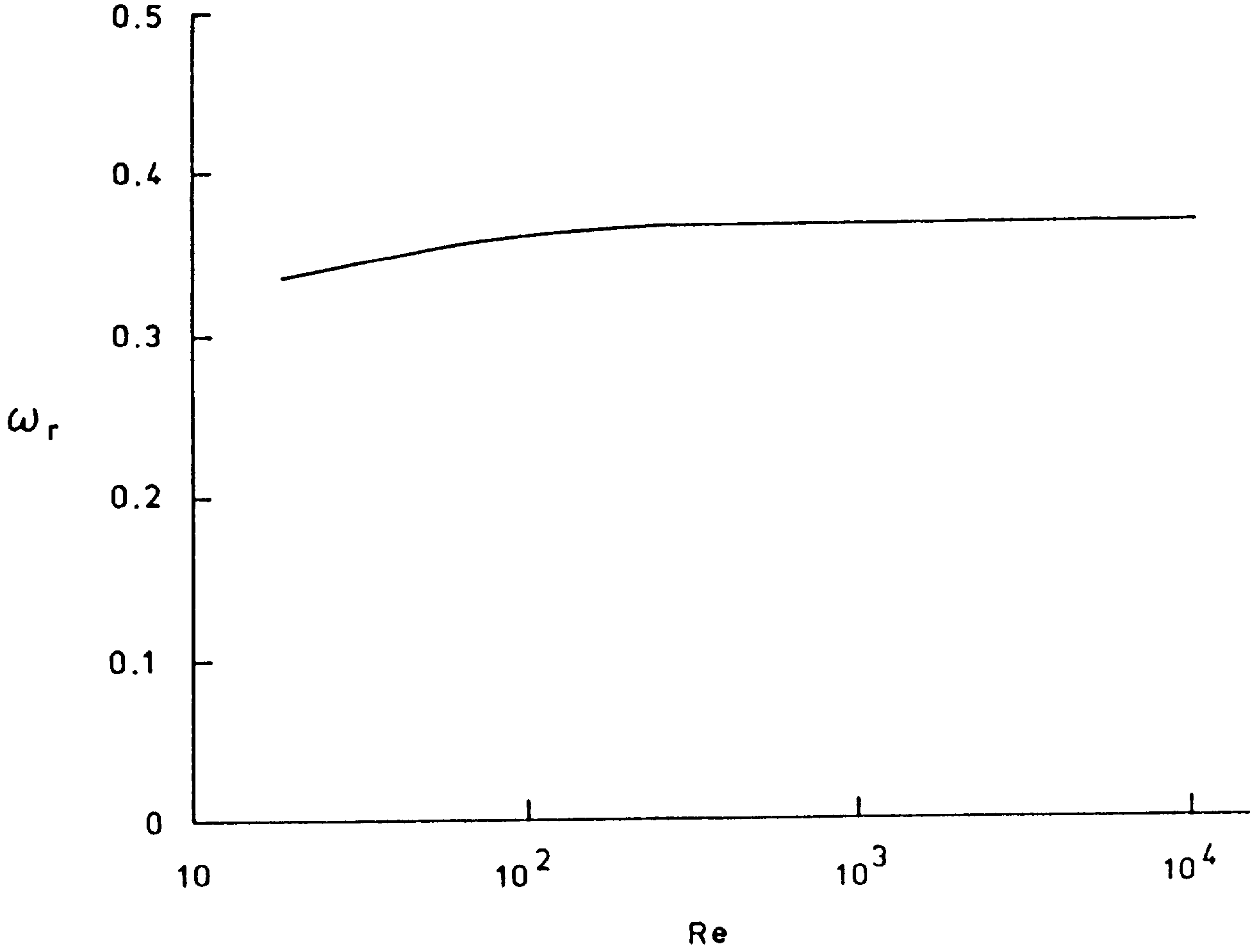

Fig. 4.26 Influence of Reynolds number on the real part of frequency of asymmetric (n = +1) disturbances for a trailing line vortex. Here, $\alpha = 0.34$, $\tilde{q} = 0.4$.

may be why, in most of the contrails behind large commercial jets (which occur at high Reynolds numbers), the axisymmetric mode is the dominant and persistent form, while in wind tunnel tests, which are conducted at much lower Reynolds numbers, both modes are present equally. The amplitudes and the phases of the disturbance eigenfunctions are presented in figures 4.27a-4.27h. Remember that disturbances having $|n| = 1$ are the only ones with non-zero radial and azimuthal velocity on the centerline. This fact is clearly demonstrated in figures 4.27a and 4.27c. Although the peaks occur on the centerline, a considerable amount of the perturbation's energy is just outside of the core. This feature was explained earlier when discussing the axial phase speed of the wave. Figure 4.27e shows the variation of the perturbation amplitude in the axial direction with radial distance. The peak is positioned just inside of the core with a significant part of the perturbation immediately adjacent to the outer part of the core. The overall observation of the eigenfunctions indicates that this instability is much tighter in radial extent than that of the $n = 0$, disturbance. A significant point to be made here is the fact that, unlike inviscid modes, no higher unstable modes were found for either the axisymmetric or asymmetric form of instability. This was tested extensively by going to successively higher values of N (number of Chebyshev polynomials) than the number needed to obtain convergence. This point has to be explored further.

Much work needs to be done with regard to documenting these two new viscous modes of instability. Of particular importance is the variation of the perturbation quantities with respect to the swirl parameter $\tilde{q}$. However, neither space nor time allows for such an extensive study here (Recall that this was only to be a test case for calibrating the numerics.). A more detailed study should follow in the near future and will be reported elsewhere.

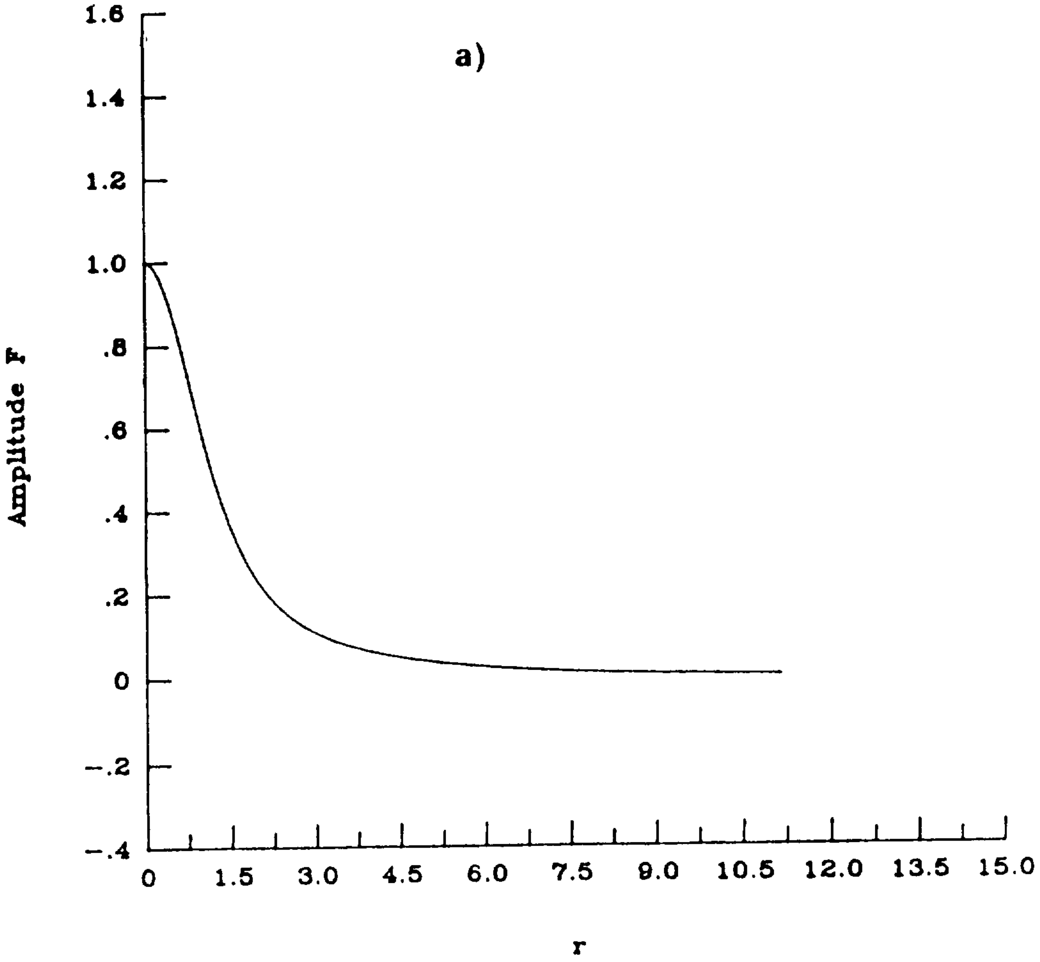

Fig. 4.27 Spatial distribution of amplitude and phase of various eigenfunction components of an asymmetric ($n = +1$) perturbation for a trailing line vortex. a) and b) radial velocity, c) and d) azimuthal velocity, e) and f) axial velocity, g) and h) pressure. Here, $\alpha = 0.34$, $\tilde{q} = 0.4$, and Re = 50.

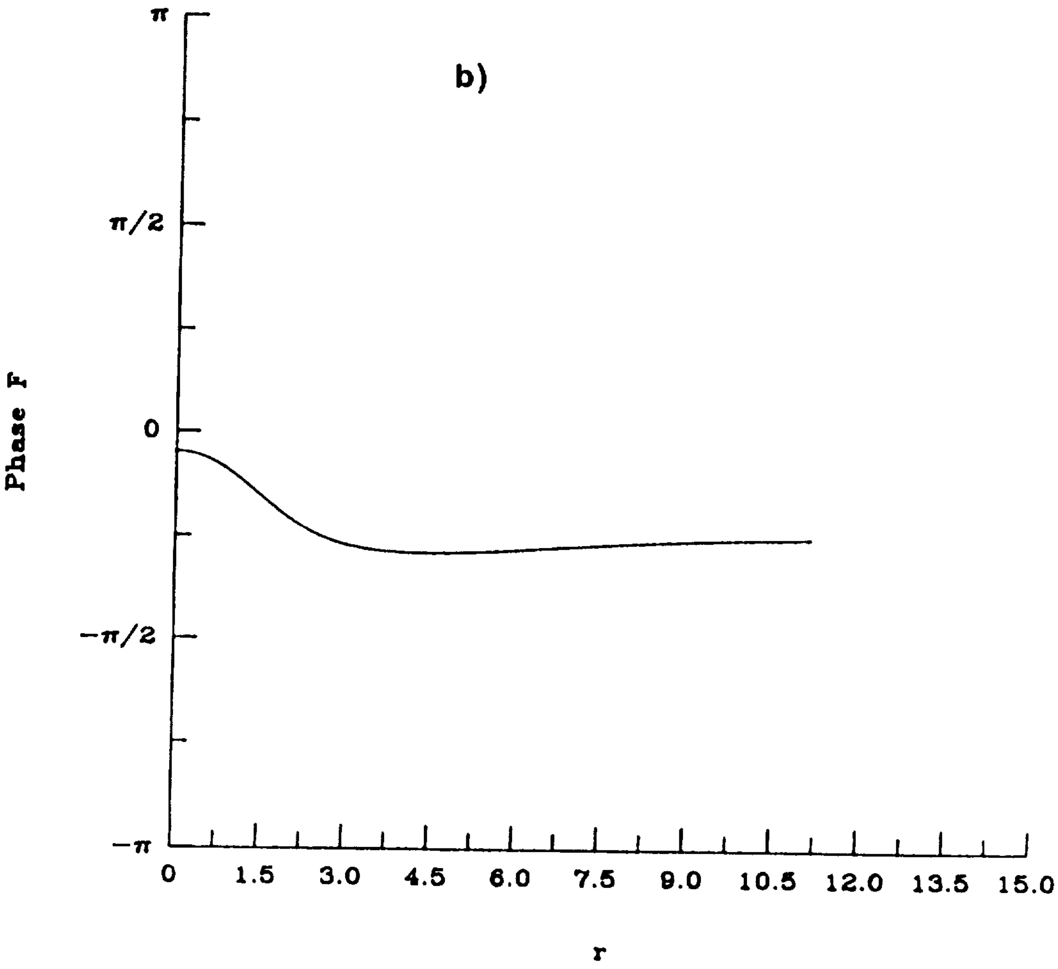

Fig. 4.27b) Continued.

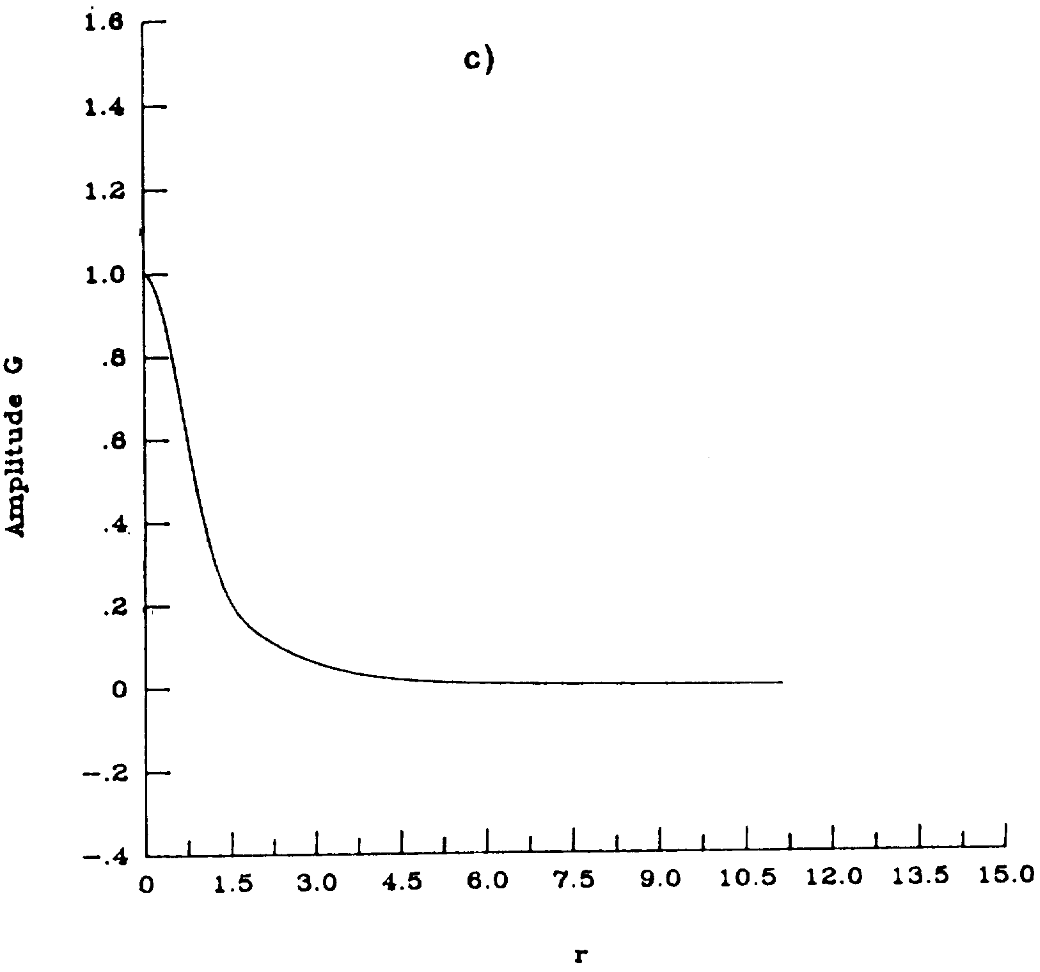

Fig. 4.27c) Continued.

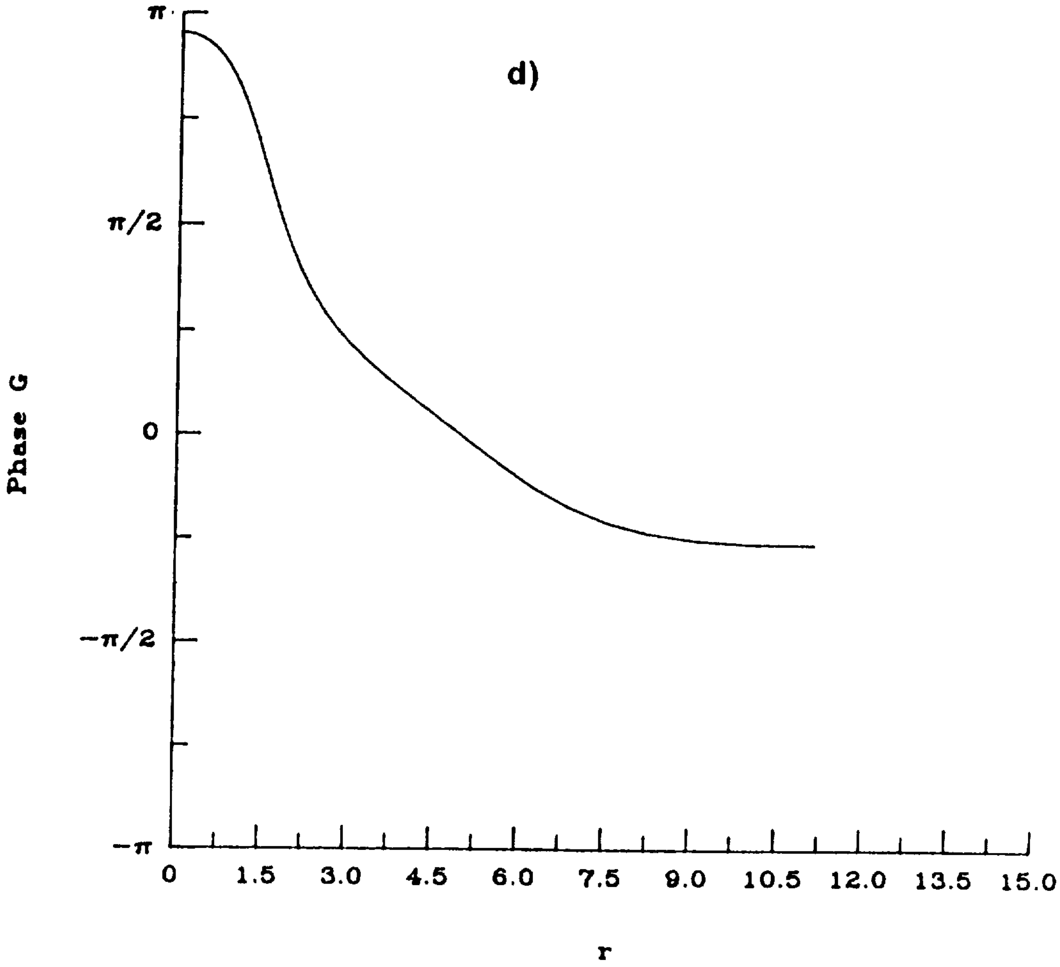

Fig. 4.27d) Continued.

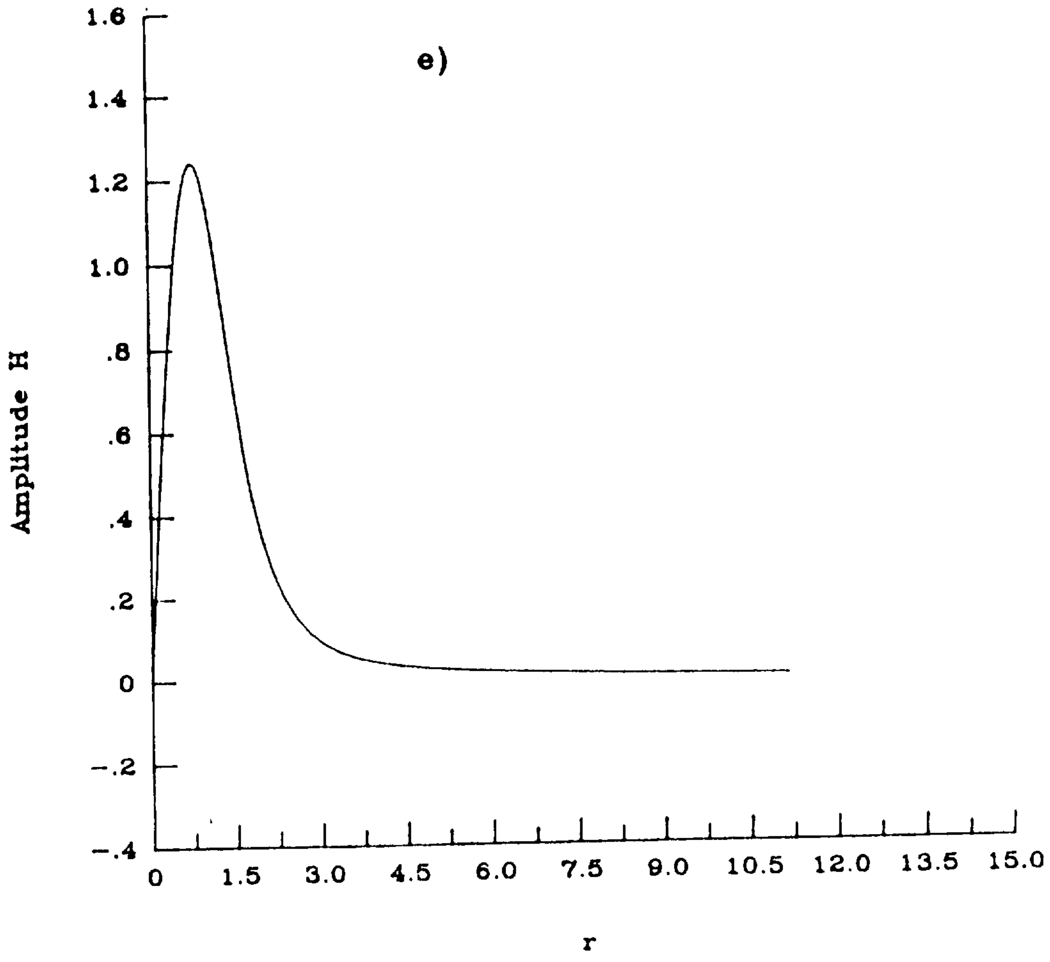

Fig. 4.27e) Continued.

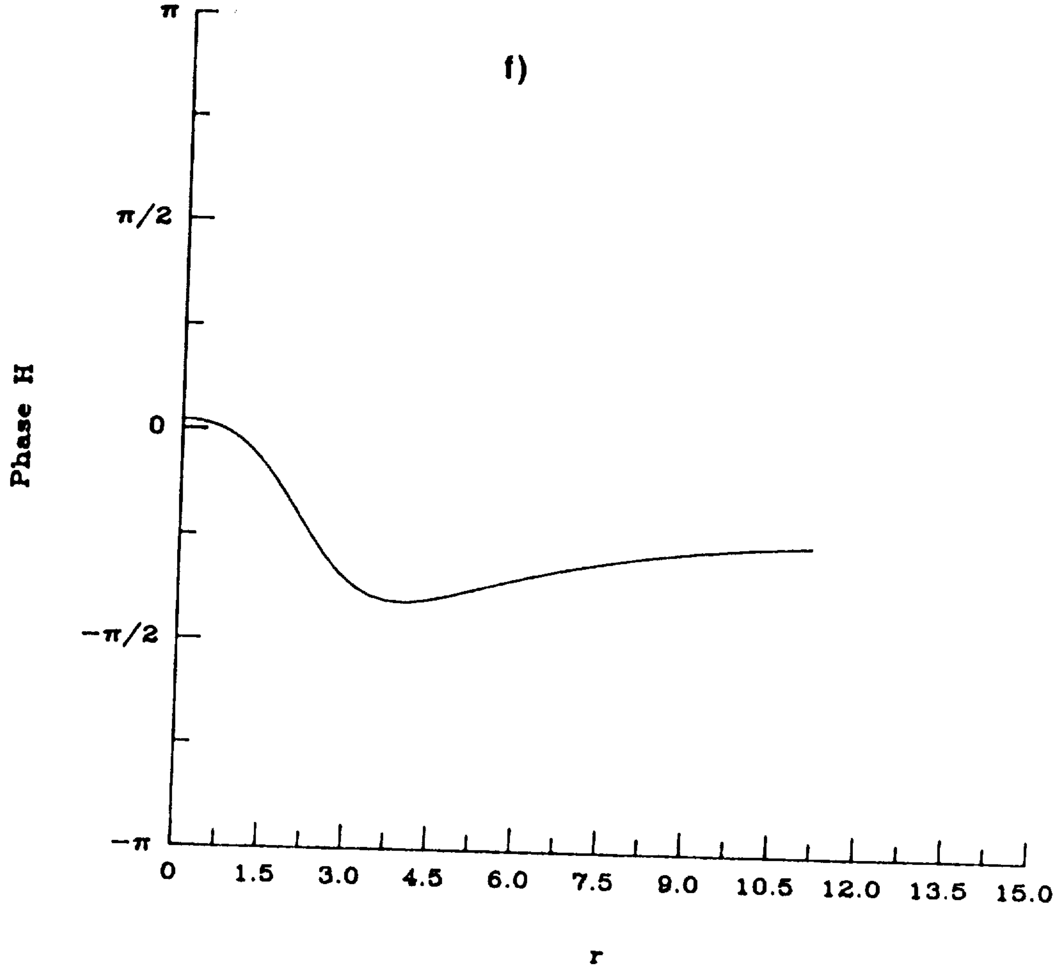

Fig. 4.27f) Continued.

C-2

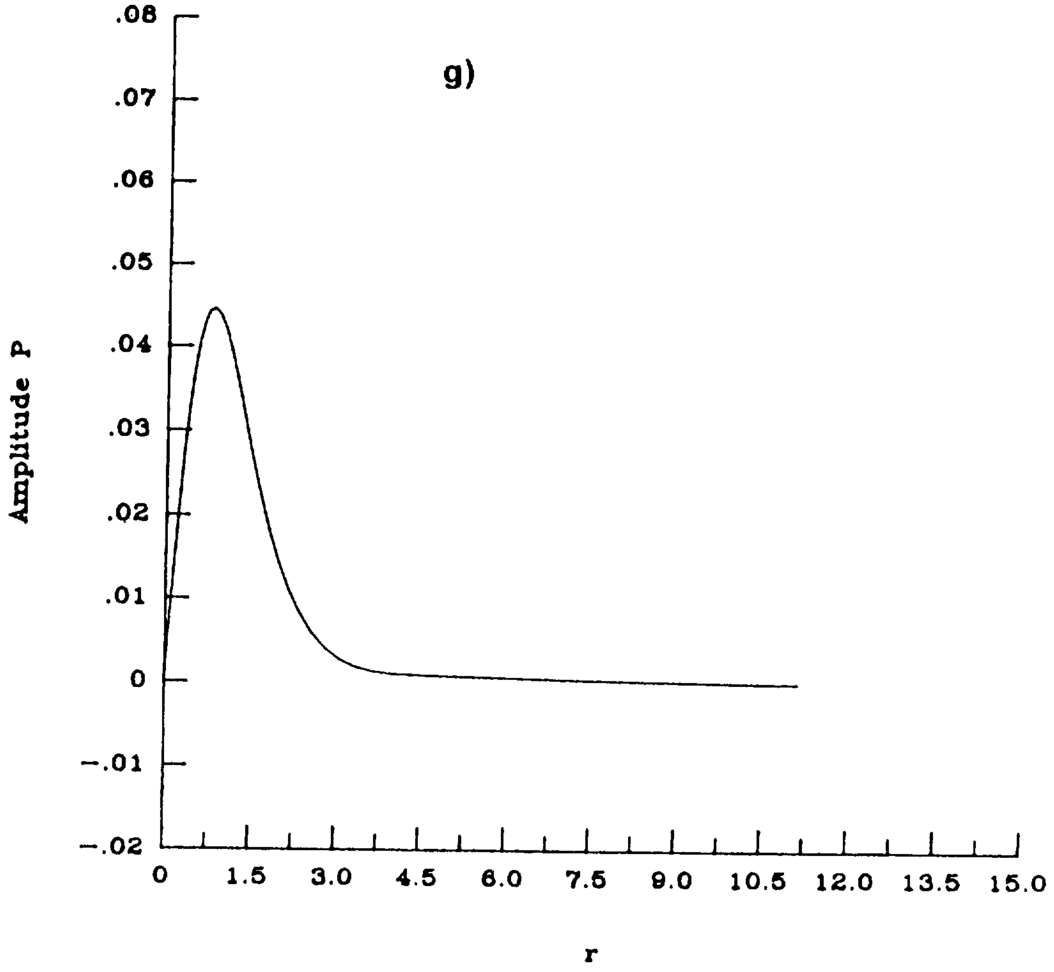

Fig. 4.27g) Continued.

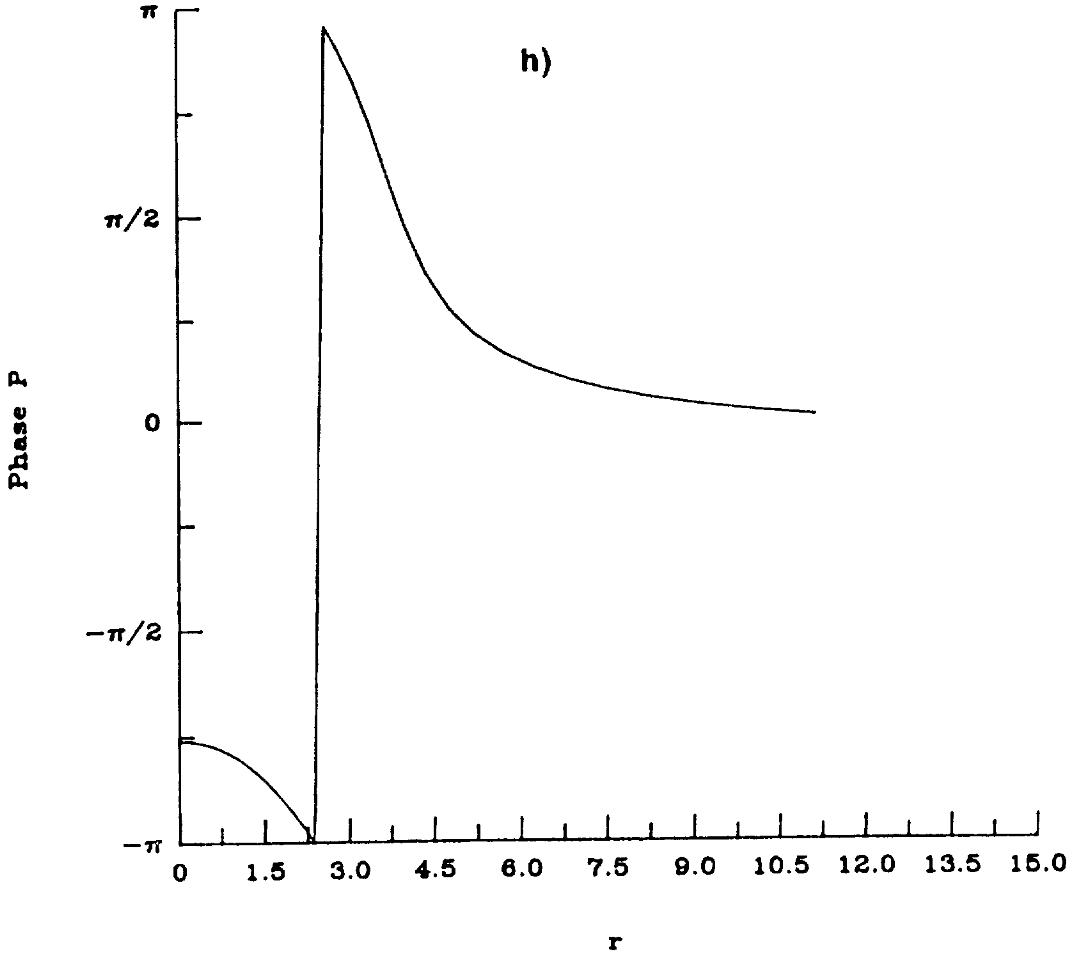

Fig. 4.27h) Concluded.

Finally, before concluding this chapter, two important facts related to the discovery of the new viscous modes are:

1. Batchelor's vortex represents a good approximation to trailing line vortices and can be employed for further stability studies.

2. Although the stability calculations were conducted for a laminar vortex, the excellent agreement obtained with experimental measurements and contrail photos, which involve mostly turbulent vortices, indicate that these long wave viscous instability modes, once activated, do not interact significantly with the surrounding turbulent field and are not influenced strongly by the magnitude of the scaling parameters.

Chapter 5

RESULTS AND DISCUSSION

In this chapter, the results obtained using the three-dimensional profiles of Donaldson and Sullivan [33] are presented. Due to the wealth and variety of solutions possible from their compilation as well as constraints on computer resources and time, representative velocity profiles had to be chosen. In each case, care was taken to insure that the selected profiles approximated trailing line vortices as closely as possible. In section one, the stability of a single cell vortex is studied. The second section contains the results for a comprehensive study of a two cell vortex. The third section is devoted to the case of a three cell vortex which is studied less extensively than that of a two cell vortex. Except in the case of the three cell vortex where the effect of high values of azimuthal wavenumber, n, on the stability characteristics were obtained, the calculations are limited to n = 0, ±1, and ±2.

Before proceeding further, two points need to be emphasized. First, unless specified otherwise, the axial gradient term, ϕ, as defined in Eq. (2.5), is included in the governing equations even though all of the calculations are conducted at high Reynolds numbers. It will be shown that although the effect of this term on the modes with negative n is negligible, it causes drastic changes in the case of positive azimuthal wavenumbers. Secondly, rather than using $\tilde{q}$ (as defined in Eq. (4.2)) the alternate parameter, q, which is defined as the ratio of the maximum swirl velocity to the centerline axial velocity, has been used to delineate the stability characteristics.

As mentioned in the introduction, in the case of swirling pipe flows, the existence of center- as well as wall-modes of instability has been established by previous research efforts. In addition, previous investigations have identified ring modes as those which occur at some intermediate radius. This investigation has shown that compound instability modes which will be called <u>co-instabilities</u> occur for many types of swirling flows. The results of the present work show, for the first time, cases where center instability modes coexist with wall modes and/or with ring modes, as well as other combinations. These different types of compound instability modes will be described as they occur. It is obvious here that mode identification has become a confusing and complex matter. Originally, the word "mode" was used to separate disturbances having different azimuthal wavenumbers. The discovery of higher modes associated with each negative value of n and now the presence of center-, ring- and wall-modes of instability has created an untenable situation. Thus, to simplify the text (and stop repeating "mode"), from here on center modes will be indicated by $\hat{C}$, ring modes by $\hat{R}$ and wall modes by $\hat{W}$. Therefore a combination of a center mode and a ring mode is identified as $\hat{C}\,\hat{R}$ with similar identification applying to any other combinations. The word mode will be used only in its original context, that is to represent a specific value of the azimuthal wavenumber and the higher modes associated with that particular value.

5.1 Stability of a Single Cell Vortex at Re = 4000

The three components of the velocity profile associated with this vortex are shown in figure 5.1. The radial variation of the azimuthal velocity V, presented in figure 5.1b, is identical to that of an unconfined trailing line vortex. The variation of the growth rate with axial wavenumber for an axisymmetric disturbance (n = 0) is shown in figure 5.2 for q = 0.19 and 1.0. No sign of instability was observed. Furthermore, as α increases the flow becomes more stable. The variation of ω_r with α is presented in figure 5.3. It seems that for q = 1.0, the axisymmetric mode is almost stationary. This is in accordance with the criterion (Eq. (1.6)) obtained by Ito et al. [21]. The effect of Reynolds number on the axisymmetric mode at q = 1.0 is presented in figures 5.4 and 5.5 for $\alpha = 1.0$ and 0.3, respectively. Although the flow becomes less stable as Re increases, an unstable state is never reached.

The variation of the growth rate with α for the asymmetric mode (n = 1) is shown in figure 5.6 for q = 0.8 and 0.4. The flow is clearly stable and becomes more stable as α increases. The real part of frequency versus axial wavenumber is plotted in figure 5.7. The calculations for the case n = 2 produced similar results, showing mainly that this profile is highly stable with respect to the modes having $n > 0$; at least for the range of parameters studied here. The above conclusion has been reached in the case of inviscid disturbances for Long's vortex by Foster and Duck [23].

Figure 5.8 shows the variation of the growth rate, ω_i, with α associated with the asymmetric mode n = -1, for q = 0.4. Similar to the case of a trailing line vortex, the instability is a very explosive one with higher modes present. Here, only the two most unstable modes are plotted for

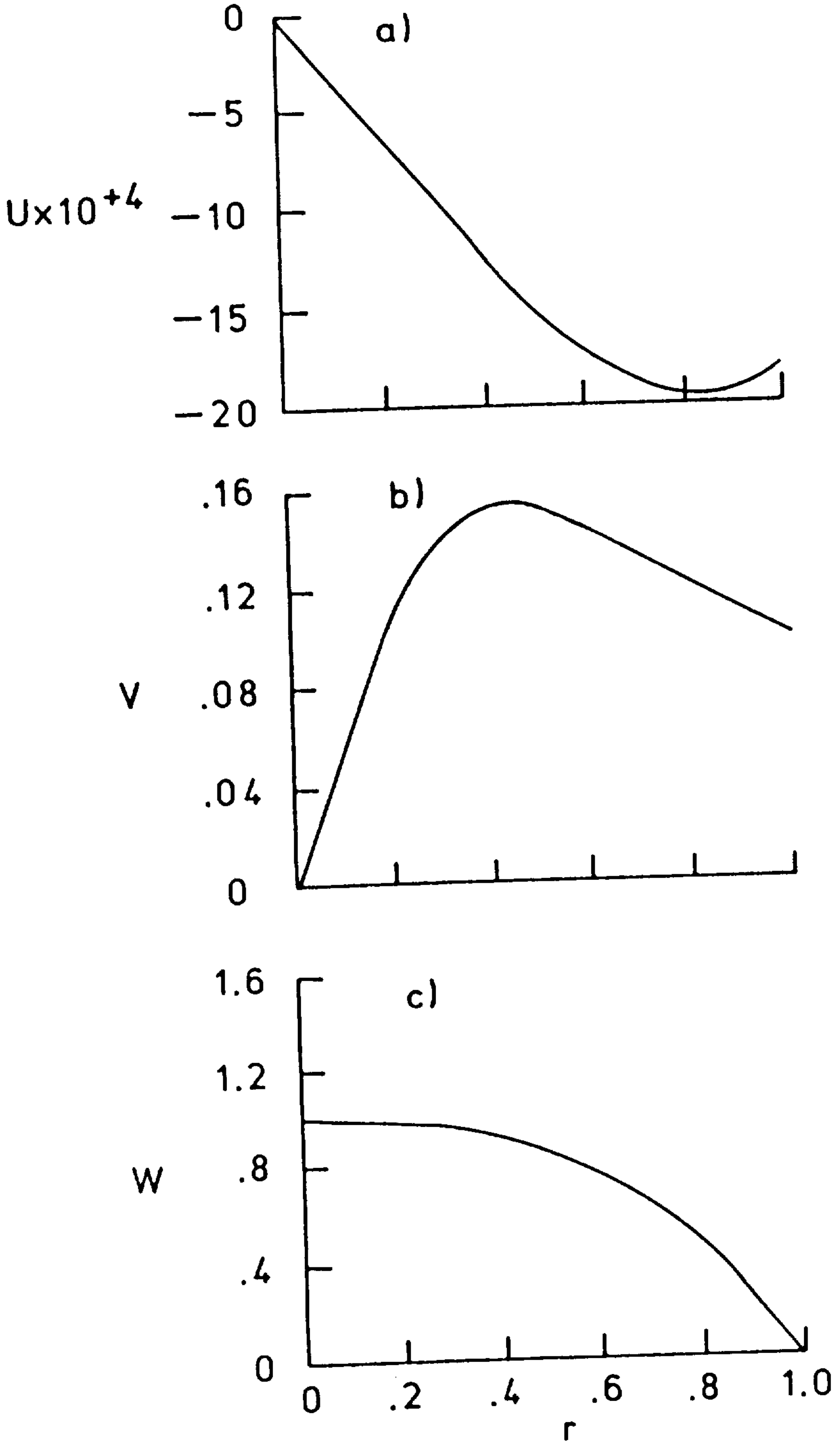

Fig. 5.1 Velocity components for a single cell vortex in a rotating, porous pipe.

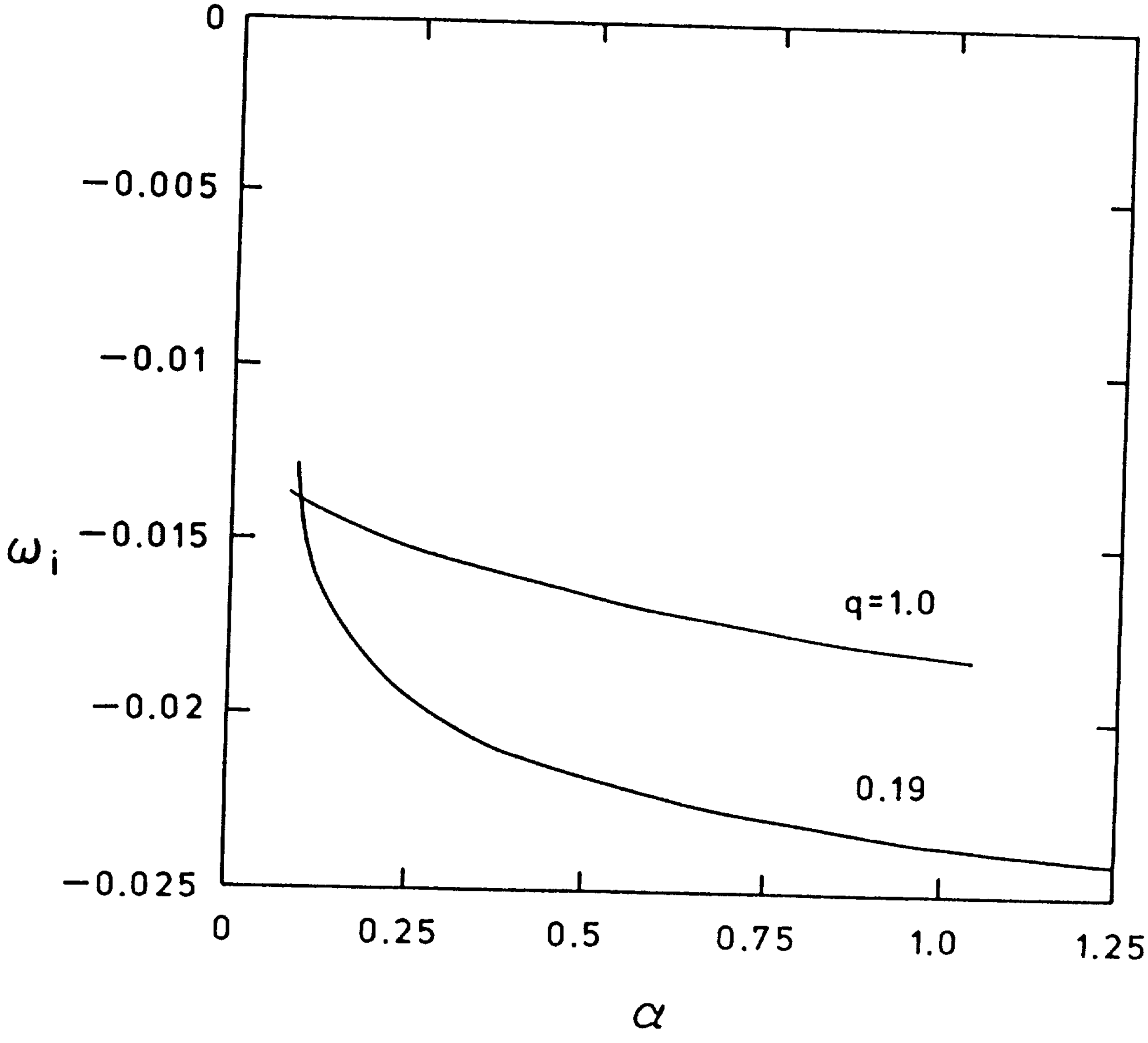

Fig. 5.2 Variation of the growth rate of axisymmetric (n = 0) disturbances with wavenumber for a single cell vortex. Here, Re = 4000, $\psi \neq 0$.

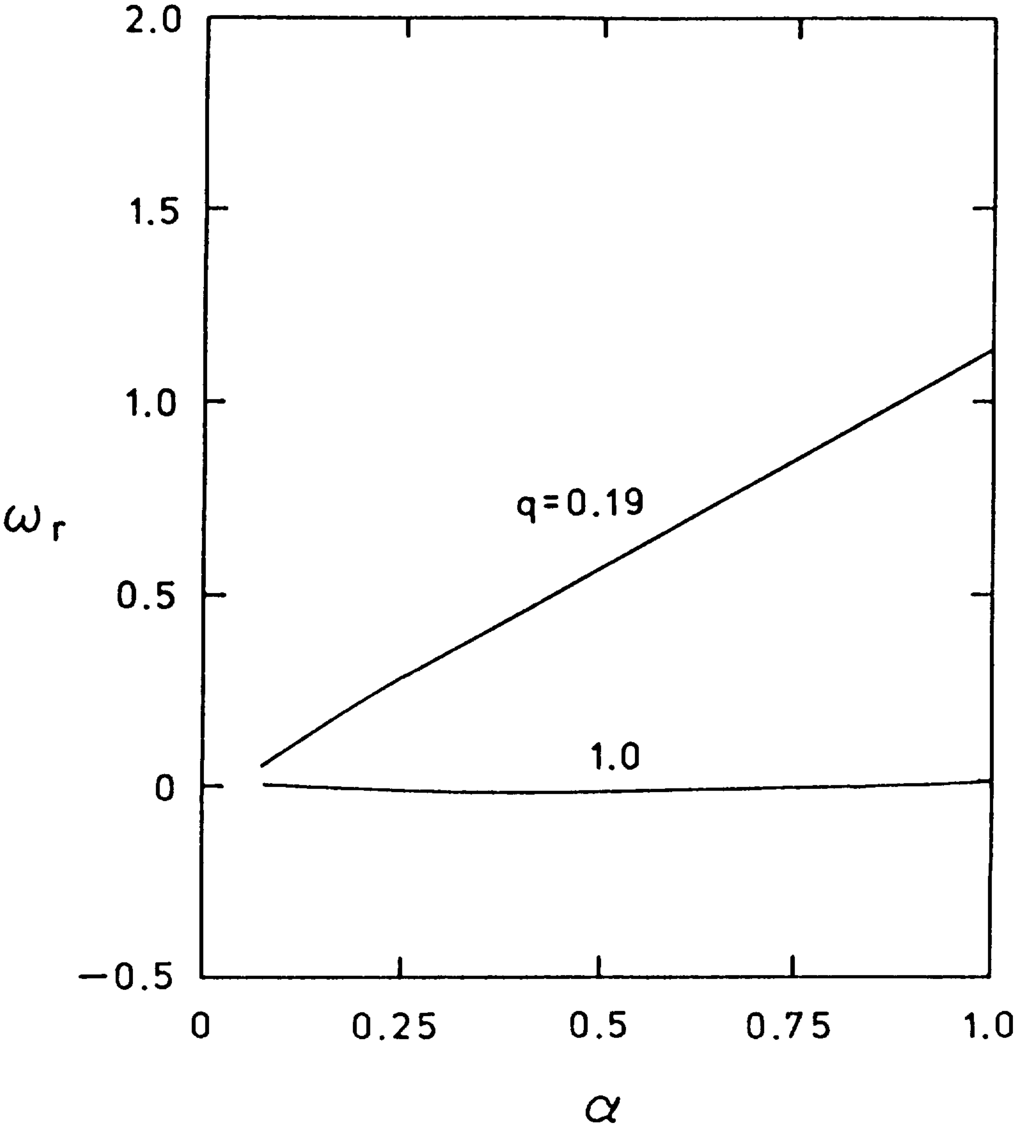

Fig. 5.3 Variation of the real part of frequency of axisymmetric ($n = 0$) disturbances with wavenumber for a single cell vortex. Here, $Re = 4000$, $\psi \neq 0$.

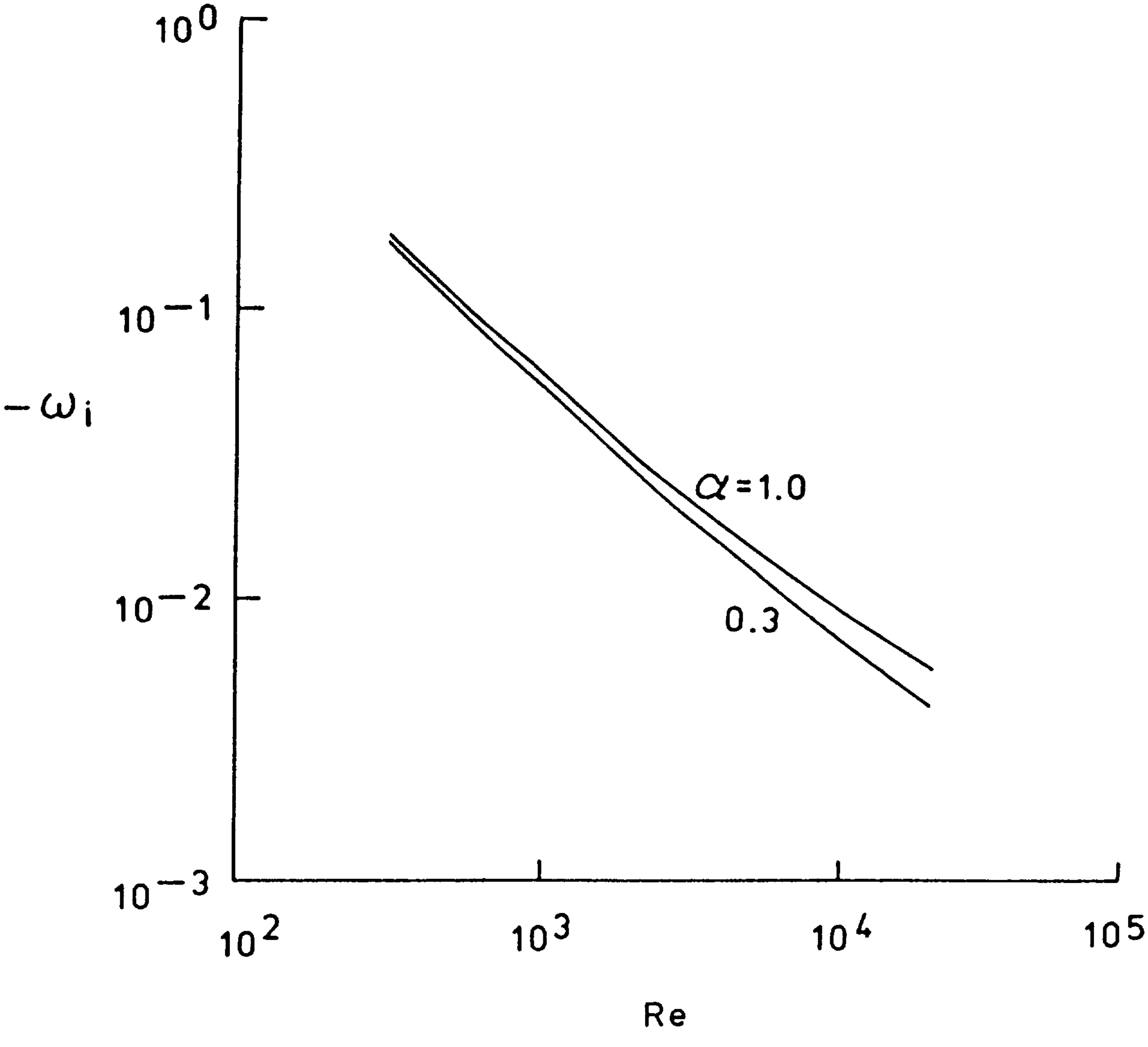

Fig. 5.4 Influence of Reynolds number on the growth rate of axisymmetric ($n = 0$) disturbances for a single cell vortex. Here, $q = 1.0$, $\psi \neq 0$.

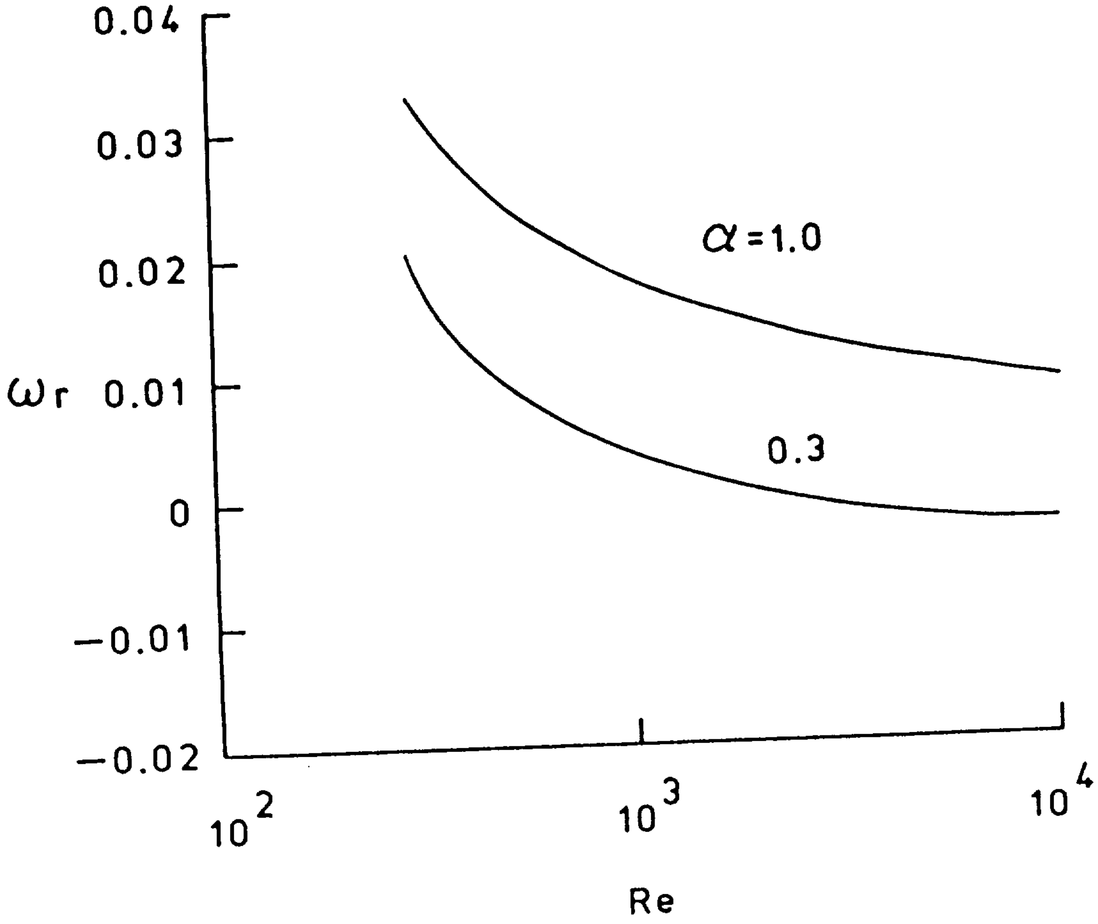

Fig. 5.5 Influence of Reynolds number on the real part of frequency of axisymmetric ($n = 0$) disturbances for a single cell vortex. Here, $q = 1.0$, $\psi \neq 0$.

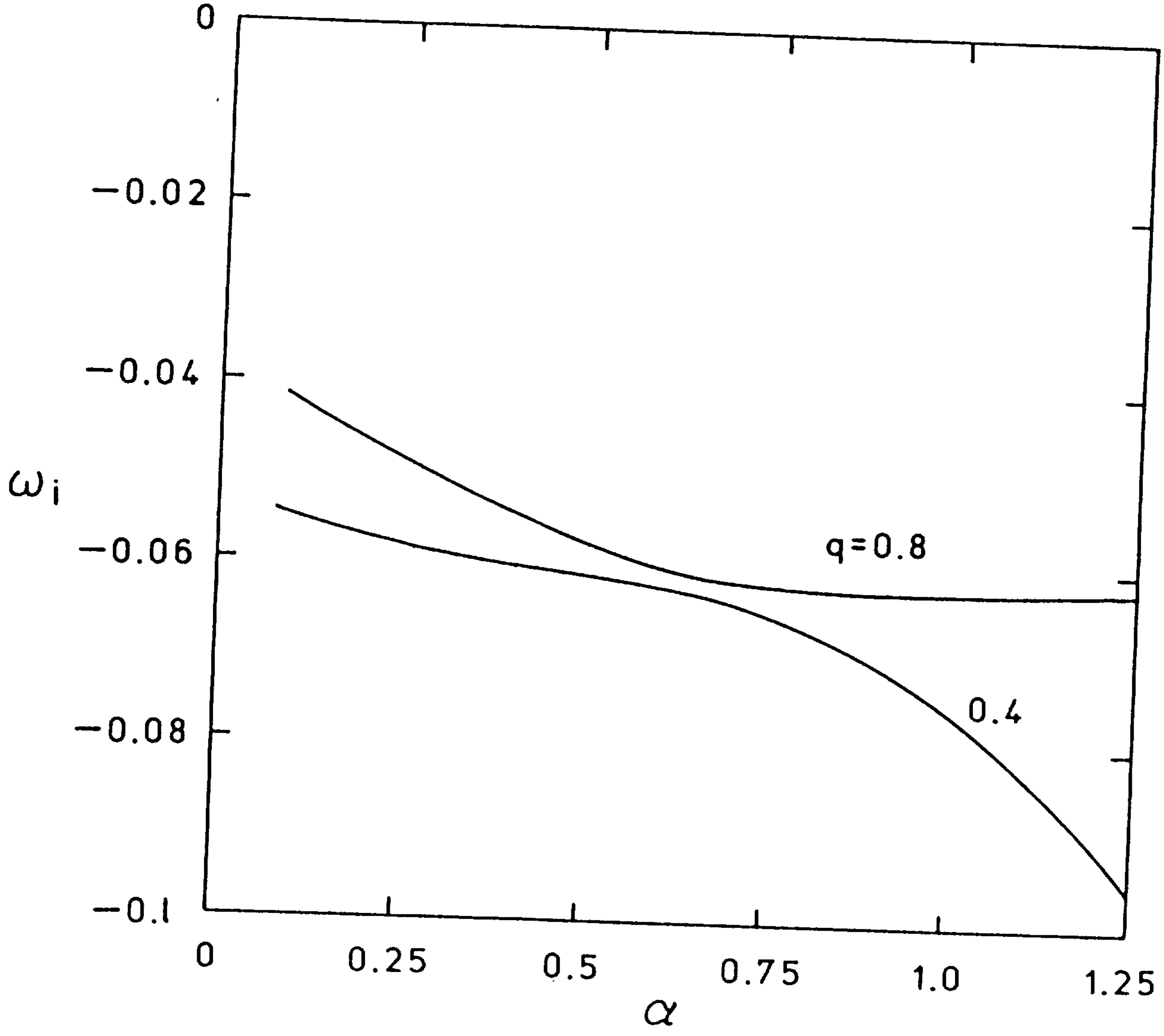

Fig. 5.6 Variation of the growth rate of asymmetric (n = +1) disturbances with wavenumber for a single cell vortex. Here, Re = 4000, $\psi \neq 0$.

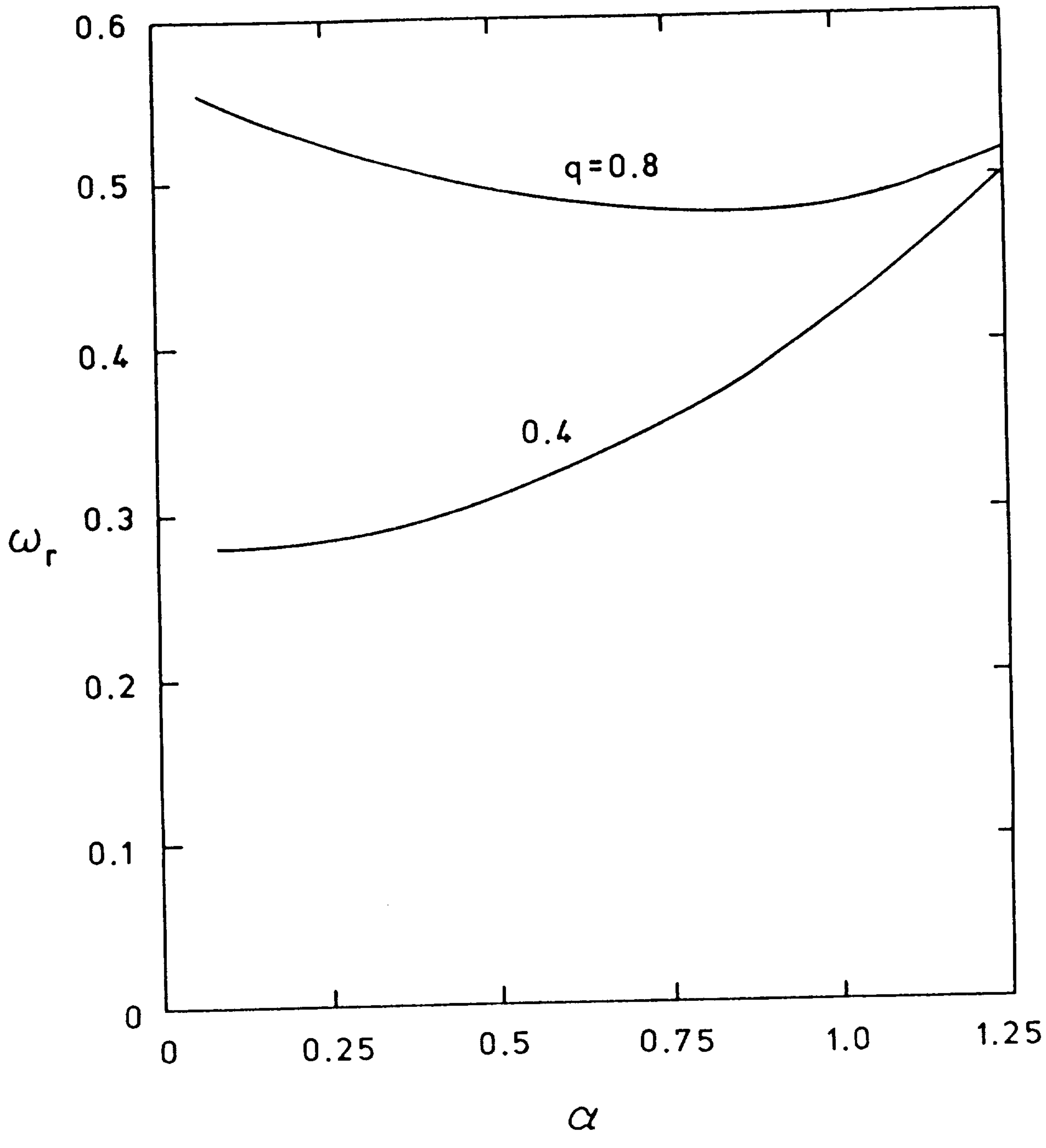

Fig. 5.7 Variation of the real part of frequency of asymmetric (n = +1) disturbances with wavenumber for a single cell vortex. Here, Re = 4000, $\psi \neq 0$.

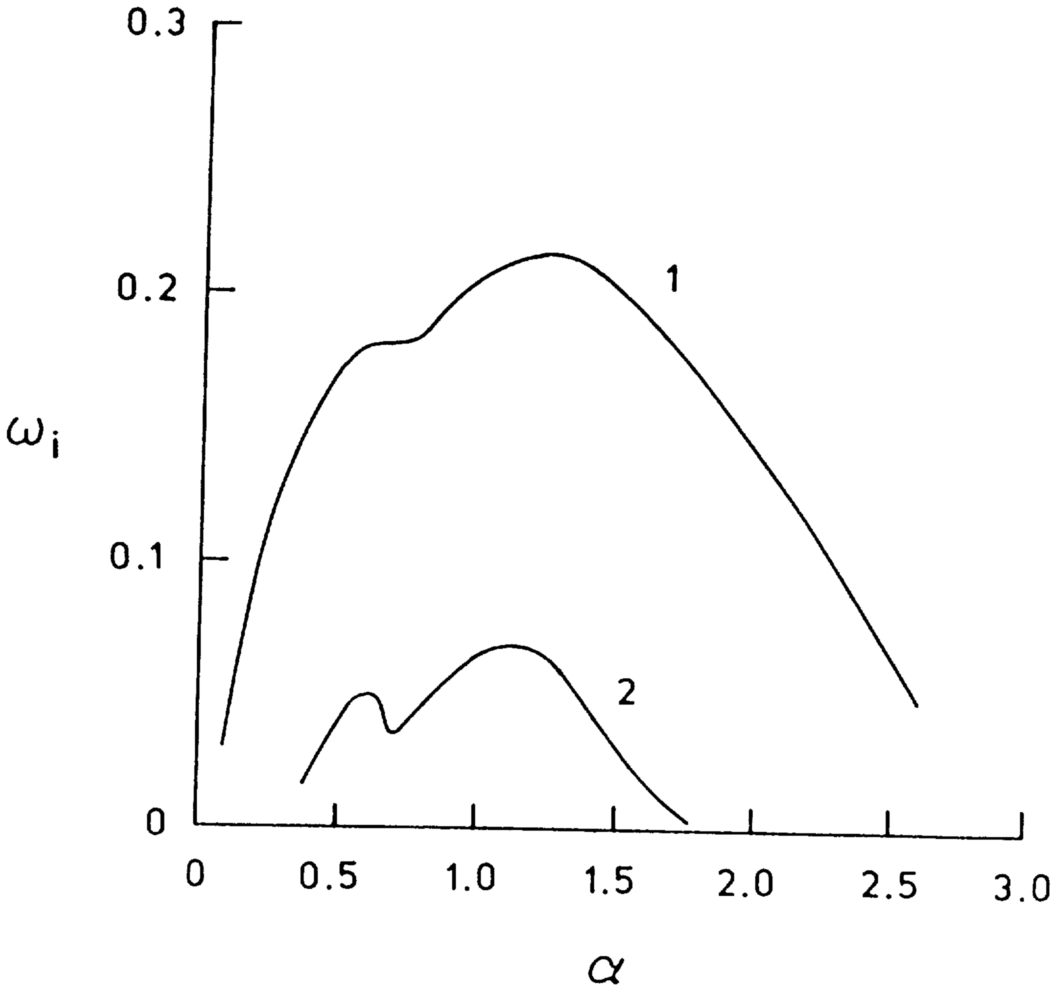

Fig. 5.8 Variation of the growth rate of asymmetric (n = -1) disturbances with wavenumber for a single cell vortex. Here, q = 0.4, Re = 4000 and $\phi \neq 0$

clarity. However, there are at least two major differences between this instability and the one associated with Batchelor's vortex. First, this instability exists at higher axial wavenumbers, α. Second, both stability modes show evidence of co-instabilities. That is, lobes are apparent on either side of $\alpha \simeq 0.7$. Varying α does not show co-instabilities directly, and in fact, co-instabilities could exist when growth rate curves show no evidence of unusual behavior. It is important to note that change near $\alpha =$ 0.7, suggests a shift in the dominant type of instability. Furthermore, it is noted that the stability curves in this figure are similar to the trailing line vortex curves shown in figure 4.4, for $0 < \alpha < 0.7$. The co-instabilities were checked by looking at the eigenfunctions of the disturbance at several values of α. That study of eigenfunctions revealed that this indeed was the case, which pointed to a disturbance having a very complex structure with several peaks in its amplitude.

The possibility of coexistence of several different modes was first mentioned in the work of Leibovich and Stewartson [26]. Subsequently, it was shown in the inviscid asymptotic analysis of Duck [32] that, for large negative n, there are two critical layers associated with the Batchelor's profile. He showed that the peaks in the disturbance eigenfunction are situated near these critical points (incidentally his eigenfunction curves show this multiple peak phenomena, but only for the higher modes, with no such effect for the primary mode). In the case of small negative n, Duck has stated that there is only one critical layer in the flow field. Depending upon the value of α, multiple peaks in the eigenfunctions for the single and multiple cell vortices do exist in the present calculations. We will discuss this later in the context of two cell vortices. There we will show that the peaks in the eigenfunctions could be used to distinguish the type or types of modes present (namely center, ring and wall modes).

We will also discuss this co-instability feature in detail for the more interesting case of a two cell vortex. Setting $\phi = 0$, the calculations were repeated and the results are plotted in figure 5.9. A comparison of figures 5.8 and 5.9 indicates that the effect of the axial gradient term, ϕ, is negligible. Actually, this turned out to be true (in the case of single cell as well as multiple cell vortices) whenever $n < 0$. The changes in ω_r with α, for the two modes shown in figure 5.8, are plotted in figure 5.10. Notice the kink in the higher mode curve which occurs roughtly at $\alpha \simeq 0.7$. The inviscid nature of the asymmetric mode, $n = -1$, is revealed in figure 5.11 for $q = 0.4$ and $\alpha = 1.0$. The behavior is very similar to the trailing line vortex case presented in figure 4.6. As the Reynolds number increases, the growth rates, ω_i, increase very rapidly and asymptote to constant values. In fact, in the case of the primary mode at Re = 4000, the inviscid value of the growth rate is almost achieved. The variation of the real part of frequency, ω_r, with Re is shown in figure 5.12. Variation in the real part of ω over a wide range of Reynolds numbers is small. The effect of higher swirl on the growth rate of the asymmetric mode ($n = -1$) is presented in figure 5.13. At $q = 0.8$, the lobe in the higher mode has disappeared while primary mode "splitting" has become more acute. There is a substantial increase in the growth rate of the first mode, particularly at higher values of axial wavenumber, α. The variation of the real part of the frequency with α for this disturbance is shown in figure 5.14 for $q = 0.8$. Notice the shift in the ω_r of the first mode (which results in the kink) even though the two distinct sections of the curve have similar slopes.

The behavior of the growth rate with α for disturbances having $n = -2$ is shown in figure 5.15 for $q = 0.8$. Here, the peaks associated with the lower values of the axial wavenumber are the dominant ones. Overall the growth rate

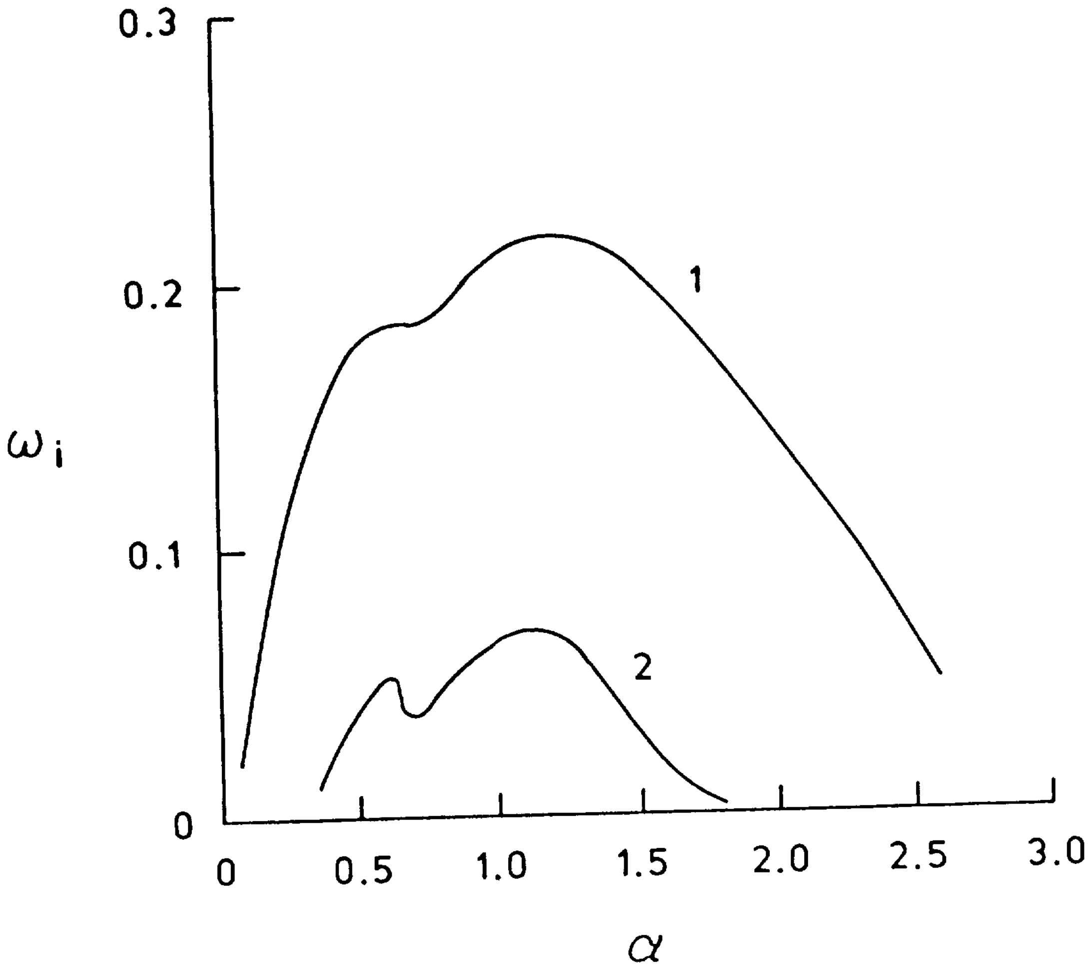

Fig. 5.9 Variation of the growth rate of asymmetric ($n = -1$) disturbances with wavenumber for a single cell vortex. Here, $q = 0.4$, $Re = 4000$ and $\psi = 0$.

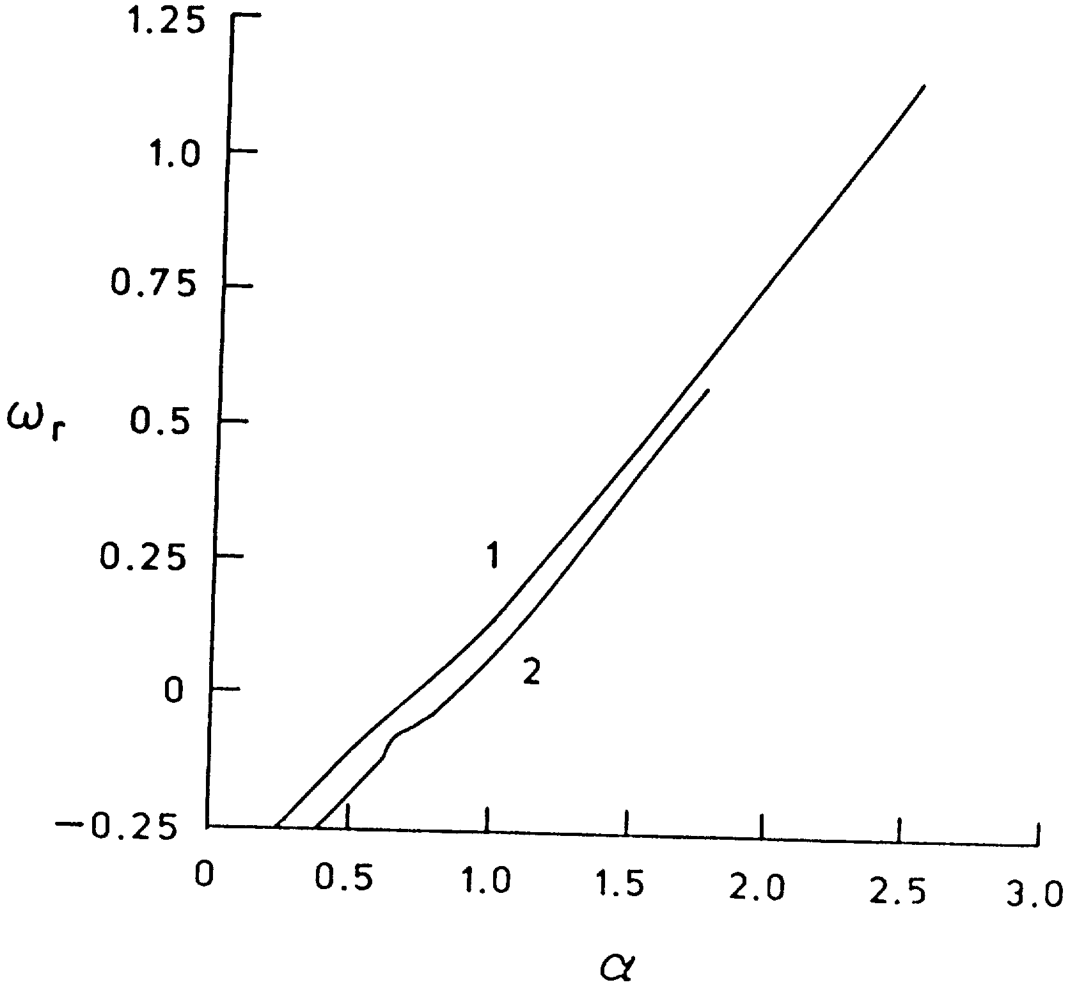

Fig. 5.10 Variation of the real part of frequency of asymmetric (n = -1) disturbances for a single cell vortex. Here, q = 0.4, Re = 4000 and $\psi \neq 0$.

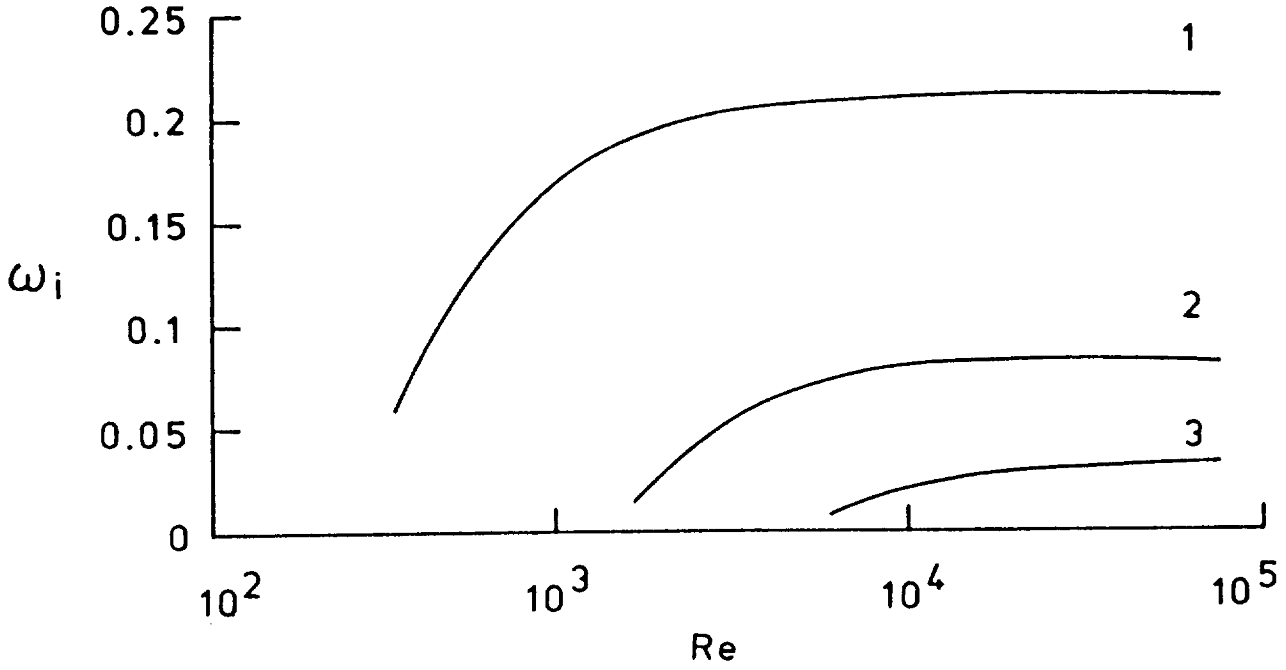

Fig. 5.11 Influence of Reynolds number on the growth rates of asymmetric (n = -1) disturbances for a single vortex. Here, α = 1.0, q = 0.4 and $\psi \neq 0$.

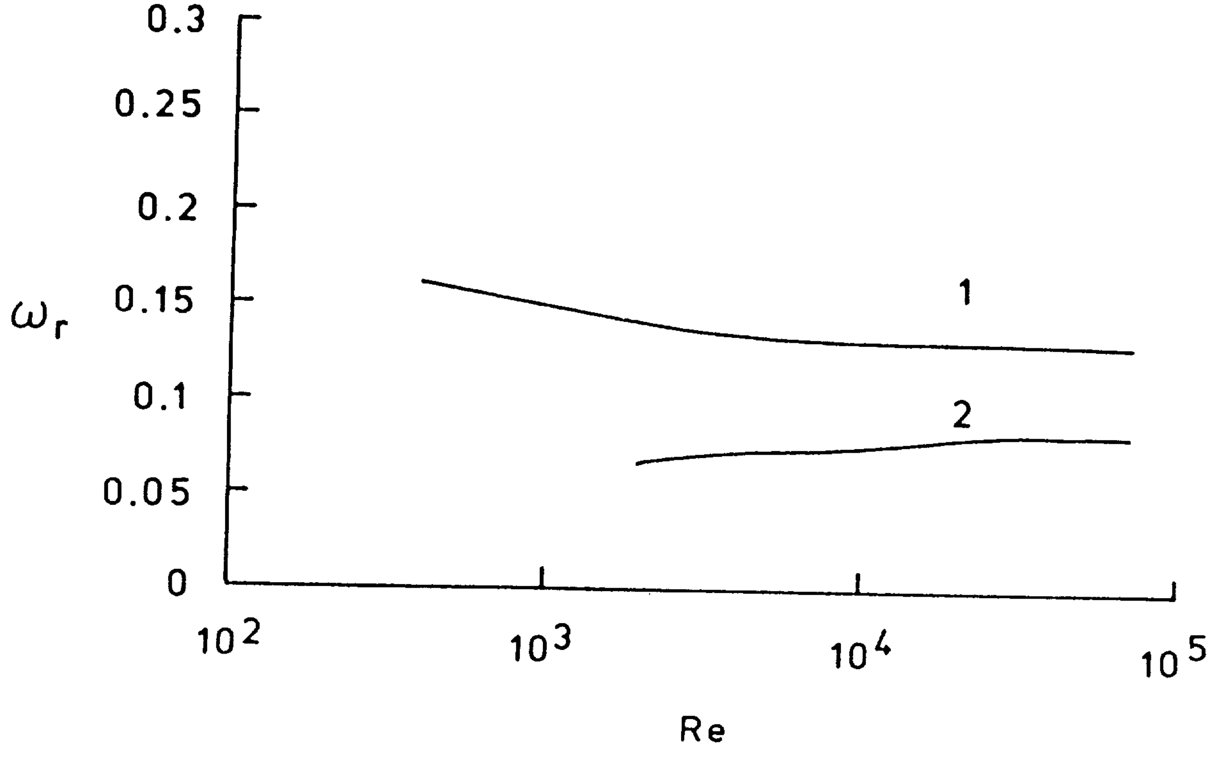

Fig. 5.12 Influence of Reynolds number on the real part of frequency of asymmetric (n =-1) disturbances for a single cell vortex. Here, α = 1.0, q = 0.4, and $\psi \neq 0$.

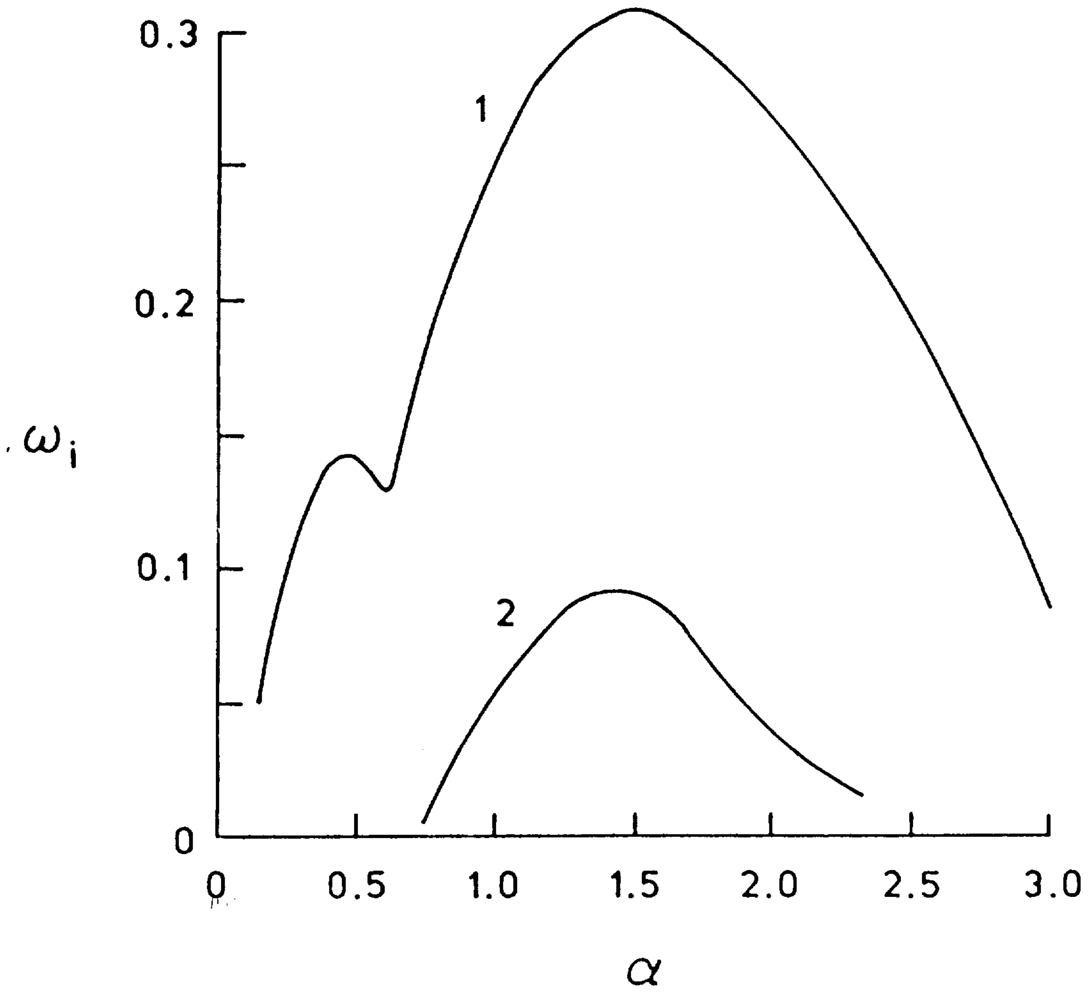

Fig. 5.13 Variation of the growth rate of asymmetric (n = -1) disturbances with wavenumber for a single cell vortex. Here, q = 0.8, Re = 4000, and $\psi \neq 0$.

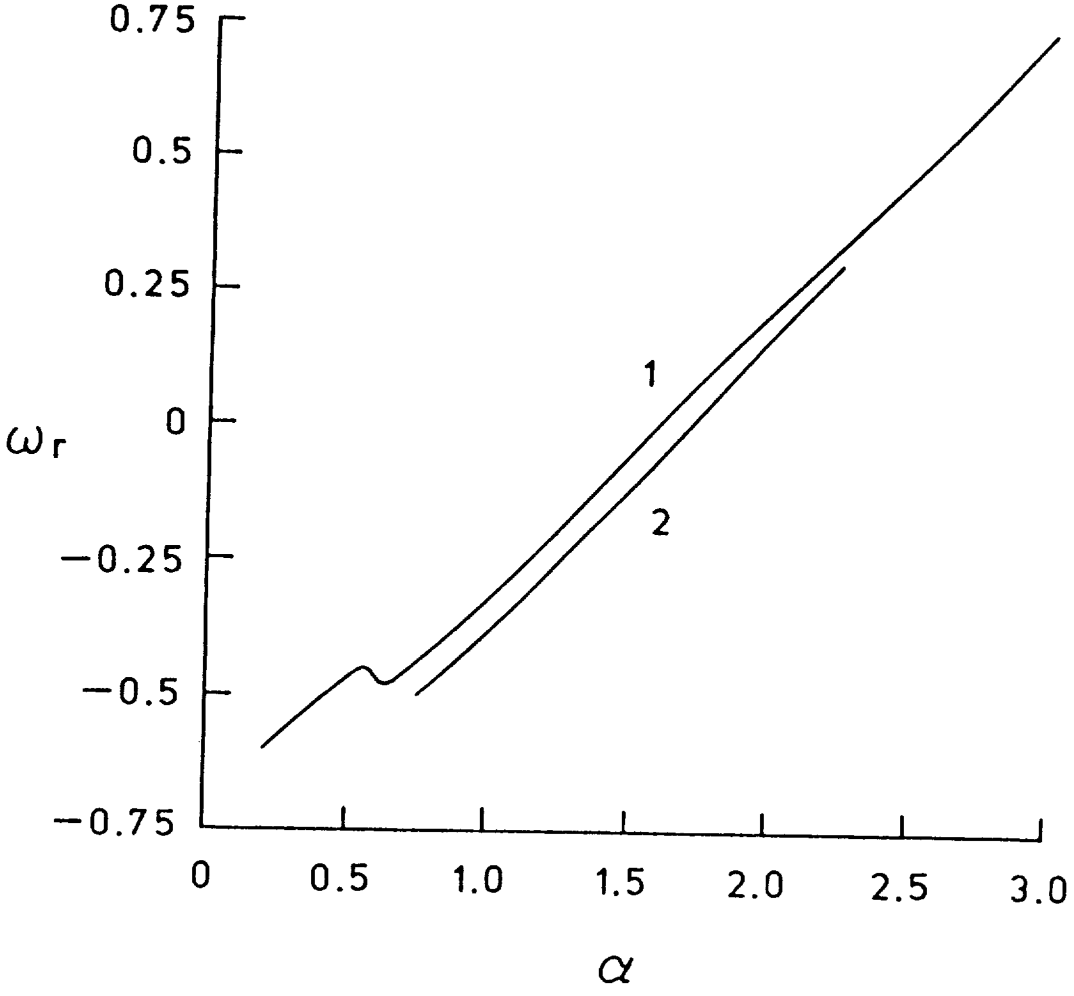

Fig. 5.14 Variation of the real part of frequency of asymmetric (n = -1) disturbances with wavenumber for a single cell vortex. Here, q = 0.8, Re = 4000, and $\psi \neq 0$.

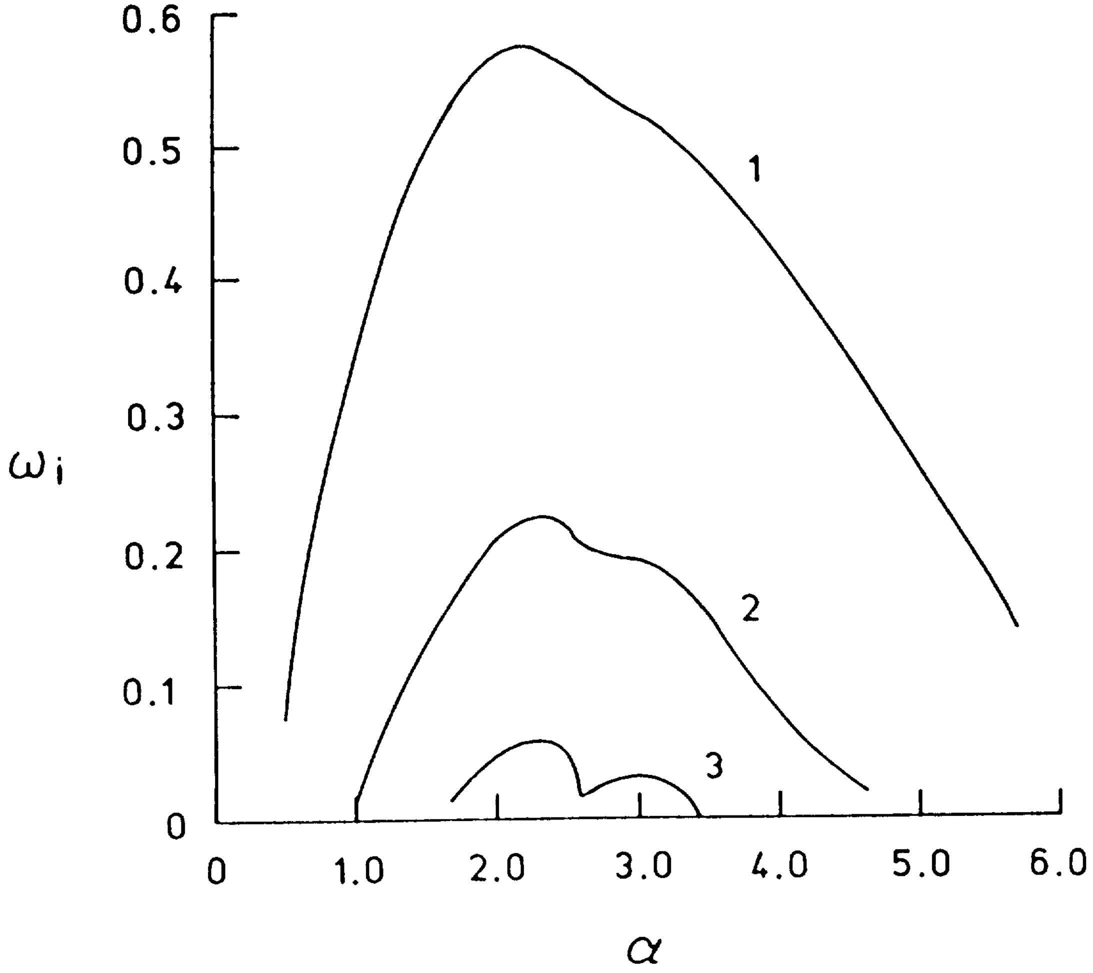

Fig. 5.15 Variation of the growth rate of $n = -2$ disturbances with wavenumber for a single cell vortex. Here, $q = 0.8$, $Re = 4000$ and $\psi \neq 0$.

indicates a twofold increase over the values of ω_i for Batchelor's vortex (figure 4.2). Also, the instability presists over a much larger range of the axial wavenumber, α. The problem of mode identification, as pointed out by [26], is demonstrated in figure 5.16. Note how closely the two curves follow each other. In fact, as the neutral curve is approached, the real part of both frequencies become indistinguishable when they are displayed graphically. However, contrary to the remarks made by Leibovich and Stewartson [26], at no time did we encounter difficulties with the convergence of the first few eigenvalues. Rather, the difficulty is caused by the successively smaller increments of α needed to follow the same eigenmode. This in turn would make global calculations very expensive rather than impossible.

The variation of the growth rate with Re for the $n = -2$ mode at $q = 0.8$ and $\alpha = 2$ is presented in figure 5.17. Clearly the instability is an inviscid one. The real part of the frequency, shown in figure 5.18, indicates little variation with Reynolds number, especially at high Re.

5.2 Stability of a Two Cell Vortex at Re = 10000

The three components of the velocity profile are shown in figure 5.19. Again, note the similarity between the azimuthal velocity profile to that of a trailing line vortex. Also there is an inflectional point in the axial component of velocity between $r = 0.6$ and $r = 0.8$. The variation of growth rate with axial wavenumber for the axisymmetric mode ($n = 0$) is shown in figure 5.20, for $q = 0.5$ and 1.0. Obviously, increasing the swirl has a destabilizing influence. However, the surprising effect here is the enormity of the growth rates obtainable with this mode. In fact, the maximum growth rate is orders of magnitude larger than the viscous mode of the Batchelor's

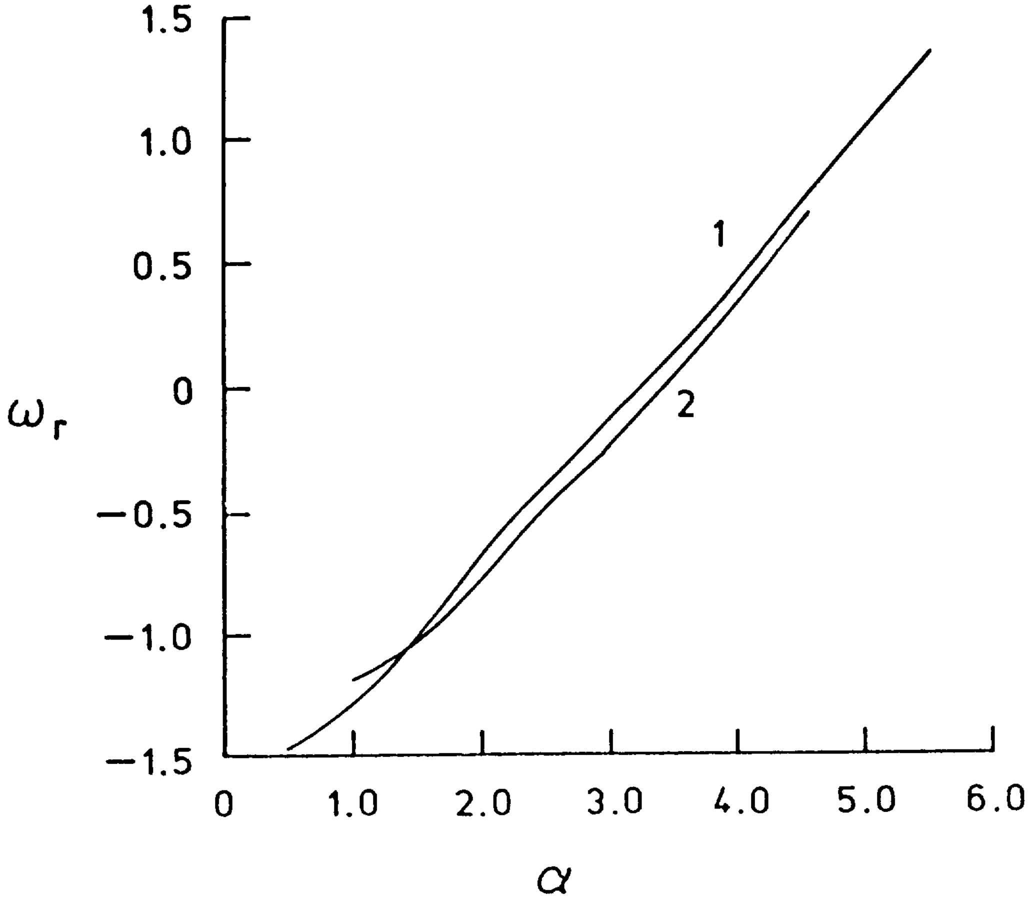

Fig. 5.16 Variation of the real part of frequency of n = -2 disturbances with wavenumber for a single cell vortex. Here, q = 0.8, Re = 4000 and $\psi \neq 0$.

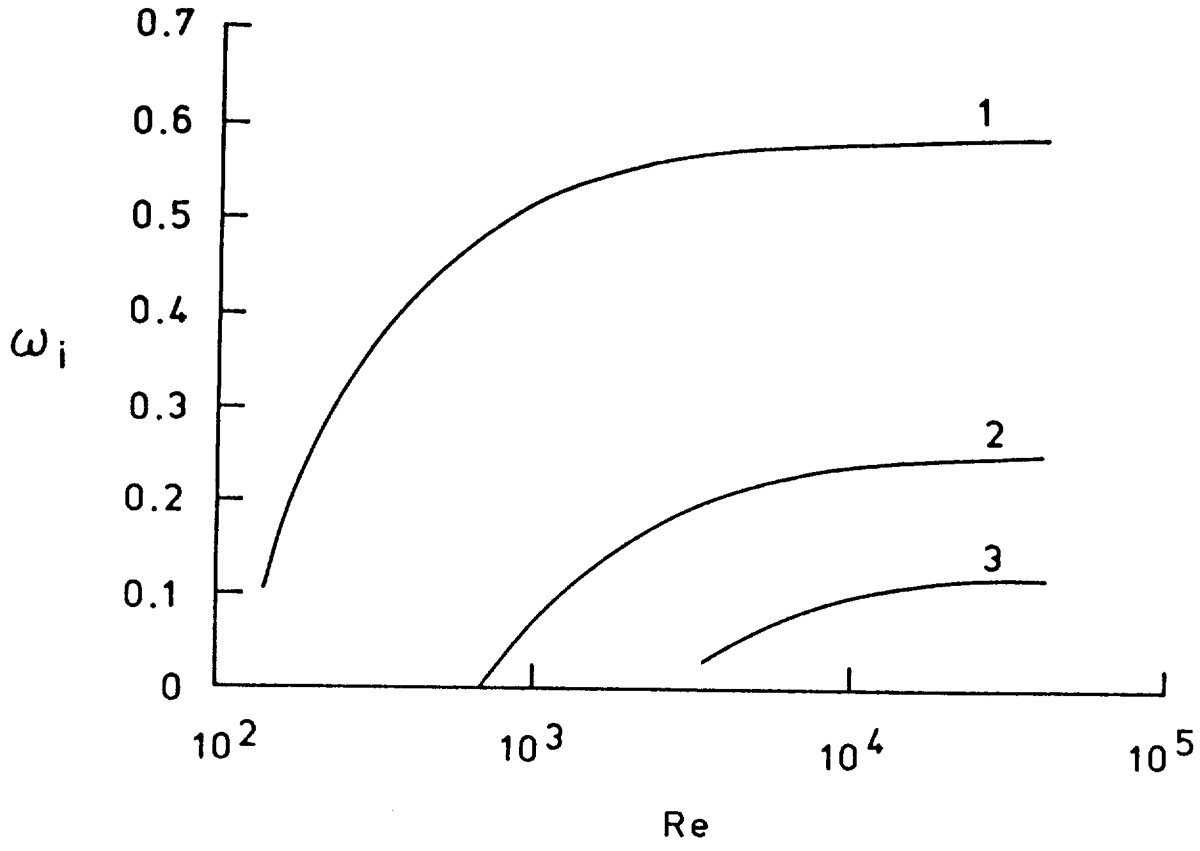

Fig. 5.17 Influence of Reynolds number on the growth rate of $n = -2$ disturbances for a single cell vortex. Here, $\alpha = 2.0$, $q = 0.8$, and $\psi \neq 0$.

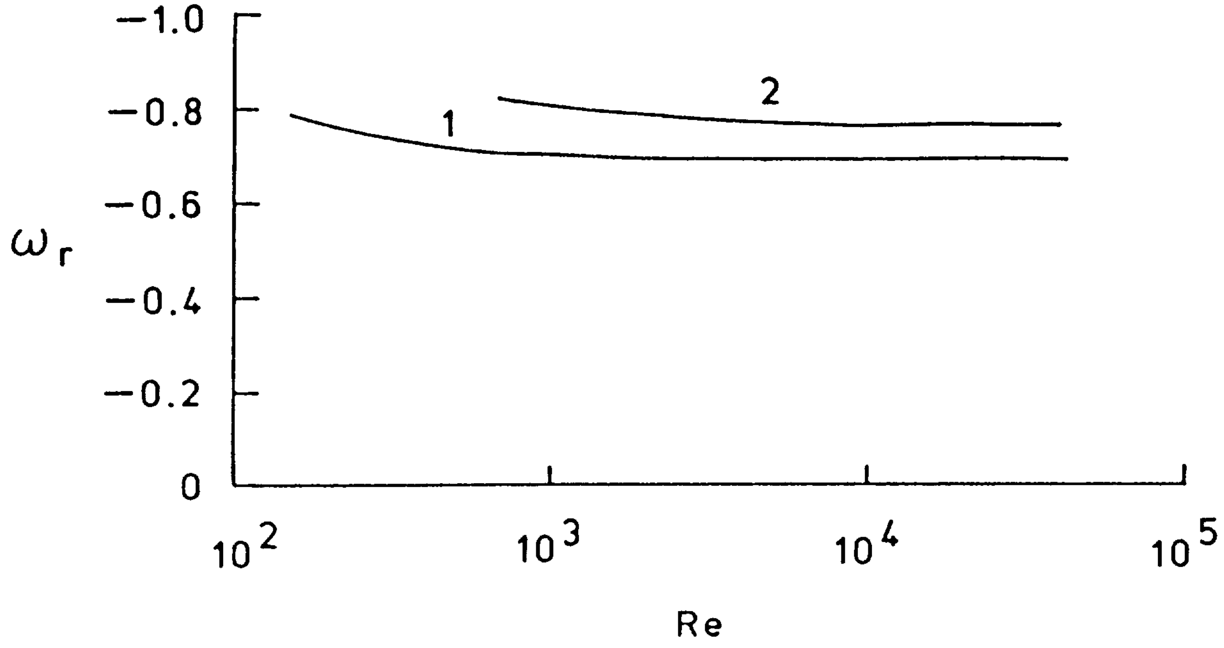

Fig. 5.18 Influence of Reynolds number on the real part of frequency of n = -2 disturbances for a single cell vortex. Here, $\alpha = 2.0$, $q = 0.8$, and $\psi \neq 0$.

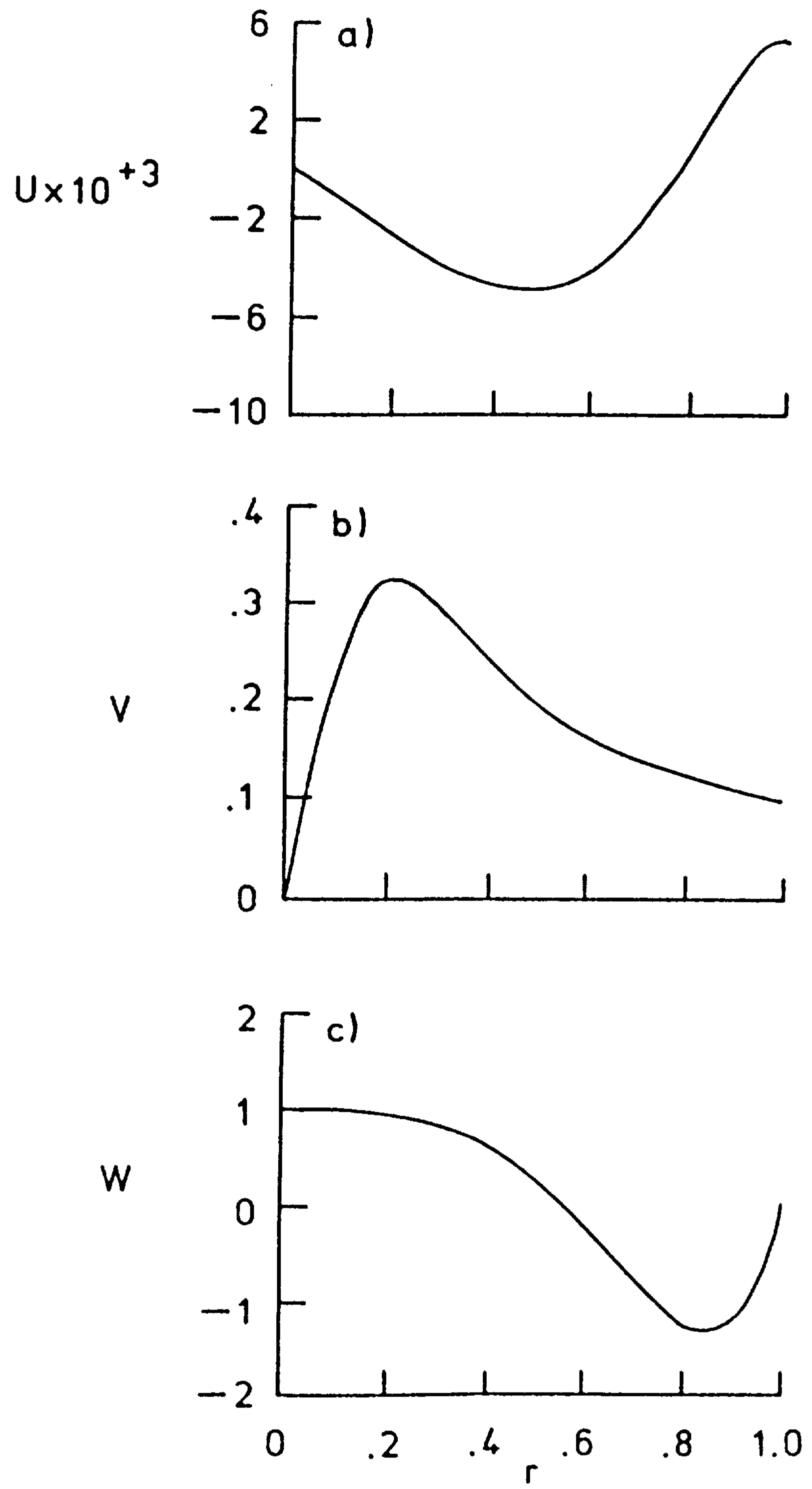

Fig. 5.19 Velocity components for a two cell vortex.

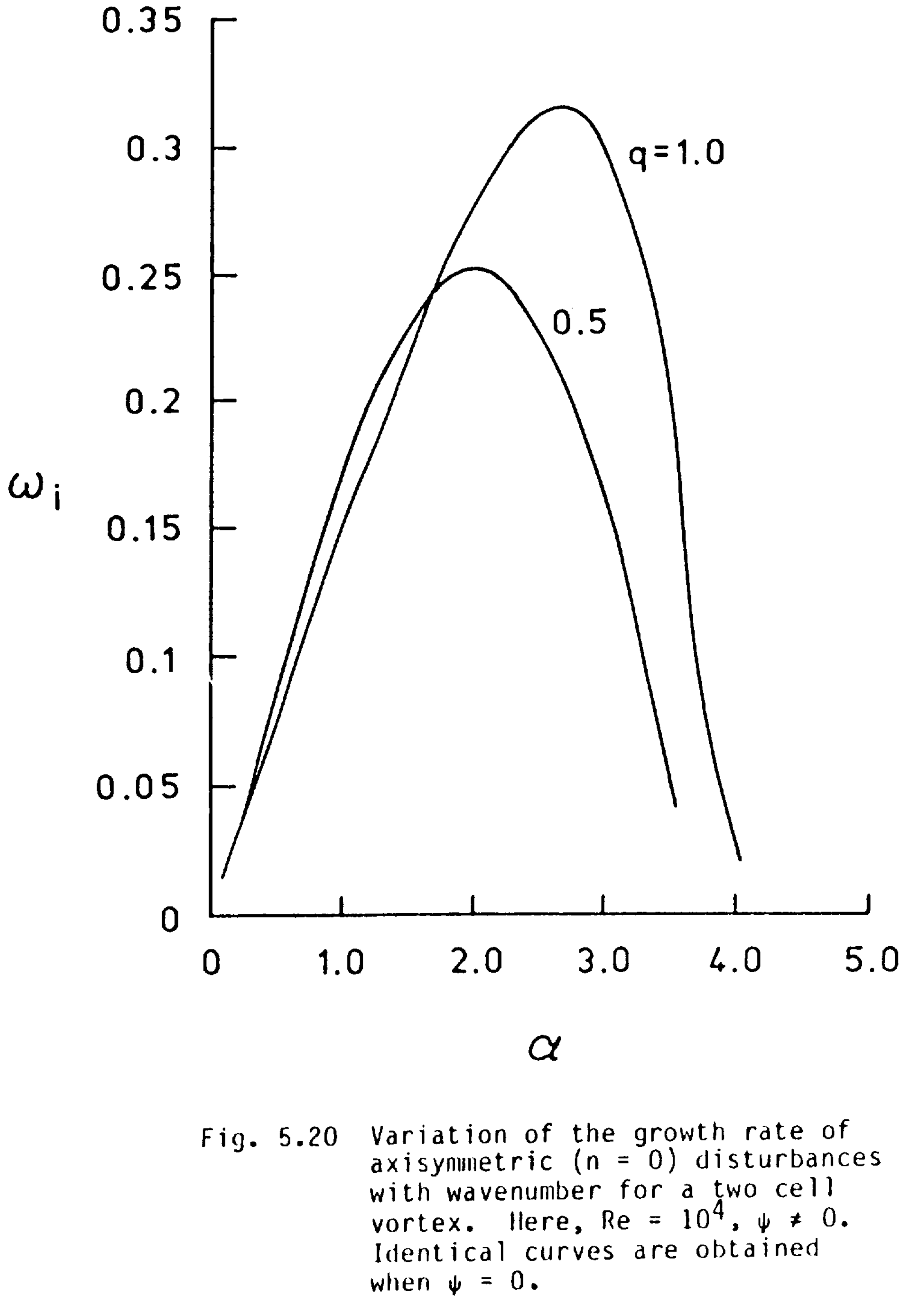

Fig. 5.20 Variation of the growth rate of axisymmetric (n = 0) disturbances with wavenumber for a two cell vortex. Here, Re = 10^4, $\psi \neq 0$. Identical curves are obtained when $\psi = 0$.

vortex. No axisymmetric mode of instability has been reported previously (regardless of whether the vortex was single cell or multiple cell) and the explosive growth rates make this discovery even more significant.

The question that had to be answered concerning the axisymmetric instability was whether it was caused by the multiplicity of cells in the core or as a natural manifestation of the solid pipe wall boundary condition which is absent in the case of a trailing line vortex in an infinite domain. Figures 5.21a through 5.21d represent the eigenfunctions associated with this instability. For the sake of space, we will show only the amplitudes in this section. In figure 5.21a, it is shown that wall presence has resulted in a second peak in the radial component of the eigenfunction. A similar situation exists for the axial component of the eigenfunction except that the magnitude of the peak close to the wall is much less than that of the center peak. However, based on the shape of the eigenfunctions close to the centerline, the similarity between this mode and the axisymmetric viscous mode of Batchelor's vortex is striking. Overall this is a $\hat{C}$ type disturbance with most of the perturbation energy being concentrated near the centerline. The variation of ω_r with α for the axisymmetric disturbance is presented in figure 5.22. It must be mentioned that the effect of setting ϕ equal to zero on this mode was negligible. The variation of ω_i with Reynolds number for $q = 1.0$, and $\alpha = =$ 2.0, is displayed in figure 5.23. The growth rate increases as Re increases, attaining its maximum value at moderate Reynolds numbers and then asymptoting to a constant value or dropping slightly. This mode clearly is an inviscid one. The variation of ω_r with Re is shown in figure 5.24. The curve is almost a straight line with constant slope.

Figure 5.25 shows the variation of ω_i with α for an asymmetric mode (n = 1) with $q = 0.4$. The first mode, which has much larger growth rates, is a

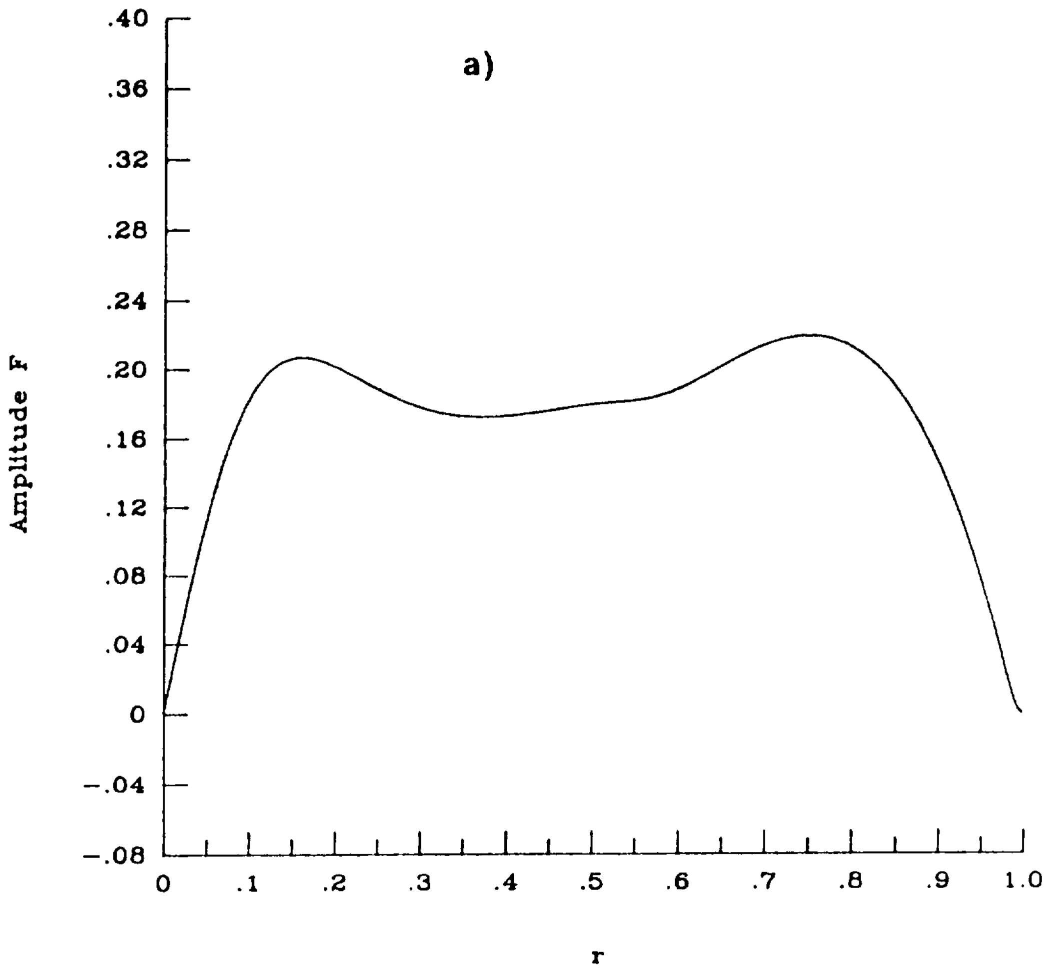

Fig. 5.21 Amplitude of eigenfunction components of axisymmentric (n = 0) perturbation for a two cell vortex. a) radial velocity, b) azimuthal velocity, c) axial velocity, d) pressure. Here, $\alpha = 2.25$, $q = 1.0$, $Re = 10^4$, and $\psi \neq 0$.

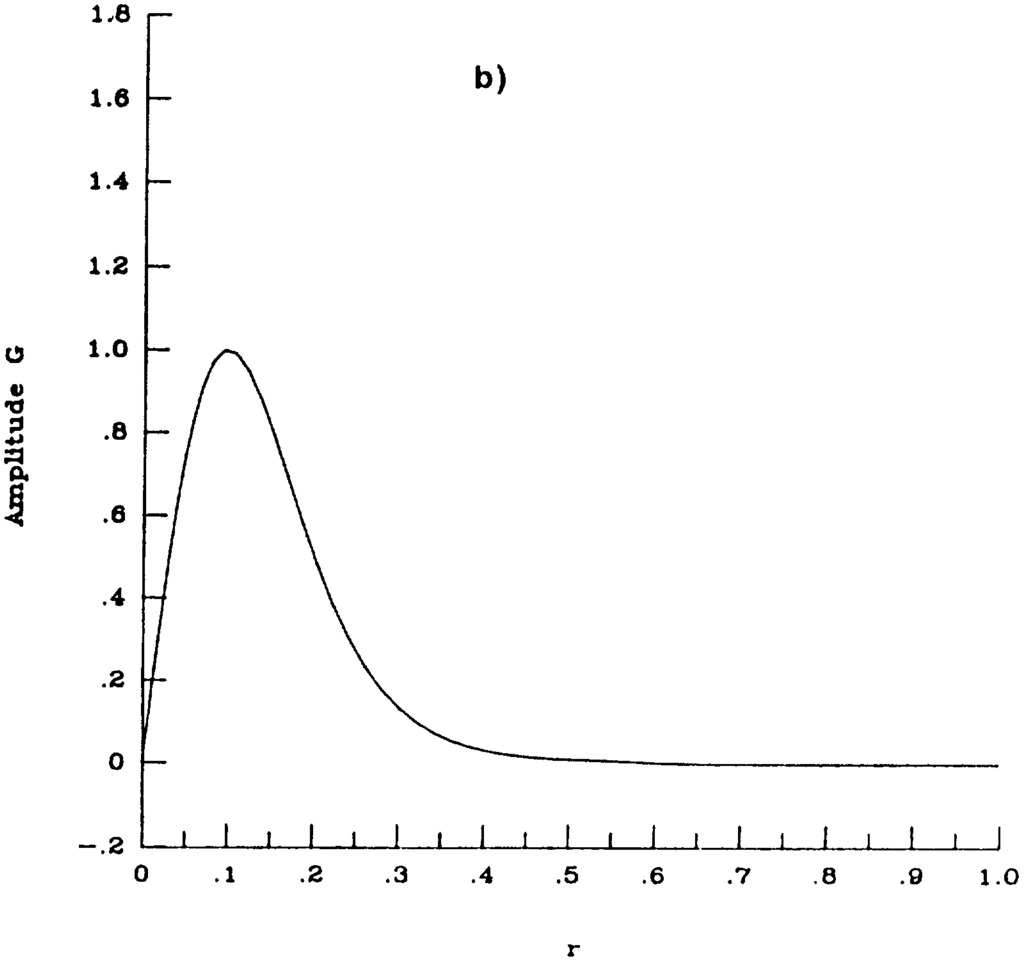

Fig. 5.21b) Continued.

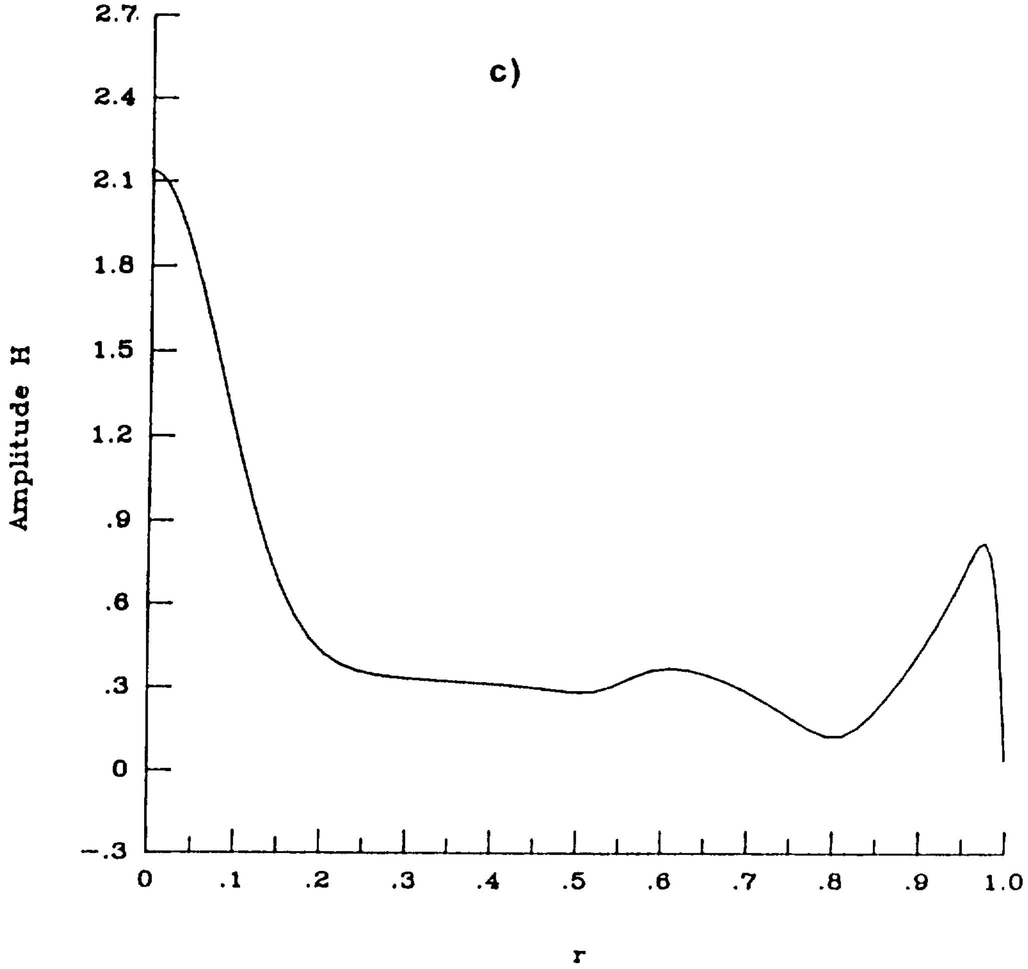

Fig. 5.21c) Continued.

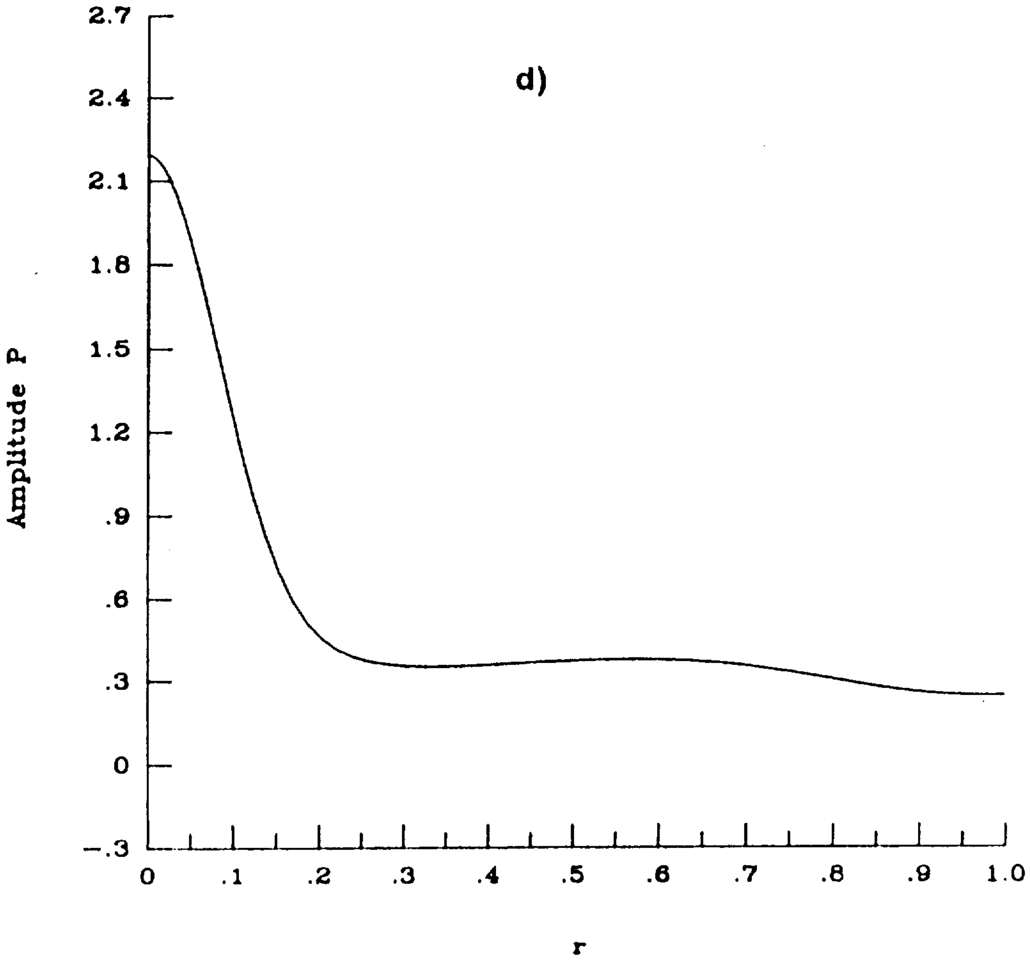

Ref. 5.21d) Concluded.

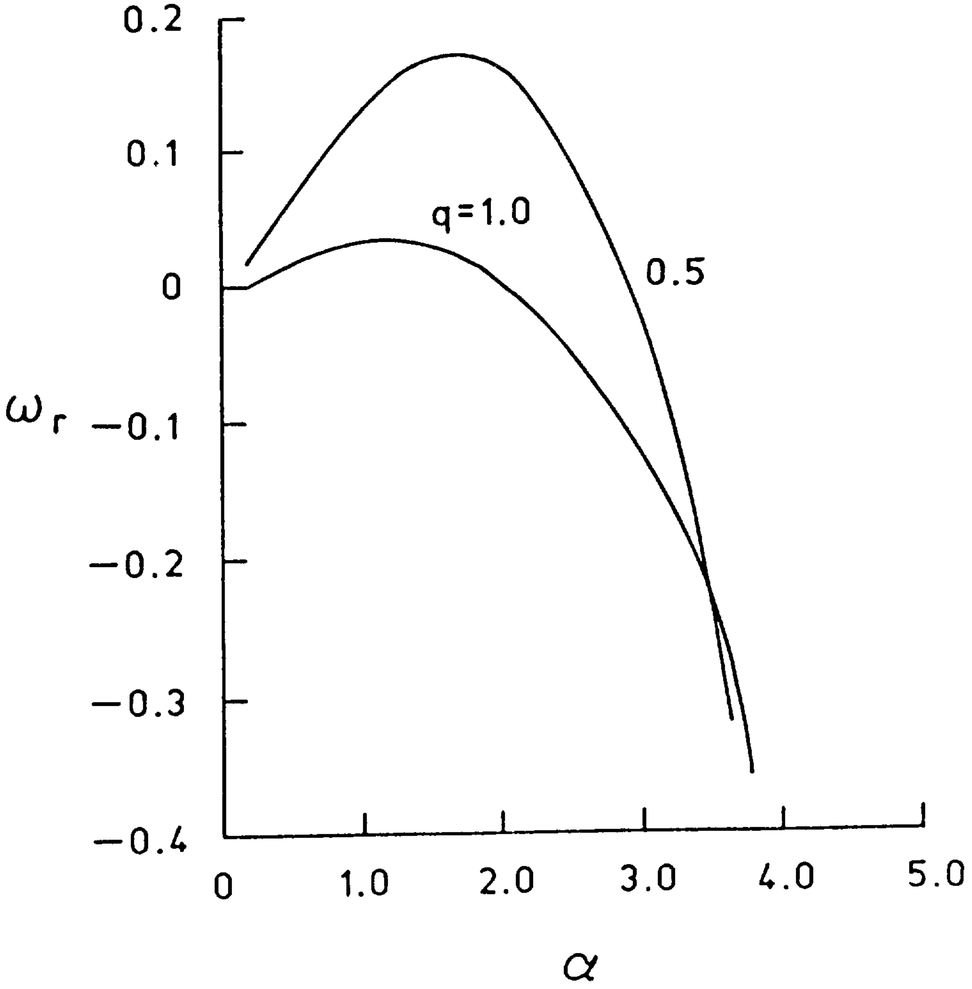

Fig. 5.22 Variation of the real part of frequency of axisymmetric (n = 0) disturbances with wavenumber for a two cell vortex. Here, Re = 10^4, $\psi \neq 0$. Identical curves are obtained when $\psi = 0$.

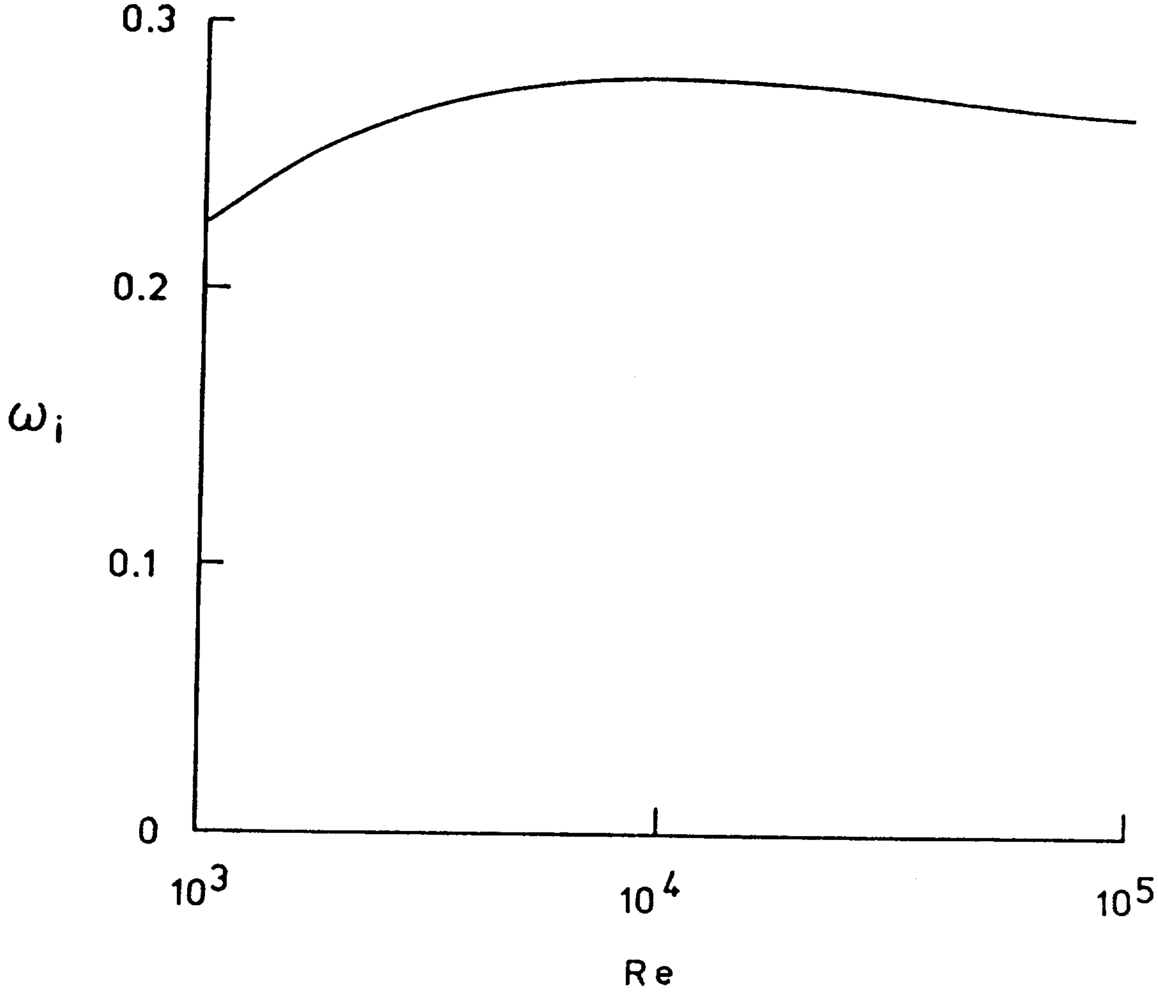

Fig. 5.23 Influence of Reynolds number on the growth rate of axisymmetric ($n = 0$) disturbances for a two cell vortex. Here, $\alpha = 2.0$, $q = 1.0$, and $\psi \neq 0$.

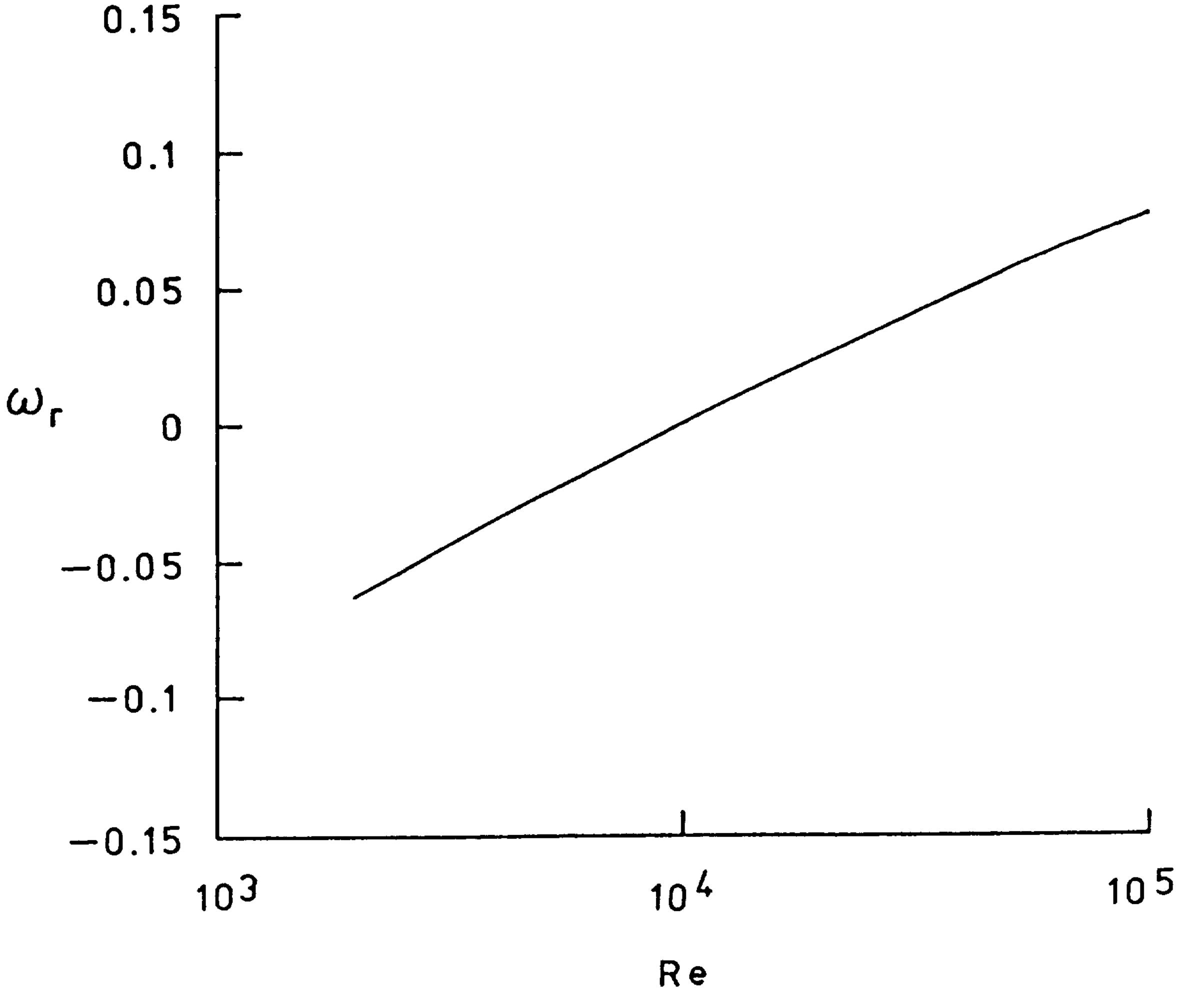

Fig. 5.24 Influence of Reynolds numbers on the real part of frequency of axisymmeric ($n = 0$) disturbances for a two cell vortex. Here, $\alpha = 2.0$, $q = 1.0$, and $\psi \neq 0$.

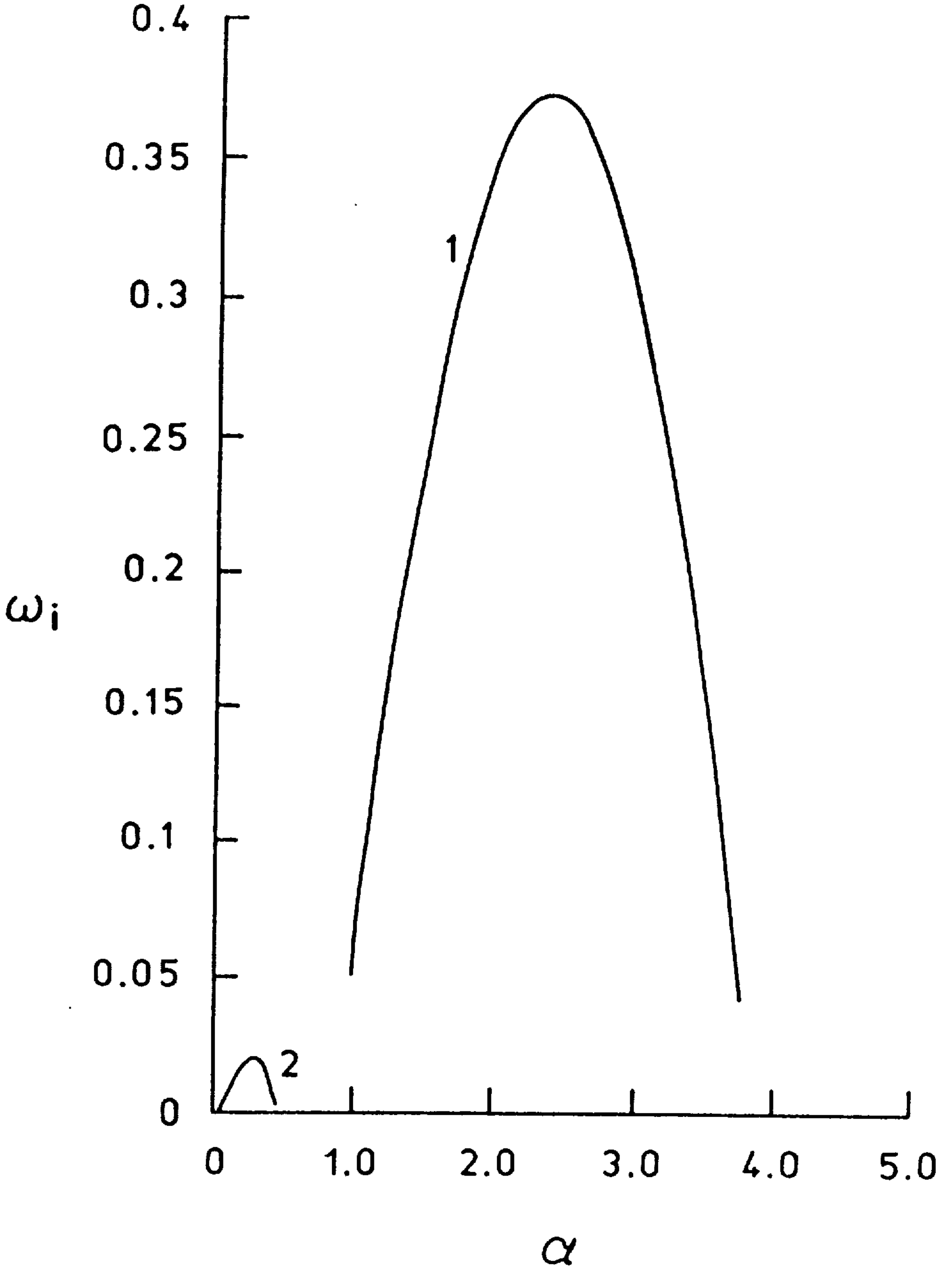

Fig. 5.25 Variation of the growth rate of asymmetric (n = +1) disturbances with wavenumber for a two cell vortex. Here, q = 0.4, Re = 10^4, and $\psi \neq 0$.

short wave instability while the second mode exists only at the low end of the wavenumber spectrum (long wave instability). The effect of setting $\psi = 0$ on these modes is presented in figure 5.26. While there is hardly any change in the primary mode, note the significant drop in the growth rate of the second mode. The term associated with ψ represents the non-parallel effect in the velocity profiles of Donaldson and Sullivan [33]. The second mode is displayed in more detail in figure 5.27. The instability is clearly a long wave instability. Note that at this particular value of the Reynolds number (Re = 10000) the growth rates are orders of magnitude higher than the $n = 1$ viscous mode associated with the trailing line vortex represented in figure 4.25. The real part of frequency of the second mode is presented in figure 5.28. The variation of ω_r with α is linear. It was found that ω_r did not vary with ψ. Setting ψ equal to zero, the eigenfunctions of the first and second modes were obtained. The eigenfunctions associated with the second mode (at $\alpha = 0.2$) are displayed in figures 5.29a through 5.29d. The resemblance between these curves and the eigenfunctions for the asymmetric viscous mode of the trailing line vortex (figures 4.27a-4.27h) is striking. The only observable difference is the position of the peak in the axial component of the eigenfunction. Here the peak occurs close to $r \simeq 0.7$, which is natural since, as mentioned earlier, the inflectional point in the axial component of mean velocity is situated very close to this value of r. However, the second mode is basically a $\hat{\mathbf{C}}$ type perturbation. The eigenfunctions of the first mode (at $\alpha = 2.5$) plotted in figures 5.30a through 5.30d revealed the existence of co-instability even though the growth rate curve does not show any multiple peaks and is smooth. At this value of α, the perturbation is a $\hat{\mathbf{C}}\,\hat{\mathbf{R}}\,\hat{\mathbf{W}}$ type. Notice how different the structure of this disturbance is when compared to that of the second mode even though both have

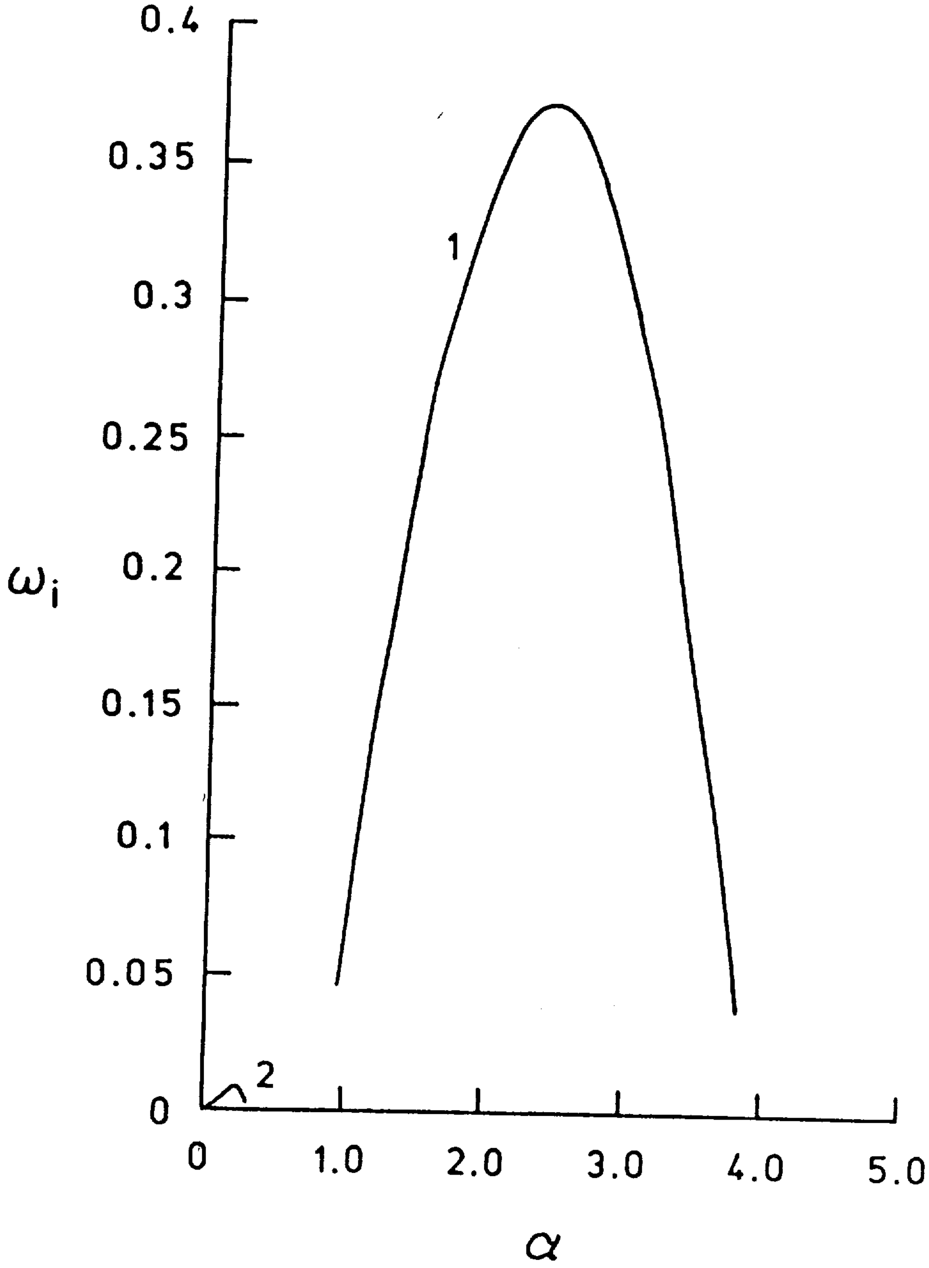

Fig. 5.26 Variation of the growth rate of asymmetric ($n = +1$) disturbances with wavenumber for a two cell vortex. Here, $q = 0.4$, $Re = 10^4$ and $\psi = 0$.

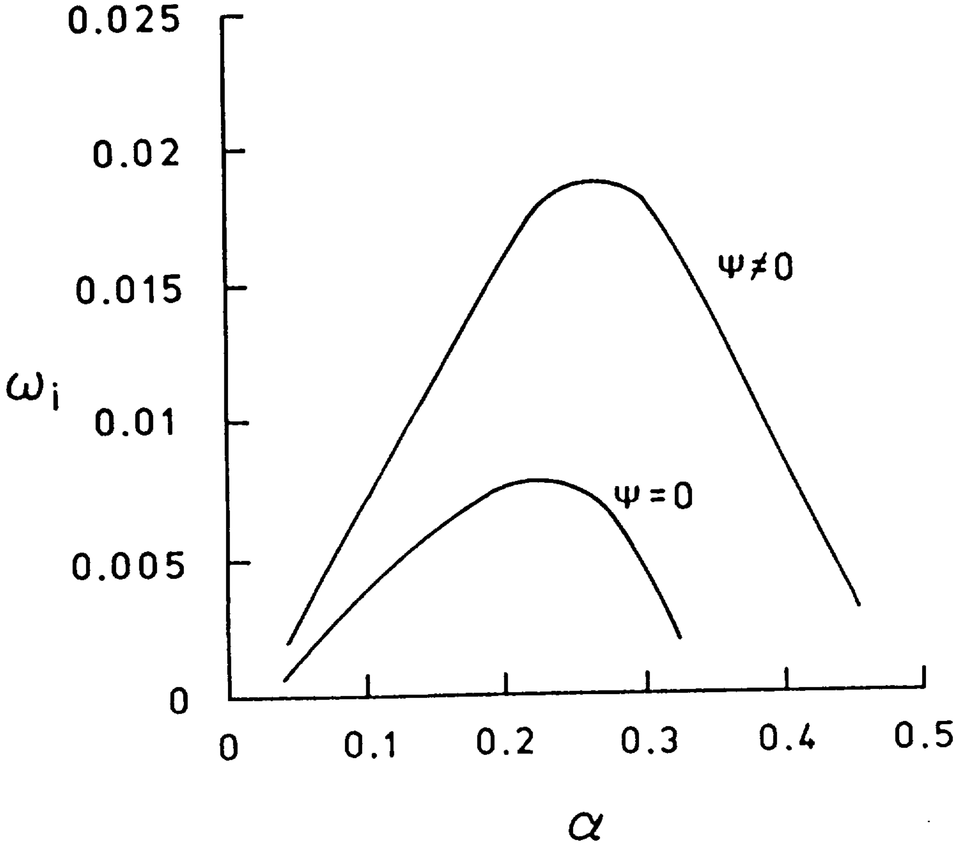

Fig. 5.27 Detailed representation of the variation of the growth rate of the asymmetric ($n = +1$, second mode) disturbances with wavenumber for a two cell vortex. Here, $q = 0.4$, $Re = 10^4$ and the influence of nonparallel effects ($\psi \neq 0$) is also shown.

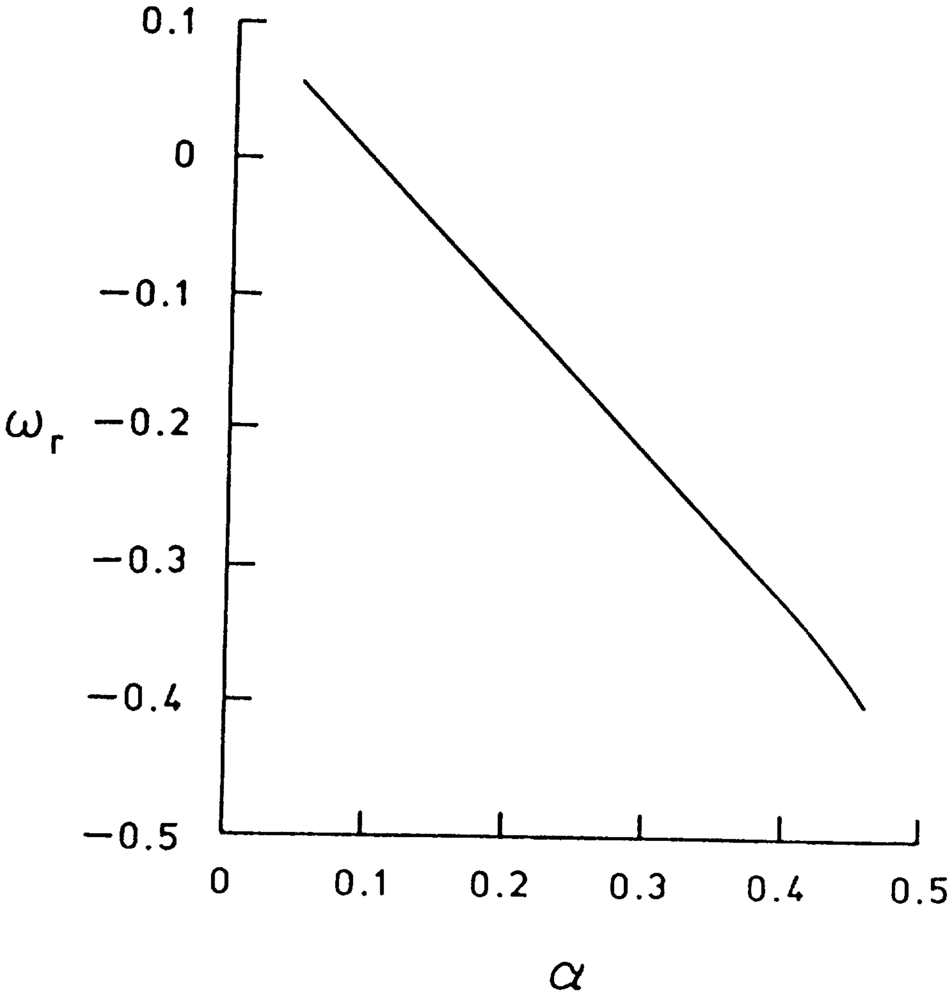

Fig. 5.28 Variation of the real part of frequency of asymmetric (n = +1, second mode) disturbances with wavenumber for a two cell vortex. Here, $q = 0.4$, $Re = 10^4$, and $\psi \neq 0$. Identical curve is obtained when $\psi = 0$.

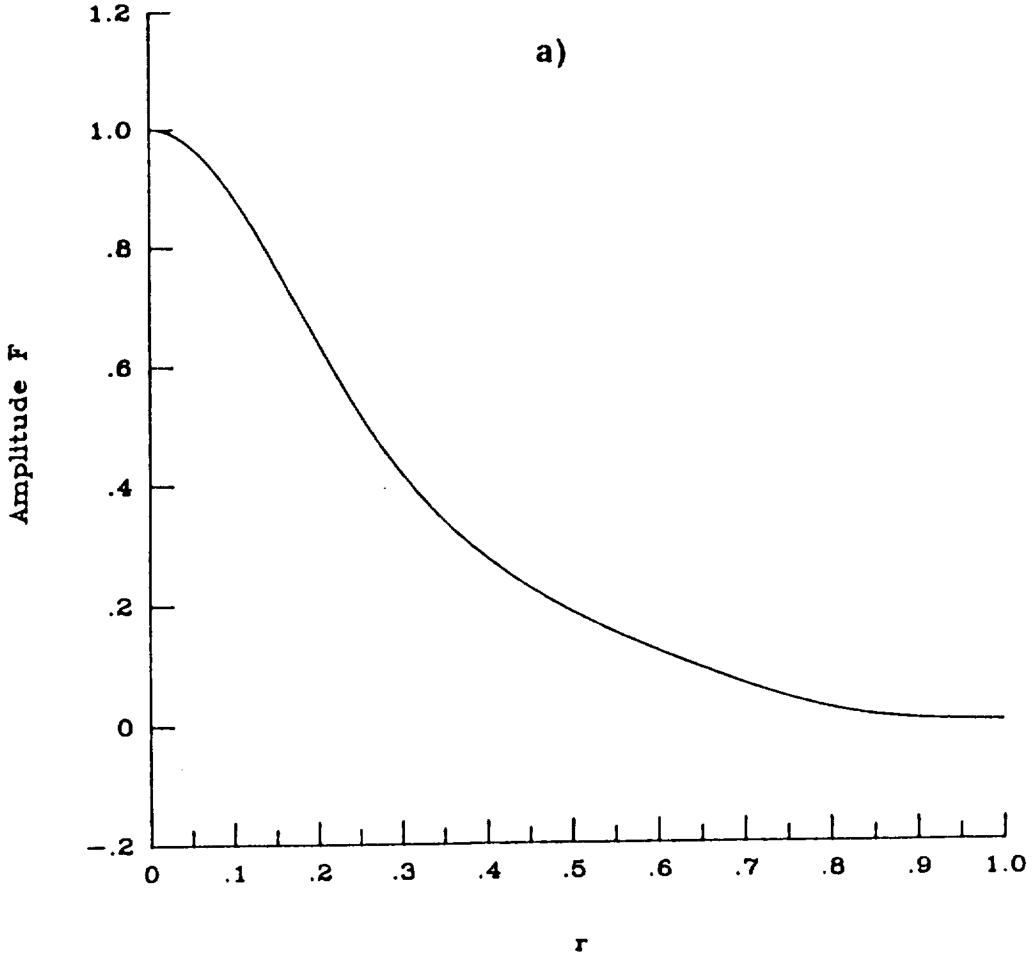

Fig. 5.29 Amplitude of eigenfunction components of asymmetric (n = +1, second mode) perturbation for a two cell vortex. a) radial velocity, b) azimuthal velocity, c) axial velocity, d) pressure. Here, α = 0.2, q = 0.4, Re = 10^4, and ψ = 0.

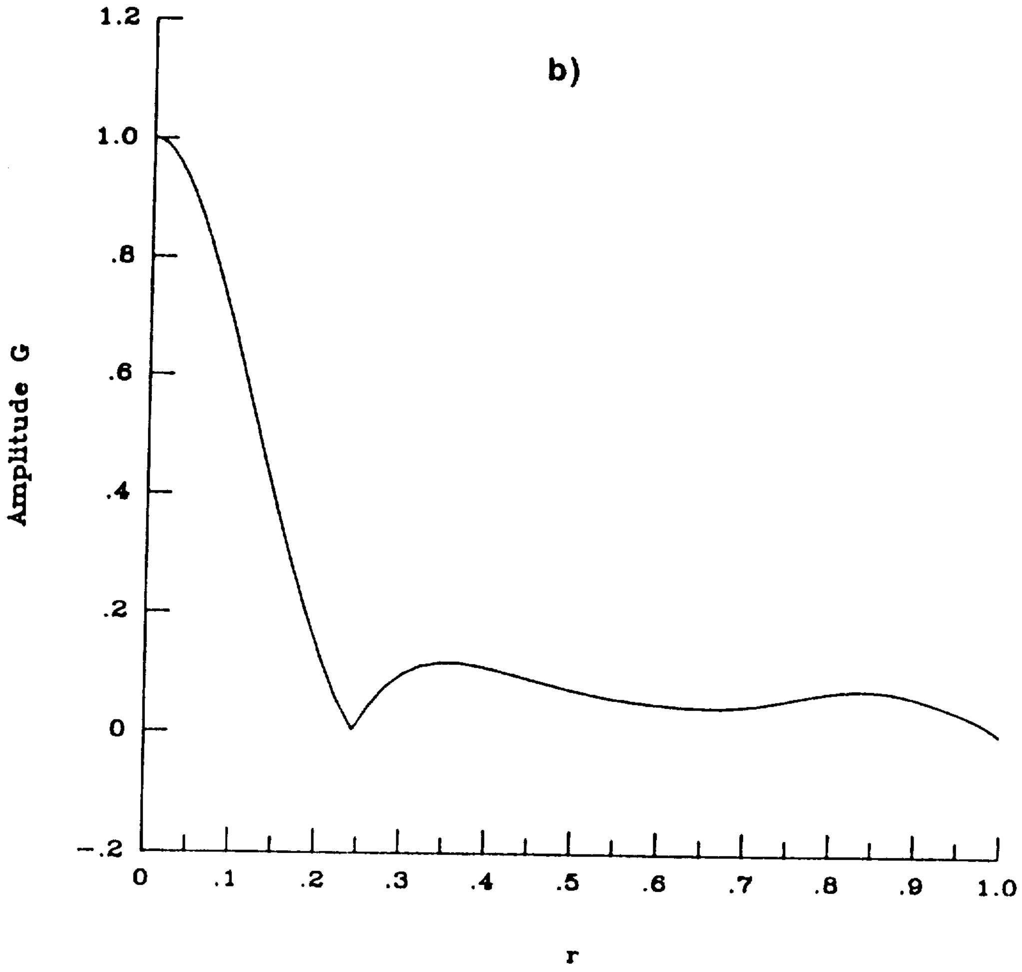

Fig. 5.29b) Continued.

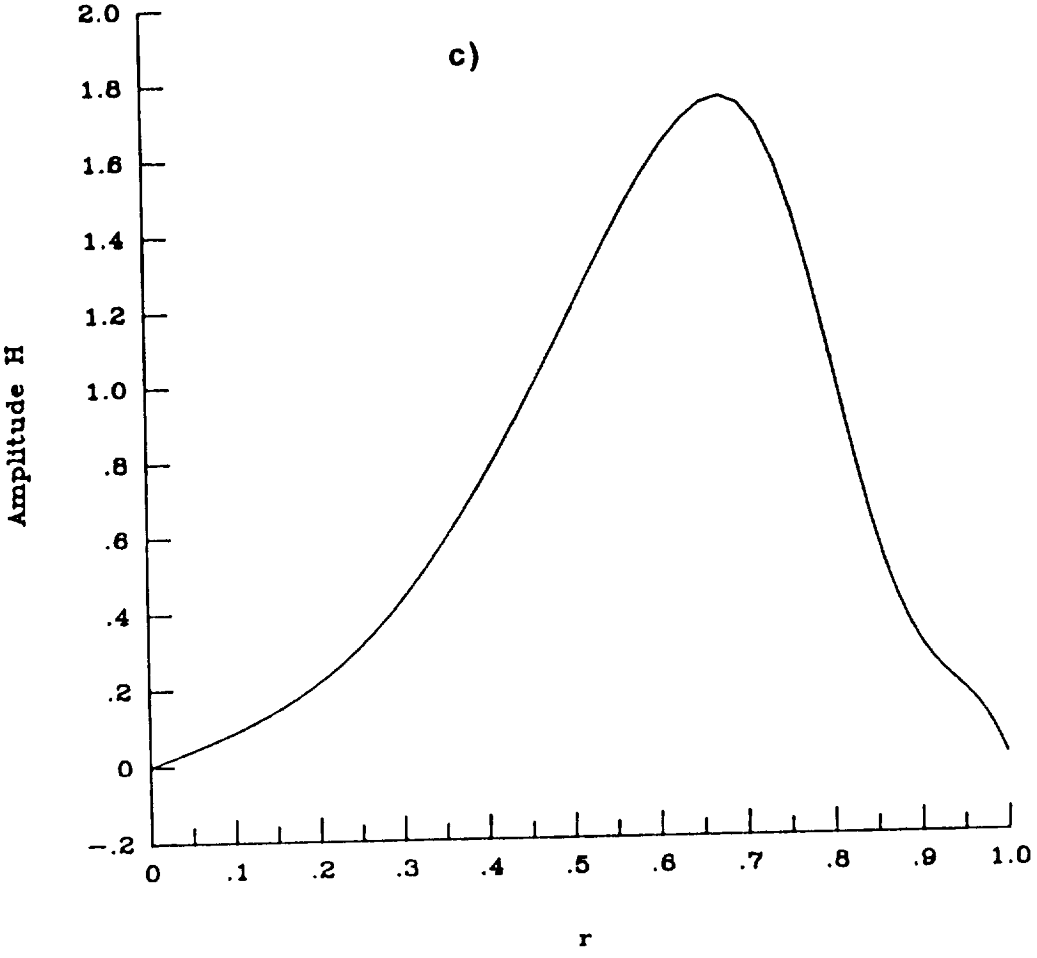

Fig. 5.29c) Continued.

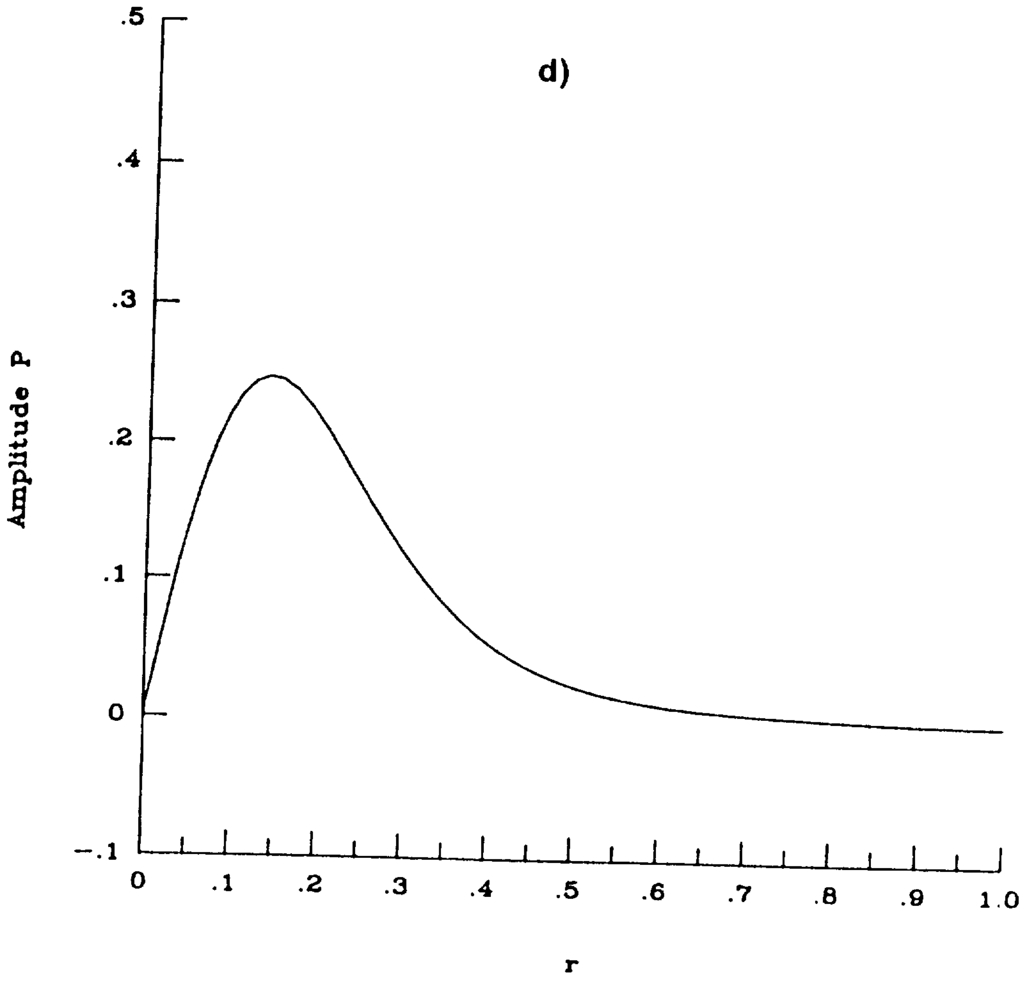

Fig. 5.29d) Concluded.

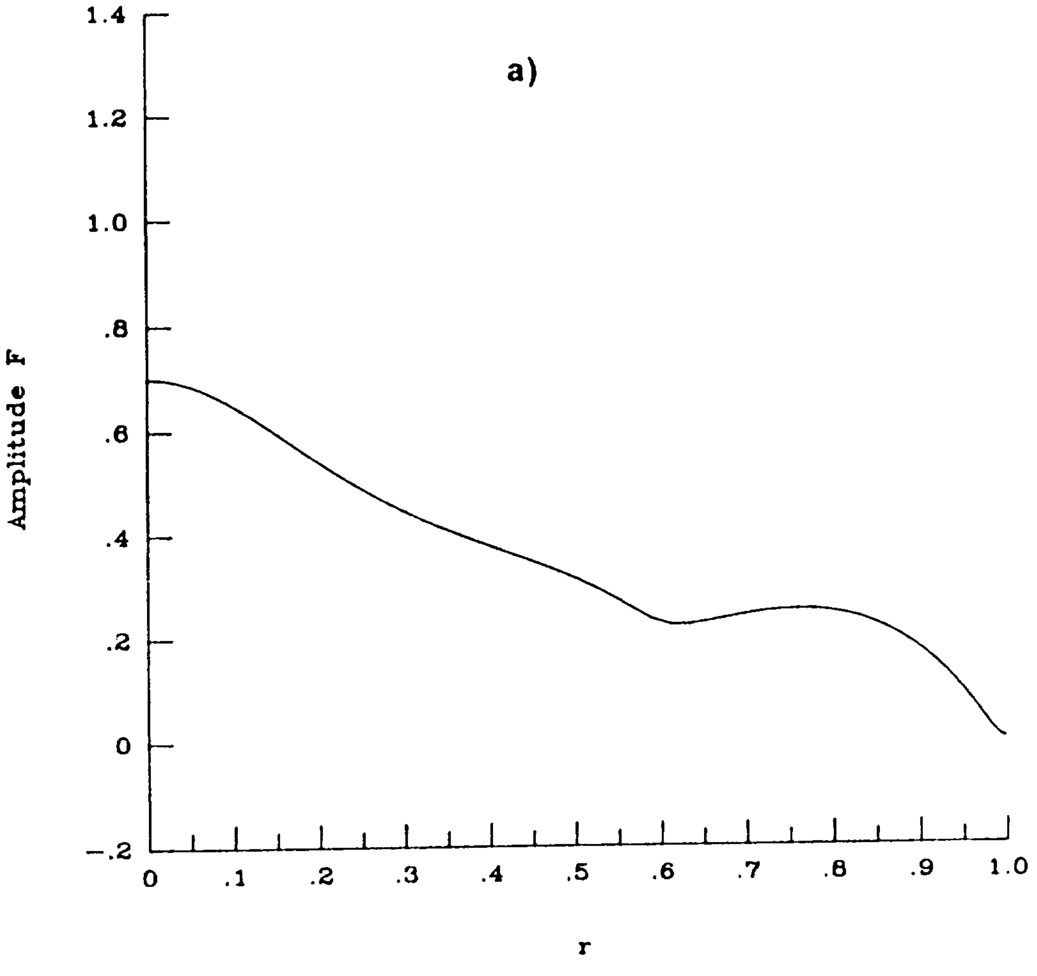

Fig. 5.30 Amplitude of eigenfunction components of asymmetric ($n = +1$, first mode) perturbation for a two cell vortex. a) radial velocity, b) azimuthal velocity, c) axial velocity, d) pressure. Here, $\alpha = 2.5$, $q = 0.4$, $Re = 10^4$, and $\psi = 0$

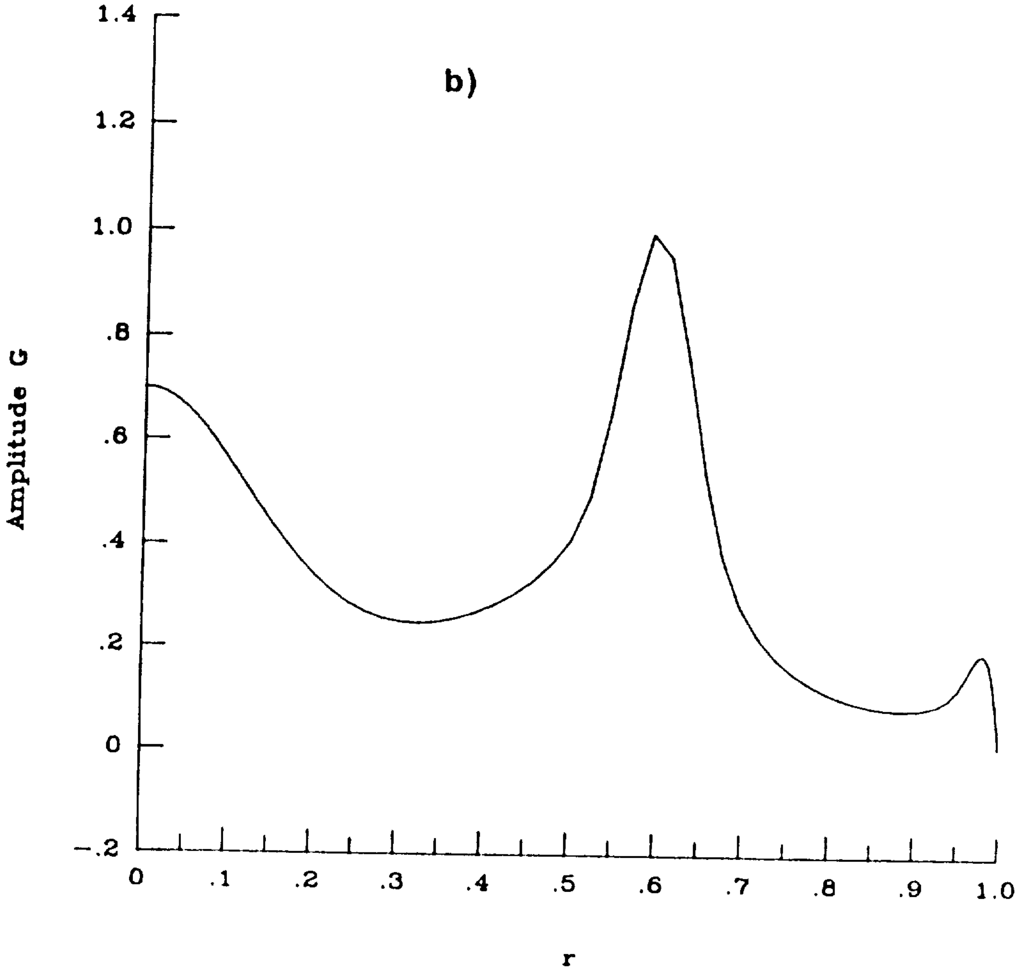

Fig. 5.30b) Continued.

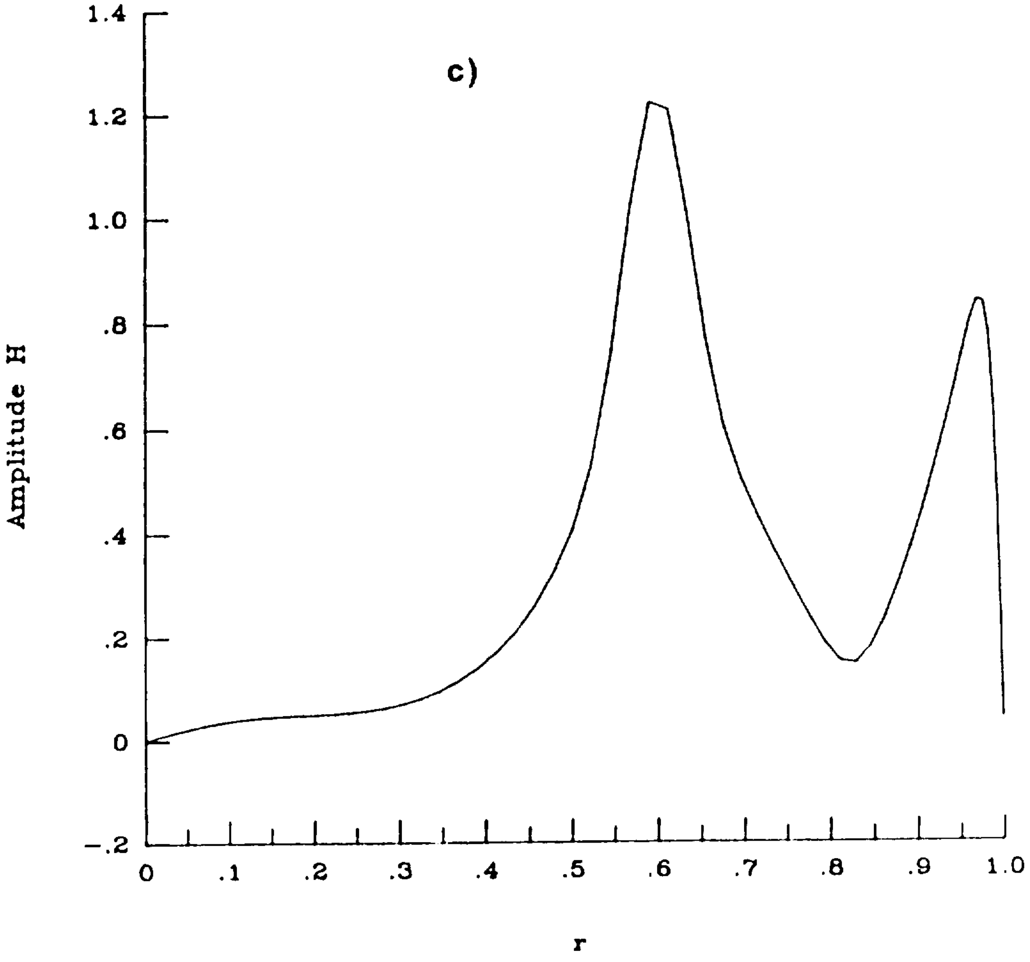

Fig. 5.30c) Continued.

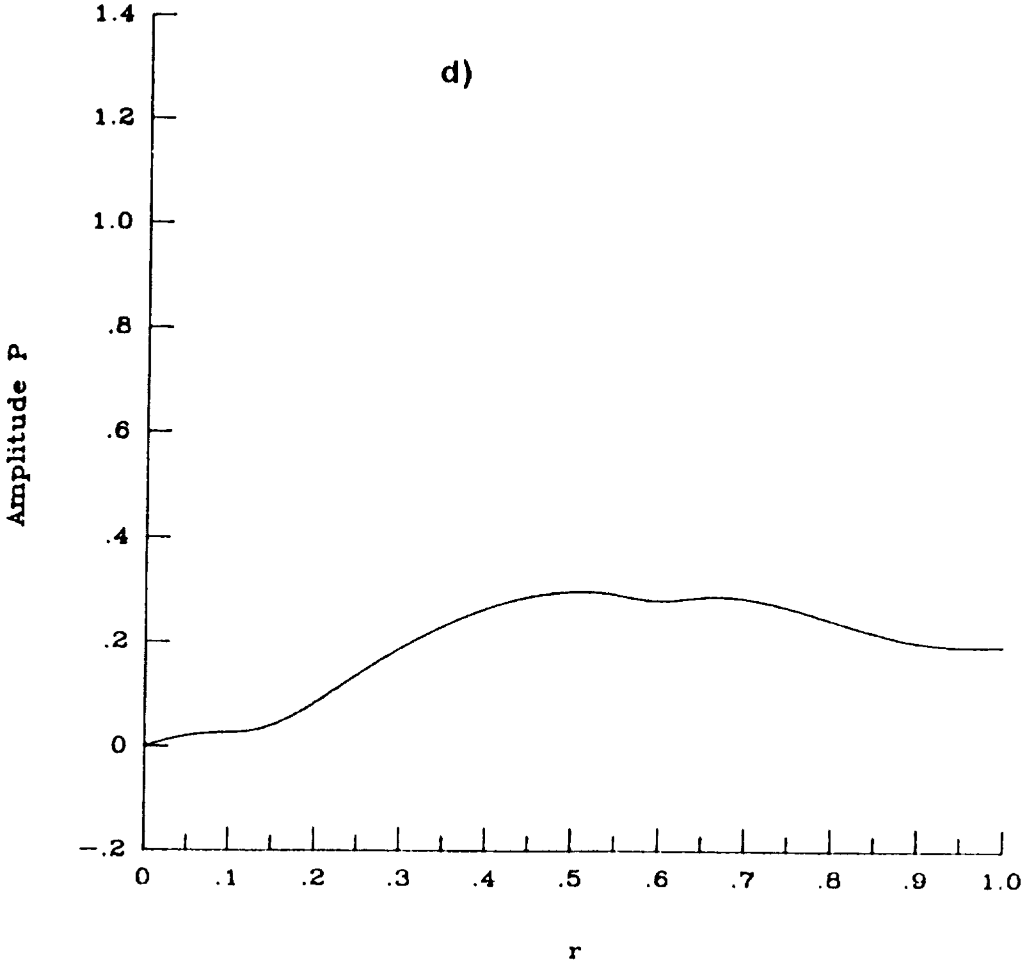

Fig. 5.30d) Concluded.

the same value of n. The behavior of the growth rate at a higher value of q for the n = 1 disturbance is presented in figure 5.31. The primary mode indicates a slight damping effect. Figure 5.32 shows how ω_r of the primary mode varies with the axial wavenumber for q = 0.8. The inviscid nature of the first mode at q = 0.8 and $\alpha = 2.5$ is shown in figure 5.33. The growth rate, ω_i, drops slightly as Re increases. However, calculations at much higher values of Re are needed to determine the asymptotic value of the growth rate, ω_i. The variation of the real part of frequency with Reynolds number is presented in figure 5.34. There is considerable change in the magnitude of ω_r over intermediate values of Re. The behavior of the second mode at this higher value of swirl parameter (q = 0.8) is displayed in figure 5.35. The higher amount of swirl has resulted in higher growth rates as well as increasing the range of axial wavenumber, α, where instability exists. However, the instability still is a long wave one. The real part of frequency of the second mode varies very rapidly with α as shown in figure 5.36. The curve obtained with $\psi = 0$ is identical to figure 5.36 where $\psi \neq 0$. The viscous nature of the second mode is displayed in figure 5.37 for $\alpha = 0.5$ and q = 0.8. Note that as the Reynolds number becomes large the effect of the ψ term is diminished. Also at high Re, the destabilizing effect of viscosity is greatly diminished. Figure 5.38 indicates little influence of Reynolds number on ω_r for the second mode.

The variation of the growth rate with α at q = 0.8 for the n = 2 mode is shown in figure 5.39. This is a long wave instability very much like the n = 1 case presented in figure 5.27. For this mode, no sign of instability at high values of α was observed. The variation of ω_r with α for this mode is presented in figure 5.40. The effect of viscosity on the n = 2 mode at α = 0.5 and q = 0.8 is displayed in figure 5.41. At high Reynolds numbers, the

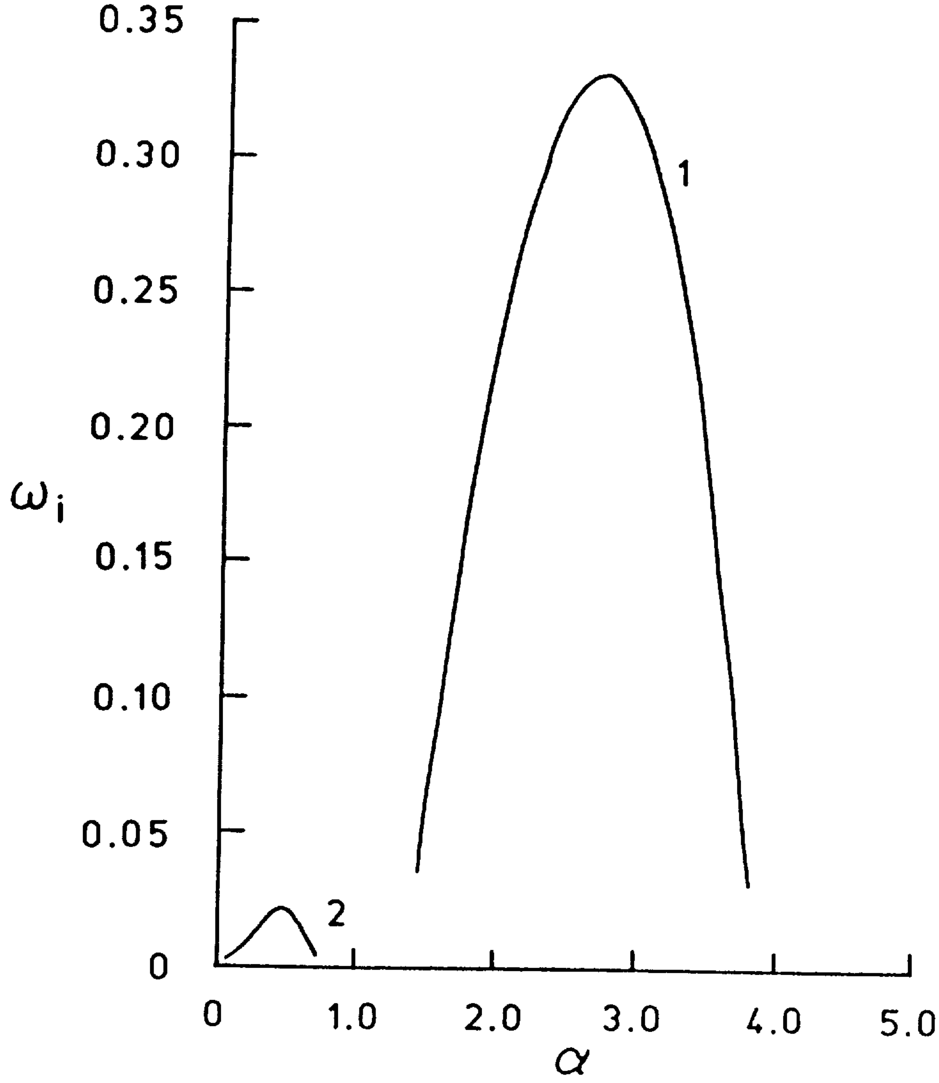

Fig. 5.31 Variation of the growth rate of asymmetric ($n = +1$) disturbances with wavenumber for a two cell vortex. Here, $q = 0.8$, $Re = 10^4$, and $\psi \neq 0$.

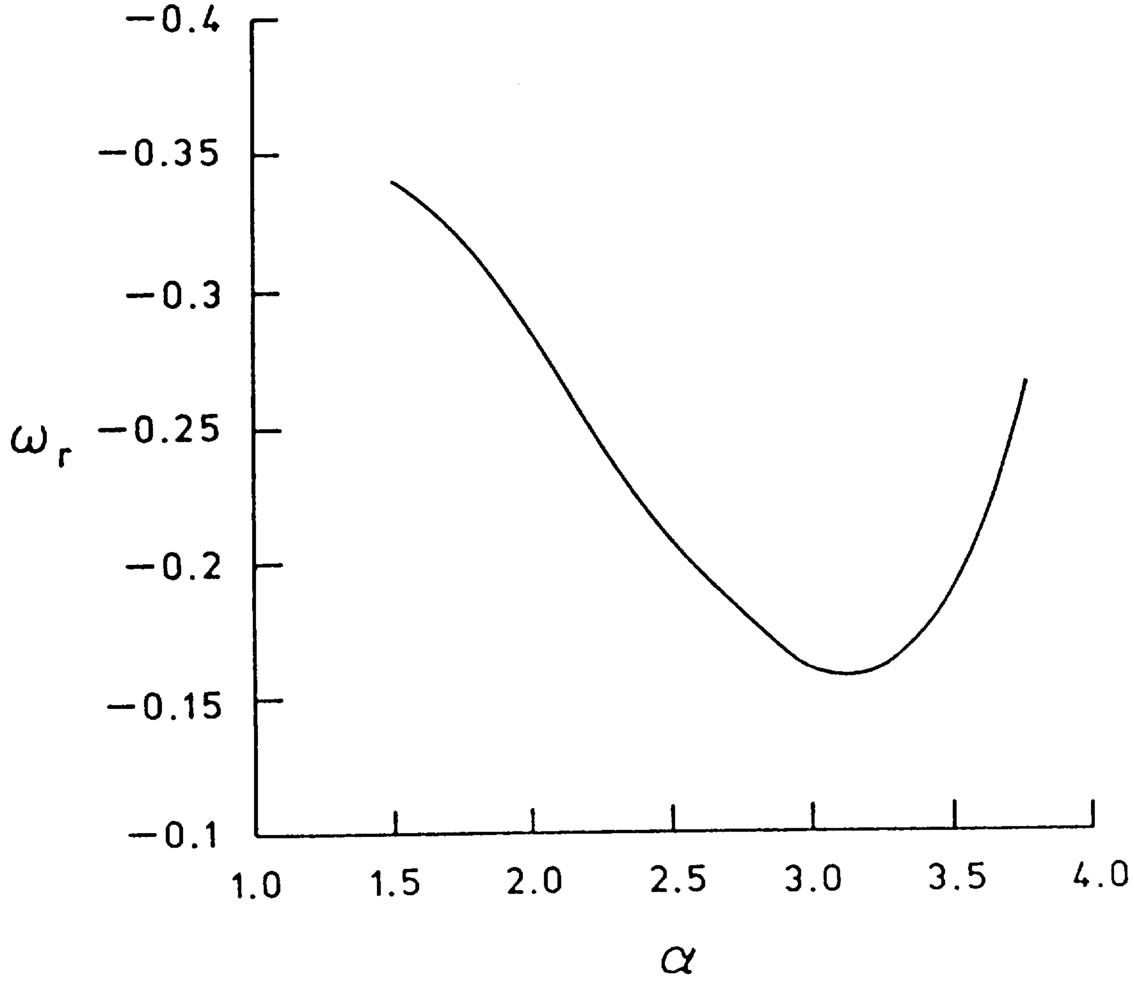

Fig. 5.32 Variation of the real part of frequency of asymmetric ($n = +1$, first mode) disturbances with wavenumber for a two cell vortex. Here, $q = 0.8$, $Re = 10^4$, and $\psi \neq 0$

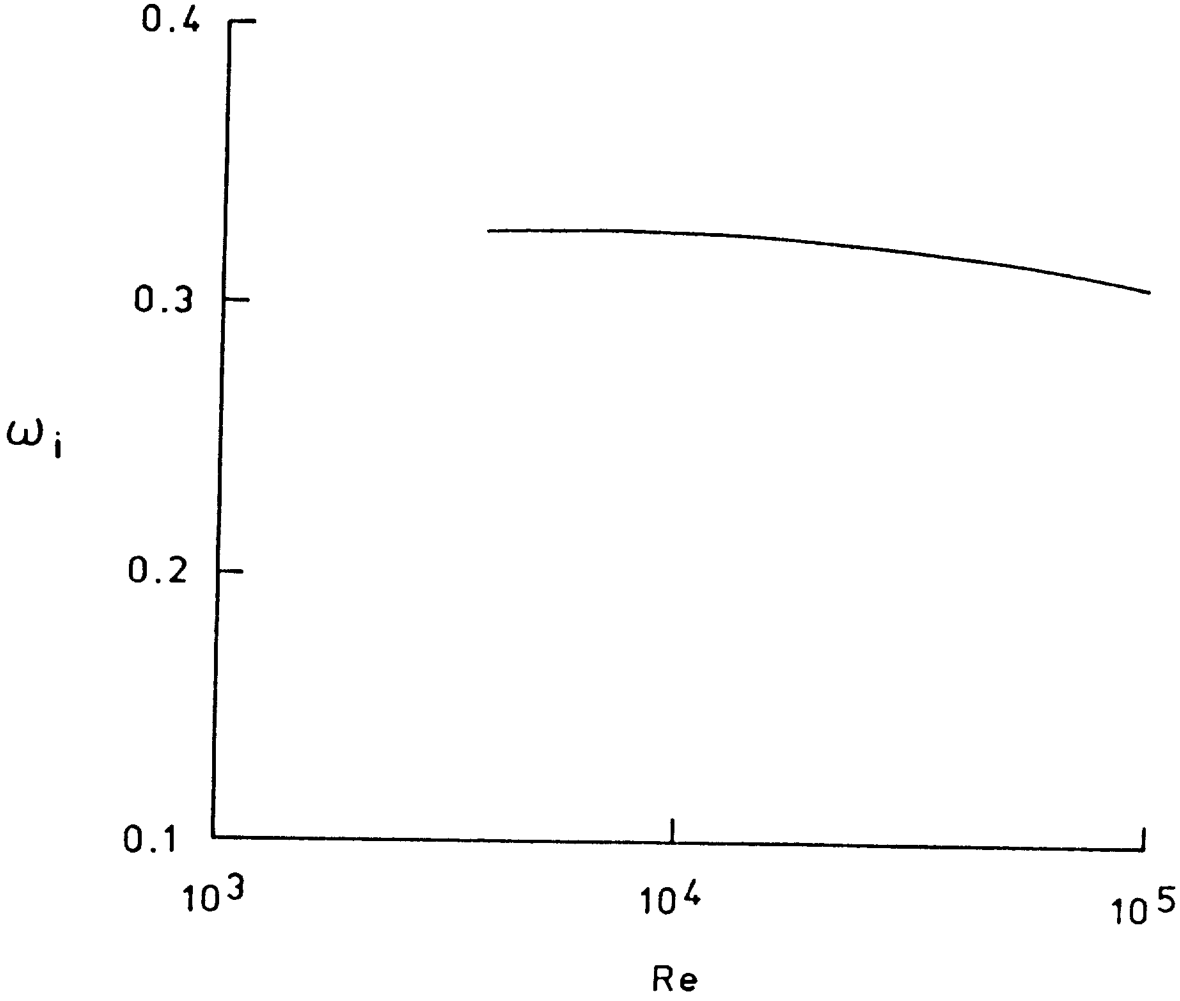

Fig. 5.33 Influence of Reynolds number on the growth rate of asymmetric (n = +1, first mode) disturbances for a two cell vortex. Here, $\alpha = 2.5$, $q = 0.8$ and $\psi \neq 0$.

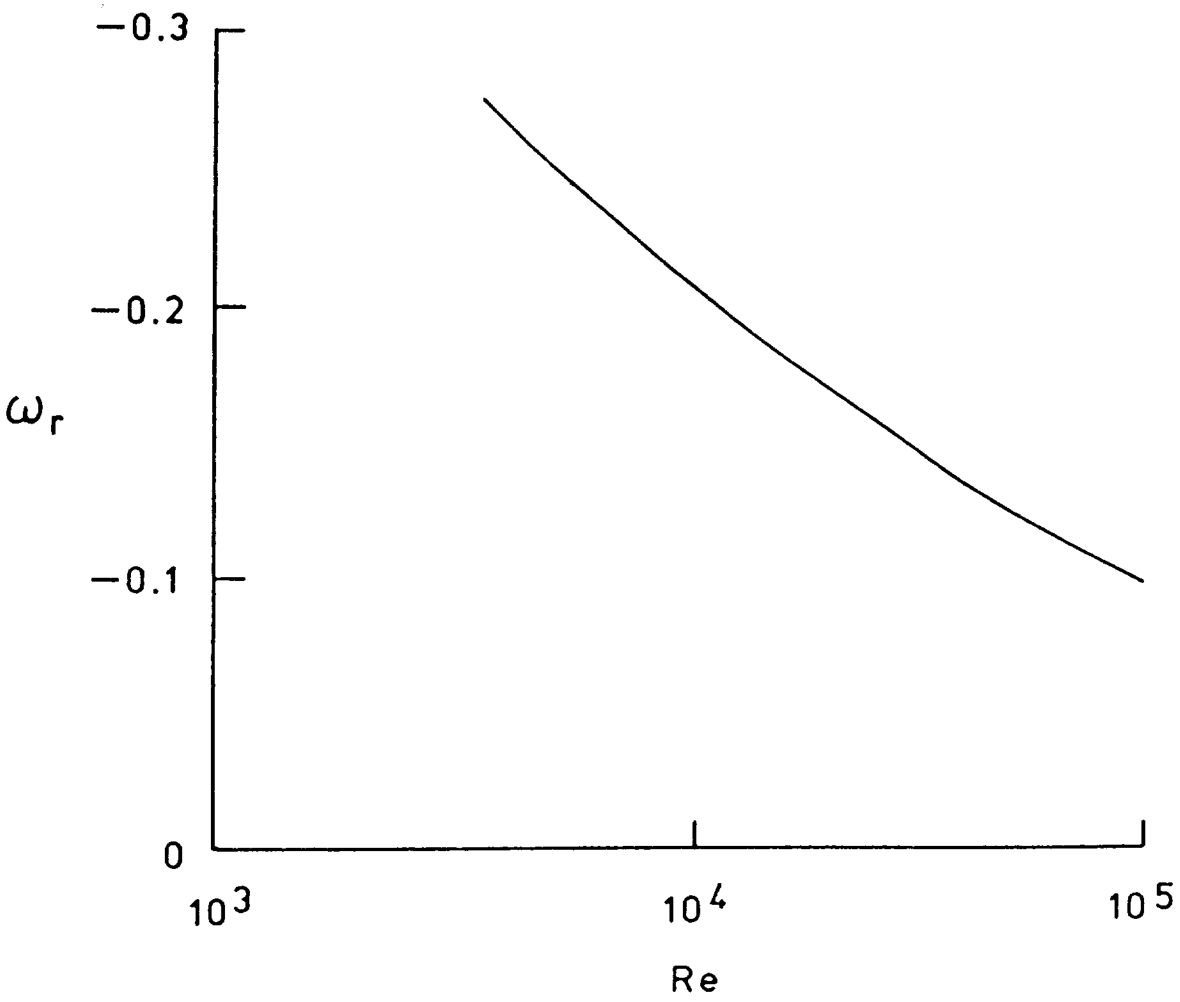

Fig. 5.34 Influence of Reynolds number on the real part of frequency of asymmetric ($n = +1$, first mode) disturbances for a two cell vortex. Here, $\alpha = 2.5$, $q = 0.8$ and $\psi \neq 0$.

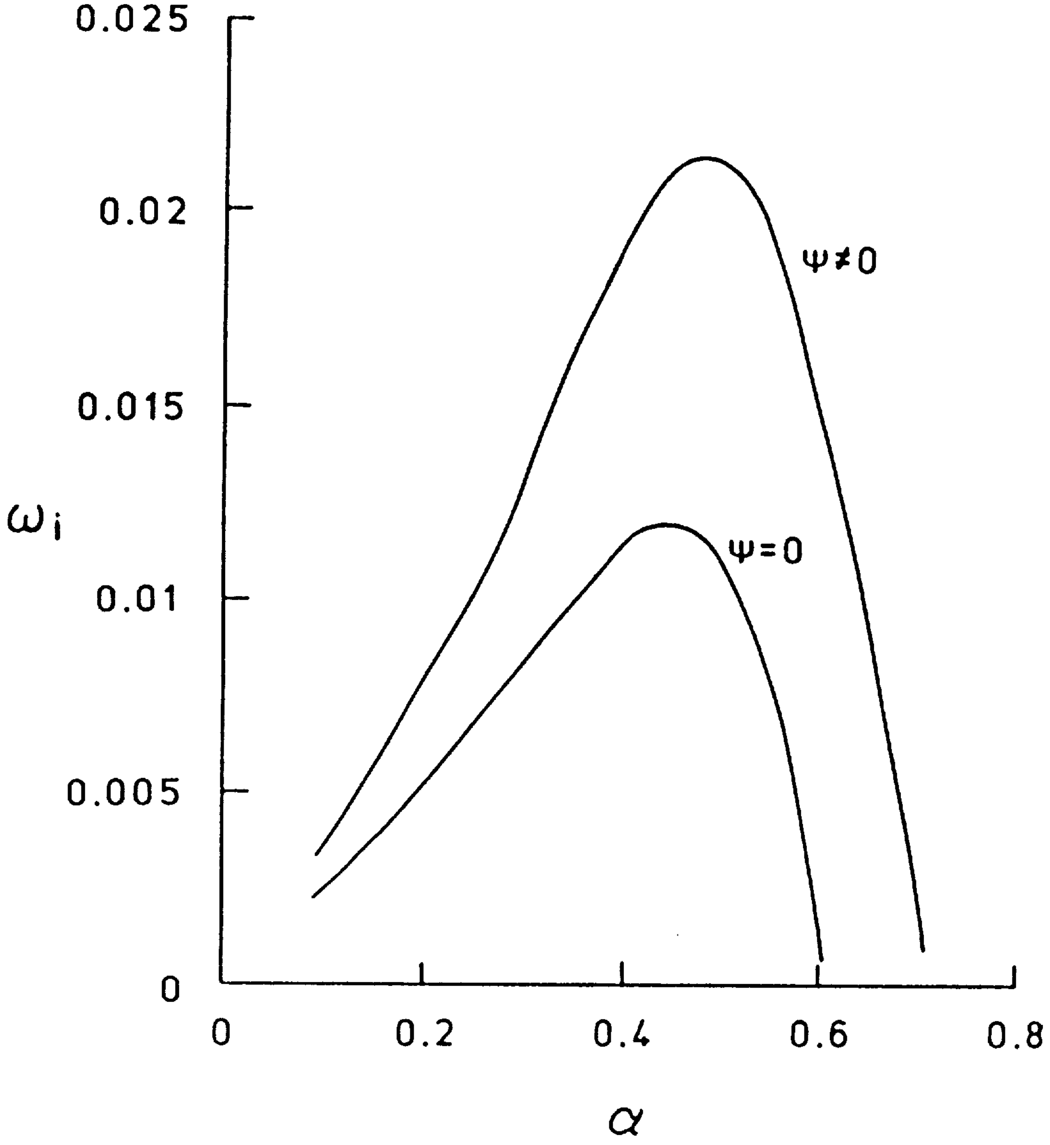

Fig. 5.35 Influence of nonparallel effects on the variation of the growth rate of asymmetric (n = +1, second mode) disturbances with wavenumber for a two cell vortex. Here, q = 0.8, Re = 10^4.

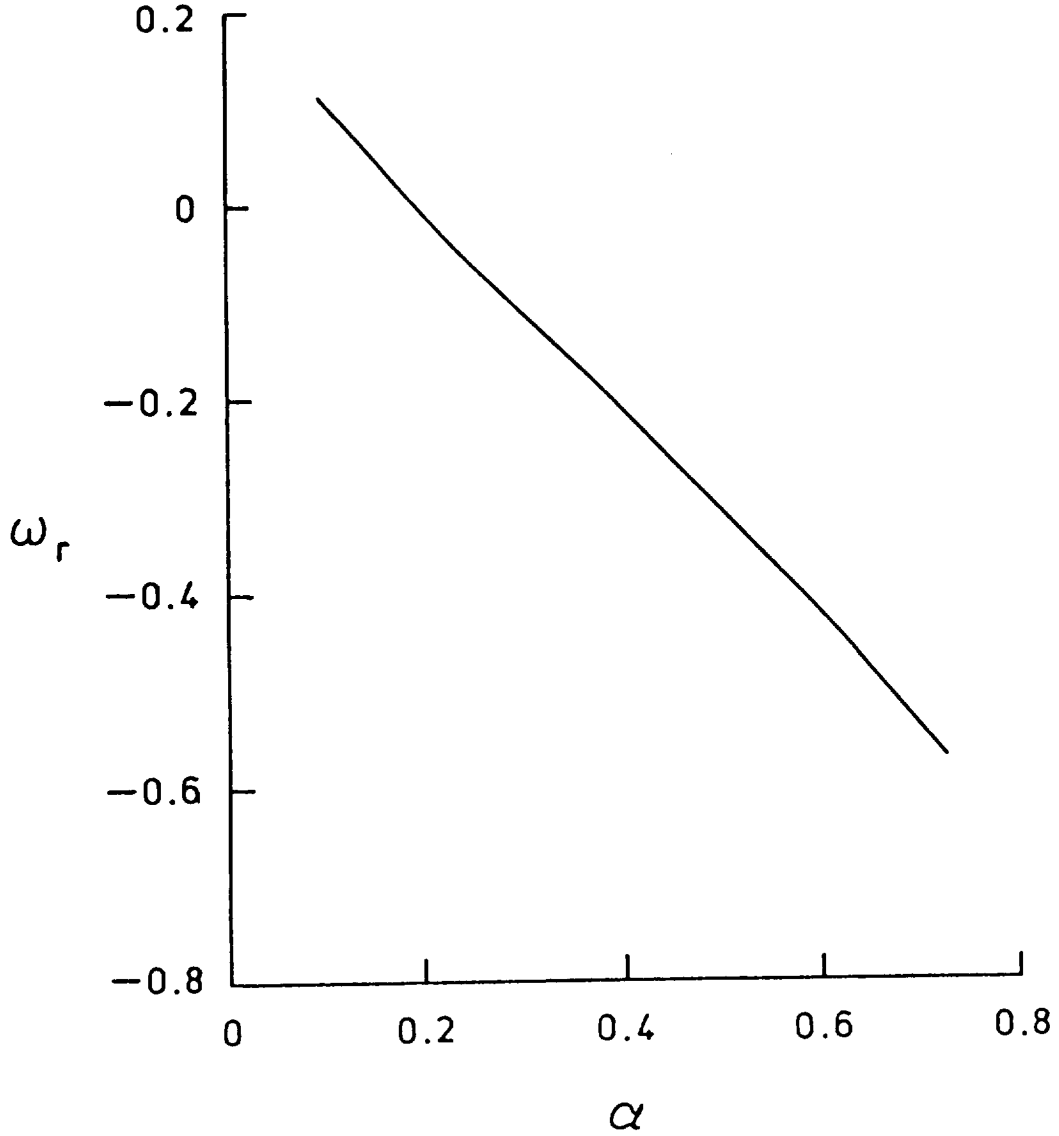

Fig. 5.36 Variation of the real part of frequency of asymmetric (n = +1, second mode) disturbances with wavenumber for a two cell vortex. Here, q = 0.4, Re ≠ 10^4 and $\psi \neq 0$. Identical curve is obtained when $\psi = 0$.

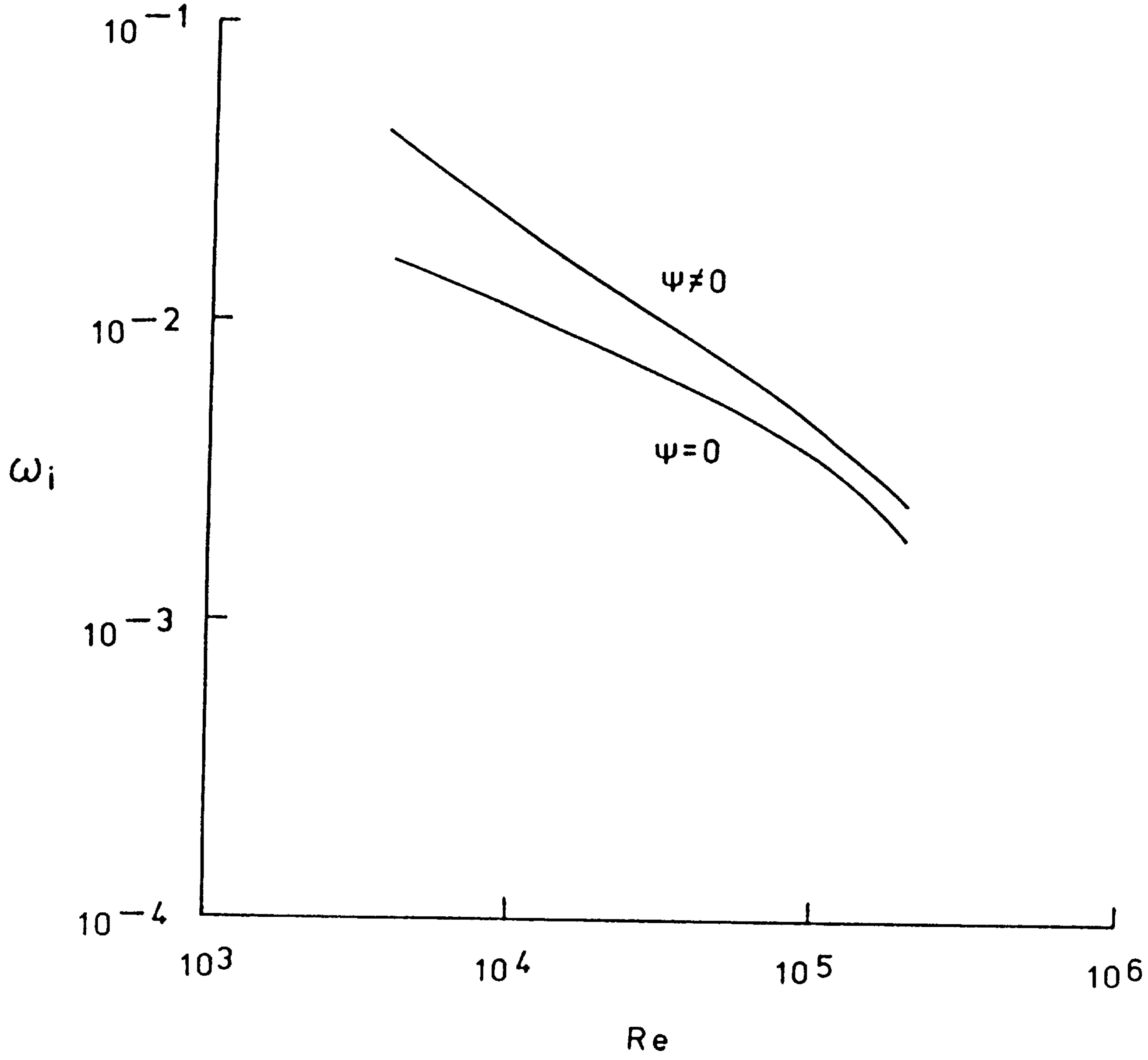

Fig. 5.37 Influence of Reynolds number on the growth rate of asymmetric (n = +1, second mode) disturbances for a two cell vortex. Here, $\alpha = 0.5$, $q = 0.8$.

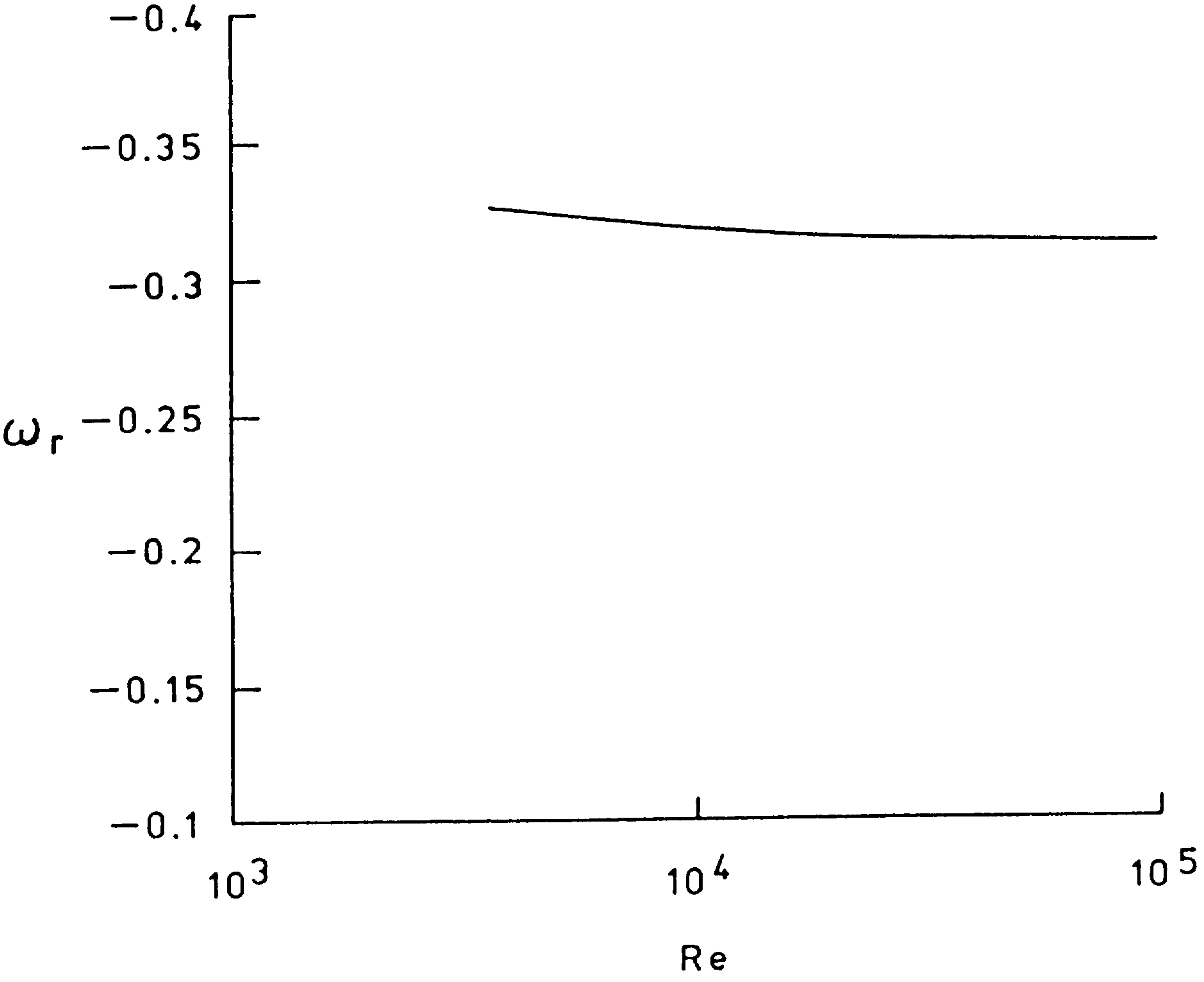

Fig. 5.38 Influence of Reynolds number on the real part of frequency of asymmetric (n = +1, second mode) disturbances for a two cell vortex. Here, $\alpha = 0.5$, $q = 0.8$ and $\psi \neq 0$. Identical curve is obtained when $\psi = 0$.

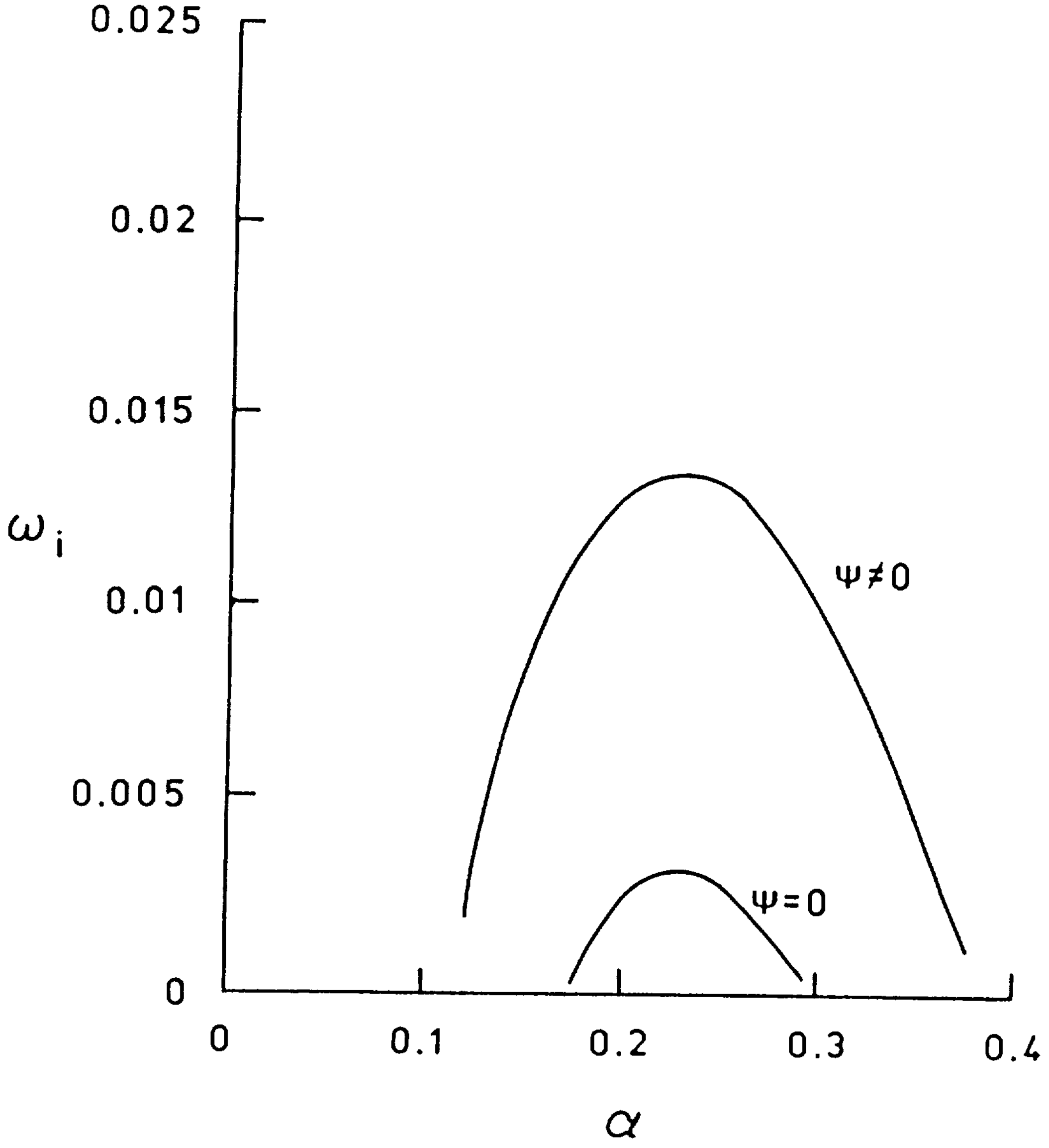

Fig. 5.39 Influence of non-parallel effects on the variation of the growth rate of n = +2 disturbances with wavenumber for a two cell vortex. Here, q = 0.8, Re = 10^4.

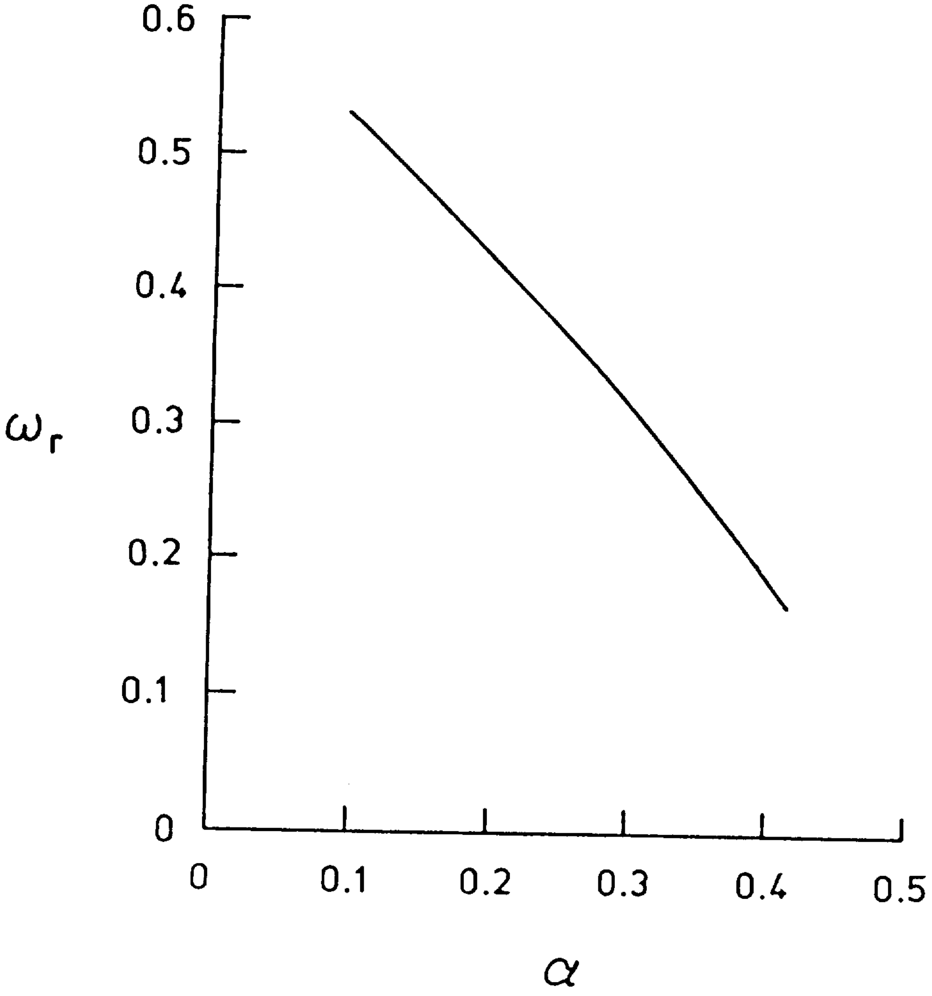

Fig. 5.40 Variation of the real part of frequency of $n = +2$ disturbances with wavenumber for a two cell vortex. Here, $q = 0.8$, $Re = 10^4$ and $\psi \neq 0$. Identical curve is obtained when $\psi = 0$.

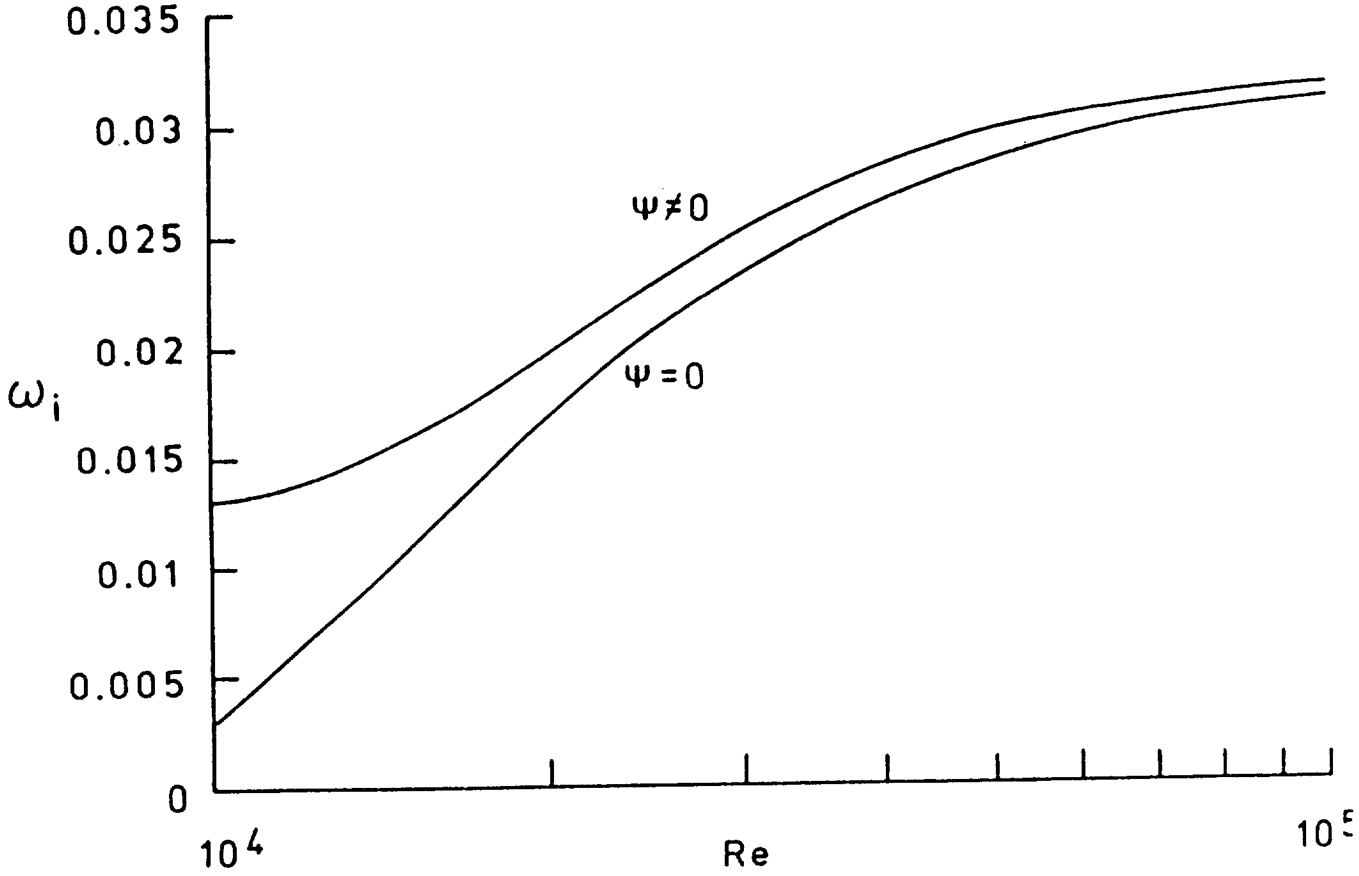

Fig. 5.41 Influence of Reynolds number on the growth rate of $n = +2$ disturbances for a two cell vortex. Here, $\alpha = 0.25$, $q = 0.8$.

contribution from the ϕ term is small. However, the behavior at low Re is uite different. It was found that as the Reynolds number decreases, the urve associated with $\phi \neq 0$ dipped to a minimum value. Even though not shown, urther decreases in the value of Re caused the growth rate, ω_i, to attain arge values, becoming infinite as Re → 0. The effect which was pointed out y Lessen (private communication) is an artifact of the non-parallel mean flow and means that the viscosity is causing the vortex core to spread at an infinite rate. By inspection of figure 5.41, the growth rate is asymptoting to a constant value as Re increases which makes this mode more likely to be an inviscid one. This instability needs further testing. The dependency of ω_r on Reynolds number for the n = 2 mode is displayed in figure 5.42. There is a slight increase in the value of the real part of the frequency as Re increases. The effect of setting $\phi = 0$ on ω_r was negligible and hence is not presented here.

The variation of the growth rate with axial wavenumber at higher values of the swirl parameter (q = 1.2) is shown in figure 5.43. The added rotation has a destabilizing effect especially on the curve associated with $\phi = 0$. The peak growth rate is slightly shifted to higher α with a net increase in the range of axial wavenumber where instabilities are present. Variation of ω_r with α at this q, shown in figure 5.44, indicates a similar trend to that of the q = 0.8 case. However, note that the slope of the present curve is much smaller in comparison to the case displayed in figure 5.40.

The variation of growth rate, ω_i, with α for the n = -1 mode at q = 0.4 is shown in figure 5.45. The complexity of each individual curve shows signs of co-instabilities especially at the low end of the axial wavenumber spectrum. The maximum growth rates are twice as large as the growth rates associated with the trailing line vortex presented in figure 4.4. Also note

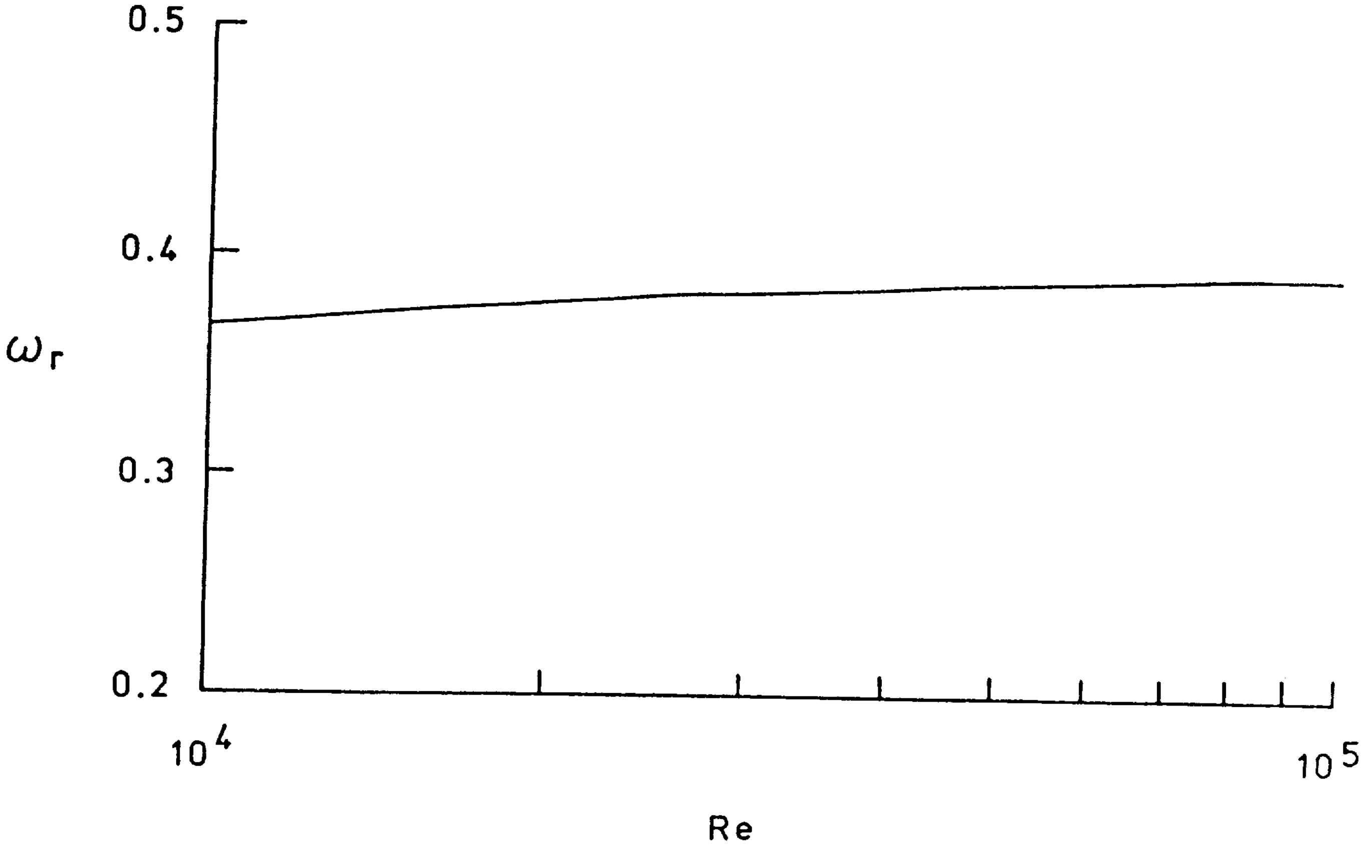

Fig. 5.42 Influence of Reynolds number on the real part of frequency of $n = +2$ disturbances for a two cell vortex. Here, $\alpha = 0.25$, $q = 0.8$ and $\psi \neq 0$. Identical curve is obtained when $\psi = 0$.

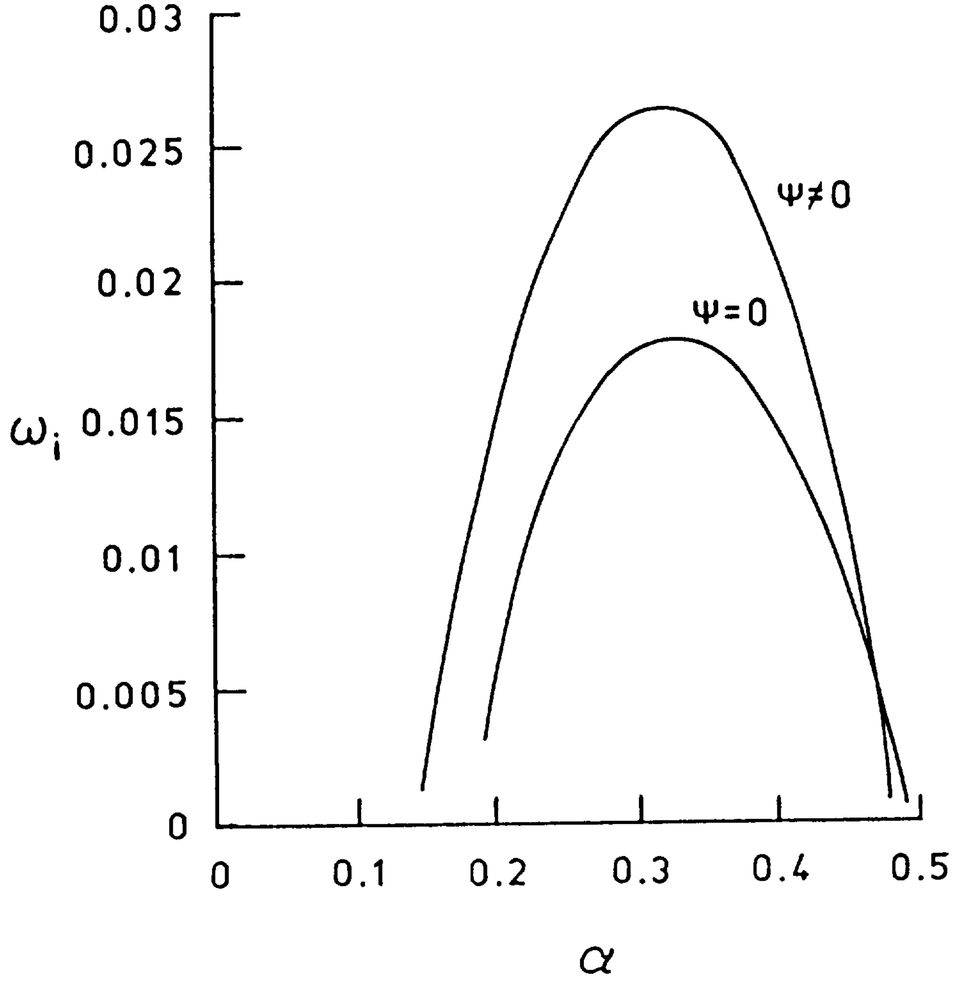

Fig. 5.43 Variation of the growth rate of $n = +2$ disturbances with wavenumber for a two cell vortex. Here, $q = 1.2$, $Re = 10^4$.

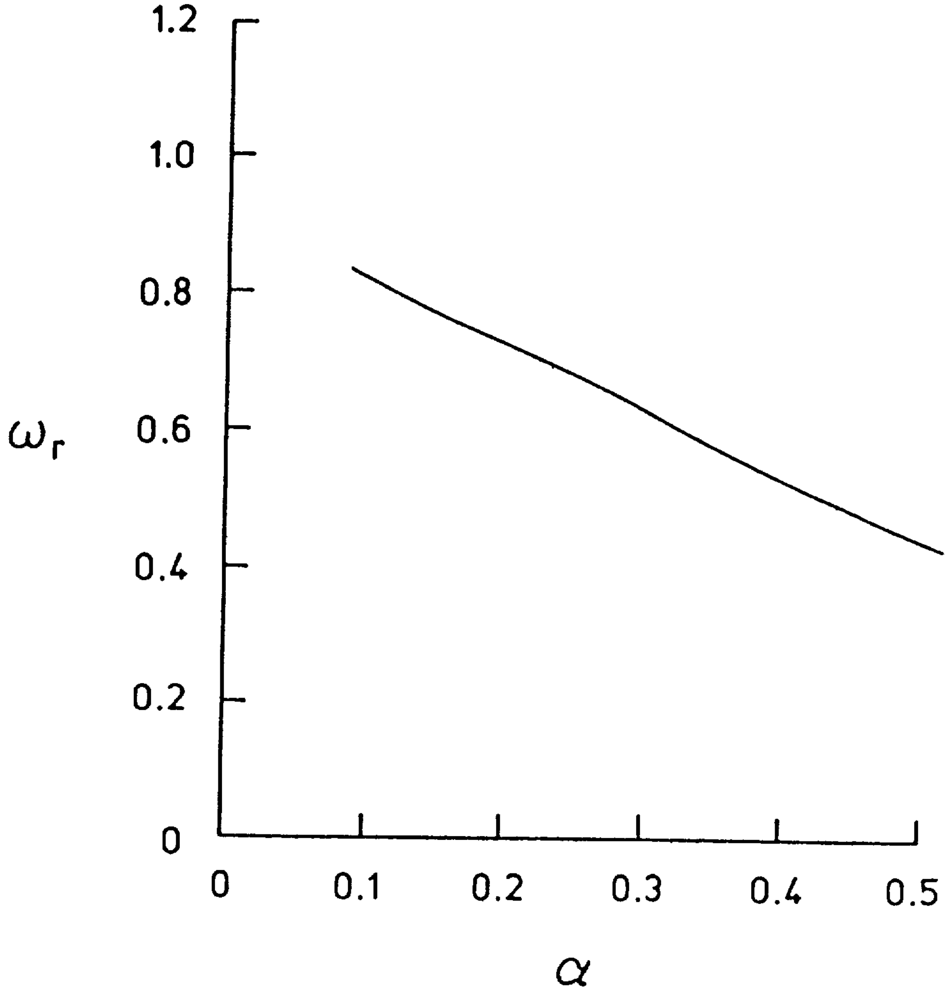

Fig. 5.44 Variation of the real part of frequency of n = +2 disturbances for a two cell vortex. Here, q = 1.2, Re = 10^4, and $\psi \neq 0$. Identical curve is obtained when $\psi = 0$.

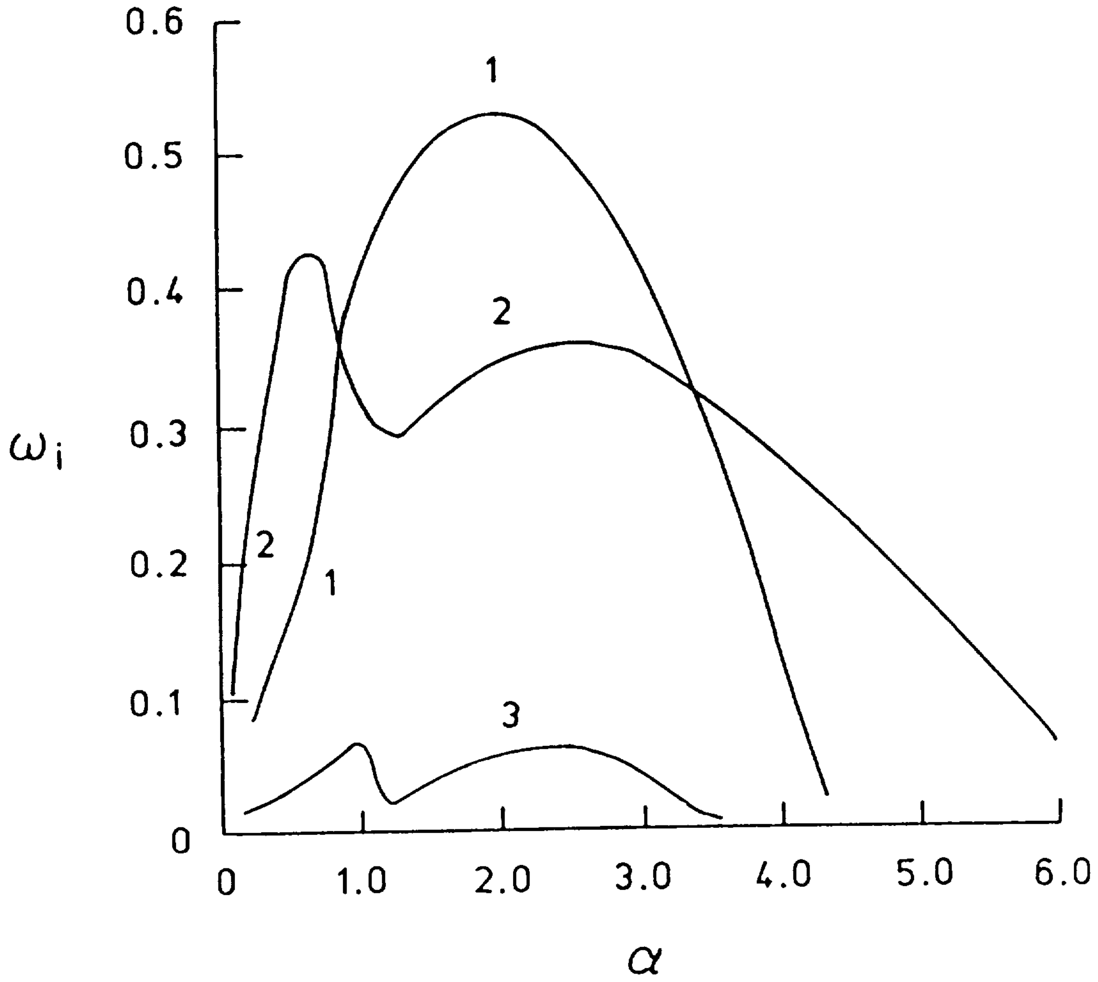

Fig. 5.45 Variation of the growth rate of asymmetric (n = -1) disturbances with wavenumber for a two cell vortex. Here, q = 0.4, Re = 10^4, and $\psi \neq 0$.

the enormously widened ranges of α where instabilities are present. It must be mentioned that higher modes were present in this case but they have been omitted for clarity. However, the most important feature of the present figure is the crossing of the curves associated with the first and second modes. This is the first time that such an effect has been observed. In all of the previous works (including Batchelor's vortex, Long's vortex and rotating Poiseuille pipe flow) each successively higher mode was entirely engulfed by the previous mode (e.g. figure 4.4). In such a flow, as has been pointed out by Maslowe and Stewartson [20], once the value of α exceeds the neutral mode value for the primary mode, the flow becomes stable to all such inviscid disturbances. This is not the situation here and it seems that this is a property of the multiple cell vortices. But the question that remains is why Foster and Duck [23] did not observe such an effect in their inviscid study of a two cell Long's vortex. Of course, it must be emphasized that their calculations were for a vortex in an infinite domain.

Another point to be made here is that the crossings of the instability curves has made numbering of these modes quite arbitrary. Such difficulty has been encountered previously in the case of rotating pipe flows by Cotton and Salwen [18]. In the present section, we have numbered each mode according to their maximum growth rates. The variation of ω_r with axial wavenumber for the first two modes are shown in figure 5.46. It seems that there is a degenerate point occurring near $\alpha \simeq 0.8$. At this particular value of α, the complex frequency for the first mode, ω_1, is approximately equal ω_2. Although figure 5.46 does not indicate that such a state is reached exactly, many such degenerate points were encountered by Cotton and Salwen [18] in their viscous study of rotating Poiseuille pipe flow. The inviscid nature of the $n = -1$ mode at $\alpha = 0.6$ and $q = 0.4$ is presented in figure 5.47. As Re

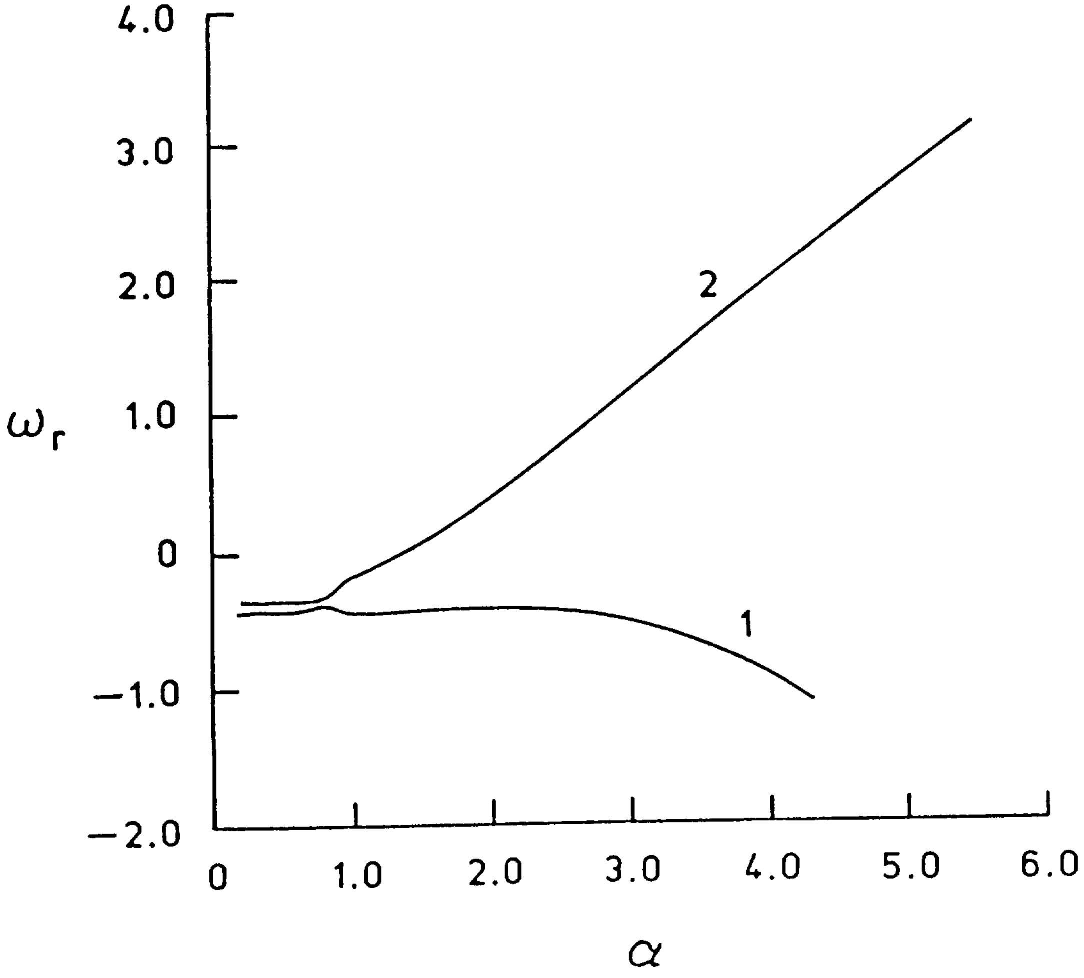

Fig. 5.46 Variation of the real part of frequency of asymmetric (n = -1) disturbances with wavenumber for a two cell vortex. Here, q = 0.4, Re = 10^4, and $\psi \neq 0$.

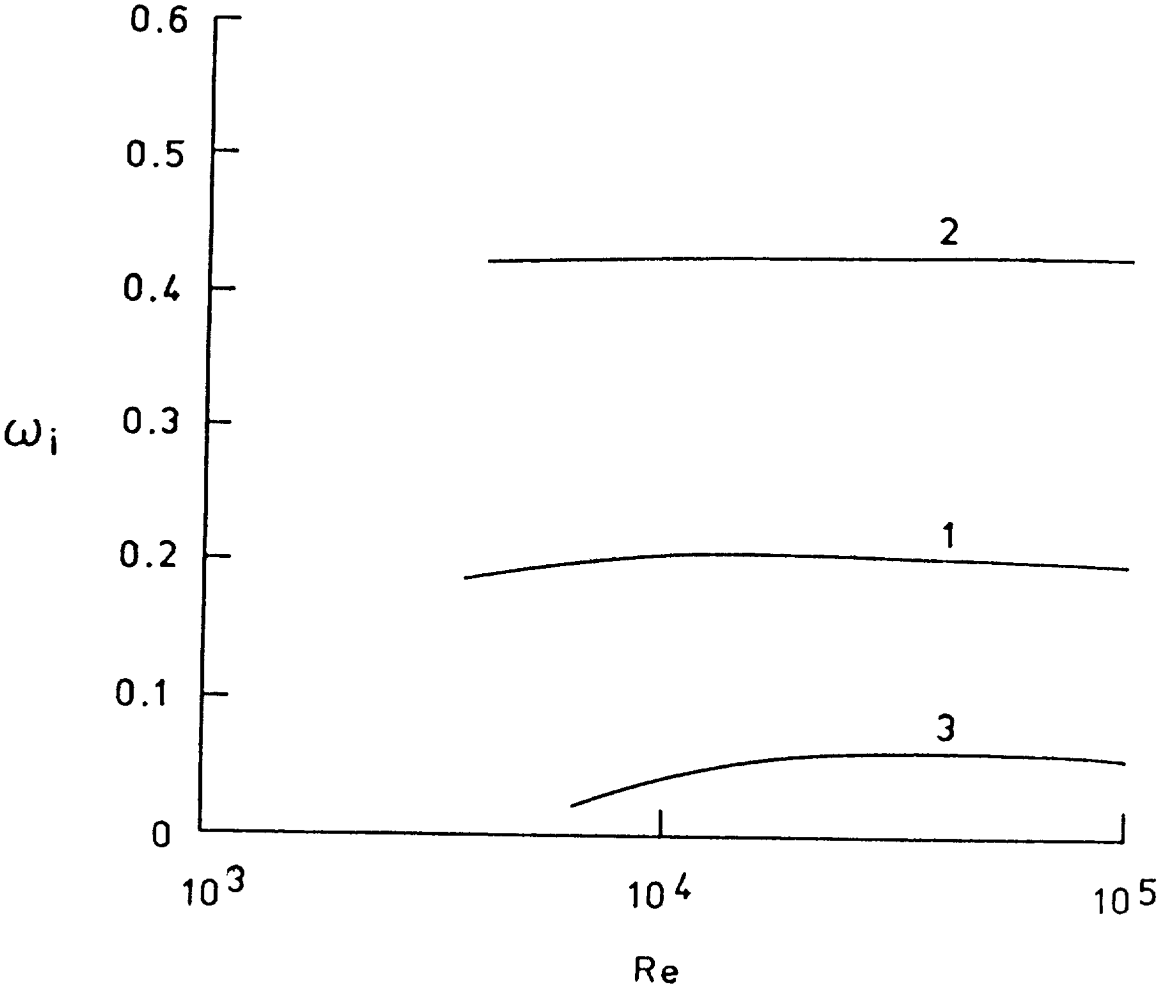

Fig. 5.47 Influence of Reynolds number on the growth rate of asymmetric ($n = -1$) disturbances for a two cell vortex. Here, $\alpha = 0.6$, $q = 0.4$, and $\psi \neq 0$.

increased beyond 10,000, the curves show little variation with the Reynolds number. Figure 5.48 shows a similar trend in the case of the real part of frequency, ω_r. The inviscid behavior of this mode at higher values of α ($\alpha = 2.5$) is shown in figure 5.49. The variation of the growth rate with axial wavenumber for the $n = -1$ mode at $q = 0.8$ is shown in figure 5.50. Again, the evidence of co-instabilities is very clear. The addition of swirl has had a strong destabilizing effect. However, one important feature is the resemblance of the instability curves for $0 < \alpha \lesssim 1.0$ to that of the trailing line vortex shown in figure 4.4.

At this point, it is interesting to look at the nature of the co-instabilities (compound instability modes) associated with the primary mode. This task can be accomplished by moving in axial wavenumber space from high values of α towards the low end of the spectrum while looking at the shape of the eigenfunctions at selected values of α. For the sake of space, we are going to show only the radial component of the eigenfunction since this is the component most frequently dealt with in the open literature. It was found that the nature of radial eigenfunction is typical enough in highlighting the basic mechanism involved in co-instabilities so that we can omit displaying the other components of the disturbance eigenfunctions. Figure 5.51a displays the variation of the radial perturbation with radial distance at $\alpha = 4.0$. Most of the energy of the wave is concentrated at the wall and center part of the flow with the peak occurring at $r \simeq 0.6$. For this axial wavenumber, the disturbance is an $\hat{\mathbf{R}}\,\hat{\mathbf{W}}$ type. At $\alpha = 3.0$, as shown in figure 5.51b, a small peak in the eigenfunction has appeared at $r = 0$. However, most of the energy remains in the outer part of the flow and still the perturbation can be considered an $\hat{\mathbf{R}}\,\hat{\mathbf{W}}$ type. But the situation is quite different at $\alpha = 2.6$ which is shown in figure 5.51c. Here, the center mode has become the dominant mode

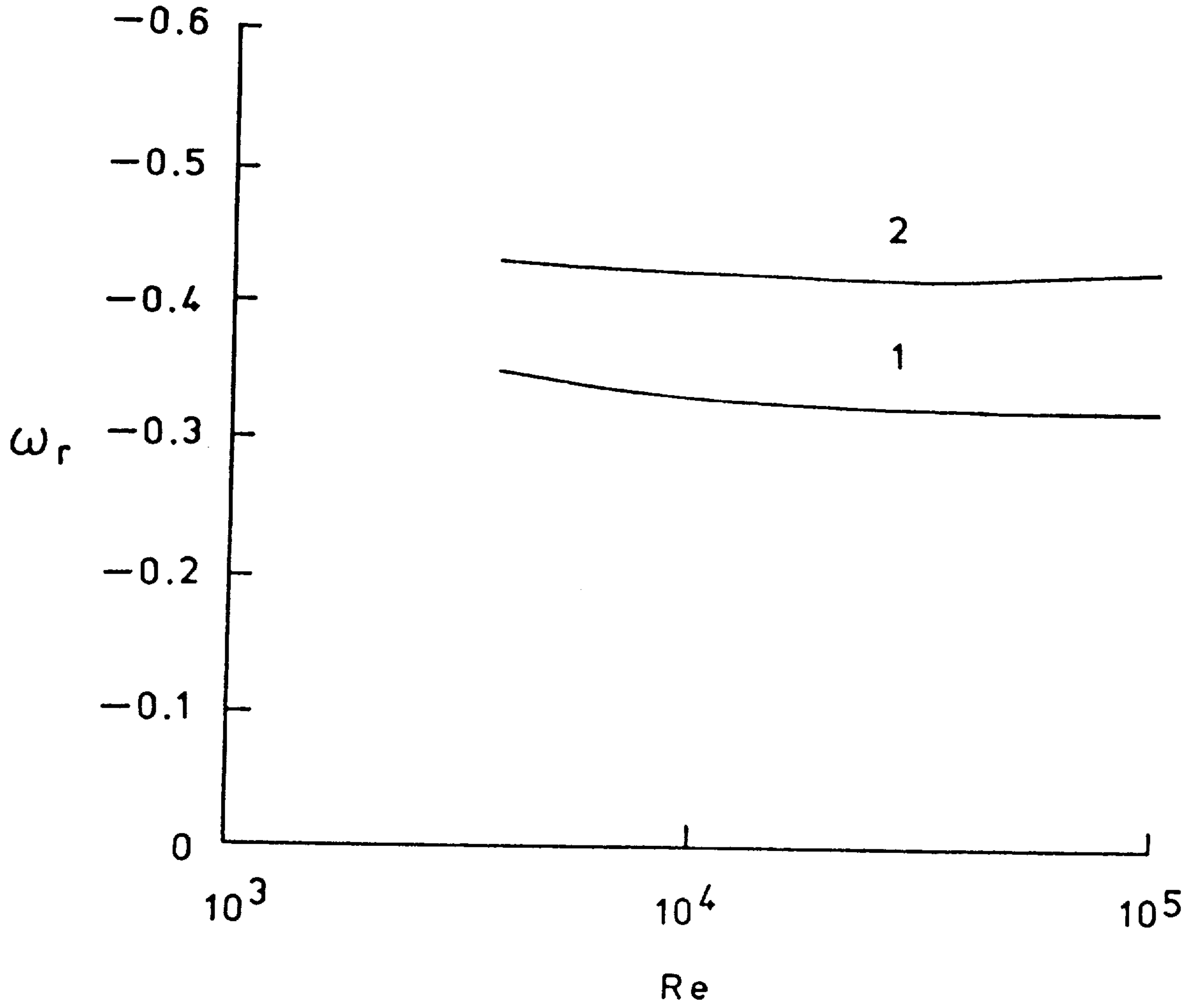

Fig. 5.48 Influence of Reynolds number on the real part of frequency of asymmetric (n = -1) disturbances for a two cell vortex. Here, $\alpha = 0.6$, $q = 0.4$, and $\psi \neq 0$.

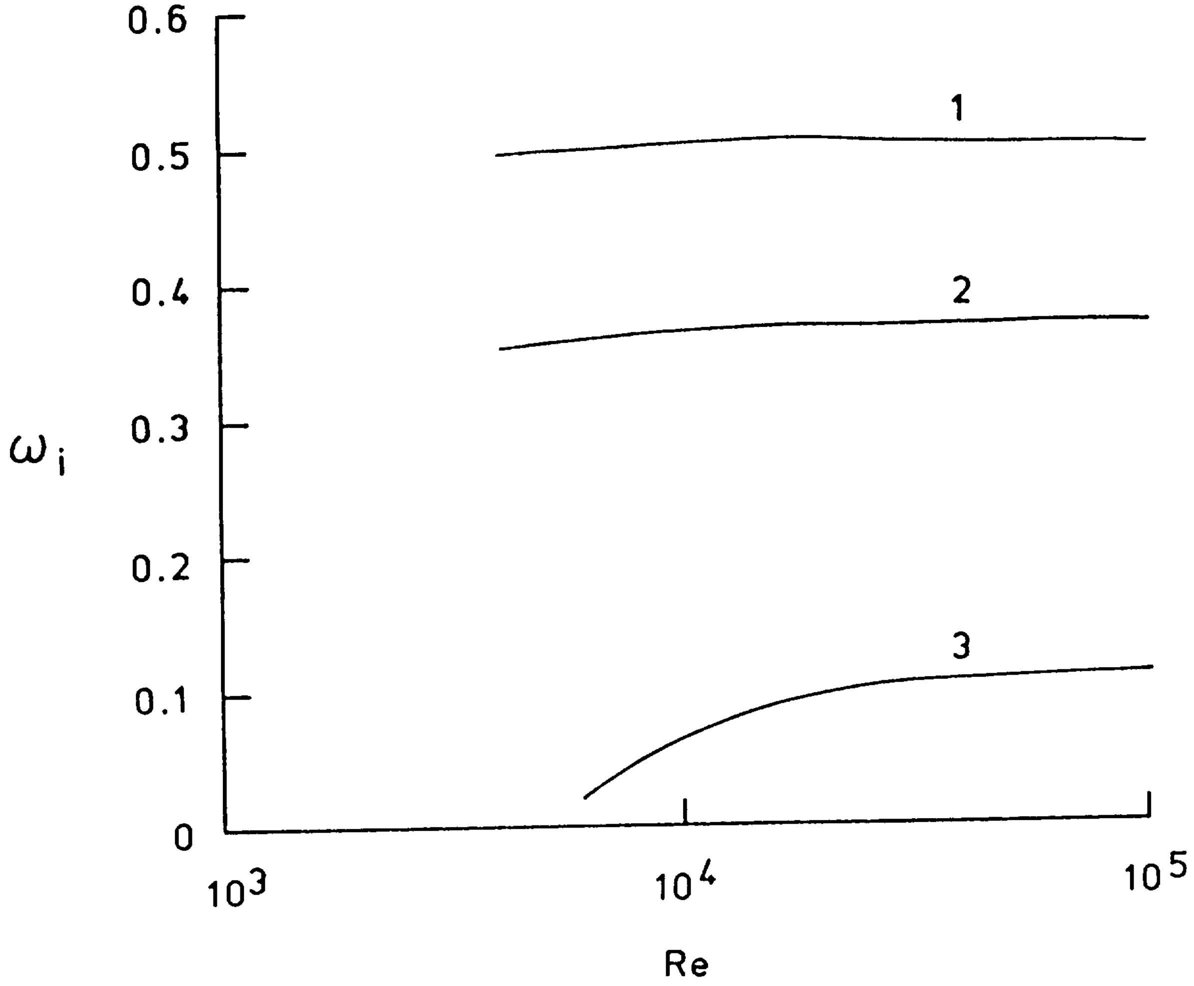

Fig. 5.49 Influence of Reynolds number on the growth rate of asymmetric ($n = -1$) disturbances for a two cell vortex. Here, $\alpha = 2.5$, $q = 0.4$, and $\psi \neq 0$.

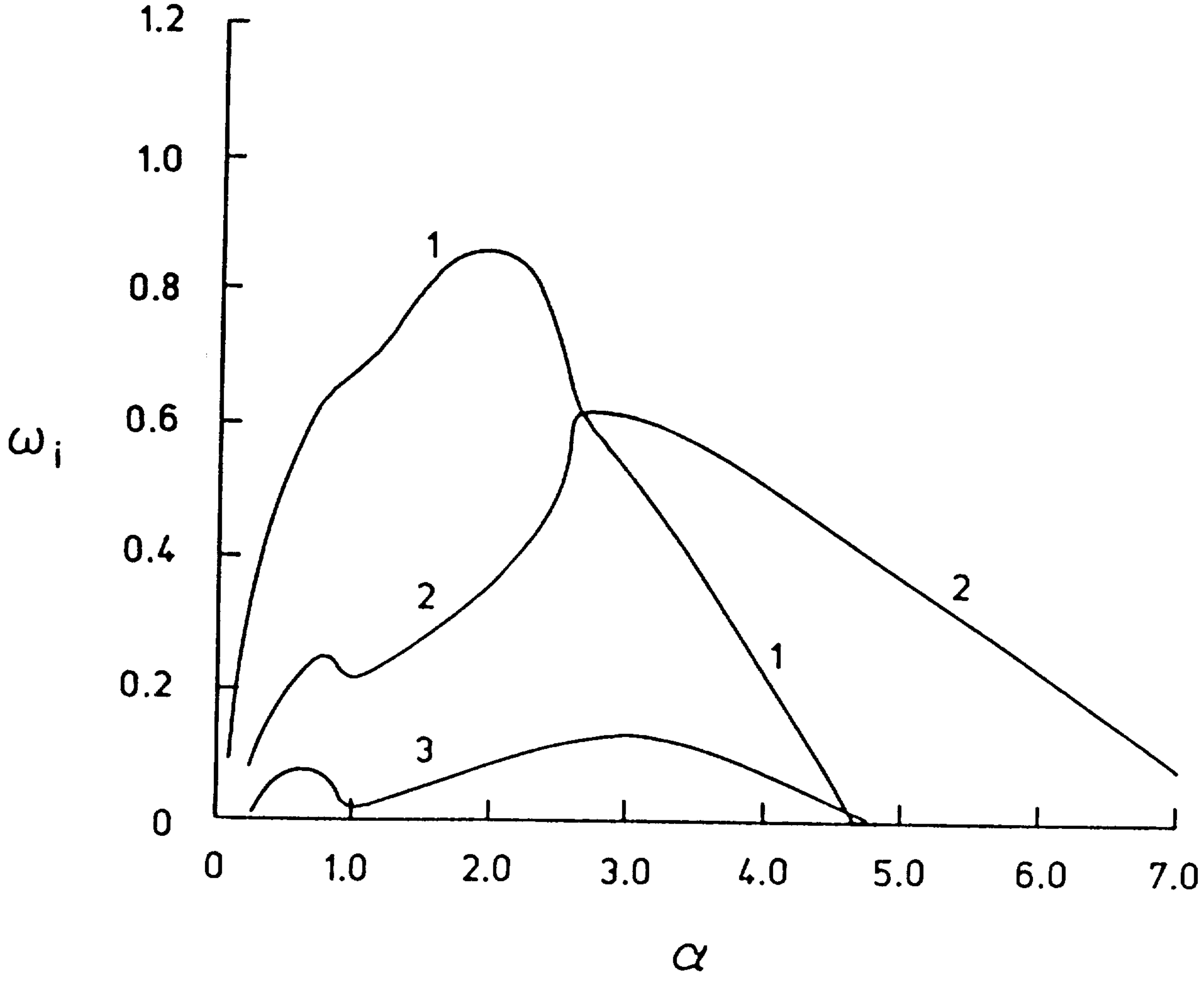

Fig. 5.50 Variation of the growth rate of asymmetric ($n = -1$) disturbances with wavenumber for a two cell vortex. Here, $q = 0.8$, $Re = 10^4$, and $\psi \neq 0$

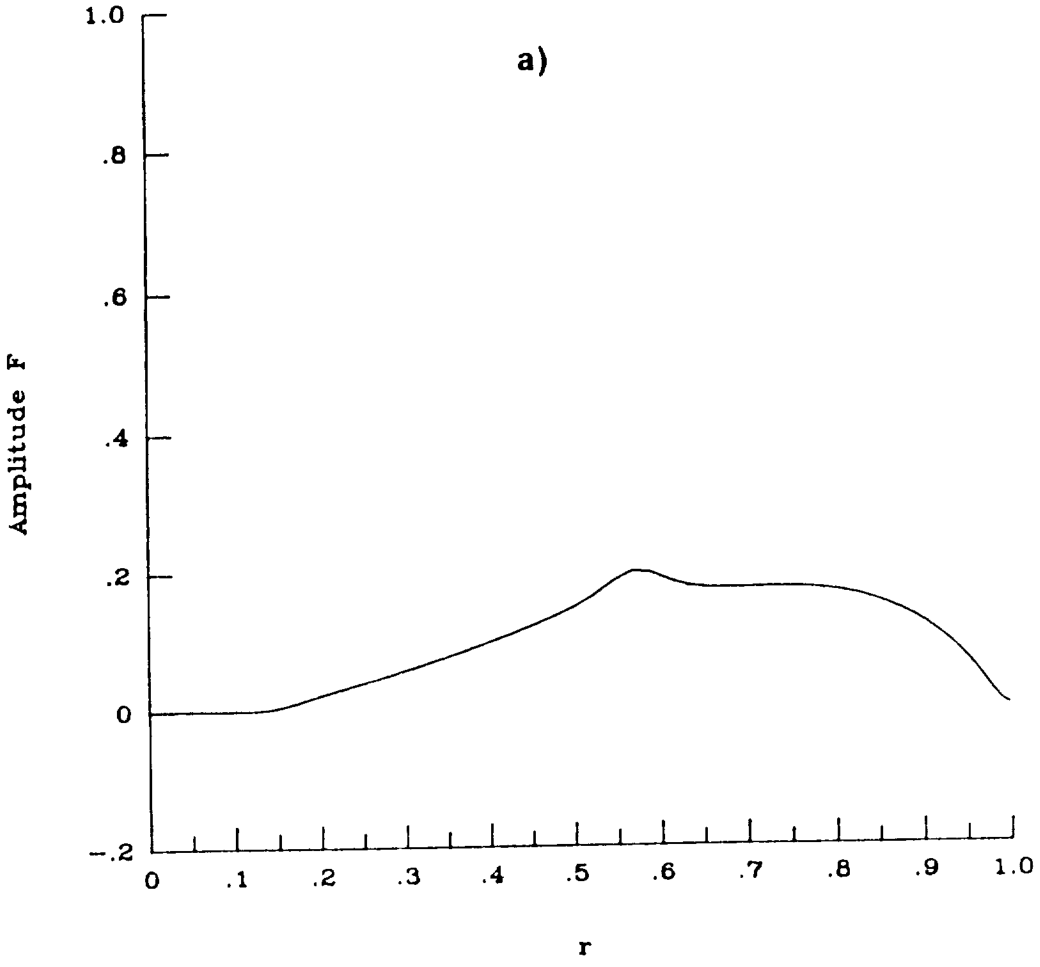

Fig. 5.51 Amplitude of radial eigenfunction component of an asymmetric ($n = -1$, first mode) perturbation for a two cell vortex. a) $\alpha = 4.0$, b) $\alpha = 3.0$, c) $\alpha = 2.6$, d) $\alpha = 2.0$, e) $\alpha = 1.1$, f) $\alpha = 0.4$. Here, $q = 0.8$, $Re = 10^4$, and $\psi \neq 0$.

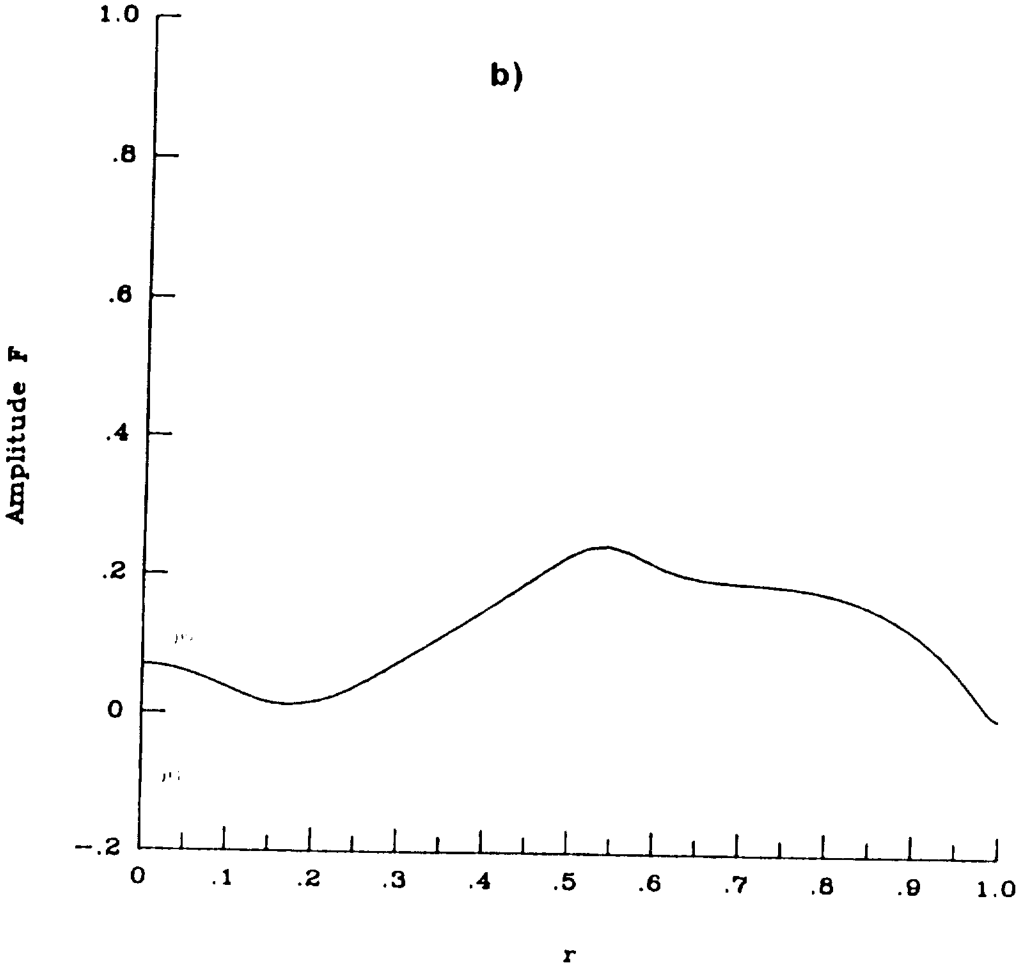

Fig. 5.51b) Continued.

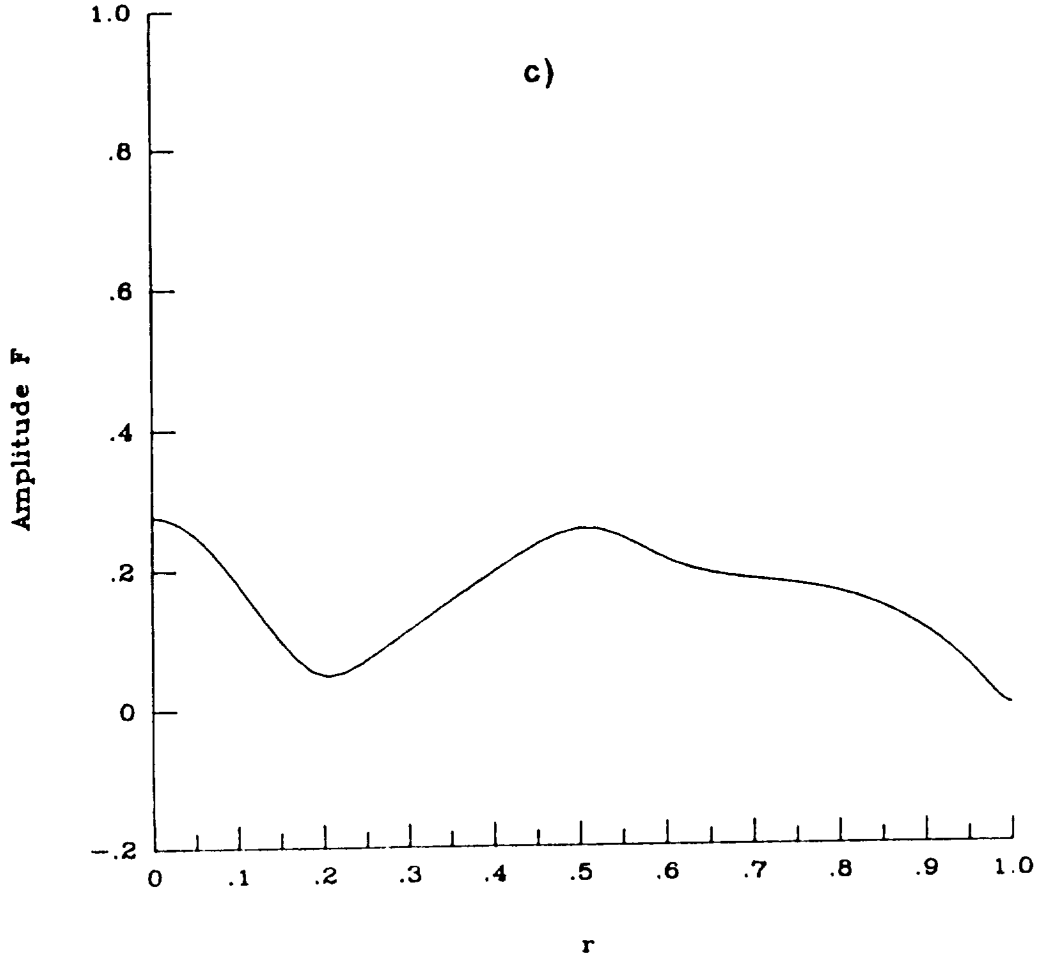

Fig. 5.51c) Continued.

although most of the energy now is distributed over the entire pipe radius. This disturbance is clearly a $\hat{\mathbf{C}}\,\hat{\mathbf{R}}\,\hat{\mathbf{W}}$ type. At $\alpha = 2.0$ (shown in figure 5.51d), the peaks associated with $\hat{\mathbf{R}}$ and $\hat{\mathbf{W}}$ have subsided and $\hat{\mathbf{C}}$ has become the only significant instability zone. The variation of the eigenfunction with radial distance for $\alpha = 1.1$ is presented in figure 5.51e. At this axial wavenumber, the two peaks in the outer flow part have almost entirely disappeared. At $\alpha = 0.4$ (presented in figure 5.51f), the $\hat{\mathbf{C}}$ type instability is the sole mode present with no sign of $\hat{\mathbf{R}}$ or $\hat{\mathbf{W}}$ type modes. For this value of α, the radial eigenfunction approximates the shape of the radial component of the $n = 1$, long wave instability (figure 4.27a) of a Batchelor vortex.

The variation of growth rate, ω_i, with axial wavenumber, α, at $q = 0.8$ for the $n = -2$ mode is shown in figure 5.52. There are signs of co-instabilities for each curve. For this disturbance, the range of α where instabilities are present, has doubled. But notice the huge growth rates of the primary mode. The maximum value of ω_i for the first mode indicates that the disturbance has very short e-folding time. Variation of the real part of frequency with α for the first two modes is shown in figure 5.53. As $\alpha \rightarrow 0$ the problem of mode jumping is very much apparent from figures 5.52 and 5.53. The behavior of $n = -2$ perturbations with Reynolds number at $q = 0.8$ and $\alpha = 1.0$ is shown in figure 5.54. The growth rate is independent of Re for Reynolds numbers as low as 4000.

It must be clear by now that the behavior of most disturbances are generally different at low values of α than those associated with high axial wavenumbers. It seems that almost all instability modes termed as viscous modes are only present in the form of long wave instabilities; while evidently the inviscid modes are only manifested in the form of intermediate or short wave instabilities.

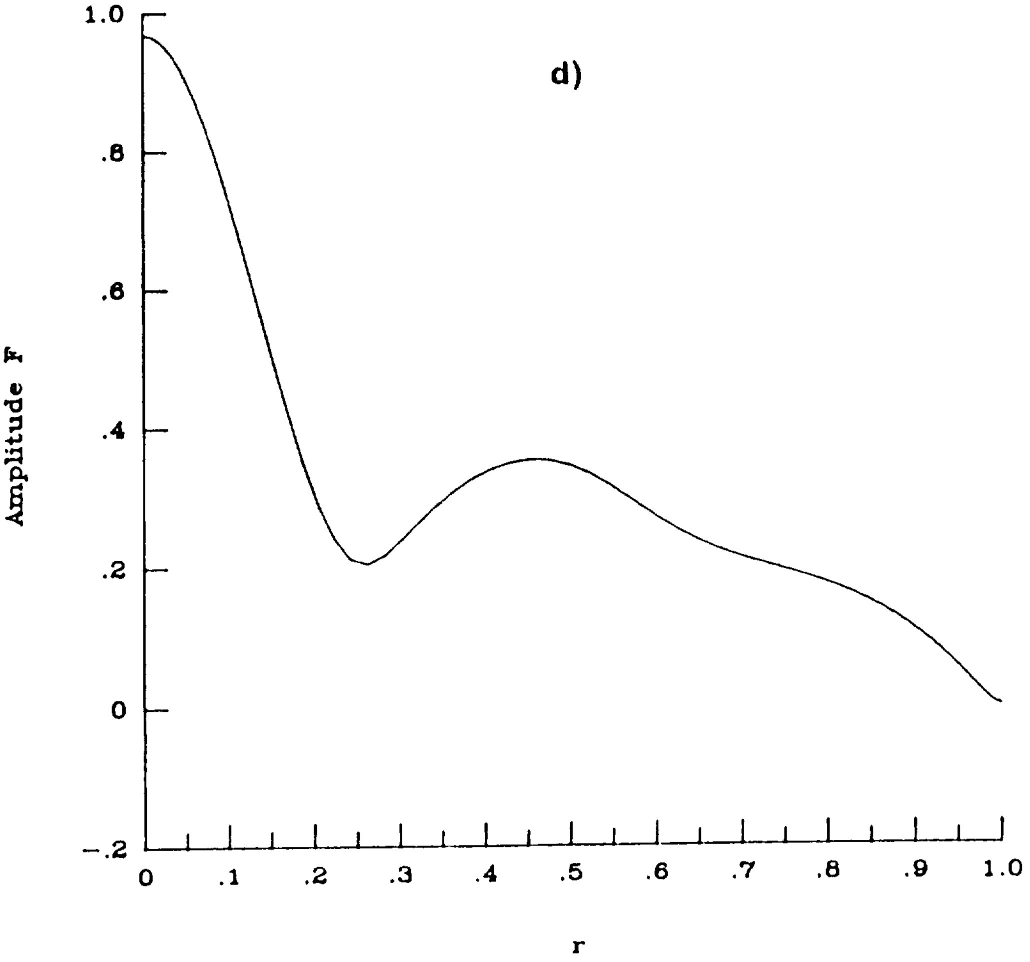

Fig. 5.51d) Continued.

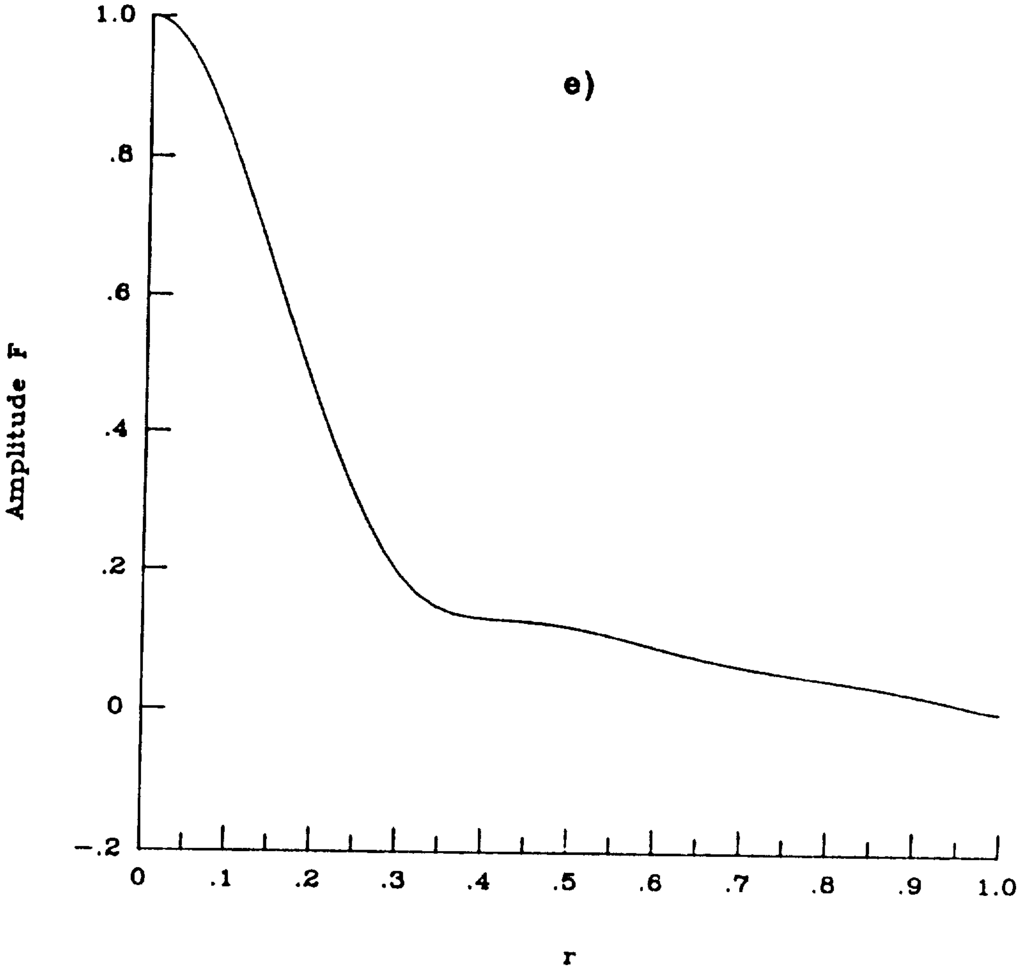

Fig. 5.51e) Continued.

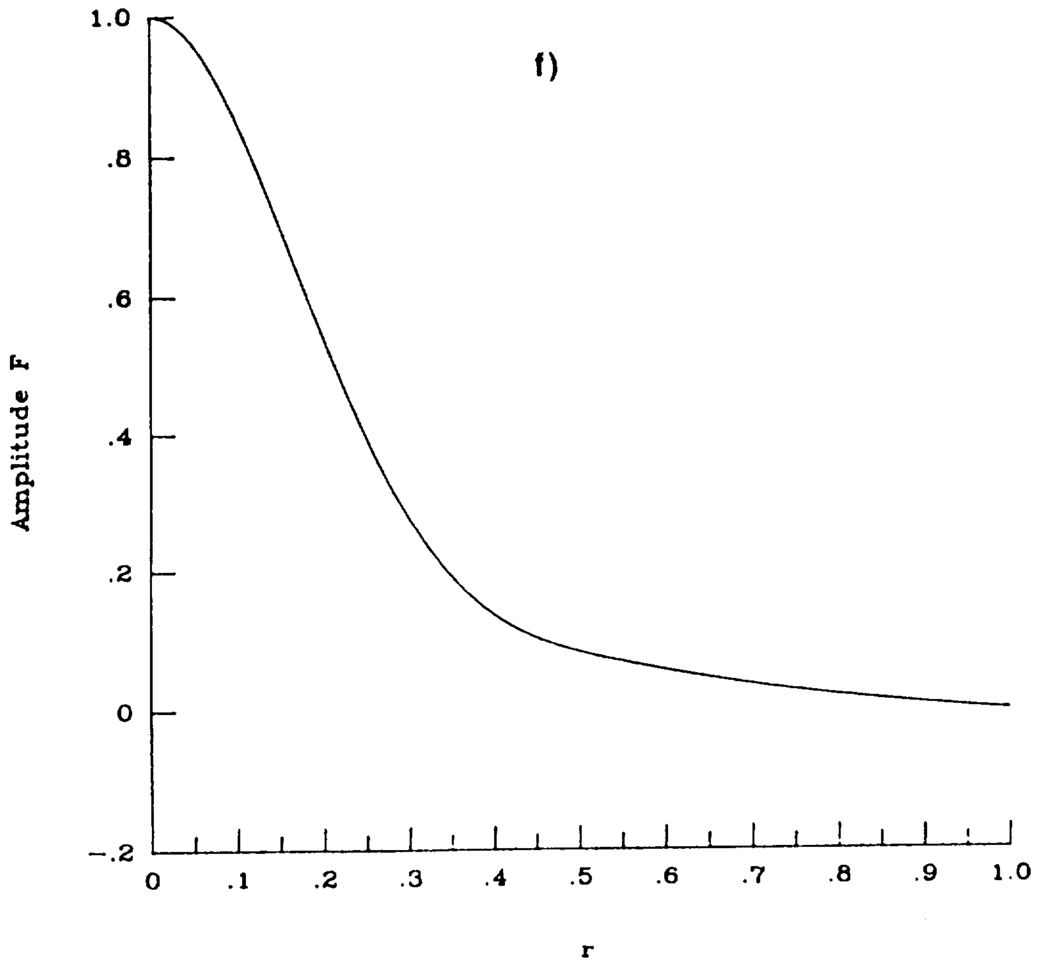

Fig. 5.51f) Concluded.

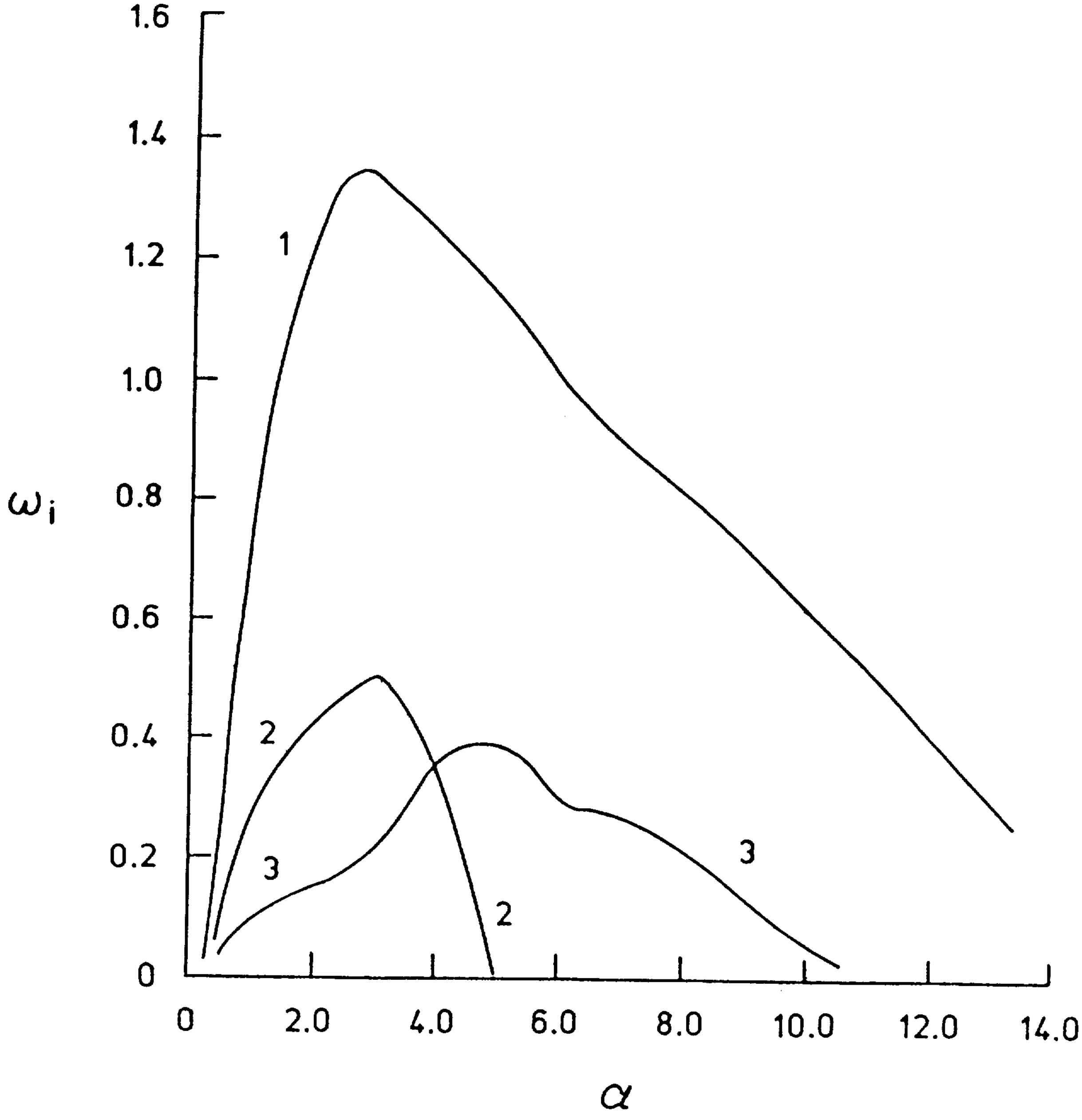

Fig. 5.52 Variation of the growth rate of $n = -2$ disturbances with wavenumber for a two cell vortex. Here, $q = 0.8$, $Re = 10^4$, and $\psi \neq 0$.

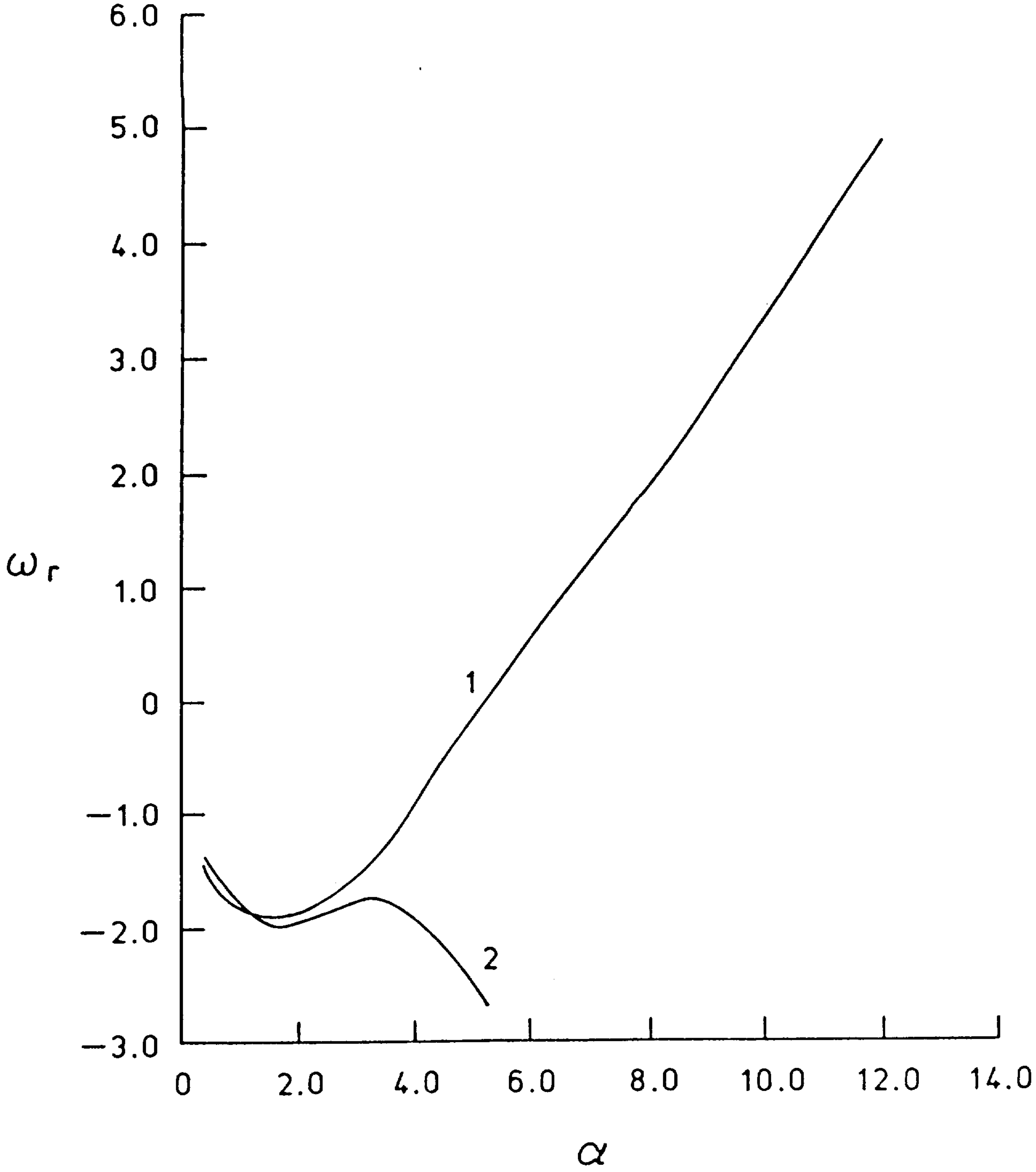

Fig. 5.53 Variation of the real part of frequency of $n = -2$ disturbances with wavenumber for a two cell vortex. Here, $q = 0.8$, $Re = 10^4$, and $\psi \neq 0$.

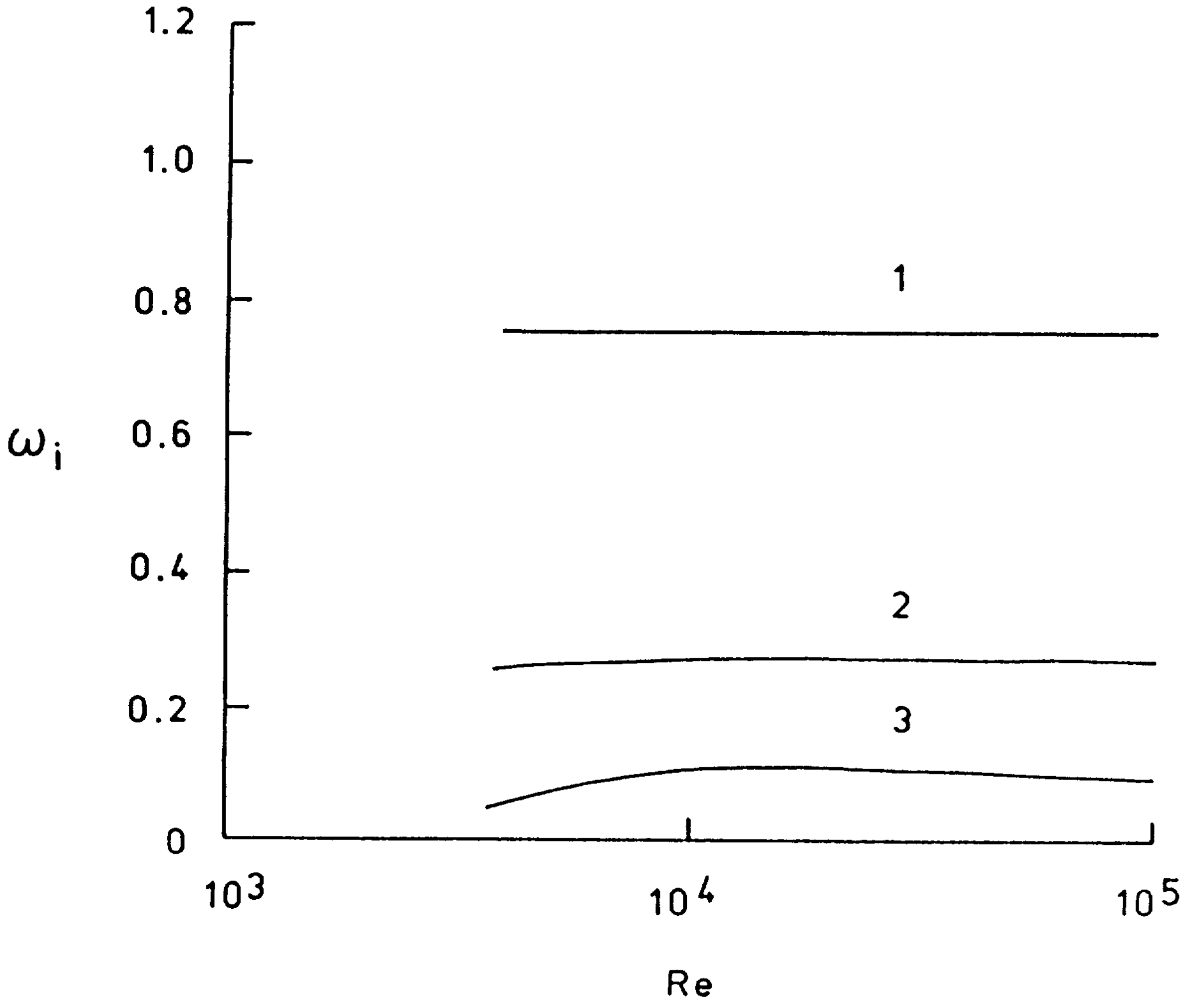

Fig. 5.54 Influence of Reynolds number on the growth rate of n = -2 disturbances for a two cell vortex. Here, α = 1.0, q = 0.8, and $\psi \neq 0$.

5.3 Stability of Three Cell Vortex at Re = 4000

Due to space limitations in this section only the variation of growth rates with α for different values of azimuthal wavenumbers are presented. In the case of the n = -4 mode, the effect of increased swirl on the instability is shown clearly. However, a detailed presentation for a three cell vortex similar in extent to that of Section 5.2 is deferred to future studies.

The three velocity components for a three cell vortex are presented in figure 5.55. Note the core expansion in the azimuthal velocity component which is caused by the flow reversal of the axial velocity on the centerline. This flow reversal has displaced the vortex from the central region and depleted the core area of any rotational kinetic energy. Hence, we expect non-parallel effects to play an important role, especially at finite Reynolds numbers.

The variation of the growth rate, ω_i, with α for the axisymmetric mode, $n = 0$, at $q = 0.19$ is shown in figure 5.56. The first mode is very similar in extent to the axisymmetric disturbance for a two cell vortex as displayed in figure 5.20. However, the second mode is peculiar since the growth rate asymptotes to a constant as α approaches zero. Further testing revealed that the second mode of instability appeared to be caused by the same mechanism discussed in the previous section in relation to figure 5.41 To test this observation, the growth rate curve was obtained again while setting $\psi = 0$, as shown in figure 5.57. The growth rate of the second mode became so small that it could not be plotted on the same scale as the first mode. It must be emphasized here that further testing is needed in order to understand the nature of this second mode of instability. Of special importance is the variation of the growth rate with Reynolds number.

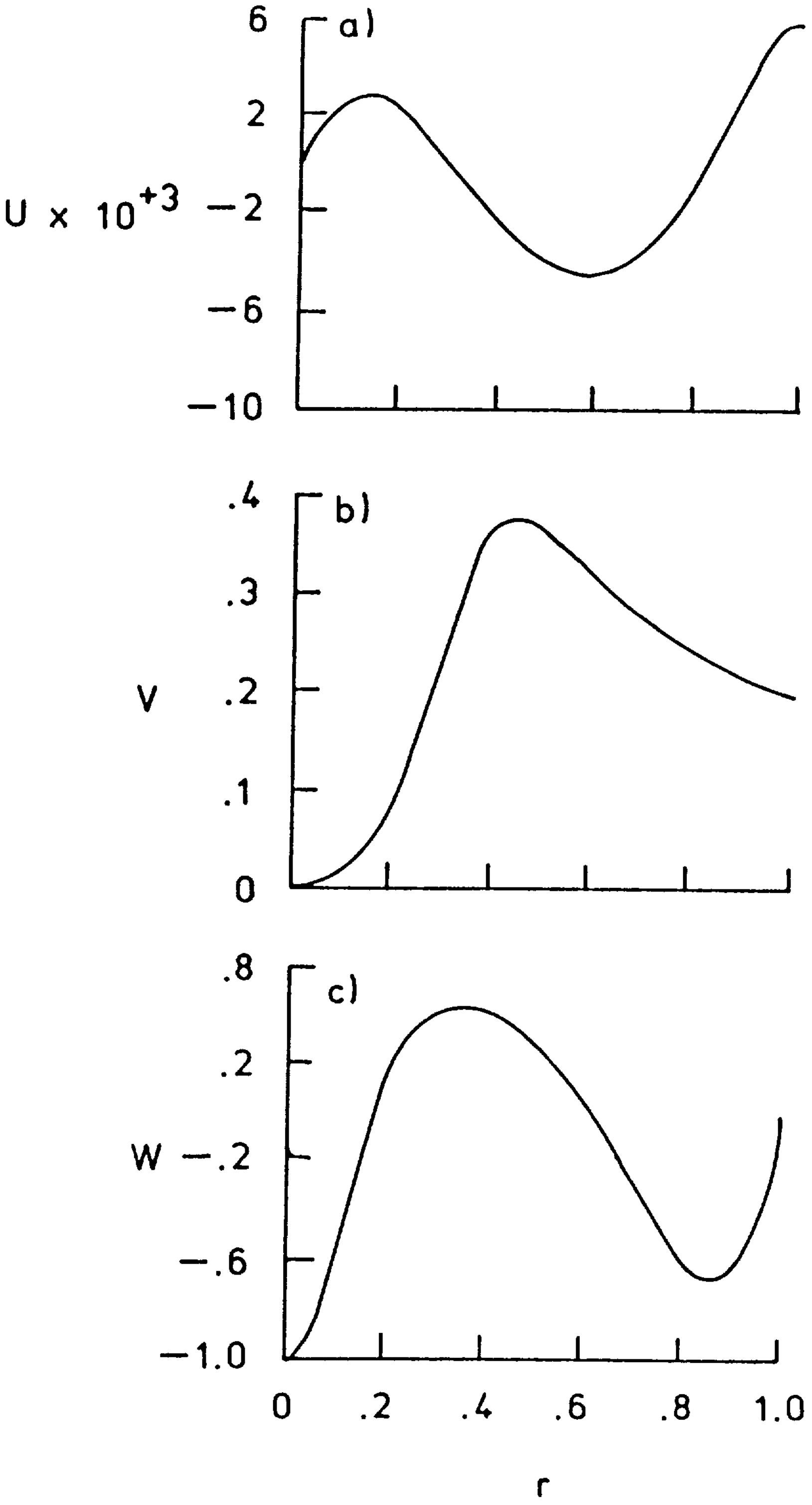

Fig. 5.55 Velocity components for a three cell vortex.

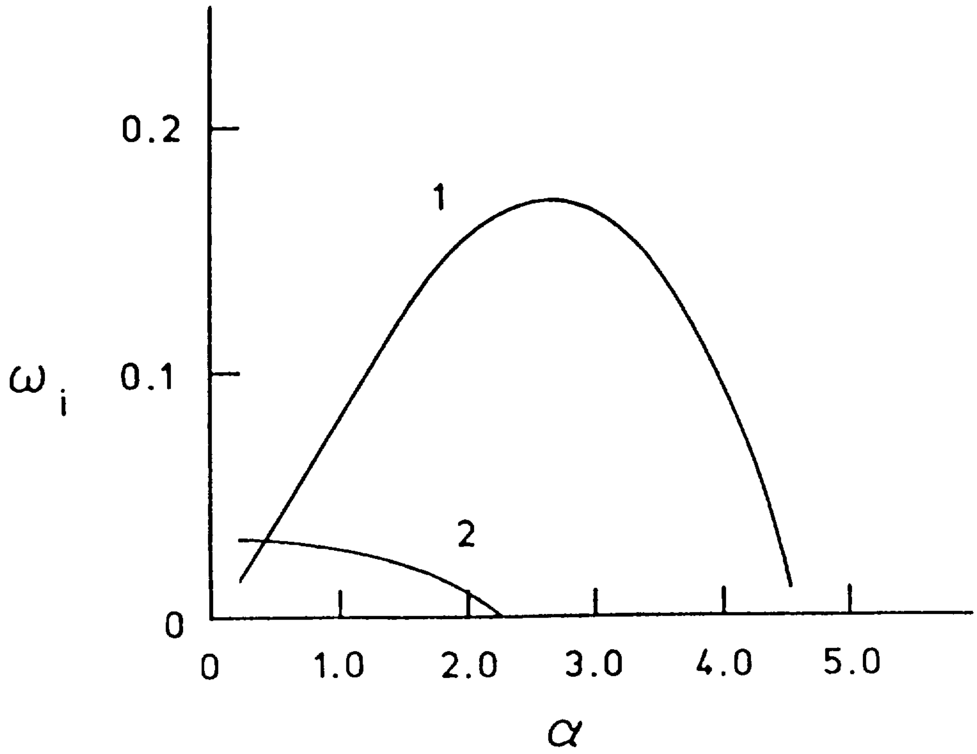

Fig. 5.56 Variation of the growth rate of axisymmetric (n = 0) disturbances with wavenumber for a three cell vortex. Here, $q = 0.19$, Re = 4000, and $\psi \neq 0$.

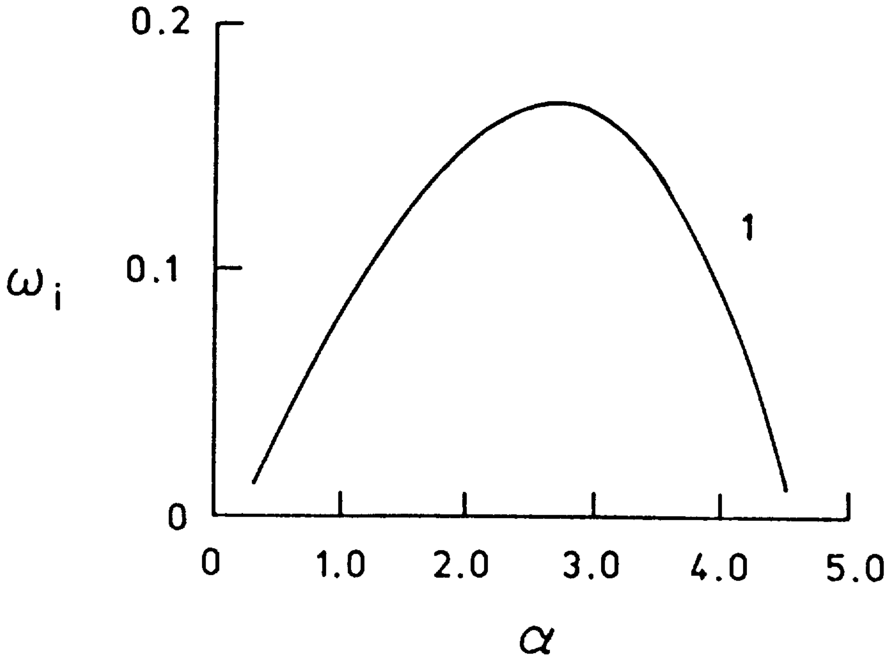

Fig. 5.57 Variation of the growth rate of axisymmetric ($n = 0$) disturbances with wavenumber for a three cell vortex. Here, $q = 0.19$, $Re = 4000$, and $\psi = 0$.

The variation of the growth rate with axial wavenumber for the asymmetric mode, $n = 1$, at $q = 0.19$ is shown in figure 5.58. The primary mode has enormous growth rates over a wide range of α. Also there is evidence of co-instabilities for the second mode. The nature of the third mode (long wave instability) makes it a prime candidate to be a viscous mode. The non-parallel term (ψ) was set equal to zero and the results are shown in figure 5.59. It is important to emphasize here that mode three did not disappear altogether, rather its amplification rate, ω_i, became very small, preventing its plot on the same scale as the other two modes. However, as in the case of axisymmetric mode, further testing is required to understand the nature of this instability. The influence of ψ on the first and second modes is negligible. Actually, in the case of $n < 0$, the parameter ψ has no drastic effect on the nature of instabilities and hence its influence will not be discussed any further in this section.

Figure 5.60 displays the variation of the growth rate with α for the $n = -1$ mode at $q = 0.19$. For this value of azimuthal wavenumber, there are two modes with comparable growth rates. Notice how different these curves are when compared to the curves obtained for the two cell vortex. Incidentally, the eigenfunctions revealed that these modes are located near the two inflectional points present in the axial velocity profile.

The behavior of growth rate with α for an $n = -2$ disturbance at $q = 0.19$ is shown in figure 5.61. The primary mode has a growth rate comparable to that of $n = -1$ perturbations as presented in the previous figure. There are signs of co-instabilities especially for the first mode. The variation of ω_i with axial wavenumber for the $n = -3$ disturbance at a swirl number of 0.19 is displayed in figure 5.62. The existence of co-instabilities is very evident.

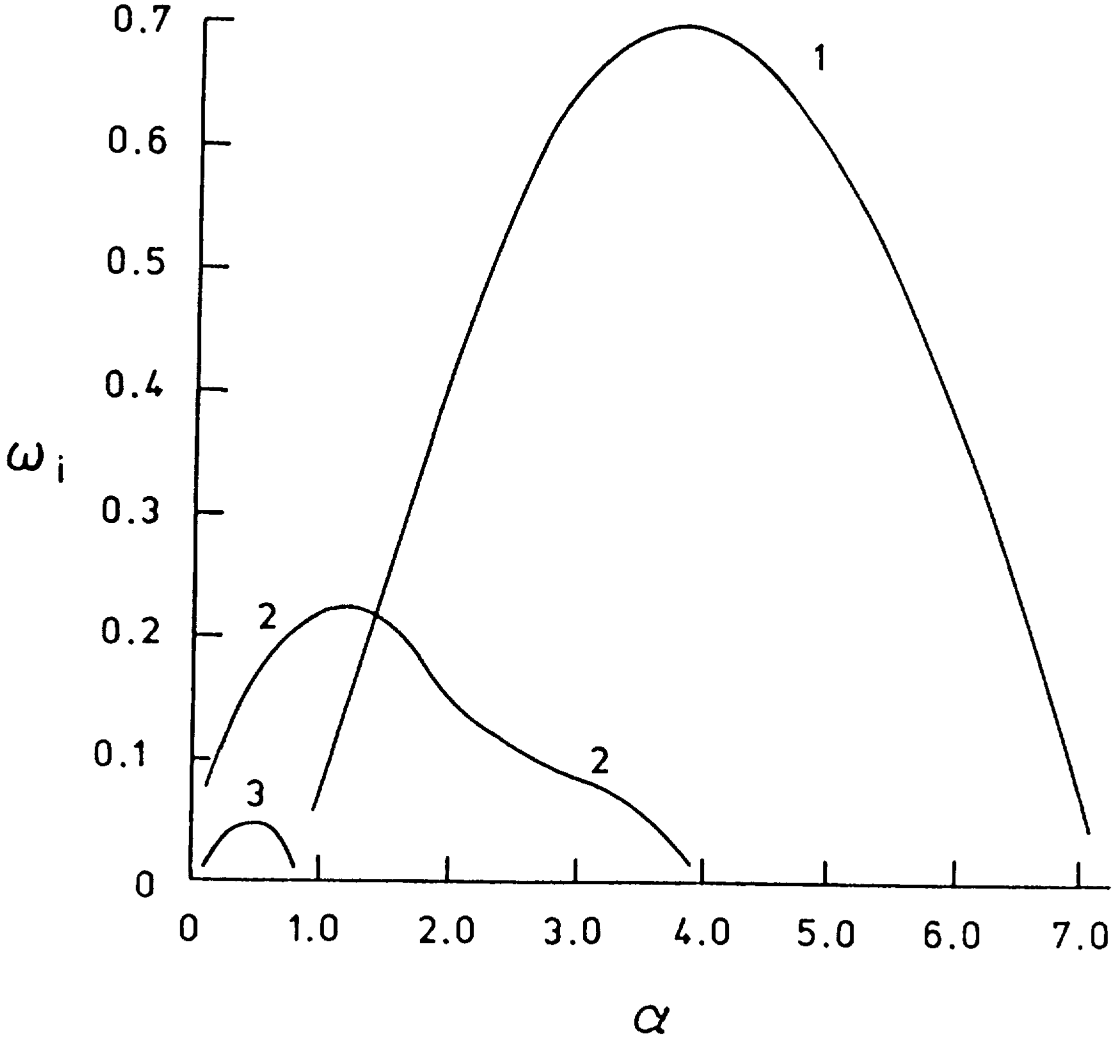

Fig. 5.58 Variation of the growth rate of asymmetric ($n = +1$) disturbances with wavenumber for a three cell vortex. Here, $q = 0.19$, $Re = 4000$, and $\psi \neq 0$.

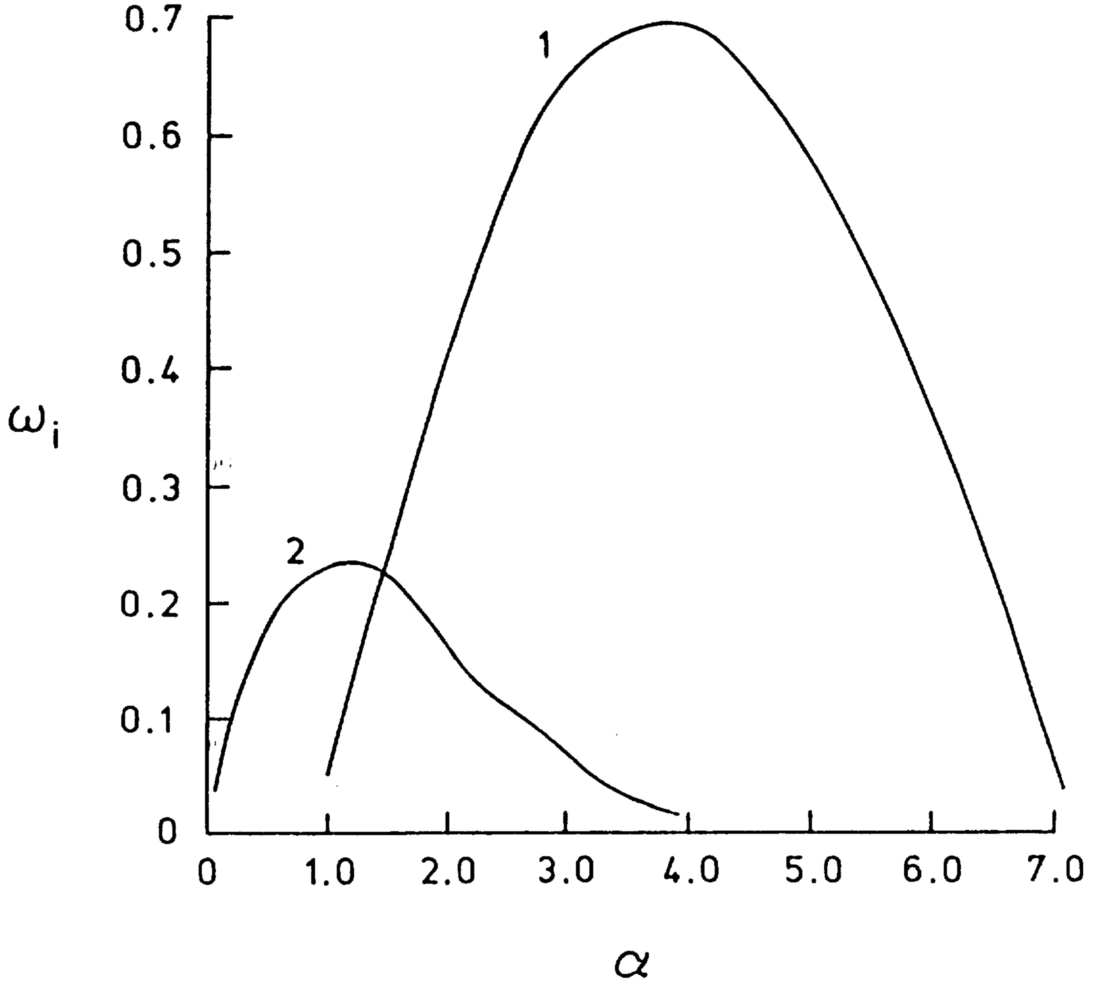

Fig. 5.59 Variation of the growth rate of asymmetric ($n = +1$) disturbance with wavenumber for a three cell vortex. Here, $q = 0.19$, $Re = 4000$, and $\psi = 0$.

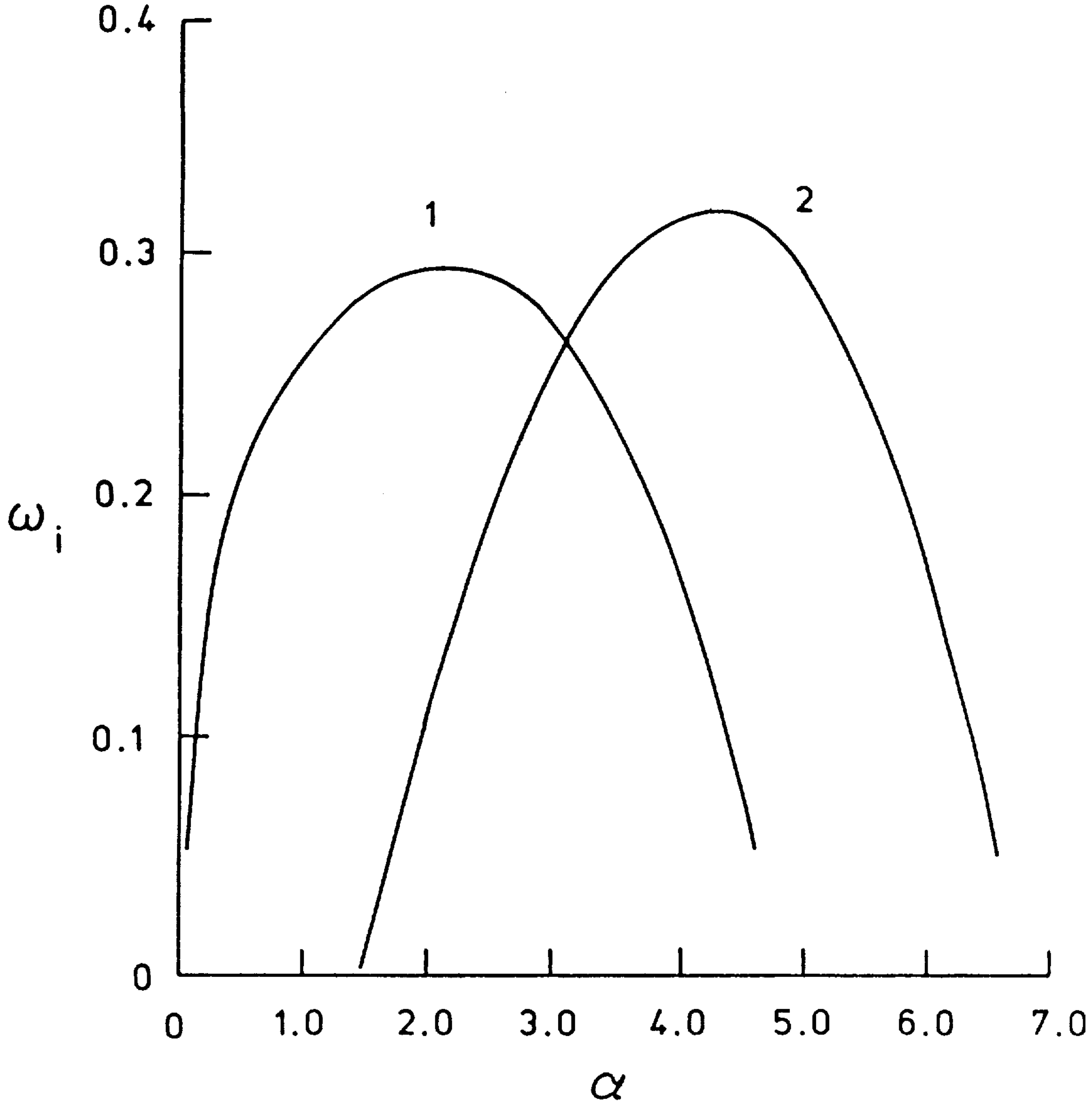

Fig. 5.60 Variation of the growth rate of asymmetric (n = -1) disturbances with wavenumber for a three cell vortex. Here, q = 0.19, Re = 4000, and $\psi \neq 0$.

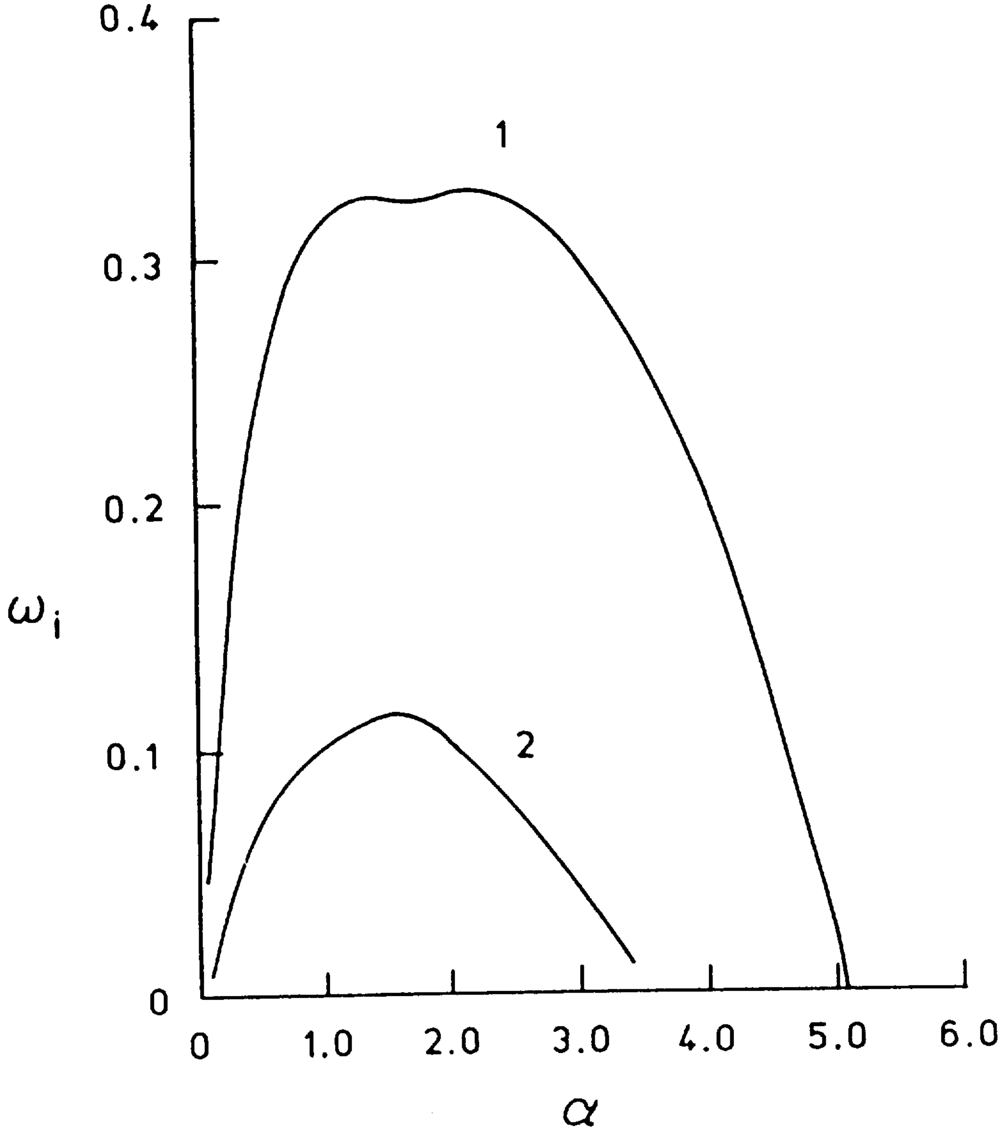

Fig. 5.61 Variation of the growth rate of $n = -2$ disturbances with wavenumber for a three cell vortex. Here, $q = 0.19$, $Re = 4000$, and $\psi \neq 0$.

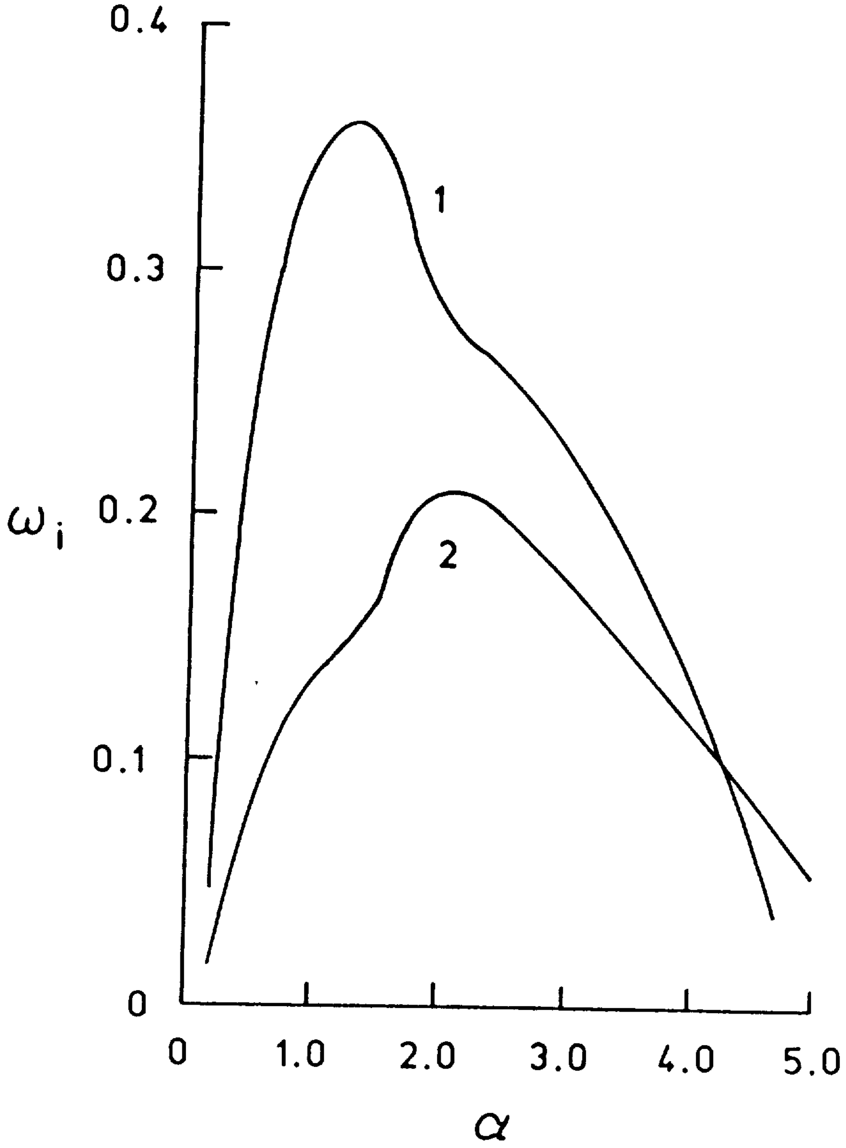

Fig. 5.62 Variation of the growth rate of $n = -3$ disturbances with wavenumber for a three cell vortex. Here, $q = 0.19$, $Re = 4000$, and $\psi \neq 0$.

Figure 5.63 displays the variation of the growth rate with α for an $n = -4$ perturbation at $q = 0.19$. Note how similar the behavior of the instability curves are compared to those of the $n = -3$ mode shown in the previous figure. Again, the co-instabilities are present for all three curves plotted in the figure. Figure 5.64 presents the results obtained at $q = 0.38$. The increase in swirl has a strong destabilizing influence on all of the modes. It has also increased the effective range of α where instabilities are present; and crossing of the second and third modes is noted. Further increases in the swirl parameter to a value of 0.57 (shown in figure 5.65) has resulted in even larger growth rates. The crossing of the second and third modes is pronounced. Additional increases in the swirl number to a value of 0.76 produces further increases in the growth rates. The results which are shown in figure 5.66 indicate that the primary mode's growth rate has very short e-folding time, attaining a maximum value of 1.22 at $\alpha \simeq 4.8$. Also, preliminary calculations indicate that in the cases of multiple cell vortices substantially more swirl is needed to stablize the flow with respect to these inviscid disturbances than is needed for a trailing line vortex.

The variation of the growth rate with axial wavenumber at $q = 0.19$ for an $n = -5$ perturbation is shown in figure 5.67. The curves show very similar behavior to those modes with lower negative azimthual wavenumbers. Finally, the variation of the growth rate with α for an $n = -10$ mode at $q = 0.19$ is presented in figure 5.68. The range of α over which the primary mode remains unstable has increased considerably. This is very much in line with the asymptotic analysis of [20, 26, 29-31] which predict that at sufficiently large negative n, the proper scaling for the disturbance axial wavenumber becomes α/n.

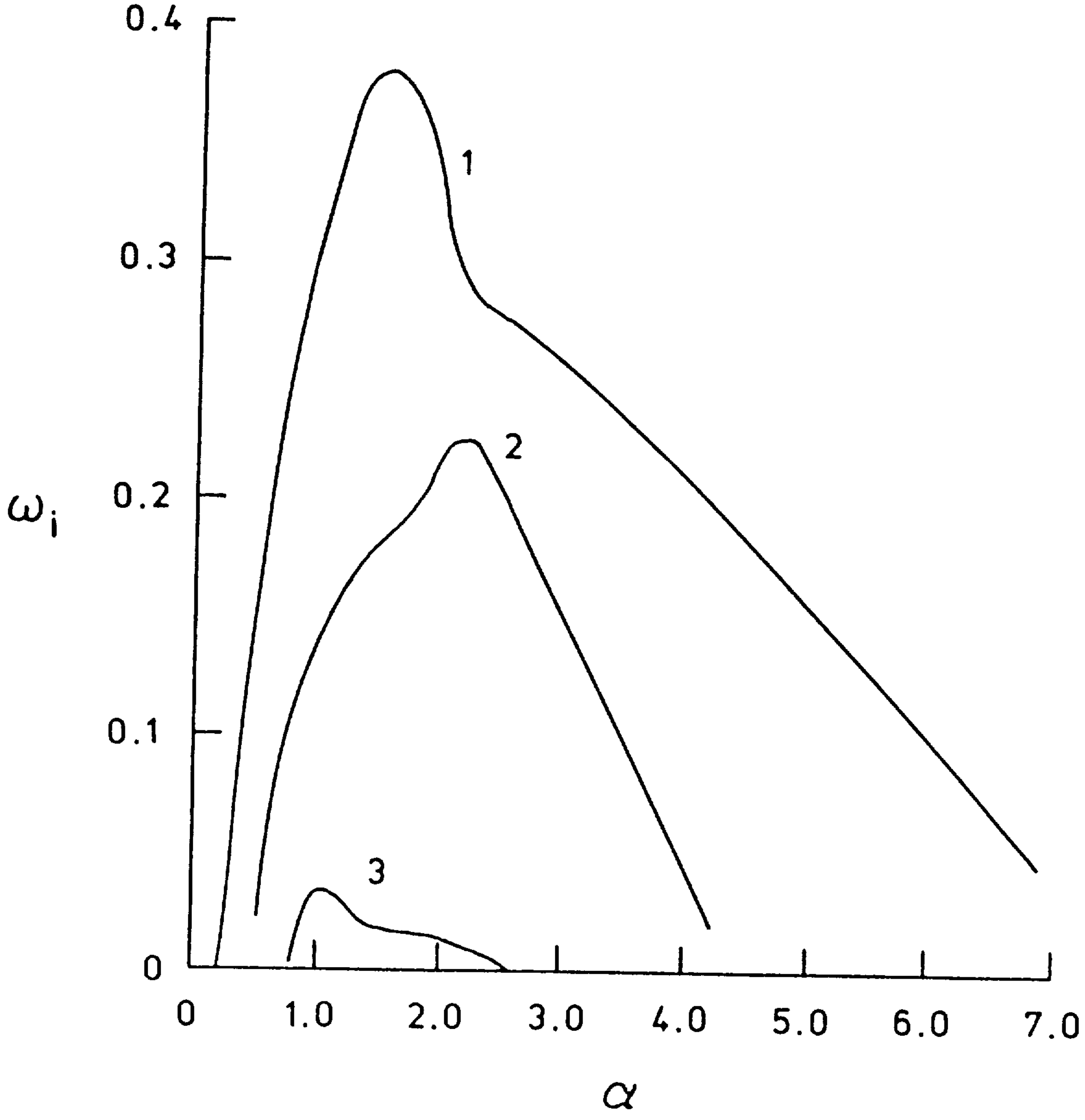

Fig. 5.63 Variation of the growth rate of $n = -4$ disturbances with wavenumber for a three cell vortex. Here, $q = 0.19$, $Re = 4000$, and $\psi \neq 0$.

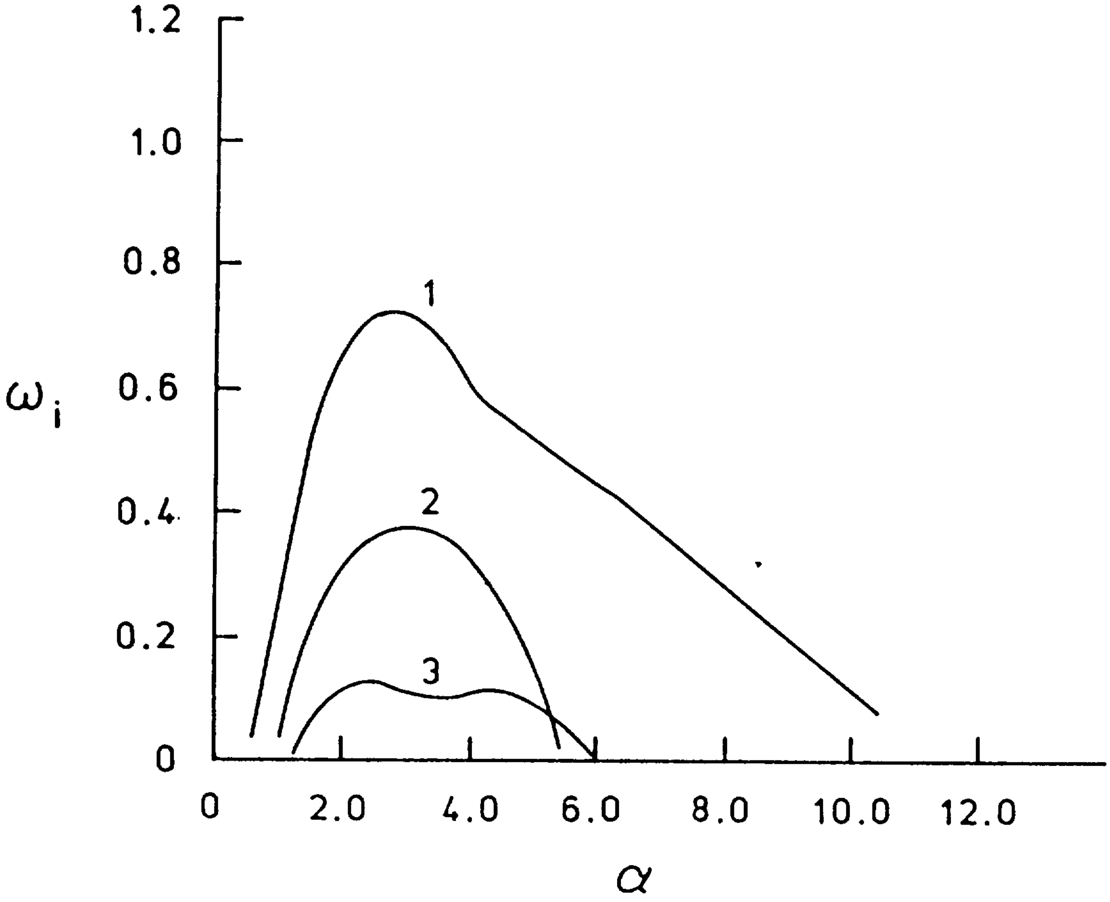

Fig. 5.64 Variation of the growth rate of $n = -4$ disturbances with wavenumber for a three cell vortex. Here, $q = 0.38$, $Re = 4000$, and $\psi \neq 0$.

C-3

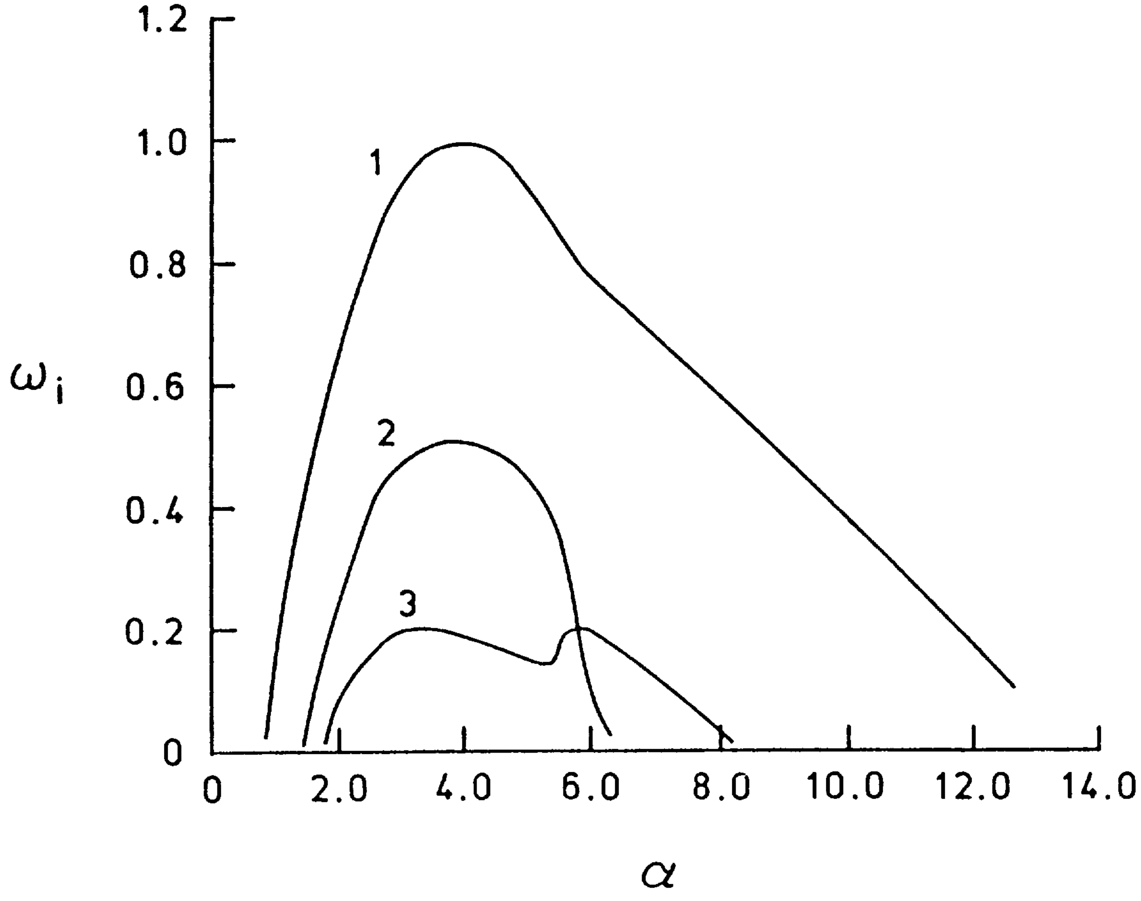

Fig. 5.65 Variation of the growth rate of $n = -4$ disturbances with wavenumber for a three cell vortex. Here, $q = 0.57$, $Re = 4000$, and $\psi \neq 0$.

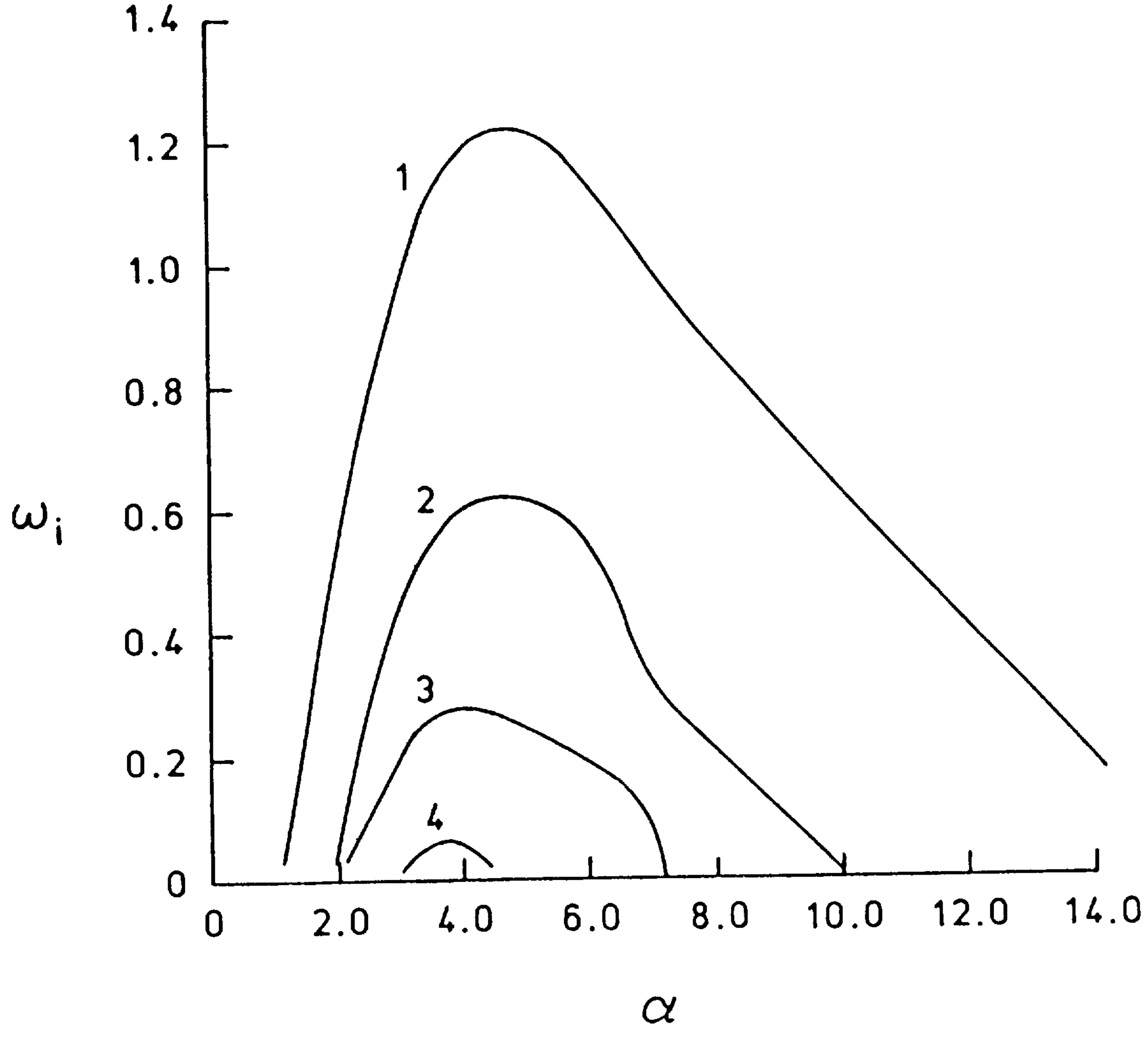

Fig. 5.66 Variation of the growth rate of $n = -4$ disturbances with wavenumber for a three cell vortex. Here, $q = 0.76$, $Re = 4000$, and $\psi \neq 0$.

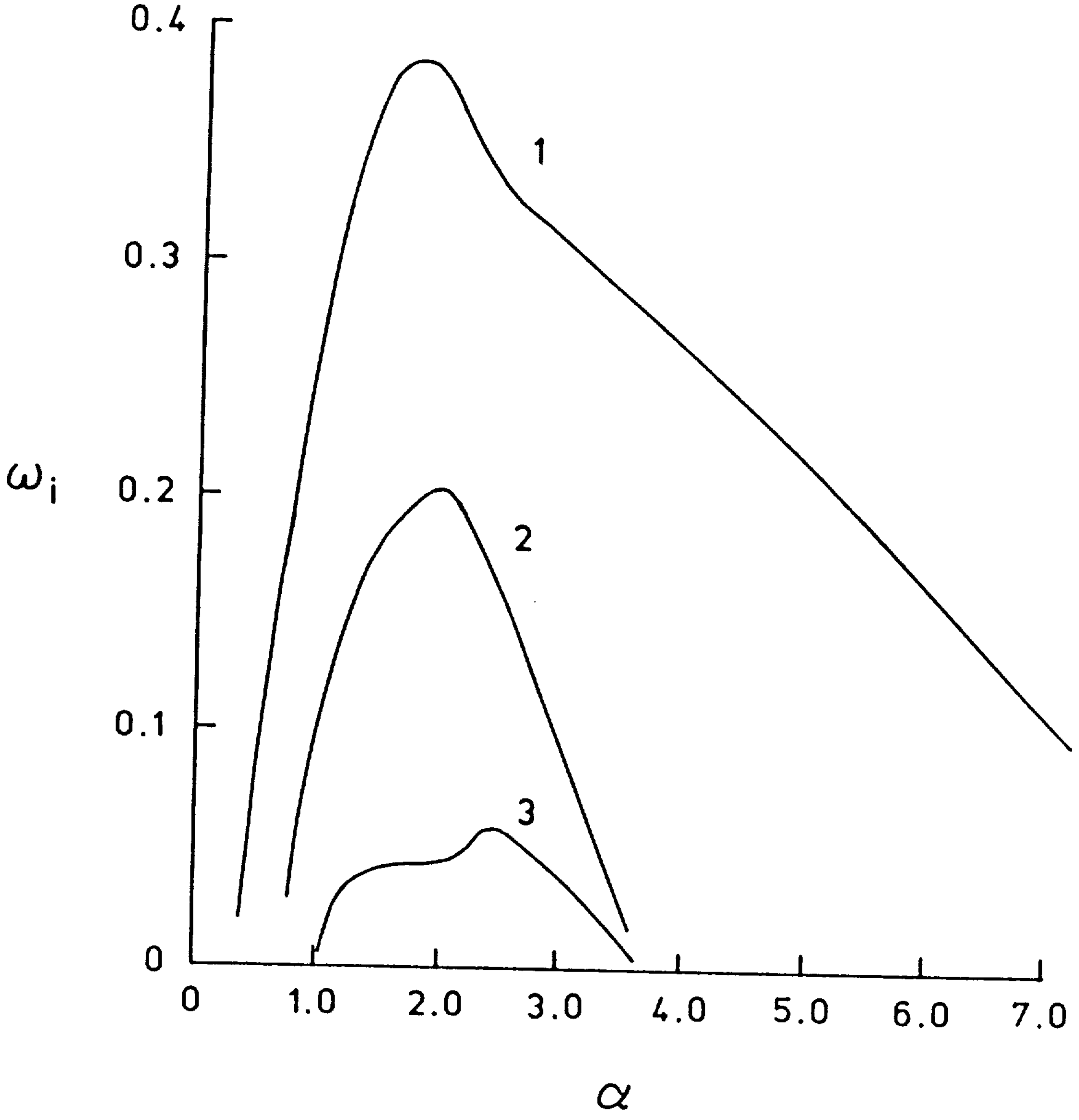

Fig. 5.67 Variation of the growth rate of $n = -5$ disturbances with wavenumber for a three cell vortex. Here, $q = 0.19$, $Re = 4000$, and $\psi \neq 0$.

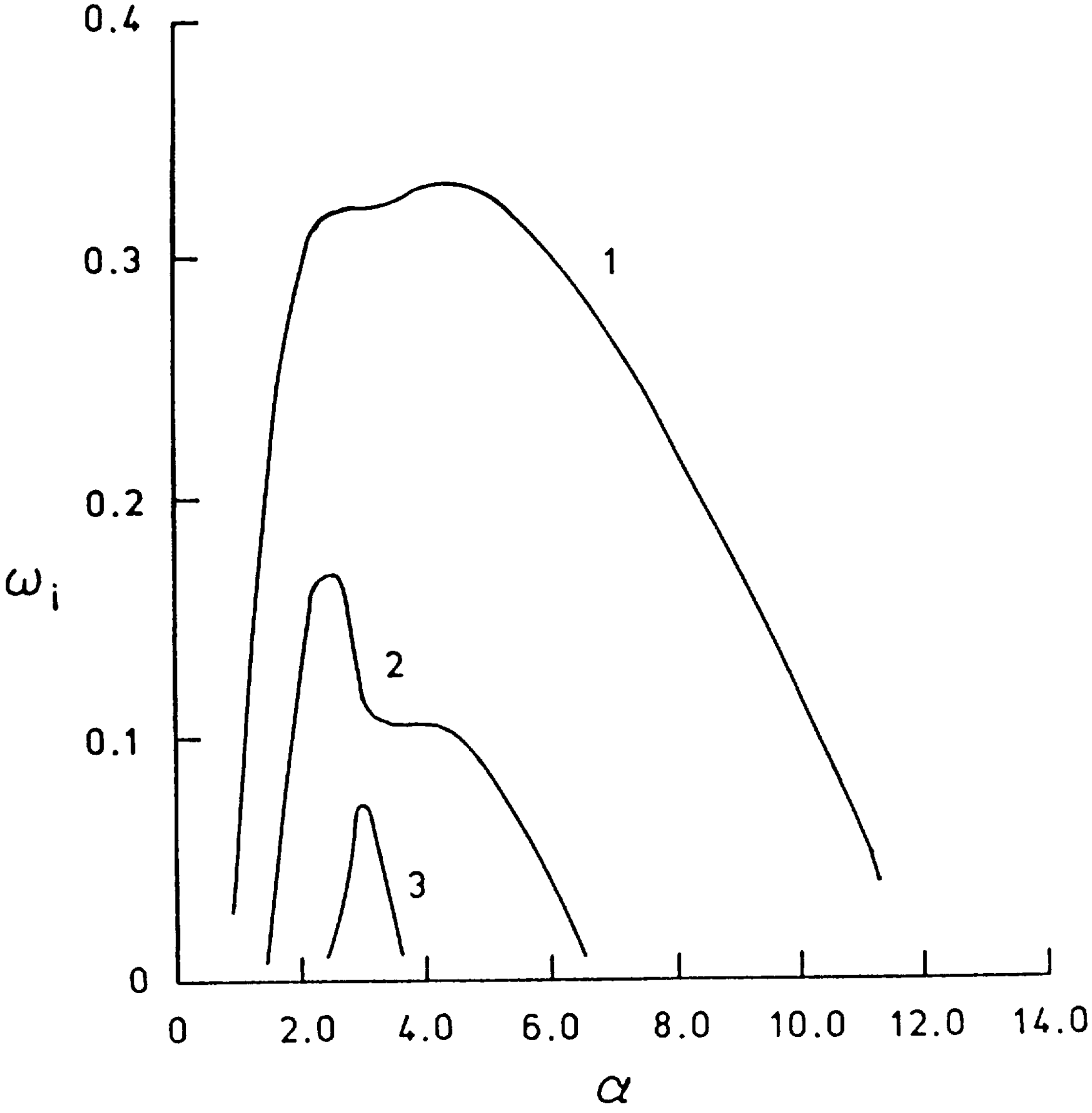

Fig. 5.68 Variation of the growth rate of $n = -10$ disturbances with wavenumber for a three cell vortex. Here, $q = 0.19$, $Re = 4000$, and $\psi \neq 0$.

One interesting observable fact here is the existence of so many significant unstable disturbances for different values of n at such a low value of the swirl parameter (q = 0.19). Also, the relatively equal strength of the various primary instabilities (we are speaking of the primary modes for different negative n) at this constant q is a bit surprising too. Both of the above features are not present for a Batchelor's vortex.

Chapter 6

CONCLUSIONS

The present study was undertaken to obtain the effects of initial mean velocity profile on the stability characteristics of a streamwise vortex with the objective of developing control and manipulation strategies for engineering applications. To that end, the temporal stability of multiple cell vortices was considered. It was shown that cell multiplicity in the vortex core has drastic effects on the stability characteristics. That is the multiple cell structure is responsive to a wide range of disturbances with different azimuthal wavenumbers. This effect is most pronounced in the case of $n > 0$ modes where previous studies of single cell trailing line vortices (as well as the two cell Long vortex) had indicated stability. Here, it was shown that multiple cell vortices are highly unstable, at least for $n = 0, +1, +2$ modes, in addition to the usual negative n modes. The enormous growth rates obtained for the axisymmetric mode ($n = 0$) was surprising since this particular type of disturbance has never been observed to be unstable before, even in the case of a two cell Long vortex. Overall, on the basis of the numerical calculations, it is concluded that the growth rates of instabilities in multiple cell vortices are substantially larger (two to three fold increases are observed) than those of a single cell trailing line vortex. It was also found that there is a substantial increase in the effective range of axial wavenumbers where instabilities are present in multiple cell vortices.

Another important feature whose existence has been shown in the present work is co-instability (short for compound instability modes). These instability modes have eigenfunctions which show features that can be characterized as center- and ring-modes as well as wall mode instability zones simultaneously. In the case of two and three cell vortices, the growth rate curves (for $n < 0$ only) possess multiple peaks (lobes) because of the co-instabilities. Although the existence of co-instability has been conjectured by previous asymptotic analyses [20, 26, 32], they had never been produced numerically.

In addition, this work has shown that viscous forces play a far greater role in vortex stability than had been believed previously. The variety of viscous modes obtained for the Batchelor vortex as well as for multiple cell vortices showed that any future stability calculations must include the effects of viscosity. Although this subtle role of viscosity was suspected by Maslowe and Stewartson [20], its extent and influence were unknown prior to this study.

These viscous disturbances, without any exceptions are long wave instabilities. Their wavelengths scale with the core radius and have maximum growth rates which are orders of magnitude smaller than the inviscid modes. However, based on experimental observation and measurements, these viscous instability modes appear to be the only physically observed modes.

Based on the present numerical calculations, multiple cell vortices have desirable instability charateristics in that breakup and dissipation of these types of trailing line vortices can be accelerated. Clearly, it is not necessary to alter the radial variation of the azimuthal component of velocity and the radial component of the velocity is quite small and probably would not be controlled. Only the axial velocity component must be modified and it is necessary to induce at least a two cell structure in the flow. The desired flow is downstream jet along the vortex axis, surrounded by an upstream flow in the outer portion of the vortex. This opportunity for accelerating vortex instability warrants further study.

The Chebyshev spectral collocation algorithm, with staggered grid, was developed to study the stability of multiple cell vortices. The method is an extension of the technique developed by Khorrami et al. [10]. The numerical stability problem has been formulated in primitive variable form, evaluating the velocity components at the grid points and staggering the pressure at the mid-grid points. The staggered pressure approach has eliminated the need for artificial pressure boundary conditions. Direct comparison with other formulations has shown that the method is robust and produces accurate results. However, comparison with the non-staggered spectral method of Khorrami et al. [10] has shown that contrary to prevailing opinion, when the artificial pressure boundary conditions are employed correctly they do not affect the accuracy or the convergence rate of the spectral methods.

While validating the accuracy and convergence behavior of the present method, two new, long wavelength viscous modes of instability for Batchelor's vortex were found. These two forms of instabilities include an axisymmetric, $n = 0$, as well as an asymmetric, $n = 1$ mode. This work has shown that the growth rates associated with these viscous disturbances are orders of magnitude less than the explosive growth rates of the inviscid perturbations. However, examination of contrail photographs [58, 62] has shown that both of these new modes can be identified in actual large trailing line vortices as well as in experimental measurements conducted in laboratory wind tunnels, [60, 61, 62]. Based on the present results, the following conclusions can be drawn:

1. Batchelor's vortex represents a good approximation to trailing line vortices and can be employed for further stability studies.

2. Although the stability calculations were conducted for a laminar vortex, the excellent agreement obtained with experimental measurements and contrail photographs, which involve mostly turbulent vortices, suggests that these long wave viscous instability modes, once activated, do not interact significantly with the surrounding turbulent field.

Finally, the numerical method used in this study can be adopted easily to include cases where density stratification or compressibility effects play an important role. From the enormous body of data on vortices in turbulent atmospheres, the role played by stratification on vortex behavior is significant. Since trailing line vortices coexist in such a background, the effects of density stratification on the instability modes must be examined.

REFERENCES

1. Howard, L. N. and Gupta, A. S., "On the Hydrodynamic and Hydromagnetic Stability of Swirling Flows," J. Fluid, Mech., Vol. 14, 1962, pp. 463-476.

2. Batchelor, G. K., "Axial Flow in the Trailing Line Vortices," J. Fluid Mech., Vol. 20, 1964, pp. 645-658.

3. Long, R. R., "Vortex Motion in a Viscous Fluid," J. Meterology, Vol. 15, 1958, pp. 108-112.

4. Long, R. R., "A Vortex in an Infinite Fluid," J. Fluid Mech., Vol. 11, 1961, pp. 611-624.

5. Leibovich, S., "Vortex Stability and Breakdown: Survey and Extension," AIAA Journal, Vol. 22, 1984, pp. 1192-1206.

6. Hall, M. G., "Vortex Breakdown," Ann. Rev. Fluid Mech., Vol. 4, 1972, pp. 195-218.

7. Hall, J. L., "An Introduction to Vortex Breakdown and Vortex Core Bursting," National Aeronautical Establishment NAE-AN-28, 1985.

8. Leibovich, S., "The Structure of Vortex Breakdown," Ann. Rev. Fluid Mech., Vol. 10, 1978, pp. 221-246.

9. Escudier, M., "Vortex Breakdown: Observations and Explanations," Prog. Aerospace Sci., Vol. 25, 1988, pp. 189-229.

10. Khorrami, M. R., Malik, M. R. and Ash, R. L., "Application of Spectral Collocation Techniques to the Stability of Swirling Flows," J. Comput. Phys., Vol. 81, 1989, pp. 206-229.

11. Rayleigh, J. W. S., "On the Dynamics of Revolving Fluids," Proc. Roy. Soc. A, Vol. 93, 1916, pp. 148-154.

12. Synge, J. L., "The Stability of Heterogeneous Liquids," Trans. Roy. Soc. Can., Vol. 27, 1933, pp. 1-18.

13. Pedley, T. J., "On the Instability of Rapidly Rotating Shear Flows to Non-axisymmetric Disturbances," J. Fluid Mech., Vol. 31, 1968, pp. 603-607.

14. Pedley, T. J., "On the Instability of Viscous Flow in a Rapidly Rotating Pipe," J. Fluid Mech., Vol. 35, 1969, pp. 97-115.

15. Metcalfe, R. W. and Orszag, S. A., "Numerical Calculation of the Linear Stability of Pipe Flows," Flow Research Report No. 25, Contract N00014-72-C-0355, 1973.

16. Maslowe, S. A., "Instability of Rigidly Rotating Flows to Non-axisymmetric Disturbances," J. Fluid Mech., Vol. 64, 1974, pp. 303-317.

17. MacKrodt, P. A., "Stability of Hagen-Poiseuille Flow with Superimposed Rigid Rotation," J. Fluid Mech., Vol. 73, 1976, pp. 153-164.

18. Cotton, F. W. and Salwen, H., "Linear Stability of Rotating Hagen-Poiseuille Flow," J. Fluid Mech., Vol. 108, 1981, pp. 101-125.

19. Duck, P. W. and Foster, M. R., "The Inviscid Stability of a Trailing Line Vortex," Z. angew. Math. Phys., Vol. 31, 1980, pp. 523-530.

20. Maslowe, S. A. and Stewartson, K., "On the Linear Inviscid Stability of Rotating Poiseuille Flow," Phys. Fluids, Vol. 25, 1982, pp. 1517-1523.

21. Ito, T., Suematsu, Y. and Hayase, T., "On the Vortex Breakdown Phenomena in Swirling Pipe Flow," Memoirs of the Faculty of Engineering, Nagoya University, Vol. 37, 1985, pp. 117-172.

22. Burggraf, O. R. and Foster, M. R., "The Stability of Tornado-Like Vortices," National Oceanic and Atmospheric Administration, PB-282 749, 1977.

23. Foster, M. R. and Duck, P. W., "The Inviscid Stability of Long's Vortex," Phys. Fluids, Vol. 25, 1982, pp. 1715-1718.

24. Lessen, M., Singh, P. J. and Paillet, F., "The Stability of a Trailing Line Vortex. Part 1. Inviscid Theory," J. Fluid Mech., Vol. 63, 1974, pp. 753-763.

25. Staley, D. O. and Gall, R. L., "Hydrodynamic Instability of Small Eddies in a Tornado Vortex," J. Atmos. Sci., Vol. 41, 1984, pp. 422-429.

26. Leibovich, S. and Stewartson, K., "A Sufficient Condition for the Instability of Columnar Vortices," J. Fluid Mech., Vol. 126, 1983, pp. 335-356.

27. Lessen, M. and Paillet, F., "The Stability of a Trailing Line Vortex. Part 2. Viscous Theory," J. Fluid Mech., Vol. 65, 1974, pp. 769-779.

28. Emanuel, K. A., "A Note on the Stability of Columnar Vortices," J. Fluid Mech., Vol. 145, 1984, pp. 235-238.

29. Stewartson, K., "The Stability of Swirling Flows at Large Reynolds Number when Subjected to Disturbances with Large Azimuthal Wavenumber," Phys. Fluids, Vol. 25, 1982, pp. 1953-1957.

30. Stewartson, K. and Capell, K., "On the Stability of Ring Modes in a Trailing Line Vortex: the Upper Neutral Points," J. Fluid Mech., Vol. 156, 1985, pp. 369-386.

31. Stewartson, K. and Brown, S. N., "Near-Neutral Centre-Modes as Inviscid Perturbations to a Trailing Line Vortex," J. Fluid Mech., Vol. 156, 1985, pp. 387-399.

32. Duck, P. W., "The Inviscid Stability of Swirling Flows: Large Wavenumber Disturbances," Z. angew. Math. Phys., Vol. 37, 1986, pp. 340-360.

33. Donaldson, C. P. and Sullivan, R. D., "Examination of the Solutions of the Navier-Stokes Equations for a Class of Three-Dimensional Vortices, Part I: Velocity Distributions for Steady Motion," Aeronautical Research Associates of Princeton, AFOSR TN 60-1227, 1960.

34. Adams, G. N. and Gilmore, D. C., "Some Observations of Vortex Core Structure," Canad. Aeronaut. Space J., Vol. 18, 1972, pp. 159-162.

35. Leuchter, O. and Solignac, J. L., "Experimental Investigation of the Turbulent Structure of Vortex Wakes," ONERA, TP, No. 1983-107, 1983.

36. Graham, J. A. H. and Newman, B. G., "Turbulent Trailing Vortex with Central Jet and Wake," The Ninth Congress of the International Council of the Aeronautical Sciences, ICAS No. 74-40, 1974.

37. Saric, W. S. and Nayfeh, A. H., "Nonparallel Stability of Boundary-Layer Flows," Phys. Fluids, Vol. 18, 1975, pp. 945-950.

38. Leonard, A. and Wray, A., "New Numerical Method for the Simulation of Three-Dimensional Flow in a Pipe," Proceedings of 8th International Conference on Numerical Methods in Fluid Dynamics, Lecture Notes in Physics 170, (Edited by E. Krause), Springer-Verlag, Berlin, 1982, pp. 335-342.

39. Orszag, S. A. and Patera, A. T., "Secondary Instability of Wall-Bounded Shear Flows," J. Fluid Mech., Vol. 128, 1983, pp. 347-385.

40. Batchelor, G. K. and Gill, A. E., "Analysis of the Stability of Axisymmetric Jets," J. Fluid Mech., Vol. 14, 1962, pp. 529-551.

41. Orszag, S. A., "Accurate Solution of the Orr-Sommerfeld Stability Equation," J. Fluid Mech., Vol. 50, 1971, pp. 689-703.

42. Zebib, A., "A Chebyshev Method for the Solution of Boundary Value Problems," J. Comput. Phys., Vol. 53, 1984, pp. 443-455.

43. Bridges, T. J. and Morris, P. J., "Differential Eigenvalue Problems in Which the Parameter Appears Nonlinearly," J. Comput. Phys., Vol. 55, 1984, pp. 437-460.

44. IMSL, IMSL Library, 9 edn. International Mathematical and Statistical Libraries Inc., 2500 City West Boulevard, Houston, TX 77042-3020, U.S.A., 1978.

45. Orszag, S. A. and Israeli, M., "Numerical Simulation of Viscous Incompressible Flows," Ann. Rev. Fluid Mech., Vol. 6, 1974, pp. 281-318.

46. Lanczos, C., "Applied Analysis," Prentice Hall, Englewood Cliffs, NJ, 1964.

47. Fox, L. and Parker, I. B., "Chebyshev Polynomials in Numerical Analysis," Oxford University Press, London, 1968.

48. Gottlieb, D. and Orszag, S. A., "Numerical Analysis of Spectral Methods: Theory and Applications," Soc. Indus. & Appl. Math., Philadelphia, 1977.

49. Hussaini, M. Y., Streett, C. L. and Zang, T. A., "Spectral Methods for Partial Differential Equations," Transactions of the First Army Conference on Applied Mathematics and Computing, ARO Report 84-1, U.S. Army, Feb. 1984, pp. 883-925.

50. Gottlieb, D., Hussaini, M. Y. and Orszag, S. A., "Theory and Applications of Spectral Methods," in Spectral Methods for Partial Differential Equations, (Edited by R. G. Voight, D. Gottlieb and M. Y. Hussaini) Soc. Indus. & Appl. Math., Philadelphia, 1984, p. 1.

51. Malik, M. R. and Poll, D. I. A., "Effect of Curvature on Three-Dimensional Boundary-Layer Stability," AIAA Journal, Vol. 23, pp. 1362-1369.

52. Wilkinson, J. H., "The Algebraic Eignevalue Problem," Oxford University Press, Fair Lawn, NJ, 1965.

53. Lessen, M., Sadler, S. G. and Liu, T. Y., "Stability of Pipe Poiseuille Flow," Phys. Fluids, Vol. 11, 1968, pp. 1404-1409.

54. Salwen, H., Cotton, F. W. and Grosch, C. E., "Linear Stability of Poiseuille Flow in Circular Pipe," J. Fluid Mech., Vol. 98, 1980, pp. 273-284.

55. Malik, M. R., Zang, T. A. and Hussaini, M. Y., "A Spectral Collocation Method for the Navier-Stokes Equations," J. Comput. Phys., Vol. 61, 1985, pp. 64-88.

56. Grosch, C. E. and Orszag, S. A., "Numerical Solution of Problems in Unbounded Regions: Coordinate Transforms," J. Comput. Phys., Vol. 25, 1977, pp. 273-296.

57. Paillet, F., "Hydrodynamic Stability of an Axisymmetric Swirling Wake," Ph.D. Dissertation, The University of Rochester, Rochester, New York, 1973.

58. Bisgood, P. L., "Some Observations of Condensation Trails," Royal Aircraft Establishment TM FS 330, 1980.

59. Crow, S. C., "Stability Theory for a Pair of Trailing Vortices," AIAA Journal, Vol. 8, 1970, pp. 2172-2179.

60. Sarpkaya, T. and Daly, J. J., "Effect of Ambient Turbulence on Trailing Vortices," AIAA Journal of Aircraft, Vol. 24, 1987, pp. 399-404.

61. Singh, P. I. and Uberoi, M. S., "Experiments on Vortex Stability," Phys. Fluids, Vol. 19, 1976, pp. 1858-1863.

62. Strange, C. and Harvey, J. K., "Instabilities in Trailing Vortices: Flow Visualization Using Hot-Wire Anemometry," AGARD-CP-342, 1983.

Report Documentation Page

1. Report No. NASA CR-4261	2. Government Accession No.	3. Recipient's Catalog No.
4. Title and Subtitle A STUDY OF THE TEMPORAL STABILITY OF MULTIPLE CELL VORTICES		5. Report Date November 1989
		6. Performing Organization Code
7. Author(s) MEHDI R. KHORRAMI		8. Performing Organization Report No.
		10. Work Unit No. 505-60-31-07
9. Performing Organization Name and Address OLD DOMINION UNIVERSITY RESEARCH FOUNDATION P.O. BOX 6369 NORFOLK, VIRGINIA 23508-0369		11. Contract or Grant No. NAG1-530
		13. Type of Report and Period Covered CONTRACTOR REPORT
12. Sponsoring Agency Name and Address NATIONAL AERONAUTICS AND SPACE ADMINISTRATION LANGLEY RESEARCH CENTER HAMPTON, VIRGINIA 23665-5225		14. Sponsoring Agency Code

15. Supplementary Notes

PRINCIPAL INVESTIGATOR: ROBERT L. ASH

LANGLEY TECHNICAL MONITOR: JOHN B. ANDERS, JR.

PROGRESS REPORT FOR THE PERIOD ENDING 10/31/88

16. Abstract

The present study documents in detail the effect of initial mean velocity field on the stability characteristics of longitudinal vortices. The temporal stability of isolated multiple cell vortices is considered. The types of vortices studied in this work include single cell as well as two and three cell vortices. It is shown that cell multiplicity in the vortex core has drastic effects on the stability characteristics. On the basis of numerical calculations, it is concluded that the growth rates of instabilities in multiple cell vortices are substantially larger (two to three fold increases are observed) than those of a single cell vortex. It is also determined that there is a substantial increase in the effective range of axial and azimuthal wavenumbers where instabilities are present, but of most importance is the appearance of a variety of viscous modes of instability. In the case of vortices, these latter instabilities which highlight the importance of viscous forces have never been reported before. For the case of a two cell vortex, these effects are discussed in detail.

17. Key Words (Suggested by Author(s)) VORTEX STABILITY, MULTIPLE CELL VORTICES, SPECTRAL COLLOCATION	18. Distribution Statement UNCLASSIFIED - UNLIMITED SUBJECT CATEGORY 34

19. Security Classif. (of this report) UNCLASSIFIED	20. Security Classif. (of this page) UNCLASSIFIED	21. No. of pages 212	22. Price A10

NASA FORM 1626 OCT 86

NASA-Langley, 1989

For sale by the National Technical Information Service, Springfield, Virginia 22161-2171

☆U.S.GOVERNMENT PRINTING OFFICE:1989-727-064:06006